Okinawa Institute of Science and Technology Graduate University

Thesis submitted for the degree

Doctor of Philosophy

Scanning Probe Microscopy Studies of Metal Halide Perovskite Materials

By

Afshan Jamshaid

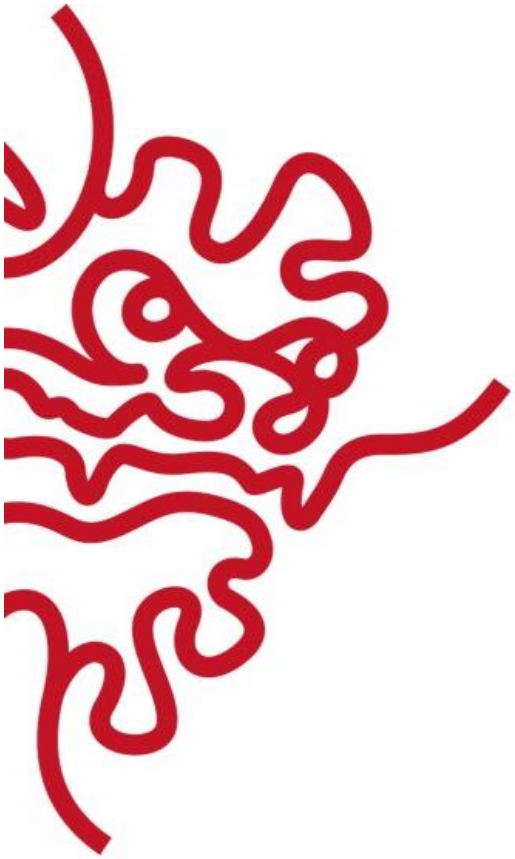

Supervisor: Yabing Qi

May 2021

Declaration of Original and Sole Authorship

I, Afshan Jamshaid, declare that this thesis entitled "Scanning Probe Microscopy studies of Metal Halide Perovskite" and the data presented in it are original and my own work.

I confirm that:

- No part of this work has previously been submitted for a degree at this or any other university.
- References to the work of others have been clearly acknowledged. Quotations from the work of others have been clearly indicated, and attributed to them.
- In cases where others have contributed to part of this work, such contribution has been clearly acknowledged and distinguished from my own work.
- The authorization from co-authors have been obtained for all co-authored work presented in this thesis.
- None of this work has been previously published elsewhere, with the exception of the following: Chapter 3 "Revealing the Atomic-level Topographies of MAI Stripe and Non-Stripe Structures, PbI_2 Stripe and Hexagonal Random Structures, and $MAPbI_3$ Perovskite" has been presented in the following conferences as following:

1. **Afshan Jamshaid,** Robin Ohmann, Jeremy Hieulle, Collin Stecker, Luis K. Ono, Yabing Qi. Atomic-Scale Analysis & Electronic Properties Characterization of $MAPbI_3$ Perovskite Material.Apr 23, 2019. MRS **(Oral Presentation)**.
2. **Afshan Jamshaid**, Robin Ohmann, Jeremy Hieulle, Collin Stecker, Luis K. Ono, Yabing Qi. Atomic-Scale Analysis of Perovskite $CH_3NH_3PbI_3$ Ultra-Thin Films by Scanning Tunneling Microscopy.Apr 22, 2019. MRS **(Oral Presentation)**.
3. **Afshan Jamshaid,** Robin Ohmann, Jeremy Hieulle, Collin Stecker, Luis K. Ono, Yabing Qi. Atomic-Scale Analysis of Perovskite $MAPbI_3$ for Light-Emitting Applications. Apr 25, 2019. MRS MRS **(Oral Presentation).**
4. **Afshan Jamshaid**, Robin Ohmann, Jeremy Hieulle, Collin Stecker, Luis K. Ono, Yabing Qi. Atomic-Scale Analysis of C $CH_3NH_3PbI_3$ by Scanning Tunneling Microscopy and X-Ray Photoelectron Spectroscopy. May 28, 2018, International Conference and Exhibition on Materials Science and Engineering Osaka Japan **(Oral Presentation).**
5. **Afshan Jamshaid,** Robin Ohmann, Jeremy Hieulle, Collin Stecker, Luis K. Ono, Yabing Qi. $CH_3NH_3PbI_3$ Atomic-Scale Analysis by Scanning Tunneling Microscopy and X-Ray Photoelectron Spectroscopy. Jan 22, 2018. International Symposium on Energy Science and Technology, OIST, Okinawa Japan **(Oral Presentation).**

Date: 12th May 2021.

Signature: 

Abstract

This thesis discusses the understanding of the structural and electronic properties of metal halide perovskite materials (e.g., $CH_3NH_3PbI_3$) as well as the interaction with additive materials at the atomic scale. Metal halide perovskite materials are currently at the core of attention because of their high-efficiency attainable when utilized in solar cell applications as well as lost fabrication cost. However, the stability of these perovskite materials and perovskite-based solar cells is still a major challenge. The proposed atomic-scale research helps address the thermal instability and ambient air induced degradation issues commonly observed in perovskites. Incorporation of additive materials into the perovskite was reported to be an efficient strategy to enhance the stability. Cl and KI have been found to be eligible candidates but studies on the fundamental processes at the atomic scale of these additives are scarce. Therefore, we comprehensively investigated Cl incorporation in $MAPbI_3$ at the atomic scale by combining scanning tunneling microscopy (STM), X-ray photoelectron, ultraviolet, and inverse photoemission spectroscopy. For the Cl concentration of 14.8 ± 0.6%, STM images confirm the presence of Cl ions on the $MAPbI_3$ ($MAPbI_{2.59}Cl_{0.21}$) surface leading to the highest surface stability found from the viewpoint of both thermodynamics and kinetics by density functional theory and molecular dynamics calculations. This study evidence that Cl can substitute I ions of the surface structure and/or fill the surface I-vacancies and further enhance the structural stability of $MAPbI_3$. Upon the $PbCl_2$ deposition on $MAPbI_3$, only Cl ions were observed in $MAPbI_3$ surface crystal structure while Pb ions were not observed by LT-STM. Before investigating the $PbCl_2$ interaction with $MAPbI_3$, the atomic structures of metallic-Pb and $PbCl_2$ on Au (111) substrate need be studied by LT-STM. For the $PbCl_2$/Au (111) system, a myriad of structures such as the intact form of $PbCl_2$ as well as dissociated species in the forms of Cl ions, Cl-Cl dimer, Pb, and Pb-Pb dimers were observed. Furthermore, the KI additive was investigated by LT-STM, which reveals the I-I square atomic structure. After deposition protocol optimization, KI was deposited on $MAPbI_3$ and characterized by XPS confirming K incorporation in $MAPbI_3$. As a future plan, LT-STM studies can be conducted to find the optimal concentration of KI for enhancing the $MAPbI_3$ surface stability. Also, it is important to point out that STM can be used to characterize mainly the surface atomic structures of perovskite materials.

Acknowledgments

First, I would like to greatly appreciate my supervisor, Prof. Yabing Qi, for his always strong experimental and moral support and for providing me the best supervision during the 4 years of Ph.D. at his lab. He was always there in every rough and tough situation during experiments with his full support and to make the best researcher and scientist out of me with his sharpened scientific knowledge. My very special thanks to our group leader Dr. Luis K. Ono for being the best teacher who patiently taught me STM and trained me over UHV systems with his strong technical skills for my experiments. He provided me the best scientific mentorship throughout my Ph.D. journey. I am very grateful for his all-fruitful scientific discussions and supporting my new, crazy ideas, and being available all the time to teach me data analysis and helped me in instruments troubleshooting. Additionally, I thank Prof. Yoshinori Okada and Prof. Pinaki Chakraborty for reviewing my research progress annually and provided the valuable feedback on my research.

I would like to thank all the current and former group members of the Energy Materials and Surface Sciences Unit. From you all, I learned a lot during working in a lab and having lunch together every day. I would also like to thank my DFT collaborators for their great calculations in Chapter 3 and 4. Furthermore, I thank Dr. Jesse Everett for helping in proofreading my thesis.

I am grateful to the OIST for providing me an opportunity to be a part of this great scientist's family, who always work together and finds new ways to explore fundamental sciences in every preeminent way.

Finally, I would like to acknowledge my parents Jamshaid Khan and Mussarat Jamshaid for their endless efforts, and brother Ashhad Jamshaid and sister Ana Sadaf Jamshaid for providing me a shoulder anytime in my every stressful time. Last but not least, thanks to my adorable niece Safa Zubair, nephews Ahyan Asjad, Azlan Asjad, and Sarim Zubair to make me cheer up with their innocent and lovely moves.

I am greatly thankful to my friends Amine Betul Nuriseria Aladag, Swathy Babu, Manana Kutsia, Jigyasa Arora, and Maira Pasha for their time and emotional support to help me stay balanced during my time here at OIST.

List of Abbreviations

Au (111)	Gold single crystal
CB (M)	Conduction Band (Minimum)
DFT	Density Function Theory
DOS	Density of States
Es	Surface Energy
E_T	Total Energy
ETL	Electron Transport Layer
Fm	Fermi Level
FTIR	Fourier Transform Infrared Spectroscopy
FTO	Fluorine-doped Tin Oxide
GCIB	Gas Cluster ion Beam
GB	Grain Boundary
HTL	Hole Transport Layer
IE	Ionization Energy
IPES	Inverse Photoelectron Spectroscopy
ITO	Indium-doped Tin Oxide
Jsc	Short-circuit current
K-cell	Knudsen Cell
KI	Potassium Iodide
MA	Methylammonium
MAI	Methylammonium Iodide
$MAPbBr_3$	Methylammonium Lead Bromide
$MAPbI_3$	Methylammonium Lead Iodide
MD	Molecular Dynamics
OHP	Organic-inorganic Hybrid Perovskite
Pb	Lead
$PbBr_2$	Lead Bromide
$PbCl_2$	Lead Chloride
PbI_2	Lead Iodide
PCBM	Phenyl-C61-Butyric acid Methyl ester
PCE	Power Conversion Efficiency
PEDOT: PSS	poly (3,4ethylenedioxythiophene): polystyrene sulfonate
PES	Photoelectron Spectroscope
PSCs	Perovskite Solar Cells
PTAA	poly (triarlyamine)
PVSK	Perovskite
QCM	Quartz Crystal Microbalance
Sn	Tin
SnO_2	Tin Oxide
Spiro-MeOTAD	2,2′,7,7′-tetrakis(*N*,*N*-di-*p*-methoxyphenylamine)-9,9′-spirobifluorene
STM	Scanning Tunneling Microscope
STS	Scanning Tunneling Spectroscopy
TiO_2	Titanium Dioxide
UHV	Ultra High Vacuum

UPS	Ultraviolet Photoelectron Spectroscopy
VB (M)	Valence Band (Maximum)
Voc	Open-circuit voltage
XPS	X-ray Photoelectron Spectroscopy

Table of Contents

List of Figures and Tables

Chapter 1: General Introduction

1.1 Introduction

The current worldwide estimated power consumption of machines and gadgets is 13 TW, and is expected to go up more than 10 TW in the next 40 years. Three viable resources are available to fulfill this energy requirement. Among them, the solar energy is the only abundant and freely available source. Solar cells are used to convert sunlight into electrical energy. The lack of flexibility and transparency are limitations of the first generation Si-based solar cell applications. From the second generation, GaAs solar cells had limitations of either high cost or lower power conversion efficiency. CIGS, CdTe and a-Si:H are thin film solar cells from the second generation. a-Si:H solar cells are less important due to low power conversion efficiency of 12% and light induced degradation [1]. The third generation is organic-inorganic hybrid perovskite solar cells, which offer prospects of higher power conversion efficiency and a low-cost fabrication process in comparison with the previous generation of solar cells [2]. In this chapter, I conduct a literature review of perovskite (PVSK) materials, solar cells, existing challenging issues and the impact of additives on the improved stability of PVSK solar cells (PSCs) and the motivation of my PhD thesis research. At the end of this chapter, I will also summarize this thesis with a brief description of thesis chapters.

1.2 Organic-inorganic hybrid PSCs

In 2009, Kojima et al. used PVSKs for the first time as a light absorber in solar cells [3]. Since then, the PSCs have gained an intensive research interest in academia, due to rapidly increased efficiency from 3.8% [3] to an impressive 25.6% [4]. In addition, organic inorganic hybrid PSCs possess a high absorption coefficient [5], low-cost fabrication process, and material availability [6]. Numerous perovskite materials such as $MAPbI_3$, $FAPbBr_3$, $MAPbBr_3$, $CsPbI_3$, $MAPbI_{3-x}Br_3$, and $MASnI_3$ (MA = Methylammonium and FA = formamidinium) are used for PV (photovoltaic) applications. Among these, perovskite materials, methyl ammonium lead iodide ($MAPbI_3$) is the archetypical material, which has interesting optical and electronic properties [7] and have led to the advent of new low-cost photovoltaic (PV) technology, which can be a possible competitor to the commercially available silicon-based solar cells. This rapid rise in achievable efficiencies was realized through optimization of processing conditions and cell architectures, a better understanding of film morphology and charge transport properties, and experimentation with new materials for each layer within the cell. The critical attributes of organic-inorganic halide perovskite solar cells are fabrication simplicity, high absorption coefficient, charge carrier mobility, non-radiative recombination rate and long charge carrier diffusion length. PVSK has many advantages but unfortunately it has a few drawbacks too, such as the significant use of lead in all high performing solar cells is one negative aspect. The toxicity of lead is raising issues during fabrication and disposal. Researchers have tried replacing Pb with Sn. Sn forms a similar PVSK structure as with Pb, but theoretically Sn-based PVSK has a more suitable bandgap for photovoltaic applications. A drawback is related to the lower stability because it readily oxidizes to SnI_4. However, Pb provides high protection against oxidation [8].

Organic-inorganic hybrid perovskite bulk structures have been intensively studied. For device performance, it is essential to understand the interface structures and surfaces, but such studies have been very rare so far. To understand the structure-

property relationship of polycrystalline perovskite film ($MAPbI_3$) with different substrate interfaces and dopants, it is essential to determine the atomic structure and correlate it with the electronic and optical properties of the material. This understanding will allow building new strategies to overcome the degradation and instability problems at the device level. Different techniques, such as atomic force microscopy (AFM) [9] and transmission electron microscope (TEM) [10] supported by theoretical calculations using density functional theory (DFT) [11] have been used for exploring and mapping the unique properties of PVSK materials for resolving the solar cell related questions at the atomic scale. Among these techniques, scanning tunneling microscopy (STM) is the only technique to get atomic structure and electronic properties simultaneously. Few atomic scale studies have been done on organic and inorganic halide PVSK till today [12 13 14 15 16], which will be briefly discussed in Chapters 3 and 4.

Moreover, when exposed to moisture and UV radiation, PVSKs rapidly degrade, which hinders their production at industrial scale. Therefore, commercialization of these solar cells is still a challenge. Understanding and resolving these issues necessitates the investigation of PVSKs at the atomic scale to determine the underlying fundamental processes. Therefore, I used STM for understanding PVSK materials at the atomic scale. The atomic structure of perovskite is explained briefly in the following section.

1.2.1 Perovskite crystal structure

For understanding the atomic structure of PVSK, Figure 1.1 depicts the 3D cubic crystal structure with the general formula ABX_3. 'A' represents a cation which can be CH_3NH_3 (MA) or Cs, which is proposed to not contribute directly to the valance band structure, but manages the 3D perovskite crystal formation structural stability and as a result influences the optical properties [17]. While B is a metal cation, which can be Pb (R_B=0.119 nm) or Sn (R_B=0.110 nm) and forms the lowest edge of the conduction band. X is an anion, which is a halide (I, Cl, Br) and define the highest edge of the valence band [18]. In this structure, a larger cation A occupies a cubo-octahedral site, which is shared with twelve smaller X anions, and the small cation B holds the site in octrahedra shared with six X anions [18] as depicted in Figure 1.1(b).

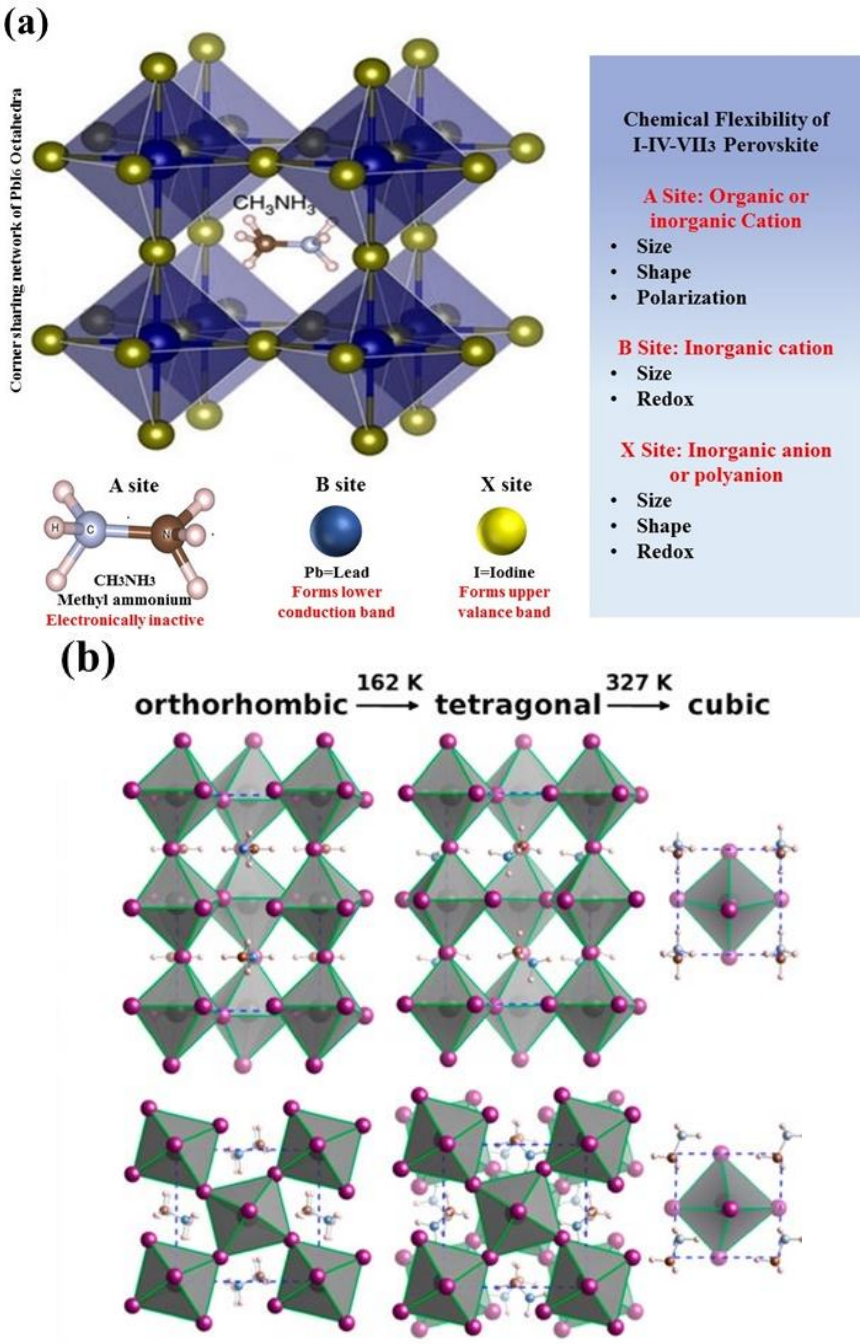

Figure 1.1: Perovskite crystal structure and phase transitions. (a) Perovskite 3D cubic crystal structure [18], (b) The atomic structure of α phase, β phase, γ phase, of $CH_3NH_3PbI_3$. Reproduced from Ref [19].

The Goldschmidt tolerance factor t and the octahedral factor μ are shown in equations (i) and (ii) and are used for the analysis of PVSK structure [20]. With this equation we can assume the perovskite crystal structure and stability.

$$\text{Tolerance factor: } t = (R_A + R_X)/\sqrt{2(R_B + R_X)} \qquad \text{(i)}$$

Equation (a) defines the ratio of the distance R_A (A large cation ionic radius) + R_X (X anion ionic radius) to the distance R_B (B small cation ionic radius) + R_X (X anion ionic radius).

The octahedral factor is given below;

$$\mu = R_B/R_X \quad \text{(ii)}$$

The ionic radius of MA is equal to 2.70 Å [21], iodine has 2.06 Å [22] and Pb has 2.02 Å ionic radius [22]. Generally, the tolerance factor lies between 0.81 and 1.11 and the octahedral factor $0.44 < \mu < 0.90$ for halide PVSKs (X = Cl, Br, I) [23]. At a finite temperature, PVSK may have a cubic structure if *t* ranges between 0.89 and 1.0 [23], but generally smaller *t* values lead to less symmetric tetragonal (β phase) or orthorhombic (γ phase) structures. Three-dimensional B-X networks could be destabilized for $t > 1$, leading to a two-dimensional (2D) layered structure. At zero temperature, in DFT calculations, the most stable phase is always the γ phase and the most unstable one is the α phase because it is difficult to satisfy $t = 1$ [24]. These constraints on heating transitions between such structures are common for any given PVSK, with the high-temperature phase generally being cubic. However, transitions between those structures at finite temperatures happen in most perovskites [25].

1.2.2 Perovskite electronic structure

The electronic structure in PVSKs is dictated by the PbI_6 (octahedral) structure. Pb 6s-I 5p σ-antibonding orbitals determine the valence band, and the conduction band is determined by the Pb 6p-I 5p π-antibonding orbitals and the Pb 6p-I σ-antibonding orbitals [8 26 27 23 28 19]. Figure 1.2 shows the band structure of $MAPbI_3$ PVSK and the atomic/ionic contributions to electronic structure. The valence band is formed by iodine ions and the Pb (cation) "p" state mostly contributes to the conduction band at the B site. The A site MA (organic cation) distribution does not directly affect the conduction band minimum (CBM) and valence band maximum (VBM), but has an impact on bond length of Pb–I, Pb–I–Pb bond angle [29], and bandgap energy. Therefore, MA ions have a key role on the structural stability and the electronic structure.

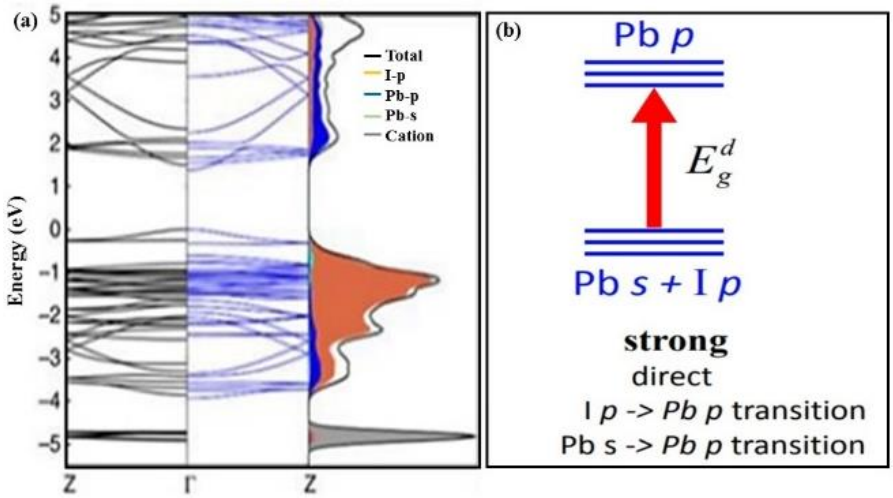

Figure 1.2: Electronic Structure of $MAPbI_3$ PVSK (a) DFT calculated bandgap. (b) Formation of lower conduction band by Pb p band and upper valance band by Pb s + I p[30]

Figure 1.2 shows the contributions of MA, Pb, and I to the density of states for $MAPbI_3$. It can be seen that the grey colored distribution about the A cation lies well below the VBM, and therefore does not contribute much to the bandgap electronically [30]. It also plays a crucial role in changing the lattice constant and stabilizing the

perovskite structure. Furthermore, the band gap of perovskite also varies with phase transition as shown in Figure 1.3 (a-d), which is the calculated band gap diagram of the phase transition. This result show that α, β and γ phases have an almost similar band gap of 1.54 eV, which is approximately equal to the experimental band gap. It indicates that a change in the bond angle of Pb-I-Pb do not considerably modify the electronic structure of $MAPbI_3$. However, the band structure of the δ phase is distinctive because the partial Pb–I bonds are broken and the 3D [Pb–I] framework is changed into the δ phase. In this phase, the coupling between Pb s and I p is weakened [30]. As a result, the VBM, which is associated with the s–p antibonding state, drops in energy, leading to an enlarged bandgap and a flat upper valence band [30]. Moreover, with phase transitions, the diffusion length and charge carrier mobility vary as a function of the perovskite crystal structure as shown in Figure 1.3 (e-f) [25]. Therefore, phase transition can strongly affect the electronic properties of PVSK material.
PSCs with different architectures and their working principles will be explained briefly in the next section.

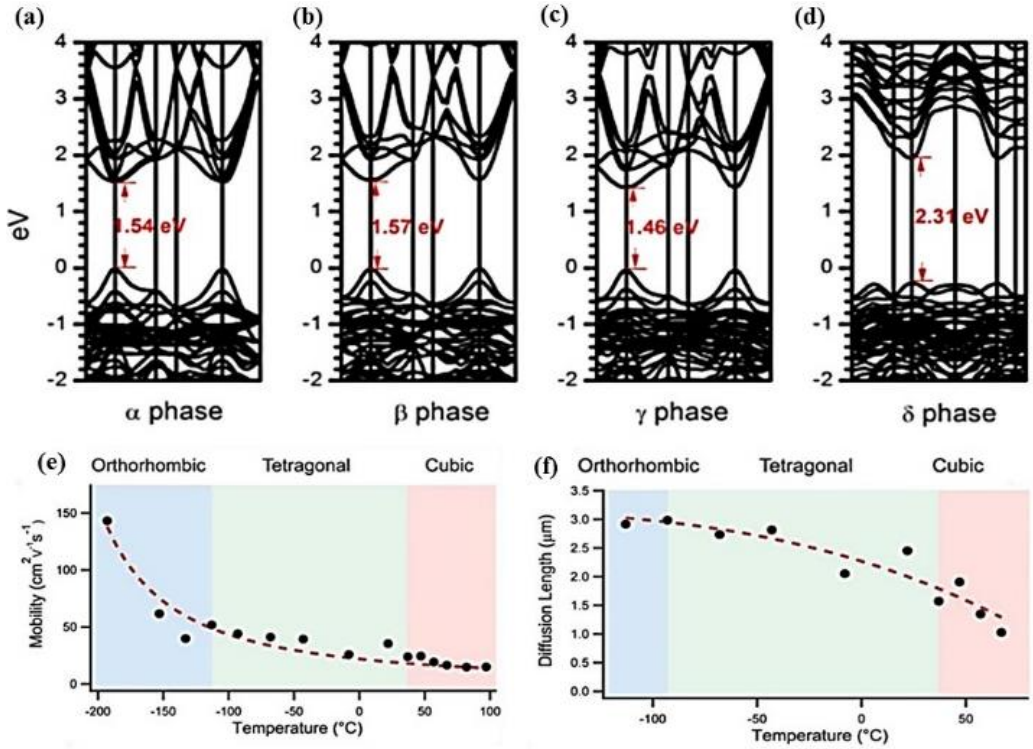

Figure 1.3: Band structure of (a) α phase, (b) β phase, (c) γ phase, and (d) δ phase $CH_3NH_3PbI_3$. Using the same tetragonal supercell for the calculation of α phase as used for β and γ phases. Reproduced from Ref [24]. (e) Temperature dependent mobility and (f) diffusion lengths as predicted for band-like transport in different phases (orthorhombic, tetragonal and cubic) of $MAPbI_3$ perovskite [25].

1.2.3 PSCs architecture

Various architectures have been employed to assemble the PSCs. Mainly, two conventional architectures p-i-n and n-i-p are used as PSCs architectures, as depicted in Figure 1.4 (a-c), in which the perovskite photoactive film is sandwiched between two

electrodes in different configurations. The main difference between the two architectures is the current flow in the opposite direction. In n-i-p PSCs architecture, the electron transport layer (ETL) is deposited on top of the transparent conductive oxide (TCO)/glass. Meanwhile, in p-i-n architecture, the hole transport layer (HTL) is deposited on top of TCO/glass. Furthermore, the n–i–p and p-i-n type perovskite solar cell can be categorized into mesoporous and planar architecture. In mesoporous architecture, a mesoporous layer of the ETL material, is deposited on top of the compact ETL layer and in planar architecture only a compact layer of material is used as the ETL. The purpose of the mesoporous layer is to increase the effective surface area of contact at the perovskite/ETL heterojunction, which increases the charge transfer and PCE (power conversion efficiency).

The planar PSCs architecture is advantageous regarding low-cost production and ease of fabrication but still shows lower stability in comparison to the mesoporous architecture [31]. In general, the device configurations consist of five different layers; (i) TCO, (ii) the mesoporous or planar ETL, (iii) the light harvesting layer (PVSK materials), (iv) the HTL, and (v) the metal like gold (Au) [3], silver (Ag) [32], or non-metal electrode such as carbon (C) [33]. For the charge transport processes in PSCs, ETL and HTL used can be organic or inorganic materials. TCO is the top electrode and is used for the photon access to the active/absorber layer. Therefore, the transparency is the ultimate importance of this layer. For this purpose, ITO (indium tin oxide) or FTO (fluorine tin oxide) are used where aluminum, gold or silver are used as back/bottom electrode in the solar cells [3 34]. The perovskite active layer (e.g., $MAPbI_3$) absorbs photons from sunlight, with which electrons in the valence band of the PVSK get excited across the band gap (1.55 eV) to the conduction band, and create an electron-hole pair. The excited electrons injected to the conduction band of ETL (TiO_2, PCBM= Phenyl-C61-butyric acid methyl ester) from PVSK migrate to FTO and flow through the external circuit to HTL (Spiro-MeOTAD=2,2',7,7'-Tetrakis[N,N-di(4-methoxyphenyl)amino]-9,9' spirobifluorene,PEDOT:PSS= poly(3,4-ethylenedioxythiophene) and recombines as shown in Figure 1.4 (d). Perovskite solar cells have gained considerable attention not only due to their high PCE, but also because of their easy fabrication, low cost, and compatibility with roll-to-roll printing and some other mass production techniques. Different methods have been developed to fabricate perovskite solar cells because the fabrication method is one of the critical factors that influences solar cell performance and stability. There are two conventional methods used which are (i) one step [35] and (ii) two-step solution processing [36]. However, for producing high PCE with low potential for degradation, other methods are introduced such as vapor assisted solution processing [37], hybrid chemical vapor deposition [38], vacuum depositions [39], spray coating [40], room temperature solvent-solvent extraction [41] and doctor blading [42]. More, a perovskite absorber has also suggested by Monteiro Lunardi et al. to be coupled with conventional silicon solar cells to increase tandem solar cells efficiency [43]. In the near future, we may use the existing established conventional solar cells manufacturing plants for the mass production of PSCs [44]. To scale up the production of PSCs, many techniques such as doctor blading [42], spray coating [40] and other printing process have been employed, but regarding PCE; still, the efforts so far lag behind lab-scale devices. To date, with the small area, high PCE perovskite solar cells have been successfully fabricated at the lab level. However, for mass production, it is necessary to produce large area cells >200 cm^2 [45]. For this purpose, recently "New Energy and Industrial Technology Development Organization (NEDO) and Panasonic have announced the world's largest film-based

perovskite photovoltaic module. The module is 802 cm^2 (30 x 30 cm^2) and achieves a PCE of 16.09%, overcoming the difficulties of increasing size and efficiency at the same time" [46]. For large area solar cells, some issues like instability and low PCE need to be solved, which hinder the transfer of PSCs devices from the laboratory to industry. To overcome those issues, the first method is to change the chemical composition and tune the bandgap and increase the charge generation in PVSK materials by doping. Secondly, increasing the grain size will decrease cracks and pinholes, so the bulk defect recombination and electric leakage will be reduced and V_{oc} will be increased. To resolve these issues of perovskite materials, it is necessary to understand the fundamental physics of these materials at the atomic scale, which is the primary focus of my research. In PSCs, the material of each layer plays an important role in achieving not only high PCE but also improving stability and lowering degradation.

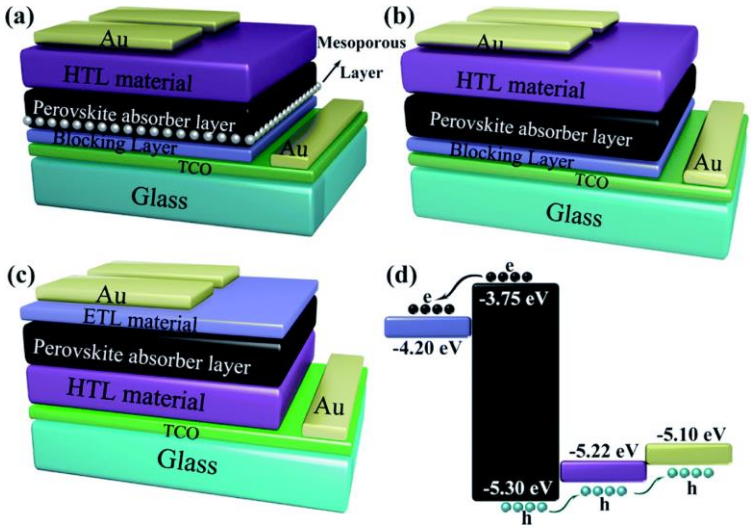

Figure 1.4: Schematic diagram of different structural configurations of perovskite solar cell. (a) mesoporous (b) planar (c) inverted planar structure, and (d) working principle of perovskite solar cell [47].

1.3 Perovskite solar cell layers

1.3.1 Substrates

In several solar cell technologies, glass, plastic [48], flexible silver mesh [49] and conducting polymers [50] are used as substrates for efficiently transmitting sunlight to the absorber/active layer of the device. Moreover, paper was also used as a substrate in PSCs because of its flexibility, light weight, abundance, low-cost fabrication with large area printing and recyclability but only achieved 2% PCE [51]. However, in my experiments, I used Au (111) as a substrate, because scanning the surfaces of PVSK with STM required a conductive substrate.

1.3.2 Transparent conductive oxide based top electrode

For solar cells, the top layer must be a thin transparent and conducting layer such as TCO. The function of this transparent layer is to let the maximum number of photons

access the active/absorber (PVSK) layer. For this purpose, typically ITO and FTO are often used in solar cells. ITO is an n-type semiconductor with wide band gap [52-53 54] and is an attractive choice in PSCs because of its properties such as high optical transmission, (85% transparency), high electrical conductivity (10^{-5} Ohm*cm) and strong adhesion to the glass substrate, but ITO is utterly damaged by heating more than 400 ºC [55]. In comparison with ITO, FTO has excellent electrical properties ($4.3x10^{-4}$ Ohm*cm) as well as high transmission properties, i.e., 86% transparency and cannot be damaged easily with high temperature during device fabrication [56]. In flexible solar cells, TCO is not suitable for the top layer because of its mechanical stiffness. Therefore, graphene replaced TCO as a transparent conducting layer in flexible solar cells with 17% PCE [57].

1.3.3 Electron transport layer (ETL)

In PSCs, the PCE and stability strongly depend on the ETL material type and morphology because it facilitates electron collection and smooth transport from the absorber layer to its respective electrode in the device [58]. Therefore, use of ETLs often improves the fill factor (FF), promotes a high short circuit current (J_{SC}), and contributes to enhanced device efficiency. It must have the following properties for achieving high PCE solar cells like it must have a wide band gap, anti-reflective, good electron mobility and compatible energy levels to the active layer energy levels to block the hole transport and favor the electron transfer. Additionally, it should have a compact structure which is free of pinholes. These pinholes cause current leakage because they make contact between active/absorber layer and TCO [59]. So far, many inorganic potential ETLs have been analyzed such as TiO_2 [59], SnO_2 [60], ZnO [61] $BaSnO_3$[62], SnO_2[63], WO_3[64] and In_2O_3 [65]. However, these ETL materials are not suitable for flexible PSCs. Therefore, for future flexible PSCs, low temperature process able organic ETLs such as C_{60} (fullerene based molecules) and PCBM (phenyl-C_{61}-butyric acid methyl ester) have attained broad attention as well as it is found that they reduce the defect density at the interface, which is the main cause of charge recombination [66,67]. Moreover, C_{60} helps to minimize the trapped charge induced degradation in the presence of moisture [68], while PCBM is also reported to be more hydrophobic and help to protect the active layer from moisture-induced degradation [69].

1.3.4 Active/absorber layer

Perovskite solar cells have been broadly investigated due to its high PCE, longer diffusion length, low-cost fabrication, large absorption coefficient, direct and tunable band gap. PCE of perovskite solar cell is strongly dependent on the absorber layer morphology, compactness, and crystallinity. Perovskite has the general ABX_3 structure and commonly composed of an organic-inorganic monovalent cation A = MA^+, Cs^+, FA^+, Rb^+, and divalent cation B = Pb^{2+}, Sn^{2+}, and halide anion X = I^-, Cl^-, Br^-. The crystal and electronic structure of perovskite is explained briefly in section 1.2.1 and 1.2.2. $MAPbI_3$ and $FAPbI_3$ are intensively used for perovskite solar cells, and the all inorganic $CsPbI_3$ has lower PCE < 2.9% but higher stability [70]. $FAPbI_3$ is thermally stable in comparison with $MAPbI_3$, but FA based PVSK layers have amorphous delta phase which make it unsuitable for photovoltaic applications [71] and have PCE of 13.5−18%, [72,73] which is lower than $MAPbI_3$. $MAPbI_3$ absorber layers are compact and suitable for photovoltaic applications and have achieved PCE of ~20%, but present instability issues [74,75]. For improving the $MAPbI_3$ PVSK absorber layers, mixed cations and anions are under

extensive research. Mixed PVSK have been suggested to increase the stability and performance of devices. To date, many PVSK absorber layers are reported for the high efficiency and stable solar cells with mixed cations such as FA/$MAPbI_3$, MA/$CsPbI_3$, FA/$RbPbI_3$, and mixed halides like "MAPb(I/Cl), FAPb(I/Cl), CsPb(I/Cl), MAPb(I/Br), MAPb(I/Cl/Br), MAPb(Br/Cl), CsPb(Cl/Br), and more complex with mixed halides and cations such as MACsPb(I/Br), Rb/MA/FAPb(I/Br), Cs/MA/FAPb(I/Br)" [76].

More, the organic mixed cations $MA/FA_{1-x}PbI_3$ absorber layers showed better film quality, higher crystallinity, large grain sizes and fewer pinholes and compatible fabrication with chemical vapor deposition (CVD) [77], and doctor blading [42] with PCE of 13.4%, which is still lower than the $MAPbI_3$ PVSK layer. Park et al. [78] Zhang et al. [79] reported the cation Rb mixing in $FAPbI_3$ using different concentration and found that a phase segregation occurs with high concentration of Rb incorporation in $RbFA_{1-x}PbI_3$ PVSK lattice. While they achieved PCE of 14.9-16.2% by using a small concentration of Rb, and enhanced stability after 25 h in open air, the PCE was still lower than that of $MAPbI_3$ PCE. Halide mixing is also reported for improvement of the $MAPbI_3$ absorber layer, but mostly Cl incorporation has been studied and improved diffusion length from 1069 nm and 1213 nm was achieved, which is ten times greater than the $MAPbI_3$ diffusion length (90-105 nm) [80]. Therefore, the $MAPbI_3$ absorber layer showed the promising results for the high efficiency solar cells among other absorber layers but with the stability issues, which need be solved by mixing different cations and anions [81].

1.3.5 Hole transport layer (HTL)

In PSCs, the HTL is used to collect and transport holes from absorber or PVSK layer. For this purpose, it must have higher energy for the valence band and conduction band edge than the absorber layer to extract holes and reject electrons. The stability of solar cells is also dependent on the stability of HTL. Presently, three types of polymeric, organic and inorganic HTL are employed in PSCs. Typically, high PCE solar cells consist of organic HTL such as spiro-MeOTAD and poly-triaryl-amine (PTAA). However, Spiro-MeOTAD has an issue of thermal and poor long-term UV instability [82 83]. To overcome these drawbacks, the additives trifluoromethanesulfonyl imide (LiTSFI) and a 4-tert-Butylpyridine (t-BP) are used with organic HTLs, but unfortunately they have negative effects on the stability [84 85]. Additionally, for moisture instability of organic HTLs, various dopant-free HTLs [86] have been proposed but thermal and UV- instability remain the main issues. Therefore, to tackle thermal and moisture instabilities, inorganic HTLs like vanadium oxide (V_2O_5) [87], carbon[88] , nickel oxide (NiO_x) [89], MoO_x , WO_x [90] , spinel CoO_x [91] and Kesterite Cu_2ZnSnS_4 [72], $CuCrO_2$[92], $CuAlO_2$[93], $CuGaO_2$[94] CuS [95] CuI [96], CuO_x [30, 97] and CuSCN [98,99,100] have been applied to PSCs. By using these inorganic HTMs, PSCs exhibited stability under high temperature and humidity [101]. Recently, PSCs employing CuSCN and TiO_2 ETLs achieved 20.4% PCE, which is comparable to the Spiro-MeOTAD based solar cells with PCE of 20.9% [102]. Commonly, organic HTLs have increased PSCs cost because they are exceptionally expensive [103]. For fabricating low cost PSCs, HTL free solar cell development has been in progress since 2012 [94] and achieved 10.7% PCE [104].

1.3.6 Back/bottom electrode layer

Back or bottom electrode plays a crucial role in collecting charge carriers from the solar cell to the load circuit. For this purpose, commonly the noble metal Au is used.

However, the high cost of Au prohibits the PSCs mass production. Therefore, the other noble metal such as platinum has been used in dye-sensitized solar cell (DSSC) as it is less expensive than Au, but in PSCs it would not solve the cost and abundance drawbacks. The other crucial factor is that the back electrode must guarantee the high PCE and robust stability under high temperature and humidity, which Au provides. To replace the Au as back electrode, various other metals such as Pt, Ni, Cu, Cr and Ag have been employed in solar cells [105], but Ag and Cu are not stable and Ag electrode based solar cells degrade quickly in open air because Ag reacts with iodine from PVSK layer to form AgI [106].

Cr and Ni are chemically stable metals but the obtained PCE is quite low due to the formation of a barrier layer at the interface of the metal electrode and HTL [107]. To solve these issues, Xiao et al. proposed conductive polymers of PEDOT:PSS as a back electrode and achieved 13.07% PCE for 1cm^2 active area [108]. Carbon and its allotropes are also an alternative for the back electrode because of their high resistance to corrosion, medium reactivity, abundance and low cost [109]. Among carbon materials, graphene is the most promising candidate so far. Additionally, the carbon electrode is easy to fabricate which is one of the primary factor to be considered for PSCs commercialization other than the cost of raw material [105]. Moreover, the paintable carbon electrode PSCs achieved PCE above 14% [105]. Wei et al. designed the $MAPbI_3$ with PCE of 11.60% by using carbon inkjet printing [110].

After discussing the individual layers of PSCs, which define the significant influence on the PCE, FF, J_{SC}, defects, grain sizes, stability, and degradation. In the forthcoming section, I describe the stability and degradation issues in PVSK material followed by how to solve these issues by doping, which is the main focus of my research.

1.4 Stability challenges

With many advantages of PSCs, they have some disadvantages including instability. Instabilities and degradation occur in PSCs due to the extrinsic parameters like oxygen, UV-light, moisture, temperature, corrosive molecules and intrinsic (thermal and electric field) interaction with the available adsorption sites on the perovskite/absorber layer and HTL in air [111]. The performance of PSCs decreases over time with extrinsic and intrinsic instability. The fabrication process and material play a crucial role in the PVSK stability. Glass and carbon-based encapsulation have been employed to improve the long-term stability [112], but it increases the cost of PSCs and reduces the appeal for mass production. Therefore, it is crucial to develop the open-air stable perovskite and HTL materials. Under moisture and heat stress (110 ºC-140 ºC), $MAPbI_3$ perovskite breakdown and segregate into its two precursors MAI and PbI_2 [113]. After this, the MAI decomposes and produces highly reactive HI. In the presence of oxygen or after UV light exposure, HI degrades and damages the crystallinity. However, Zhou et al. showed that "less than 30% humidity during fabrication improves the morphology of crystal and enhance the performance of the solar cell" [114]. You et al. observed pinholes after annealing the samples in nitrogen and dry oxygen environment [115]. Thus, the question on what conditions should be employed for achieving stable solar cells still remains.

Temperature is another degradation factor, which affects the perovskite material, HTL, and ETL behavior [116]. Philippe et al. investigated the temperature effect of $MAPbI_3$ and $MAPbI_{3-x}Cl_x$ using ultra high vacuum (UHV) and observed by X-ray photoelectron spectroscopy (XPS) elemental analysis that PVSK is not stable at high temperature [117]. Moreover, the temperature and stress affect the crystal structure of

PVSK material and cause phase transition, which is the critical aspect influencing structural stability [118]. Baiki et.al [7] also confirmed the $MAPbI_3$ phase transition from tetragonal to cubic at a higher temperature. Rebecca et al. reported the effect of the phase transition on diffusion length and charge carrier mobility of the device as shown in Figure 1.3 (e-f). The graphs show that the orthorhombic to cubic phase transition, diffusion length, and charge carrier mobility decreased [25]. To avoid thermal degradation due to the phase transition, Saliba et al. reported on PSCs with the combination of three cations to consist on a small amount of Cs with MA and FA, which significantly improved the PSCs performance with reproducibility [119]. More, the grain boundaries of grains in polycrystalline perovskite films are shown to be the recombination centers, which decrease the solar cell performance [120]. Therefore, it is necessary to fabricate PVSK films with larger grains, which will reduce the grain boundaries and will increase the solar cell performance. Besides the perovskite layer degradation, ETL is also identified as playing a crucial role in the degradation process. Ito et al. reported that when mesoporous TiO_2 used as the ETL, it degrades with the UV-illumination because it is a well-known good photo-catalyst. It can absorb photons in the UV range because of its 3.2 eV band gap, which can break the perovskite layer at the interface [121]. And the other assumption is that the TiO_2 may extract electrons from the triiodide anions and form I_2 and decompose perovskite crystal structure. Moreover, TiO_2 or other metal oxide ETLs also degrade with the ambient oxygen which desorbs under UV illumination resulting in deep trap states. As a solution to this problem, a UV filter is used with TiO_2 based PSCs to achieve higher stability [122]. For interface engineering more in-depth study is required of PVSK materials to improve the device stability and efficiency for the future commercial solar cells. Currently, there is no fundamental understanding available for the origin of instabilities in perovskite materials, which limits the solar cells production at industrial scale. Therefore, understanding the fundamental mechanisms and providing solutions to enhancing the device lifetime is the next challenge to drive PSCs towards the mass production.

1.4.1 Introduction to stability properties of perovskite solar cells

A polycrystalline material is composed of microcrystallites or "grains" of the samiconductor arranged at random orientation to each other. The material is crystalline over the width of grain. The transport and recombination properties are strongly affected by the presence of interfaces or grain boundaries. The effect of grain boundries on charge transport depends on whether they lie normal to or parallel to the direction of current flow. When current is flowing across a grain boundary, the potential barriers slow down the transport of majority carriers, and limits the majority carriers towards mobility, while the potential wells drive minority carriers towards recombination centers at the grain boundary, reducing the majority carrier diffusion length and life time. The size of these effects depends upon the doping, the density of interface states, and the photogenerated carrier density [120,123].

1.5 Methods to improve the stability issue of $MAPbI_3$

To tune the bandgap and solve the extrinsic and intrinsic instability problem, doping of alkali metal cations (KI, RbI, NaI, LiI, CsI) was proposed. These dopants could increase the grain size and charge carrier lifetime [124]. Additionaly, halide (I, Br, Cl)

mixing has also been proposed to increase PVSK stability. The proposed effects of dopants on $MAPbI_3$ were briefly discussed below.

1.5.1 Halide anion mixing

To improve the stability of $MAPbI_3$, Noh et al. tested the different concentration of Br for one day at 55% and other days at 35% humidity. The results exhibited that the concentration of $x \geq 0.2$ in $MAPb(I_{1-x}Br_x)_3$ maintained PCE while for $x \geq 0$ concentration demonstrated severe PCE degradation, which might be the reason of reduction in the lattice constant because of larger I atoms substitution with small Br atoms [125]. Hence, these results show that the halides concentration significantly affects the stability of PSCs. Cl was also suggested to be a good candidate for decreasing the sensitivity of $MAPbI_3$ to moisture, temperature, and light. A doping of Cl exhibited good light-harvesting capabilities and was stable for 1000 h under light exposure [126]. More, the contribution of Cl in $MAPbI_3$ is still under debate because $MAPbI_3$ and $MAPbI_{3-x}Cl_x$ have similar light absorption ranges. However, $MAPbI_{3-x}Cl_x$ has a longer diffusion length, which makes it a better choice of the absorber layer for ETL (TiO_2) free perovskite solar cells [127]. Currently, no evidence of Cl presence in PVSK film has been confirmed by using XPS, X-ray diffraction (XRD), and energy dispersive X-ray spectroscopy (EDS). Therefore, it was suggested that Cl may diffuse to the perovskite film bottom layer. Moreover, a few assumptions are made about the improvement of the stability of PVSK material by Cl doping as follows: (i) it increased the quality of crystallinity [128], (ii) it may creep the grain boundaries [129] and decrease the deep trap states because the Cl-doped PVSK films exhibited long carrier diffusion length, (iii) it may remove the excess of MA ions, which may act as impurities or defects in films surface, (iv) it can increase the binding constant, which may give highly stable PVSK films [130]. Thermally evaporated grown ultra-thin films and scanned with STM and characterized by inverse photoemission spectroscopy (IPES), XPS and ultraviolet spectroscopy (UPS) can solve the Cl inclusion mystery, which I have done experimentally and will discuss in Chapter 4. Furthermore, it is suggested that mixing of different halides can vary the band gap of $MAPbI_3$, as it is designed for tunable bandgap approximately from 1.5 eV to 2.53 eV [131], which has also been demonstrated in my Cl-doped $MAPbI_3$ results obtained from the IPES and UPS measurements in Chapter 4.

1.5.2 Alkali metal cation mixing

To improve the PVSK film quality, different techniques have been employed to fabricate large-grain films. One technique proposed is the doping of PVSK materials with alkali metals cations because they are resistant to oxidation and reduction [132]. For this purpose, LiI [133], NaI [133 134 81], KI [134 81 124], CsI [81], and RbI [81 135] doped in $MAPbI_3$ PVSK films to improve the film quality by increasing grain sizes and passivate the vacancies in the grain boundaries which has proven high number of traps states. Among alkali metal cations, K [81 133] and Na [133] demonstrated improved PVSK films with fewer trap states and grain boundaries, and increased grain size from 140 nm to 220 nm (for K doping) and 230 nm (for Na doping). A longer carrier lifetime is confirmed for these doped films while an accumulation of K and Na is observed at the grain boundaries. Moreover, the monovalent alkali cations increased the PCE from 15.56% to 18.16%. Moreover, Son et al. confirmed the positive effect of K doping in $MAPbI_3$ is due to its small ionic radius, which fits perfectly in the crystal structure and prevents phase

transition of PVSK [81]. Mojitaba et al. also reported the positive effect of K doping in mixed cations (Cs, FA, MA) and anions (I, Br) in PVSK material [124]. Figure 1.5 shows that K filled the vacancies and depleted Br from the crystal structure of the grain boundaries. K doping also tuned the band gap to 1.78 eV and achieved the 17.9% PCE with over one-month stability test [124], which makes it ideal for tandem application. RbI doping in $MAPbI_3$ is employed for achieving the smoother and defect free PVSK films. Different concentrations of RbI were shown to controllably tune the material from n-type to p-type [135].

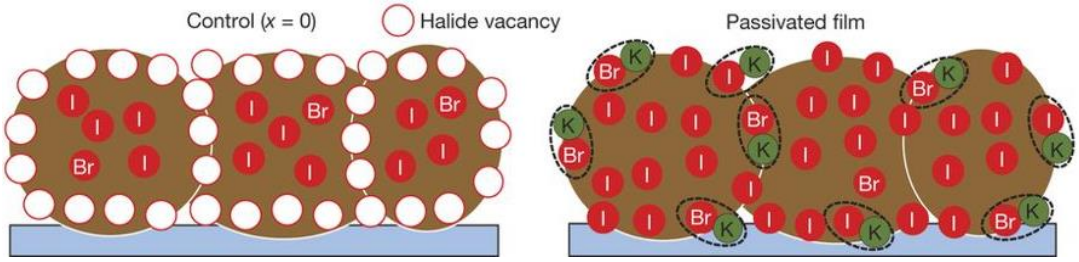

Figure 1.5: Schematic of a cross-section of a film showing halide-vacancy management in cases of excess halide, in which the surplus halide is immobilized through complexing with potassium into benign compounds at the grain boundaries and surfaces reproduced from [124].

In the race to improve PVSK films, Mojetab et al. [136] toss the coin in research community by investigating the doping effect of monovalent cation (Cu, Na, and Ag) halides with similar ionic radius to Pb^{2+}. In comparison with pristine $MAPbI_3$ perovskite, AgI films increase the V_{oc} (open circuit voltage) to 70 meV and NaI and CuBr improved the photocurrent density by $2mA/cm^2$. These dopants also increased the PCE from 14% to 15.6% with the high-quality film. In the light of above-described results, it appears that doping can maximize charge transport and passivate surface traps in devices, but the fundamental origin at the atomic scale of these effects has not been studied yet. Therefore, the desire to show the effect at the atomic scale of each additive in PVSK can lead to providing precise control of the film property for future highly stable solar cells.

1.6 Summary of all chapters

After discussing the literature review of PSCs in this chapter and how to probe the instability and performance issues in PVSKs at the atomic scale, the remaining chapters are organized as follows. Chapter 2 provides the working principles and applications of all instruments used for all experiments in this thesis, which includes low temperature scanning tunneling microscopy (LT-STM)/scanning tunneling spectroscopy (STS), Ultra high vacuum (UHV) system, X-ray photoelectron spectroscopy (XPS)/ultraviolet photoemission spectroscopy (UPS) / inverse photoemission spectroscopy (IPES). For the bulk or thick films characterization Fourier transform infrared spectroscopy (FTIR) and X-ray diffraction (XRD) were explained in details.

Chapter 3 describes the protocol optimization for the MAI growth on Au (111) by using UHV chamber and the high-resolution LT-STM images of atomic topographies. Four different atomic topographies stripe, non-stripe, iodine (I) hexagonal and snaky chain of I-I dimers were observed for MAI ultra-thin films. $MAPbI_3$ ultra-thin films of ~4 nm were fabricated by co-evaporation of MAI and PbI_2. $MAPbI_3$ showed the characteristic zigzag and I-I dimer phases by LT-STM. Bandgap of 1.45 eV was measured by UPS/IPES.

Chapter 4 describes the chlorine (Cl) incorporation on the $MAPbI_3$ by evaporation of $PbCl_2$ on the perovskite surface. LT-STM provides evidence at the atomic scale that Cl concentration plays crucial role in the $MAPbI_3$ surface stability. The optimized 14.8 ± 0.6 % Cl concentration also tuned the bandgap of $MAPbI_3$ from 1.45 eV to 1.65 eV. The bandgap tuning and surface stability was also supported by density functional theory (DFT) and molecular dynamics (MD) calculation. Based on the DFT calculation it was found that the Cl incorporated zigzag phase was less stable than dimer phase. All theoretical calculation in this thesis were performed by Prof. Wanjian Yin and Dr. Zhendong Guo from Soochow University, China.

Chapter 5 is based on the curiosity how does $PbCl_2$ interact with $MAPbI_3$ surface and subsurface layers because lead (Pb) was not observed by LT-STM measurements. For understanding the atomic-scale interaction of Pb and $PbCl_2$ with $MAPbI_3$, the protocols for the controlled growth of Pb and $PbCl_2$ MLs on Au (111) substrate were optimized by using thermal evaporation. Four hypotheses were proposed (with illustrations provided in Figures 5.1 - 5.4) for describing the interaction of $PbCl_2$ with $MAPbI_3$ surface and subsurface layers. The proposed hypotheses were supported by analyzing the $PbCl_2$ atomic structures on Au (111). Based on $PbCl_2$ sub ML coverage on Au (111) STM images, $PbCl_2$ sublimates from the thermalized evaporator both in its intact molecular and disassociated forms, which impinges the Au (111) surface. The Au (111) surface offers a relatively strong interaction with the Cl ions to adhere first. On top of this Cl layer, Pb-Pb dimers and dissociated single Pb ions were observed to form. Based on the observed results, an interesting fact was found that grain boundaries were formed for $PbCl_2$ deposited MLs on Au (111). However, metallic-Pb deposition on Au (111) did not lead to grain formation.

Chapter 6 provides the protocol optimization of KI evaporation and elucidates the atomic scale topographies. For example, the acquired ML height corresponded to ~1.45 Å. The I-I square structure was observed for KI on Au (111), which was attributed based on visualized atomic models cif files in VESTA that the K^+ ions are covered within the I octrahedra. The optimized protocol was used to deposit KI on $MAPbI_3$ surface to find the optimal concentration for the stable $MAPbI_3$ PVSK. Therefore, the first 90 s deposition was attempted but by XPS measurements, no K 2p peaks were observed in the $MAPbI_3$ thin film. In a second attempt of KI deposition, an additional 3 min (total of 4.5 min) deposition on $MAPbI_3$ lead to the detection of K 2p peaks by XPS. For the KI deposited sample, LT-STM scanning will be conducted in the future to obtain the optimal concentration ratio of KI in $MAPbI_3$ lattice for the future high stability PSCs.

Chapter 7 provides a summary of all experiments and findings in this thesis. This thesis has created the fundamental atomic scale understanding for the $MAPbI_3$ material system with improved surface stability by using controlled concentrations of additives and providing the insights for the design of the future high performance PSCs.

Chapter 2: Instrumentation and methods

2.1 Ultra-high vacuum (UHV) system

Most of the experiments discussed in this thesis were carried out under ultra-high vacuum (UHV) conditions with surface science instruments. For many surface science experiments, low pressures around 10^{-10} Torr or below are necessary, which is called UHV. For achieving UHV conditions, the vacuum chamber needs to be evacuated by a combination of pumping systems (e.g., turbo molecular pump with a roughing pump, ion pump, and others). In addition, a bake out procedure of the whole stainless steel chambers at elevated temperatures (about 150 ^{0}C) is required to remove the adsorbed water molecules and other contaminants from the chamber walls. In UHV, the residual gas molecules do not flow as the gas flow in the ambient pressure. By using the kinetic gas theory [137], we can calculate two instructive quantities.
One is the mean free path (**λ**), which is the mean distance molecules travel in the system before they bump into one another at pressure P and is given below

$$\lambda = K_B T/\sqrt{2}\pi P D^2 \qquad \text{(i)}$$

D is the diameter of molecules or atoms in a molecular beam trajectory, K_B is the Boltzmann constant and T is the temperature. The second quantity is the rate of molecules that impinge on the surface, which can be calculated from the kinetic gas theory as given below;

$$R = P \cdot A_C/\sqrt{2\pi M k_B T} \text{ (Molecules/s)} \qquad \text{(ii)}$$

Where P is the rest gas pressure, M is the molecular mass in the atomic mass unit (amu) and A_C is the surface area of the impingement rate (e.g., crucible from which molecules evaporate). Based on this formula, we can calculate the flux of molecules that impinge on the deposition substrate (e.g., Au). By using these formulas, we can quantitatively optimize our protocol for thin-film growth in UHV chambers as well as calculate the thickness of the molecular layers. Quartz crystal microbalance is also used for the thickness measurement of deposited materials on substrates.

2.2 Perovskite sample preparation

2.2.1 Substrate Au (111) cleaning by sputtering and annealing

For cleaning Au (111) after loading it into the UHV chamber from outside, I used the sputtering and annealing process. In a sputtering process, atoms or molecules on the surface of a substrate are removed using collision of energetic particles with the substrate surface as shown in Figure 2.1 (a-b). Whereas, annealing refers to a heating treatment that helps restore the substrate/material microstructure after sputtering. For sputtering, the SPECS IQE 11/35 sputter gun was used in the UHV chamber with a K.E of 0.55 keV (550 eV) and an emission current of approximately 21 μA for 30 min under chamber

pressure of 8.5×10^{-5} Torr. After sputtering, the Au (111) was heated by a W-filament with a temperature of 420 °C by applying 1.306 A current for 20 min. Each time I used 3 cycles of the same protocol to clean the Au (111) and then checked by XPS (Figure 2.1c) for cleaning confirmation before transferring it to the STM chamber or the ultra-thin film deposition.

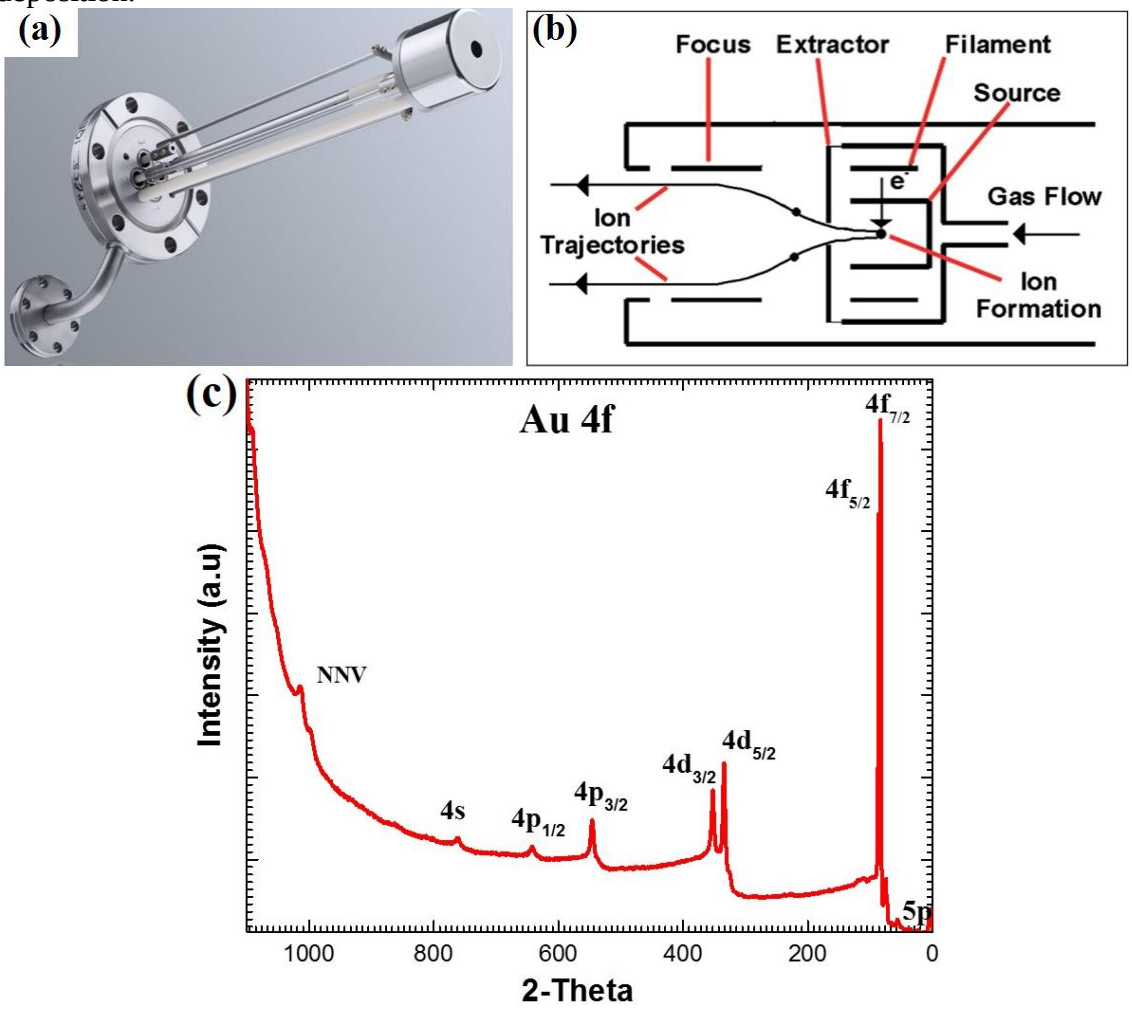

Figure 2.1: Sputtering gun. (a) SPECS sputter gun (b) Schematic diagram of Sputtering gun [138] (c) Clean Au (111) XPS spectra

2.2.2 Ultra-thin film growth by vacuum co-evaporation

Vacuum co-evaporation is a physical vapor deposition technique used to grow monocrystalline layers via the sublimation of pure solid elements from effusion cells (based on the Knudsen concept) under an ultra-high vacuum chamber to reduce impurity levels with the growth rate of 0.01Å/s. In a vacuum, co-evaporation cross-contamination is minimized because the process is performed at comparatively low temperatures than in other evaporation growth processes. In addition, in vacuum co-evaporation, we can precisely control the thickness of the layer growth on substrates, which is useful in many surface science studies. Figure 6 illustrates the controlled monolayer (ML) growth of molecules (i.e., layer by layer) on the substrate surface during the vacuum co-evaporation process. Moreover, the fully evaporated PSCs achieved more than 20% PCE and offer many advantages in comparison with solution-processed solar cells such as toxicity free

and low-cost solvents, precisely controlled film growth, and easy synthesis of films on flexible and large-area substrates [139]**.** In my experiments, I co-evaporated MAI and PbI_2 for forming $MAPbI_3$ perovskite thin films on Au (111) using vacuum co-evaporation. With this technique, high quality, smooth/flat films with few defects are achievable, which is the vital aspect for analyzing the surfaces of perovskite material and resolve the underlying fundamental processes. For solar cell fabrication, the vacuum co-evaporation technique still needs to be established at the industrial level.

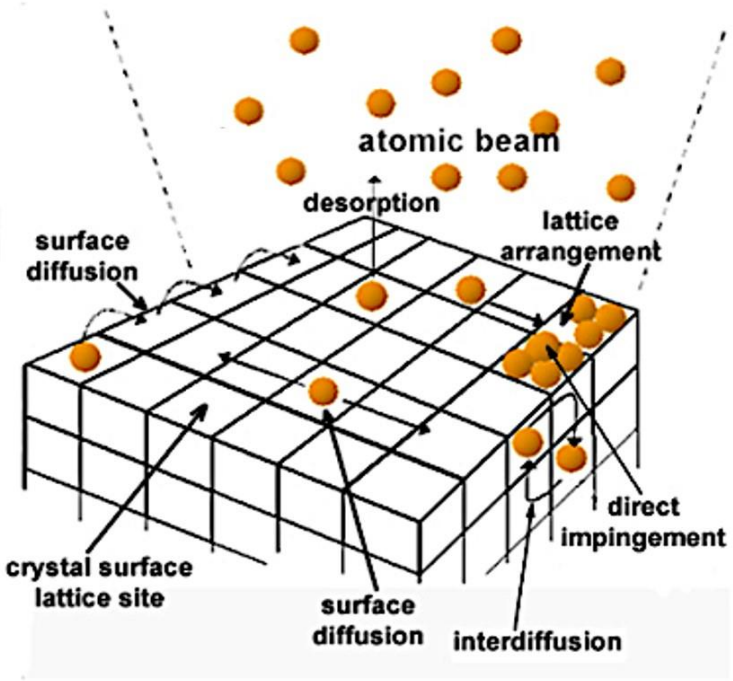

Figure 2.2: Processes occurring at the surface during vacuum co-evaporation growth reproduced from [140].

2.3 Characterization

The grown ultra-thin PVSK films were characterized by scanning tunneling microscopy (STM), scanning tunneling spectroscopy (STS), X-ray photoelectron spectroscopy (XPS), ultraviolet photoemission spectroscopy (UPS), low Energy Inverse photoemission spectroscopy (LEIPS), Fourier transform infrared spectroscopy (FTIR), and X-ray diffraction (XRD).

2.3.1 Scanning tunneling microscopy (STM)

STM is used for 2D imaging of surfaces at the atomic scale. It was invented by Heinrich Rohrer and Gerd Binnig in 1982 [141]. Our LT-STM setup is shown in Figure 2.3 and works on the quantum tunneling concept. A metallic atomically sharp tip is brought very near to the sample surface (i.e., within a few Å) and the tip to sample gap dependent current is in the order of 10 pA to nA and is used to obtain topographical information. However, small variations in the tip to sample distance influence the tunnel current because this current is exponentially dependent on the tip to sample distance W (barrier width) as defined in the equation

$$I_t \propto V_{ps}(0, E_f)e^{-2kW}$$

Furthermore, an advantage of the exponential barrier dependence is that I_t (the tunneling current) flows mainly through a few atoms at the very apex of the tip for better spatial resolution. We use the Omicron Low temperature (4.5 K/ 77K) STM setup under UHV conditions. STM imaging can be done in constant current or constant Z (height) mode. In our case, we use the constant current mode for perovskite materials. In this mode, the electronic feedback loop controls the Z-direction of the piezoelectric drive and keep the constant tunneling current during tip-sample distance recording. We can also use STM to move or manipulate an individual atom. The tip brought very close to the atom allows to pick up an atom and move it to a desired location in the lattice. STM allows reconstructing the surface topography with atomic resolution.

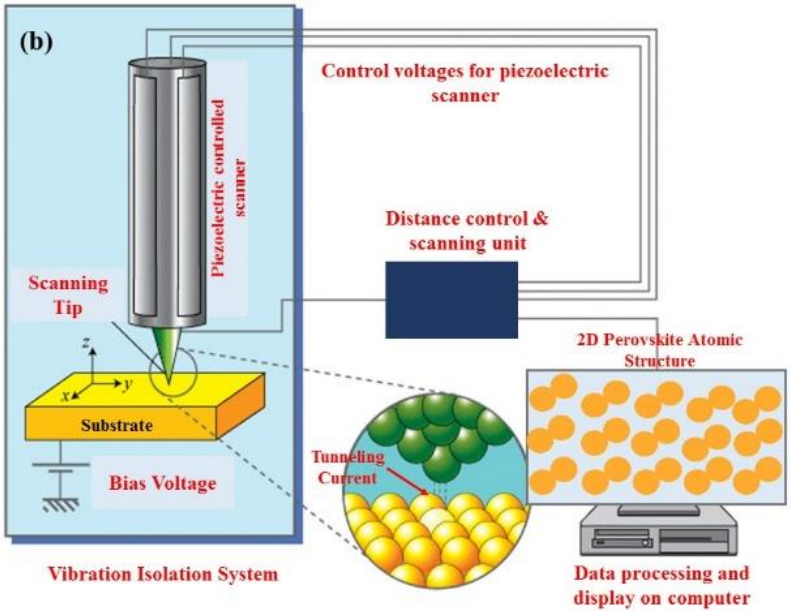

Figure 2.3: STM working principle [142].

2.3.2 Scanning Tunneling Spectroscopy (STS)

STS provides information about the local electronic properties of the material down to the sub-nanometer scale. During scanning tunneling spectroscopy, the electronic feedback loop is kept open, and the current between the tip and the sample is recorded. The obtained graph depends on the local electronic properties of the sample LDOS (local density of states). With STS we can measure the bandgap of materials. STS can also provide information about the trap states in PVSK material and link them to structural features in STM images. These trap states are considered to play a crucial role in hysteresis and low solar cell performance and were suggested to act as electron-hole recombination centers [143].

2.3.3 X-Ray Photoelectron Spectroscopy (XPS) and Ultraviolet Photoemission Spectroscopy (UPS)

X-ray photoelectron spectroscopy was first developed by Kai Siegbahn and his research group in the mid-1960s at the University of Uppsala Sweden [144]. XPS is a surface-sensitive technique that measures the elemental composition, and chemical states

of a material surface Figure 2.4 (a), which shows the semiconductor and metal XPS, VB by UPS, and CB analysis by inverse photoemission spectroscopy (IPES). XPS uses X-ray radiation from 200-2000 eV to examine the core levels in a material. In this technique, spectra are obtained by the X-ray on the solid surface to measure the kinetic energy of escaped electrons from the top 1-10 nm thickness of material. In XPS/UPS the number of emitted electrons of given kinetic energies can provide information about band energies and chemical composition. We utilize the XPS to examine the stoichiometric ratio of perovskite ultra-thin films. We used UPS for probing the valence band of the perovskite material. In UPS measurements, the source of radiation (10-45 eV) is normally a noble gas discharge lamp. For example, He I (21.22 eV) is used to examine the valance band levels information of the chemical composition of the perovskite film. The probing depth of UPS is less than 2 nm [145].

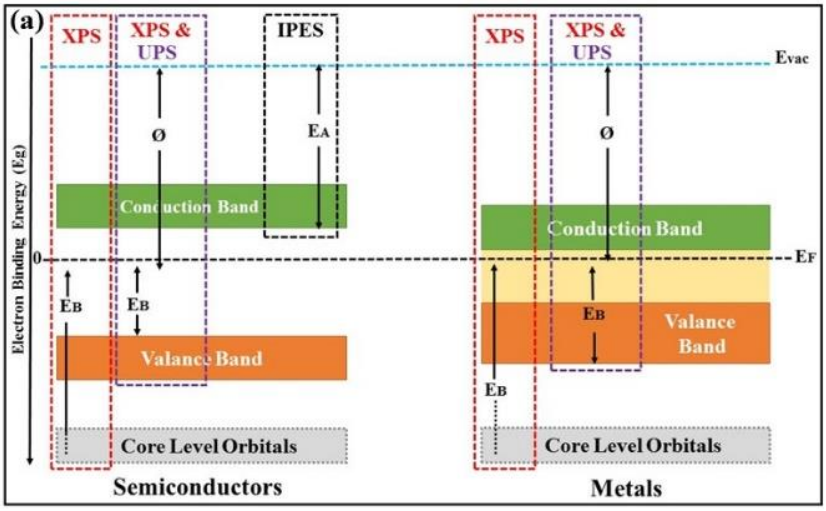

Figure 2.4: Characterization instruments.(a) XPS/UPS/IPES band characterization of semiconductors and metals. [145].

Figure 2.5 shows our custom-built UHV system, in which we transfer a sample of perovskite ultra-thin films from STM to the XPS/UPS chamber entirely under UHV conditions. With this state-of-the-art setup, atomic-scale results are correlated to the changes in energetics in functioning devices, which helps to close the gap between atomic-scale study and macroscale solar cells.

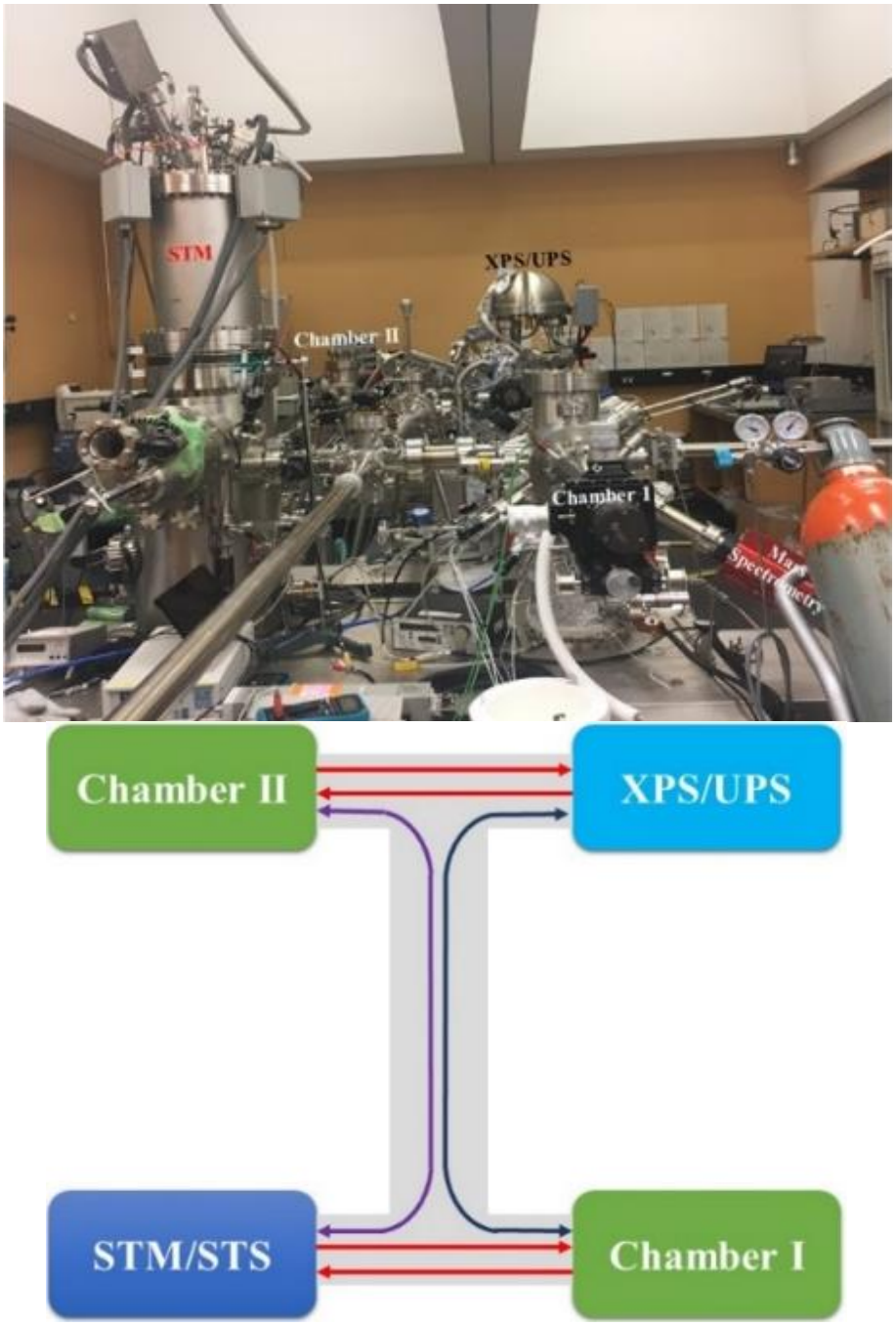

Figure 2.5: UHV system labeled with STM, vacuum chambers, and XPS/UPS setup (left), and the corresponding diagram shows the sample flow inside the UHV system.

2.3.4 Low Energy Inverse Photoemission Spectroscopy (LEIPS)

LEIPS provides information about the conduction band or the unoccupied levels and enables direct measurement of the sample electron affinity. It measures the emitted near-ultraviolet light from a sample during electron bombardment. While UPS measures the occupied levels or the valance band by analyzing the emitted photoelectrons during irradiation by UV light as depicted in Figure 2.6.

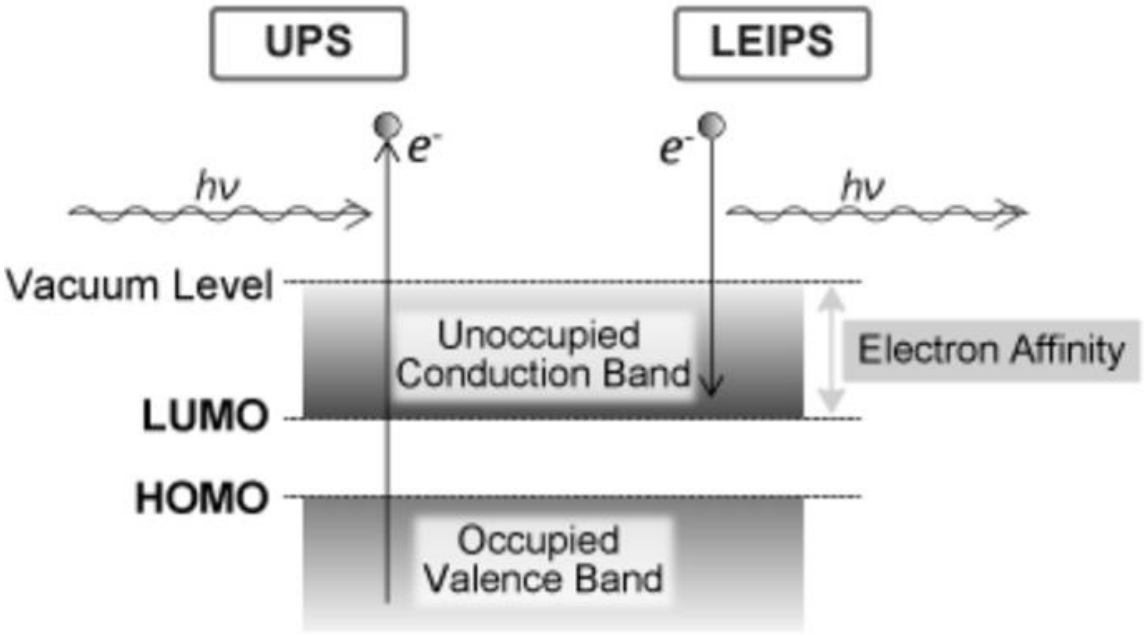

Figure 2.6: LEIPS and UPS energy diagram [146]

More, by LEIPS the organic material beam damaged is dramatically reduced in comparison with conventional IPES because it measures near UV light using low energy electrons of 5 eV or less .[147]. In LEIPS experiments, "the sample bias is adjusted to the net energy of the bombarding electrons and the low energy electron beam is set to a fixed energy" [147]. A band pass filter on the atmospheric side selects the generated UV light with 5 eV or less and the photomultiplier tube detects it and converts it to an electrical signal. The generated plot corresponds to the "photon signal intensity vs. net kinetic energy of the bombarding electrons" [147].

2.3.5 Fourier Transform Infrared Spectroscopy (FTIR)

FTIR is a method of infrared spectroscopy. Almost any compound having covalent bonds (organic or inorganic) can be probed by FTIR. The compounds absorb different frequencies of electromagnetic radiation in the infrared region. We are interested in the vibrational region (corresponding to the infrared region) for chemical purposes and the unit is called wavenumber ($\bar{\nu}$) for this vibrational infrared region. Wavenumbers are directly proportional to energy, which is the main reason that chemist prefers to use wavenumber as a unit. Wavenumber is expressed as the reciprocal of the radiation wavelength in centimeter (cm^{-1}) [148]. Figure 2.9 shows the electromagnetic spectrum, which consists of different regions corresponding to different energy (E), frequency (ν), and wavelength (λ) ranges. The inverse relationship between wavelength and frequency derives the wavenumber (cm^{-1}) unit of near, mid, and far-infrared. More, table 2.1 summarizes the spectrum regions, and the types of energy transitions, how they treat the bonds in molecules.

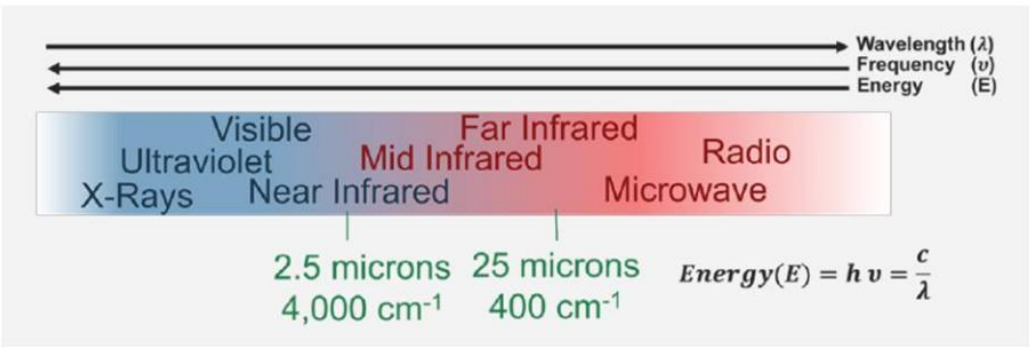

Figure 2.7: Electromagnetic spectrum.

Region of Spectrum	Energy Transition
X-rays	Bond Breaking
Ultraviolet/Visible	Electronic
Infrared	Vibrational
Microwave	Rotational
Radiofrequencies	Nuclear Spin (nuclear resonance spin) Electronic spin (electron spin resonance)

Table 2.1: Energy transitions in each region of the Electromagnetic spectrum [148]

In FTIR, in the IR region, the interactions between matter and electromagnetic fields are measured[149]. Electromagnetic waves couple with the molecular vibrations as shown in Figure 2.10. By absorbing IR radiation, the molecules get excited to a higher vibrational state [149]. The absorbed IR frequency interacts at a certain frequency with the molecule. Hence, FTIR provides fingerprint information of the sample chemical composition. [149].

In FTIR, the IR light changes the dipole moments in molecules which corresponds to specific vibrational energy as shown in Figure 2.10 [150]. Symmetric bonds do not absorb infrared radiation because these bonds do not have electrical dipoles such as H_2 or Cl_2 [148]. Equation 1 shows how vibrational energy relates to the bond spring constant (k) and reduced mass (μ).

$$v = 1/2\pi\sqrt{\frac{k}{\mu}} \qquad (1)$$

For instance, we can see in the table in Figure 2.10 that for the constant k, C-C, C=C, and C≡C show an increase of 800 cm-1 across the series. While increasing the mass(μ), substituting nitrogen and oxygen atoms in the C-C bond causes a shift of 50 cm^{-1}. These two series show that the bond type has a large effect more than mass.

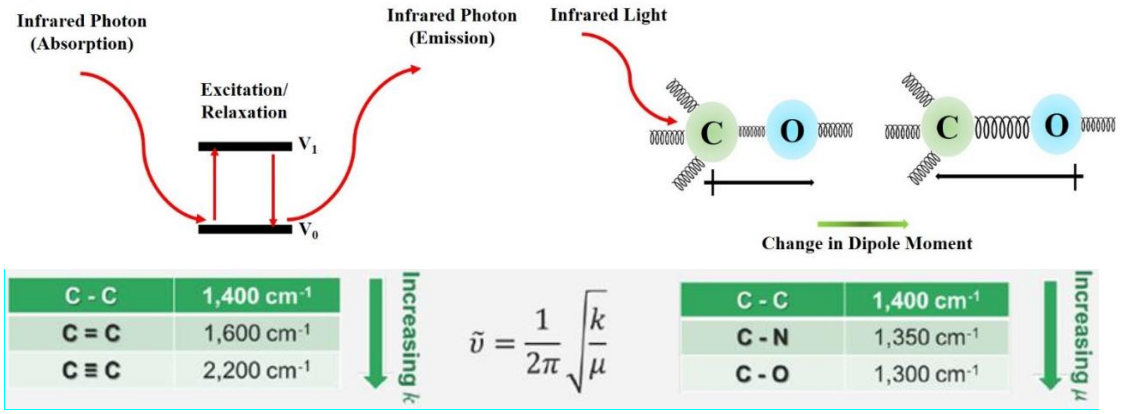

Figure 2.8: Interaction between infrared light and matter

FTIR consists of mainly three major parts: source, interferometer, and detector as shown in Figure 2.11. In IR spectroscopy, infrared radiation passes through a sample, and some being absorbed by the sample, and some passes through. The resulting spectrum represents the molecular absorption and transmission, which creates a sample of molecular fingerprints. "Like fingerprints, no two unique molecular structures produce the same infrared spectrum. This makes infrared spectroscopy useful for several types of analysis."

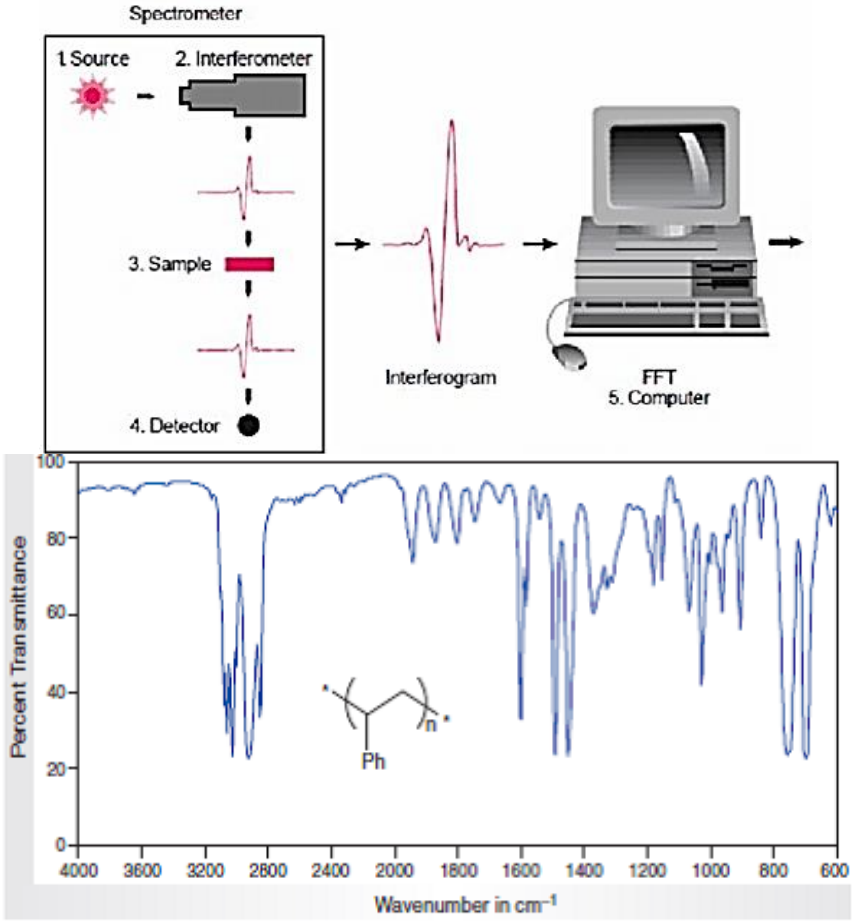

Figure 2.9: FTIR spectrometer parts source, interferometer, and detector [149].

FTIR spectroscopy is used in various modes for different materials and types. Such as transmission mode used for thin films and reflectance mode for single-crystal spectroscopy. FTIR can identify unknown materials, can determine the amounts in mixed components, and can determine the sample quality/consistency. Additionally, it provides a method of precise measurements, that do not require rigorous calibration and takes only a few seconds to measure the IR spectrum. It measures a wide variety of volatile organic and inorganic compounds.

2.3.6 X-ray diffraction (XRD)

X-ray diffraction (XRD) is a rapid analytical technique primarily used for phase identification of a crystalline material and can provide information on unit cell dimensions. The analyzed material is finely ground, homogenized, and the average bulk composition is determined. In 1912, Max von Laue, "discovered that crystalline substances act as three-dimensional diffraction gratings for X-ray wavelengths similar to the spacing of planes in a crystal lattice" [151]. Now X-ray diffraction is a common technique to study atomic spacing and crystal structures.

"X-ray diffraction is based on constructive interference of monochromatic" X-rays [151]. X-ray diffractometers consist of an X-ray tube, an X-ray detector, and a sample holder. A cathode-ray tube generates X-Rays to heat a filament to produce electrons, which are accelerated toward a target by applying a voltage. The accelerated electrons bombard the target material and produce X-rays by fluorescence. Characteristic X-ray spectra is produced by in dislodging of inner shell electrons of the target material when the electrons have sufficient energy. The intensity of the reflected X-rays is recorded by rotating the sample and detector. "When the geometry of the incident X-rays impinging the sample satisfies the Bragg Equation ($n\lambda=2d\sin\theta$) as shown in Figure 2.13 (a), constructive interference occurs and a peak in intensity occurs" [151].

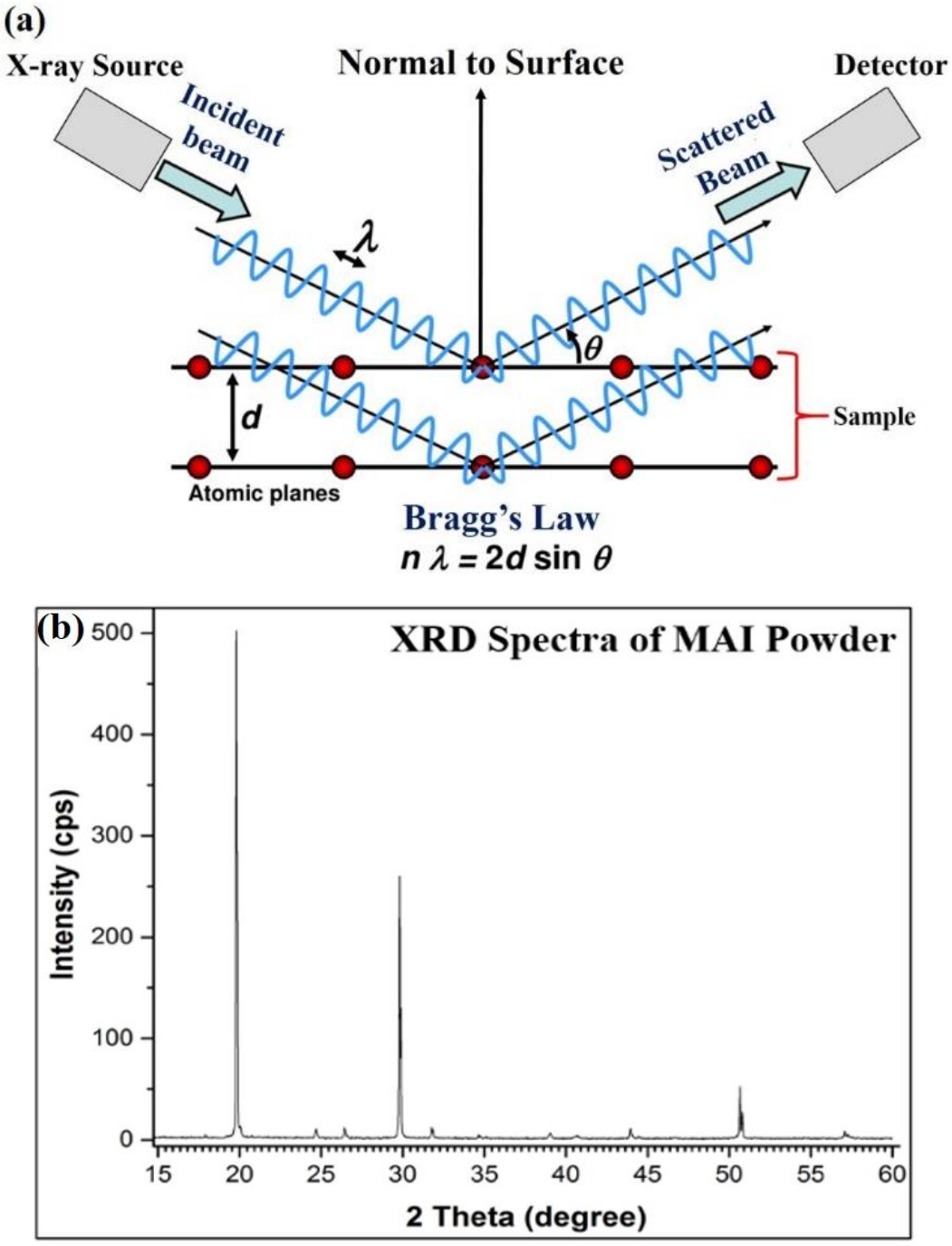

Figure 2.10: XRD (a) working principle and setup. (b) XRD Spectra

For processing the X-ray signal and recording, a detector is used, which also converts the signal to a count rate and sends it to the device for output. The data is collected at 2θ from ~5° to 70° angles that are present in the X-ray scan for typical powder patterns. XRD requires minimal sample preparation and data interpretation is relatively straight forward.

For the identification of unknown crystalline minerals and inorganic compounds, X-ray powder diffraction is widely used. Additionally, it can be used for the measurement of sample purity and textural measurements of the orientation of the grain in a

polycrystalline sample. XRD results are commonly presented as peak positions at 2θ and X-ray counts (intensity) in the form of a table or an x-y plot as shown in Figure 2.13 b.

2.3.7 Gas cluster ion beam (GCIB) sputtering

GCIB generates ionized clusters of high-energy beams for organic materials sputtering and analysis. GCIB is ideal because the beam can be tuned according to the experiments, which makes it an incredibly versatile ion source. GCIB has two features of high current and large spot size. The organic materials etching rates are several orders higher in magnitude than semiconductors and metals. Therefore, GCIB provides an excellent cluster beam to clean surfaces before analysis. Furthermore, the large clusters cause less, sub-surface damage or fragmentation [152]. A beam of Ar^{+}_{n} clusters bombards a sample with energies of several keV of n argon atoms, which forms a shallow crater on the sample surface and removes the uppermost surface layer. The sputtering rate can be controlled by the amount of removed material per time which depends on the beam energy. GCIB depth profiling analysis of organics provides minimal loss of chemical information due to ion beam damage.

2.3.8 Density functional theory (DFT)

DFT is a computational quantum mechanical modeling method of obtaining an approximate solution to the Schrödinger equation of a many-body system. DFT computational codes are used in chemistry, physics, and materials science for the investigation of a vast range of structural, vibrational, thermodynamics, electronic, and magnetic properties of materials, molecules, and defects. The properties of many-electron systems can be determined by using functions in the DFT. For the identification of the system's ground state, DFT utilizes functions of the electron density of the system. DFT is an explanatory tool increasingly used in materials discovery and computational experiments. Furthermore, previous DFT calculations provided the theoretical support for the interpretation of organic and inorganic perovskite STM studies [12]. Simulations of STM images and predictions of crystal structures discussed in this thesis were provided by collaboration with DFT theory groups. Therefore, the details of the DFT calculations are not included in this thesis but can be found in the publications.

2.4 Summary

In this chapter, we explained thoroughly the working principles of all instrumentation and methods which is used for all experiments in this thesis. Turbo and ion pumps were explained for achieving an ultra-high vacuum in the UHV system. Au (111) substrate is used for all surface science experiments. By sputtering and annealing the outside loaded Au (111) was cleaned before deposition of PVSK ultra-thin films. For fabricating PVSK and additives materials smooth surfaces, I used the vacuum co-evaporation under high vacuum which is one of the controlled evaporation processes is used for the fabrication of crystalline structures. After fabricating the ultra-thin films, for 2D imaging of surfaces at the atomic scale, STM working was explained in detail for achieving the high-resolution atomic images. Additionally, for the local electronic properties measurements, STS was explained in combination with STM. More, for the

characterization of each precursor's concentration in the ultra-thin films, XPS is described in detail with all the thickness limitations and energies. The working principle of UPS/IPES was elaborated for the bandgap measurements which is one of the crucial characterization steps for the bandgap tuning measurements before and after the additives deposition on PVSK films. The different modes of FTIR e.g. reflective and transmission modes for PVSK thick films measurements for the stability test have been described thoroughly and how in the IR region matter and electromagnetic field interact and gives the fingerprints of each molecule for identification. Before loading the precursors in the Knudsen cells for the co-evaporation under ultra-high vacuum, I used always powder XRD for confirmation of the precursors. The working principle of XRD is described by explaining the instrument in detail and showing that the results are commonly present in the peak positions at 2θ and intensity in an x-y plot for the identification of precursors in the powders or the thin and thick films of PVSK. Last but not least, the GCIB process is defined for etching the individual monolayer by monolayer for exploring the material segregation and infusion processes inside the material films. In combination with XPS, GCIB provides important information of the material to further improvements. Moreover, GCIB is an ion beam cluster source that is mainly used for organic material etching without damaging the monolayers. Finally, the DFT information provided in this chapter for understanding the DFT calculation for the STM results in the next chapters. DFT is used for the investigation of thermodynamics and kinetics of materials, molecules, and defects.

Chapter 3: Revealing the Atomic-level Topographies of MAI Stripe and Non-Stripe Structures, PbI_2 Stripe and Hexagonal Random Structures, and $MAPbI_3$ Perovskite

3.1 Introduction

Metal halide perovskite solar cells have garnered much attention from the research community since 2009 because of the power conversion efficiency (3.8% to 25.5%) and low-cost fabrication processes [153]. Despite many advantages, they have instability issues that need to be resolved. The $MAPbI_3$ perovskite structure consists of organic MA, a Pb cation, and an inorganic halide I anion to form an ABX_3 structure, as explained in Section 1.2. Experimentally and theoretically, the electronic properties and the crystallographic structures of $MAPbI_3$ have been intensively studied, from which it is known that MA stabilizes the framework of the Pb-I octahedra structure and does not actively contribute to the formation of the electronic structure of perovskite [30]. Additionally, MA plays a crucial role in the phase transitions of $MAPbI_3$ [25]. To date, four different phase transitions have been reported, including a transition from cubic (α phase) to tetragonal (β phase), tetragonal to orthorhombic (γ phase), and orthorhombic to δ phase (decreasing the temperature from 358 down to 100 K) [25]. These phase transitions take place because of the PbI_6 and MA cation dynamics. The bulk structure of $MAPbI_3$ has been extensively studied to solve the instability issues, but surface or atomic-scale studies to understand the fundamentals of these instability causes are scarce.

Moreover, no atomic-scale studies have been carried out for understanding individually the atomic structures of MAI and PbI_2. In this chapter, we investigate by LT-STM the atomic structures of both precursors MAI and PbI_2 of $MAPbI_3$. For MAI we observed two different strip and non-strip structures that form from dimers, while for PbI_2 two different structures of hexagonal stripe and random structures containing hexagonal structures are observed. The PbI_2 experimental atomic results are in good agreement with the DFT calculated results described elsewhere [154]. The PbI_2 atomic structures were observed after the first deposition of $MAPbI_3$ and overnight annealing at room temperature in UHV and confirmed by XPS measurements. In this study, we used the orthorhombic phase of $MAPbI_3$ for all experiments because the sample was kept at 4.5 K inside the STM cryostat for scanning to reduce the thermal vibrations and increase the lateral resolution as described in Section 2.3.1.

This chapter mainly focuses on the MAI and $MAPbI_3$ protocol optimization with high-resolution STM atomic topographies and XPS measurements. Furthermore, the 1.45 eV bandgap of $MAPbI_3$ was characterized by UPS/IPES.

3.2 MAI protocol optimization

Before the $MAPbI_3$ ultra-thin film fabrication, a protocol for the MAI deposition conditions needed to be optimized. Therefore, MAI deposited at different conditions on clean Au (111) substrate was studied in an ultrahigh vacuum (UHV) system by STM (base pressure $< 2 \times 10^{-10}$ Torr). The Au (111) substrate was cleaned by three cycles of Ar^+ sputtering for 60 min at a base pressure of 8.5×10^{-5} Torr followed by annealing for 20 min at 700 K at a base pressure of 2×10^{-8} Torr [12]. The protocol consists of an initial thermalization of the K-cell with MAI for four hours in the UHV chamber under the pressure of $< 2 \times 10^{-9}$ Torr. After thermalization, MAI was deposited on clean Au (111) for two different times (e.g., 1 and 2 min in total 3 min) keeping the K-cell temperature at 396 K. During the deposition of MAI (Figure 3.1), the Au (111) substrate was kept at a temperature of 132 K to ensure a high sticking coefficient of MAI.

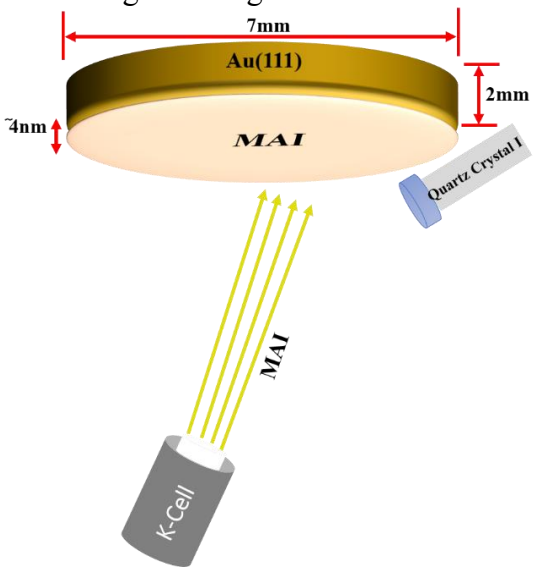

Figure 3.1: Demonstration of MAI deposition on a clean Au (111) substrate in a UHV chamber.

After evaporation, for characterization the sample was transferred into the analysis chamber (base pressure of $\sim 2 \times 10^{-10}$ Torr), which is equipped with a dual-anode (Al-Kα = 1486.6 eV and Mg-Kα = 1253.6 eV) non-monochromatic X-ray source (DAR 400, Scienta Omicron GmbH) for XPS with an energy resolution of ~0.8 eV. For 1 min evaporation of MAI, no C and N peaks were observed but only Au and I peaks were observed as shown in Figure 3.2, which confirmed that there is no MA and only I is on the surface of Au (111). In a consecutive experiment, another 2 min of MAI was deposited on the 1 min MAI deposited sample. This sample with a total of 3 min MAI deposition was characterized by XPS and showed much stronger C and N peaks, which confirmed the presence of MAI on Au (111) (Figure 3.3).

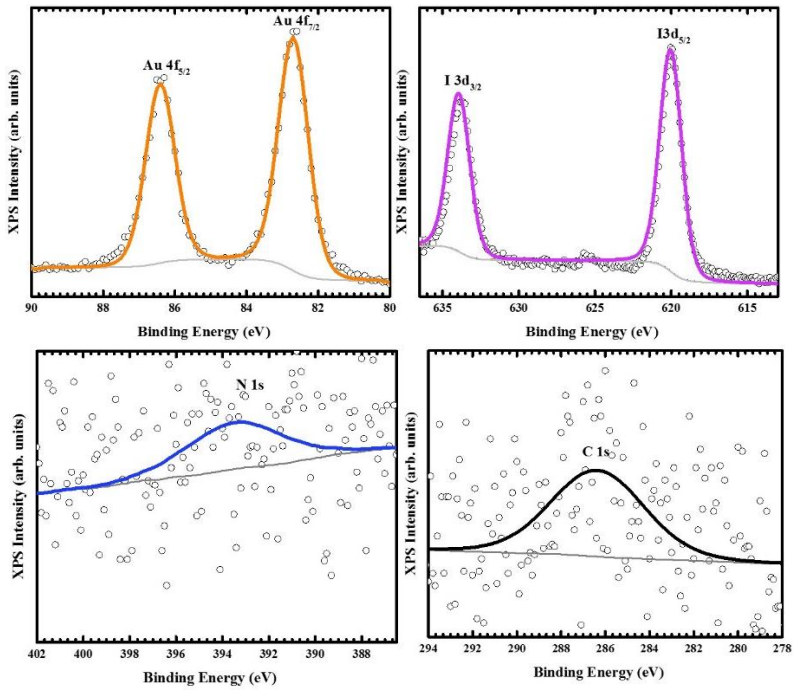

Figure 3.2: XPS spectra show the chemical information of 1 min MAI deposition on Au (111). For the quantitative analyses of peak positions, line widths, and relative areas of the Pb-4f, I-3d, C-1s, and N-1s components, the raw XPS spectra were fitted with Gaussian- Lorentzian functions in the CASA XPS software.

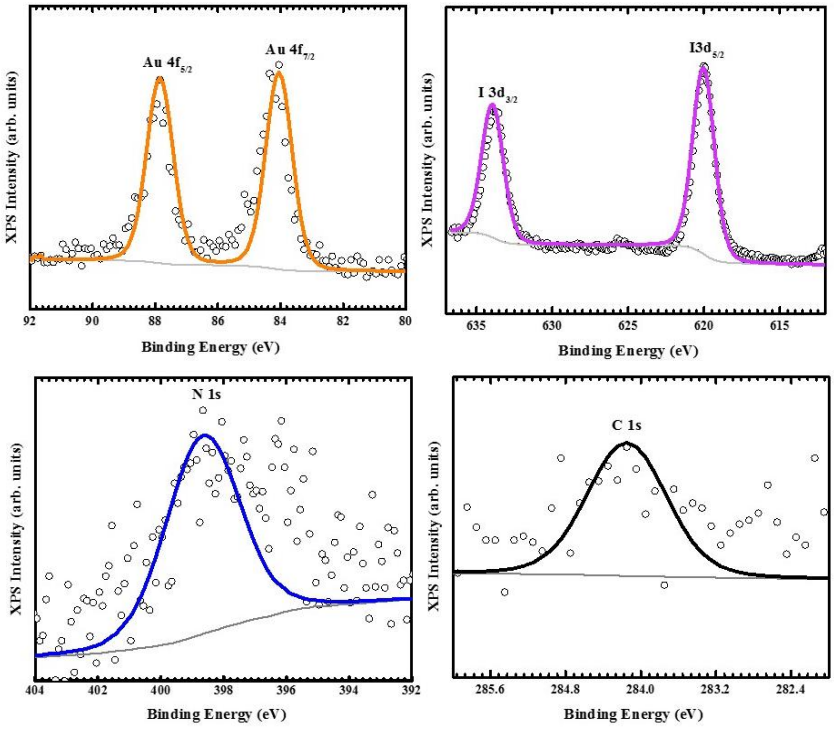

Figure 3.3: XPS spectra show the chemical information of 3 min deposited MAI precursor concentration on Au (111).

3.3 Atomic resolution imaging of MAI

The 3 min MAI sample was *in situ* transferred to a low-temperature scanning tunneling microscope (LT-STM, Scienta Omicron GmbH) for characterization. The STM measurements were performed at 4.5 K using Pt/Ir tip and with a bias voltage applied to the sample. Figure 3.4a shows the formation of MAI grains on a large area with grain sizes around 30 nm. We observed three different structures of MAI on Au (111) as shown in Figure 3.4b. The first and second monolayers (MLs) of MAI consist of snaky and random structures, while as the coverage increased the atomically smooth third ML forms as a stripe and non-stripe structures, which will be explained in detail in Sections 3.3.1 to 3.3.3. Furthermore, the analysis of line profiles (Figure 3.4 c-d) of MAI step heights reveals that the third ML of MAI structure is 2.2 Å while the first ML height is 1.8 Å. On the basis of these step heights, we propose that the stripe and non-stripe structures have heights of 2.2 Å, while the height for snaky and random structures is 1.8 Å.

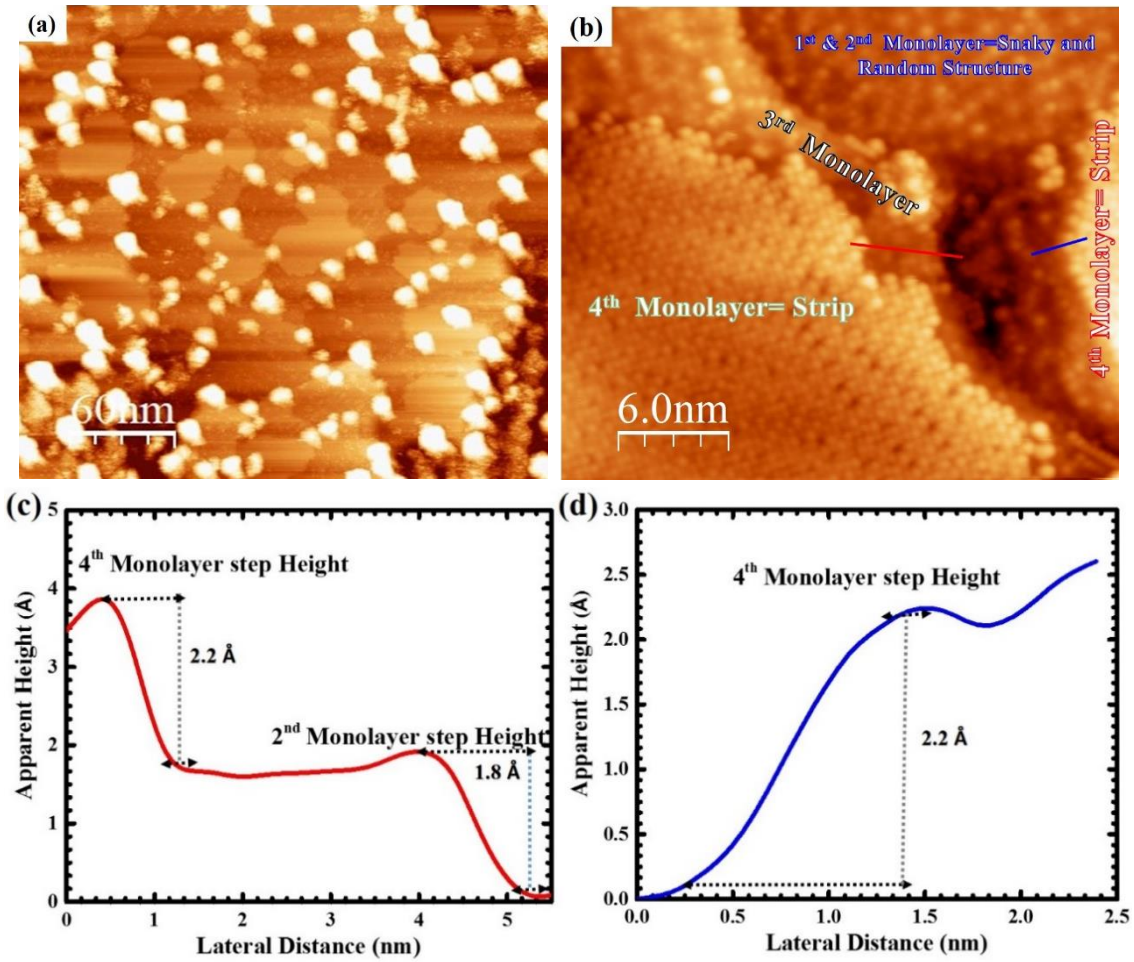

Figure 3.4: MAI structure. (a) LT-STM image of a large area of MAI grains (Scan area = 300 × 300 nm^2; Sample bias voltage = –2.5 V, Tunneling current = 17 pA). (b)Atomic structures of first, second, and third MLs of MAI (Scan area = 25 × 30 nm^2; Sample bias voltage = –2.5 V, Tunneling current = 30 pA). (c-d) Step heights of all three MLs obtained on the regions marked by red and blue solid line in (b).

3.3.1 Atomic resolution imaging of MAI: I hexagonal in the first ML and the snaky structure in the second ML

We observed that both the first and second MLs contain snaky and hexagonal structures (Figure 3.5a). It is found that the I hexagonal structure corresponds to the first ML (Figure 3.5 b), which is formed from the I hexagonal structure on Au (111) as reported in ref. [155]. Also, we observed the brighter I atoms as adatoms on the surface of the few hexagonal structures on the first ML, which is supposed to be the disassociated I from the MA molecule. Additionally, the MAI third and fourth MLs are different in structures than the structures reported [156]. Figure 3.5b shows the bright snaky structures formed from iodine-iodine (I-I) pair structure (dimer) (Figure 3.5c) on the surface of I hexagonal structures. These snaky structures are formed from the adsorption of MA molecules [157] on the surface of an I hexagonal structure ML. The dimer line profile gap 3.4 Å (Figure 3.5 d) is in good agreement with ref. [13].

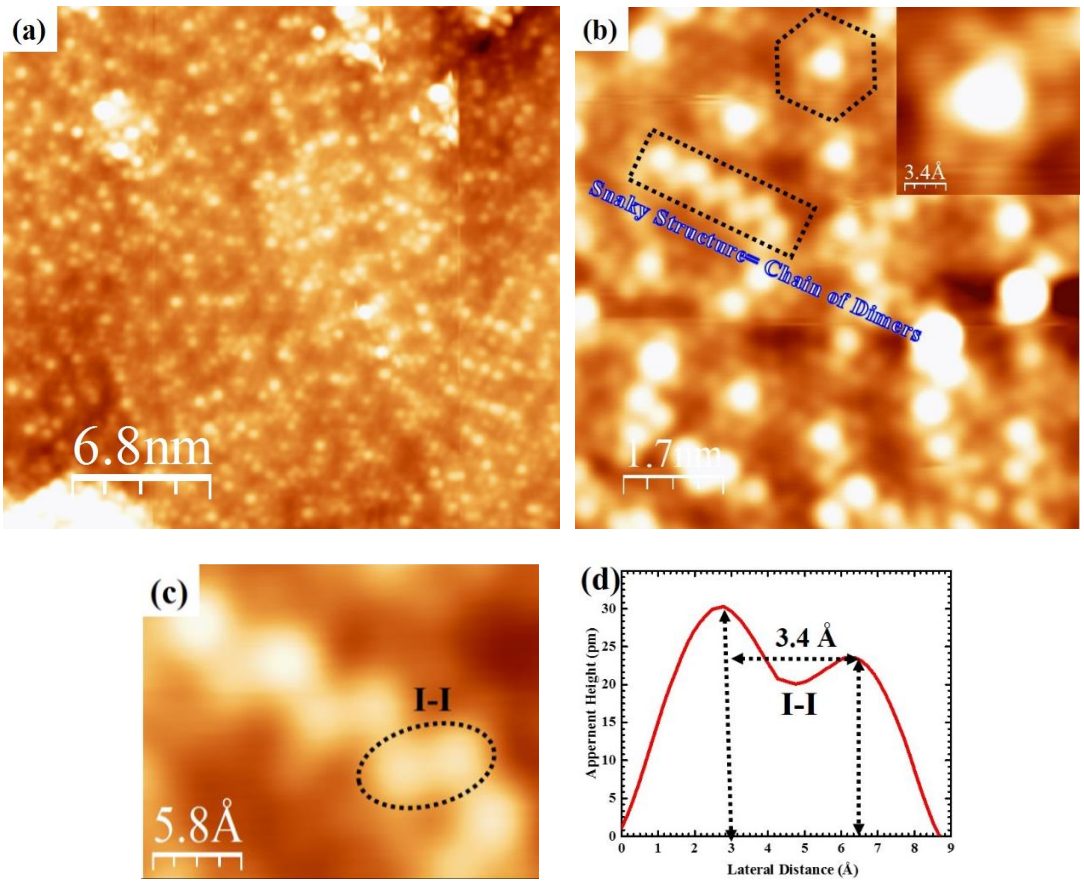

Figure 3.5: Structures of MAI in the first and second ML. (a) LT-STM image of a large area of the hexagonal and snaky structures deposited on Au (111) (Scan area = 30 × 30 nm^2; Sample bias voltage = –2.5 V, Tunneling current = 17 pA). (b) STM topography of close up of snaky structure, which contains the second ML chain of dimers and the first ML I hexagonal structure (Scan area = 7 × 7 nm^2; Sample bias voltage = –2.5 V, Tunneling current =100 pA). (c-d) Dimers structure marked by black dash ellipse in snaky structure with a line profile of dimer gap of 3.4 Å (Scan area = 20 × 25 $Å^2$; Sample bias voltage = –2.5 V, Tunneling current =100 pA).

3.3.2 Atomic resolution imaging of MAI in the fourth ML with non-stripe structure

As the coverage increased, atomically smooth molecular structures formed a non-stripe structure (Figure 3.6a) with a height profile of 2.2 Å. The non-strip structure contains filled and unfilled square structures (we label them as large and small zigzag structures that form from multiple dimers oriented in different directions as shown in Figure 3.6b-c). The unfilled square is formed from five dimers with a characteristic gap in the center of 1.4 × 1.4 nm^2. The vertically aligned two pairs of dimers have a line profile gap of 3.5 Å while the horizontally aligned one dimer has a slightly different gap of 4.4 Å (Figure 3.6d). As reported previously [12 13], the halide dimerization in the perovskite forms because of the MA molecule with two and four-fold rotations. On the basis of previous reports [12 13], we can conclude that the formation and orientation of dimers in the square structures of MAI is because of the MA dipole movement. In addition, we also observed filled squares, which were formed from five dimers, but with the center of the dimer in a different orientation (Figure 3.6e-g). MA is not visible in the STM atomic images under similar tunneling conditions. Therefore, only dimers are visualized in all LT-STM images.

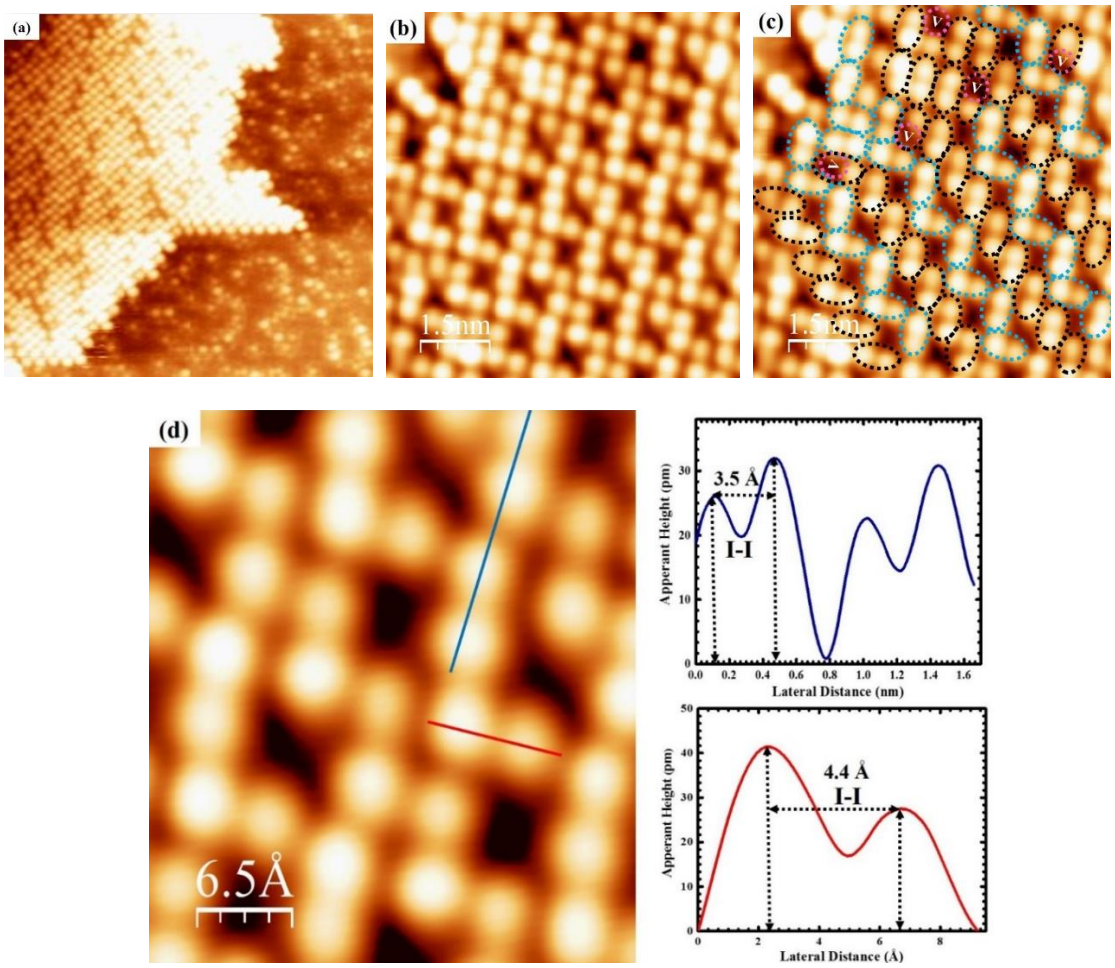

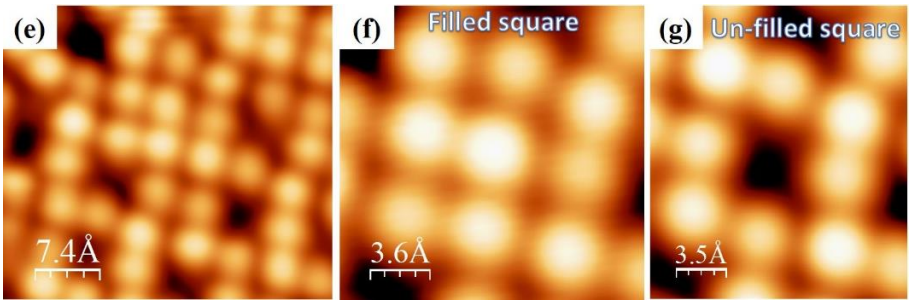

Figure 3.6: The MAI non-strip structure (a) LT-STM image of Non-stripe grain of MAI deposited on Au (111) (Scan area = 30 × 30 nm^2; Sample bias voltage = –2.5 V, Tunneling current = 100 pA).(b-c) Atomic structure of dimers oriented squares in non-strip structure (Scan area = 7 × 7 nm^2; Sample bias voltage = –2.5 V, Tunneling current = 100 pA). (d) Zoom in of the dimers formed square structure in (b) and height profile marked by solid blue and red line in (d) (Scan area = 37.5 × 33 $Å^2$; Sample bias voltage = –2.5 V, Tunneling current = 100 pA). (e-f) Close up images of filled and unfilled squares.

Additionally, a large number of I vacancies (marked as pink dashed circles) were observed in the unfilled and center-dimer-filled squares non-stripe structure as shown in Figure 3.7. The bright protrusion on the surface of the filled and unfilled square is assumed to be the dissociated I anions from the MA molecules.

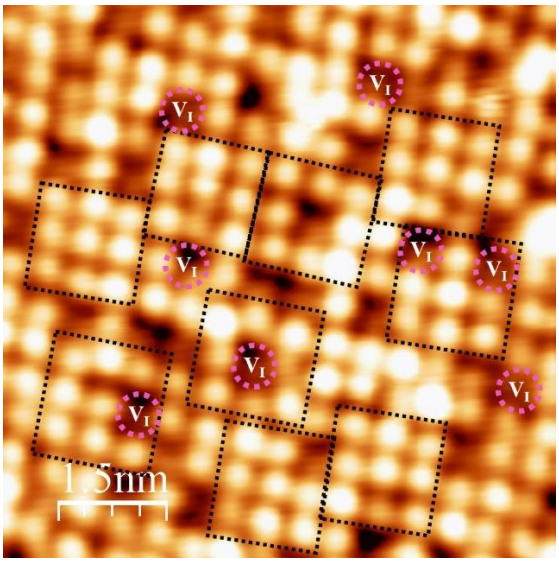

Figure 3.7: I ions vacancies in MAI non-Stripe Structure (7 × 7 nm^2, Sample bias voltage = –2.70 V; Tunneling current =100 pA).

3.3.3 Atomic Structure of MAI Stripe Structure

Another smoother molecular structure was found on the fourth layer as a stripe structure, which is formed from dimers and the disassociated I ions from MA molecules as shown in Figure 3.8a. Each stripe has a characteristic width of ~3.2 nm (inset in Figure 3.8a). In the stripe, the square structures are filled in the center with another dimer and each dimer has a gap of 4 Å from the line profile shown in Figure 3.8b-c. Each stripe is separated from another strip by the dissociated I ions from MA. Stripe structure is formed

from the series of dimers in a row and at a similar angle while in the non-stripe structure dimers were oriented at a different angle to form square structures.
Furthermore, we did not observe any defects in the stripe atomic structure while in the non-stripe structure many defects were observed. Based on our atomic-scale observation of the strip and stripe structure of MAI, we can conclude that the strip structure molecular layer might be the fifth ML on top of the non-stripe layer because the strip structure ML is more properly atomically oriented than the non-stripe structure.

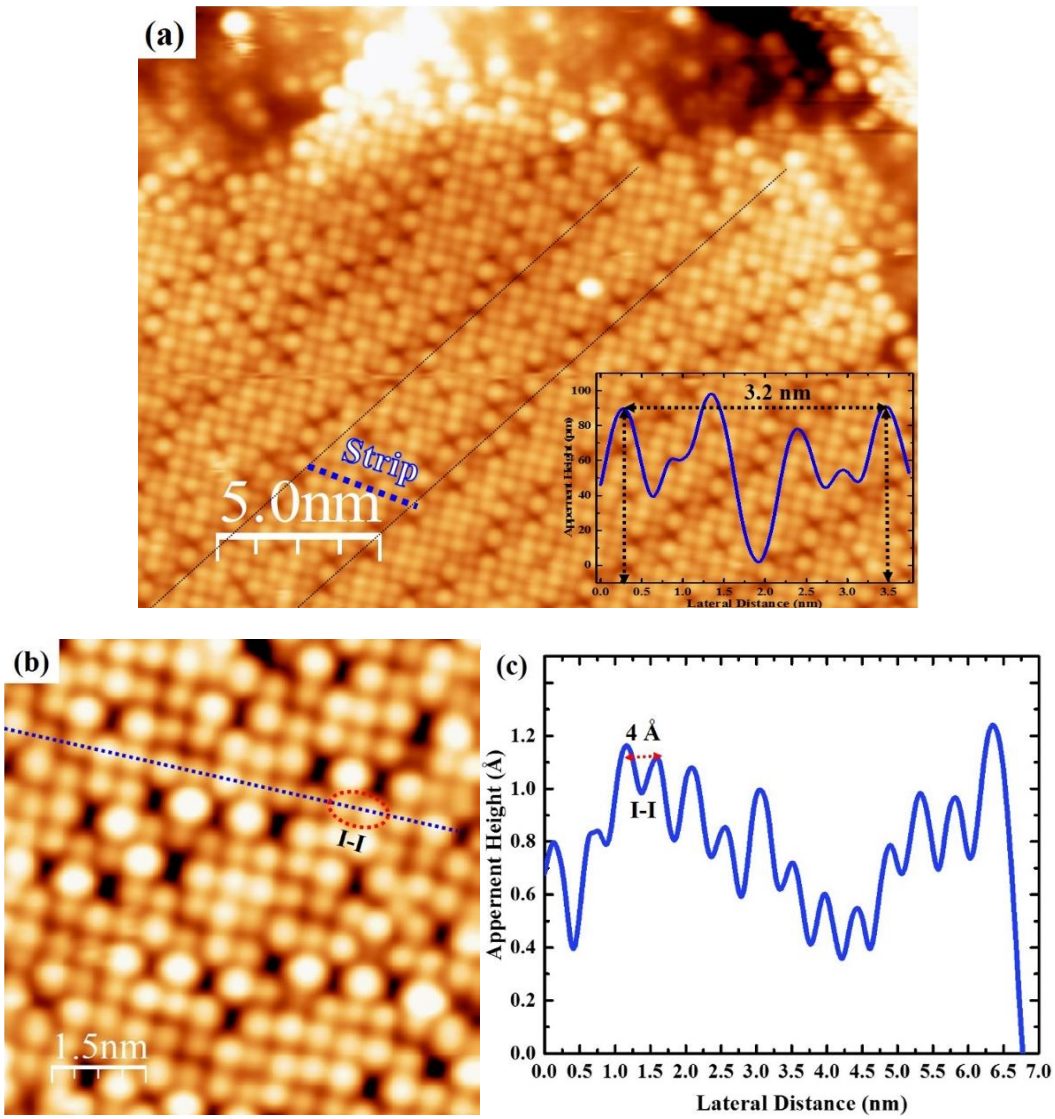

Figure 3.8: MAI-stripe structure. (a) LT-STM high-resolution image of stripe structure with inset of height profile of a stripe structure on Au (111) (15×15 nm^2 Sample bias voltage=–2.5 V, Tunneling current =17 pA). (b) LT-STM Dimers and I dissociated I ions from MA molecule (7×7 nm^2, Sample bias voltage=–2.5 V, Tunneling current=100 pA). (c) Line and height profile of the stripe structure and the dimers in the stripes in (b) marked by a blue dashed line and redellipse.

3.4 $MAPbI_3$ ultra-thin film growth by vacuum co-evaporation

First, the protocol was optimized for growing the ultra-thin polycrystalline $MAPbI_3$ ($CH_3NH_3PbI_3$) films on Au (111) substrate as shown in Figure 3.9, under UHV ($<1\times10^{-9}$ Torr) conditions. This protocol is used for all experiments of $MAPbI_3$ fabrication in this thesis. Au (111) substrate was used because it is considered chemically inert and conductive for STM and has low interaction with thin films. Before deposition, the Au (111) was cleaned by sputtering and then annealed at 700 K. The ultra-thin films of a few MLs (approx. 4 nm) were prepared by thermal evaporation, using co-deposition of the precursor molecules MAI (Power supply settings= voltage= 6.80 V, I= 0.17 A, T=377K), and PbI_2 protocol (Power supply settings= voltage= 12.30 V, I= 0.31 A, T=500K). The substrate was cooled to 130 K during deposition (3 min) to increase the adhesion of $MAPbI_3$ on Au (111) and then annealed for 3 hours at room temperature in the UHV intersection chamber to remove the excess of MAI. After annealing, the perovskite thin films were kept in the STM cryostat at a temperature of 77 K to reduce thermal drift and increase lateral resolution during scanning. All images are obtained with platinum/iridium tip with sample bias voltage in constant current mode. The tip is introduced at a distance of 2-5 Å to the sample to enter the tunneling regime, where the topography of the surface is determined with atomic resolution.

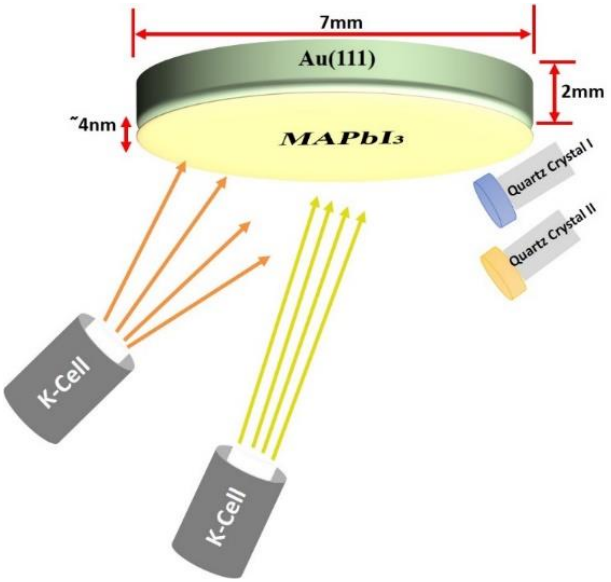

Figure 3.9: Demonstration of co-deposition of MAI and PbI_2 to form $MAPbI_3$ on clean Au (111) in a UHV chamber.

Our theory collaborators Prof. Wanjian Yin and Dr. Zhendong Guo from Soochow University China has performed the DFT calculations in this chapter for pristine $MAPbI_3$. For DFT calculations VASP code [158] was used with the Perdew–Burke–Ernzerhof (PBE) exchange-correlation functional [159] and standard frozen-core projector augmented-wave (PAW) method [160]. More details of the DFT calculations for pristine $MAPbI_3$ and Cl incorporated $MAPbI_3$ are discussed in Chapter 4.

3.4.1 Atomic resolution imaging of overnight annealed $MAPbI_3$ sample at room temperature under UHV and found the PbI_2 structure instead of $MAPbI_3$

First, the $MAPbI_3$ sample was fabricated by following the fabrication protocol given in Section 3.4. We tried adopting the fabrication parameters from She et al. [13] to deposit the $MAPbI_3$ sample in our UHV chamber. A major difference consists of the post-annealing time, where our samples were annealed at RT overnight in UHV rather than for 2 hours as reported by She et al. [13]. After annealing overnight, the sample was transferred into the STM cryostat at 77 K for scanning to achieve the atomic resolution images of the $MAPbI_3$. However, this sample seemed to only consist of the PbI_2 structure (Figure 3.10a-d), suggesting that the MAI completely desorbed from the surface and only PbI_2 was left on the Au (111) surface as shown in Figure 3.10b. To confirm that the STM observation was indeed the PbI_2 structure, the sample was transferred for XPS measurements. XPS spectra in Figure 3.11 show only Pb-4f, I-3d, and Au-4f peaks but no peaks of C-1s and N-1s, which provides the evidence that on Au (111) only PbI_2 are present and MAI has completely desorbed in the UHV chamber. Also, the observed grain sizes of PbI_2 are much larger than the observed grains of MAI in Figure 3.4a. In Figure 3.10b it is shown that two different stripes and random structures of PbI_2 formed on Au (111). Both structures contain I hexagonal structure, which belongs to the P-3m1 space group (Figure 3.12a-b) [154].

From the total height profile of ~42 pm in a random non-stripe structure, we believe that it has 2 ML and the sub-ML height is ~22 pm (Figure 3.10c) by following the height of the top layer of ~20 pm. The random non-stripe structure is formed from the I hexagonal structure, which might be because of MAI desorbing from the surface and just leaving behind the PbI_2 or it might be an I passivation layer on Au (111) [155], without having Pb in the formation of hexagonal structure exhibited by inset in Figure 3.10c. It also can be possible that Pb may diffuse into the metallic Au (111) surface as reported in ref. [161]. Moreover, the width of the topmost strips in random (Figure 3.10c) and strips in regular strips (Figure 3.10d) structures is ~2.2 nm. This may cause the sub-ML of I hexagonal structure with lattice constant 4.4 Å in a similar size in both structures.

Figure 3.10d shows the STM image of the regular stripe structure of PbI_2 and with an I hexagonal structure in the inset. In two I hexagonal structure layers, the Pb layer is sandwiched between I layers leading to non-observation of Pb protrusions in the STM images of stripe structure under the tunneling conditions where I ions appear. Furthermore, from the height profile (Figure 3.10 d) it is observed that the height of each ML of PbI_2 is around ~22 pm.

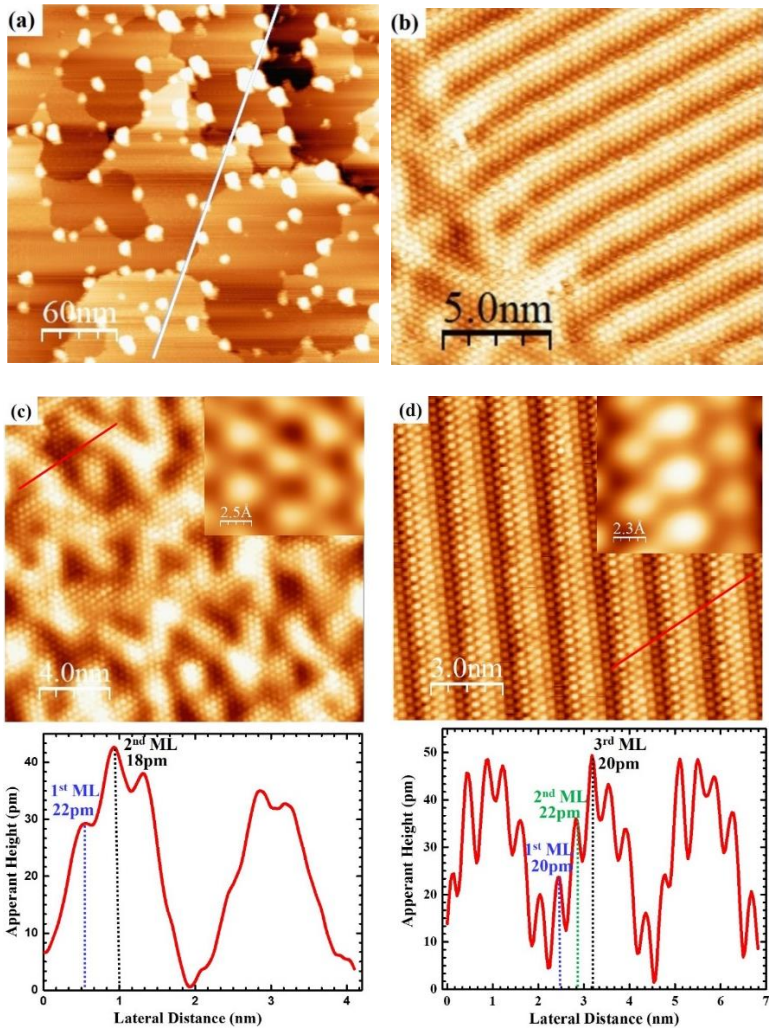

Figure 3.10: The PbI_2 stripe Structure (a) LT-STM image of large area of PbI_2 grains (Scan area = 30 × 30 nm^2; Sample bias voltage = –2.5 V, Tunneling current = 300 pA). (b) LT-STM topographies of strip and non-stripe structure of PbI_2 (Scan area = 15.5 × 15.5 nm^2; Sample bias voltage = –0.5 V, Tunneling current = 300 pA). (c) STM topographies of non-stripe/ random structure of PbI_2 with inset of hexagonal structure and outset line profile of PbI_2 lattice (Scan area = 15 × 15 nm^2; Sample bias voltage = –2.5 V, Tunneling current = 17 pA). (d) STM topographies of stripe structure of PbI_2 with inset of hexagonal structure and outset line profile of PbI_2 lattice (Scan area = 15 × 15 nm^2; Sample bias voltage = –0.5 V, Tunneling current = 300 pA).

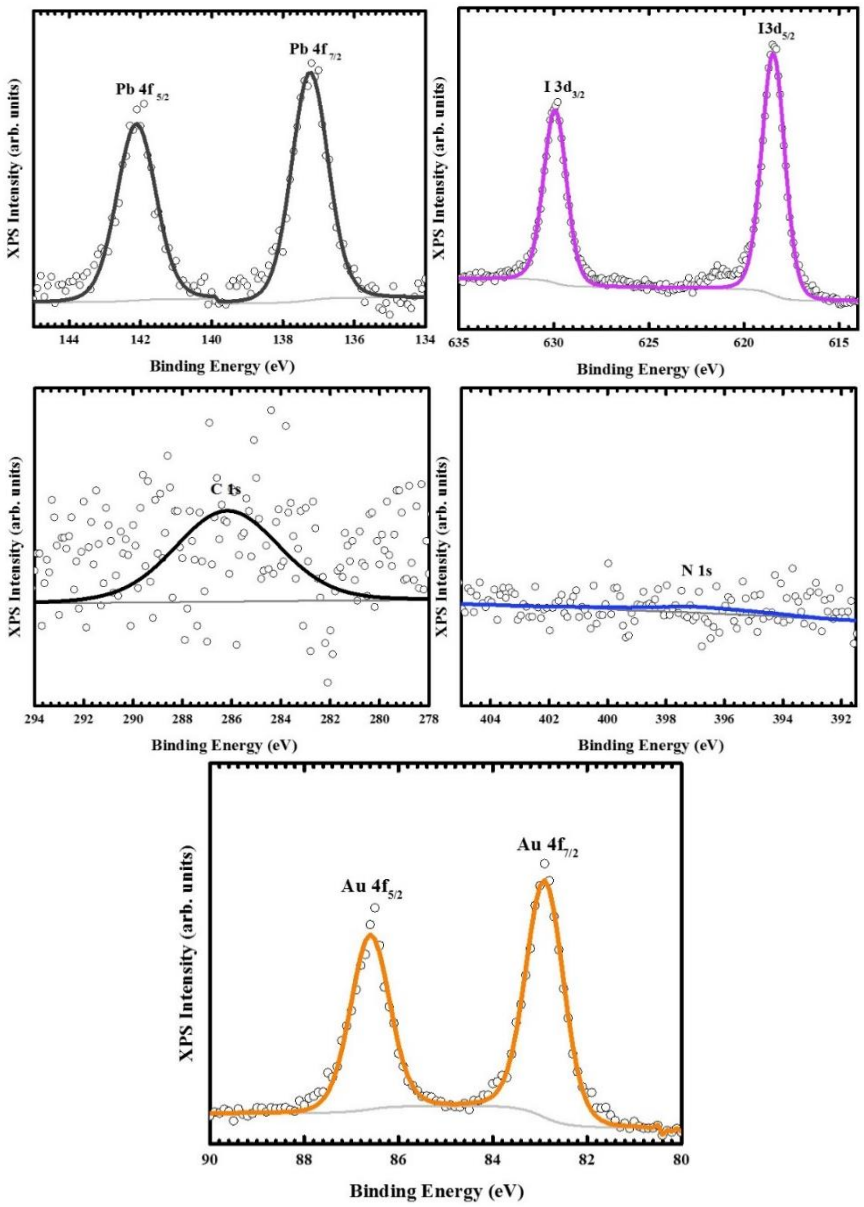

Figure 3.11: XPS spectra show the chemical information of the first trial of 3 min deposited $MAPbI_3$ on Au (111).

The comparison of experimental 4.4 Å and calculated 4.6 Å parameters (Figure 3.12a-b, c-f) of a hexagonal structure are consistent and corroborates our assumption that the observed structures are the PbI_2 structure as reported in ref. [162]. In addition, the STM high-resolution images exhibit the atomically smooth PbI_2 surface without I vacancies. On the basis of our STM high-resolution images and comparison with calculated lattice parameters of PbI_2, we can safely conclude that the overnight annealed $MAPbI_3$ sample has only PbI_2 structure on Au (111) and MAI has completely desorbed in UHV inside the chamber at RT.

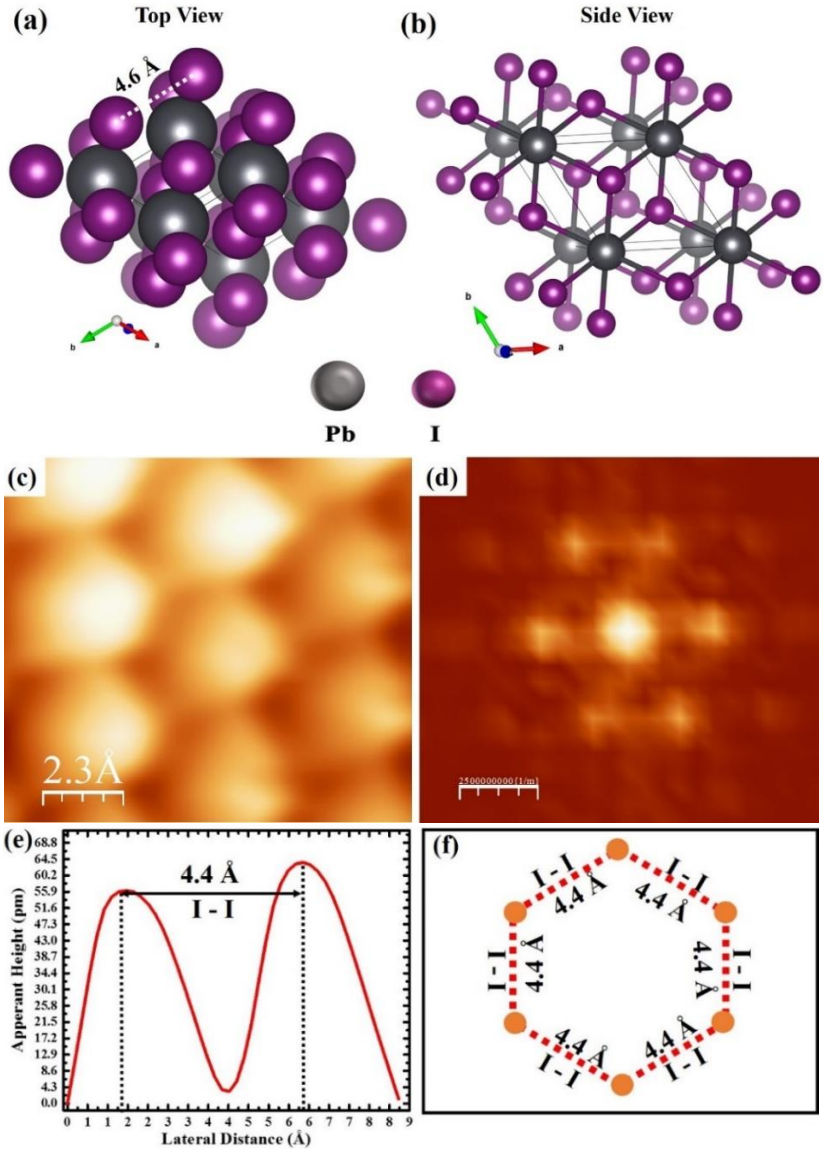

Figure 3.12: LT-STM measured and calculated PbI_2 lattice parameters.(a-b) Calculated atomic model of PbI_2 lattice parameter a=4.689 Å, b=4.689 Å, c=7.503 Å, Band Gap 2.370 eV. Point group=3m, crystal system= trigonal [154]. (c) LT-STM image of large area of PbI_2 (Scan area = 10.5 ×12 $Å^2$; Sample bias voltage= –2.5 V, Tunneling current = 50 pA). (d) Fast Fourier Transform (FFT) STM image shows the hexagonal structure of PbI_2. (e-f) Line profile of I-I = 4.4 Å for the hexagonal structure. Color code in (a),(b): Pb (dark gray).I (purple).

3.4.2 Atomic resolution imaging of the 3-hour annealed $MAPbI_3$ sample at room temperature under UHV and XPS study as a function of the concentration ratios of precursors

After the overnight annealing $MAPbI_3$ sample issue as discussed in section 3.4.1, we fabricated another sample with a similar fabrication protocol but annealed it only for 3 hours at RT in the UHV chamber and transferred it into the STM cryostat at 77 K for STM imaging. For this sample, we obtained high-resolution large-scale (300 × 300 nm^2) STM images of the atomic structure of pristine orthorhombic $MAPbI_3$ thin films as shown

in Figure 3.13 (a). From the height profile depicted in the inset of Figure 3.13(a, d), we observed the height of one grain is ~5 Å, which corresponds to 1 ML height of $MAPbI_3$ reported in ref. [13]. From Figure 3.13b, two different structure dimer and zigzag structures have been revealed. The bright protrusions are attributed to iodine anion in dimer and zigzag structure calculated in ref [13]. In both structures, unit cells contain two bright protrusions. Figure 3.13 (a, c) shows that the grain sizes are around 8 to 15 nm. The grain boundaries of grains are exhibited in Figure 3.13 (c-d), which is well decorated by dimers. The line profile of dimers (4.4 Å) and the gap between two dimers (7.6 Å) of Figure 3.13(e) are depicted in Figure 3.13(f). The experimental gaps of dimer and zigzag are in good agreement with our DFT calculated gaps (Figure 3.14a-f).

Additionally, as shown in the video (**link**) shortly after starting scanning, we observedthe migration of one I anion from a zigzag phase, converting it to a dimer phase. After a short time the previously migrated I anion from the zigzag phase, migrated further into other dimers structures. As scanning time passes, the migration or reorientation of dimers and zigzags becomes stable. This shows that in the beginning the switching between dimers and zigzags happens because the tunneling current modifies the MA orientation.

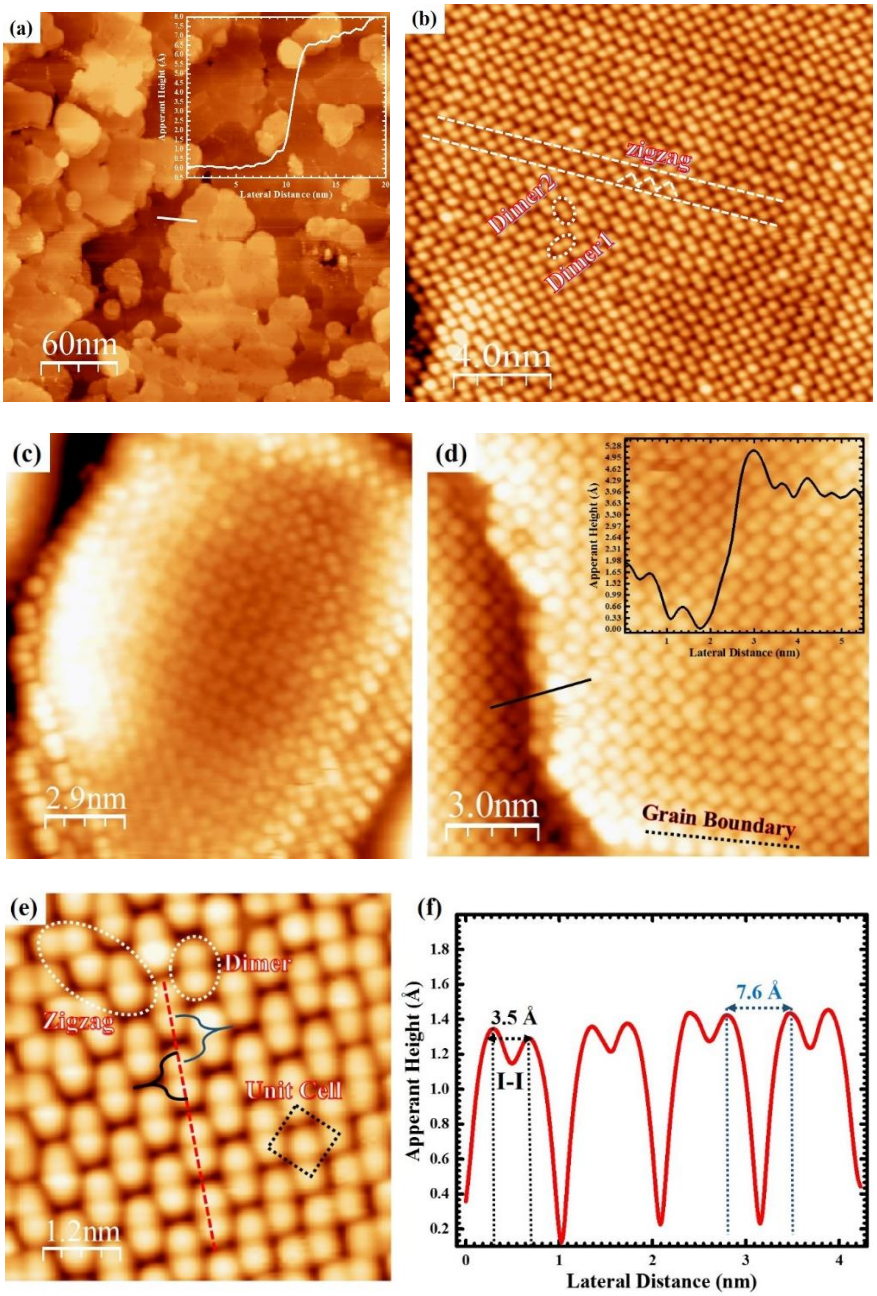

Figure 3.13: Pristine $MAPbI_3$ ($CH_3NH_3PbI_3$) atomic topographies (a) Large area of pristine $MAPbI_3$ ($CH_3NH_3PbI_3$) thickness ≈ 4 nm thin film deposited on Au (111) the typical grains (Scan area = 300 × 300 nm^2; Sample bias voltage= –2.5 V; Tunneling current = 100 pA). (b) LT-STM image dimers and zigzag phase inside of grain (Scan area = 30 × 30 nm^2; Sample bias voltage = –2.5 V, Tunneling current = 100 pA). (c-d) High resolution STM images of grains with grain boundaries and grain height (Scan area = 15x15 nm^2; Sample bias voltage = –2.7 V, Tunneling current = 50 pA). (e) High resolution image of dimer and zigzag structure (Scan area = 5 × 5 nm^2, Sample bias voltage = –2.7 V; Tunneling current = 10 pA). (f) Height and gap profiles of dimers marked by red dash line in (e).

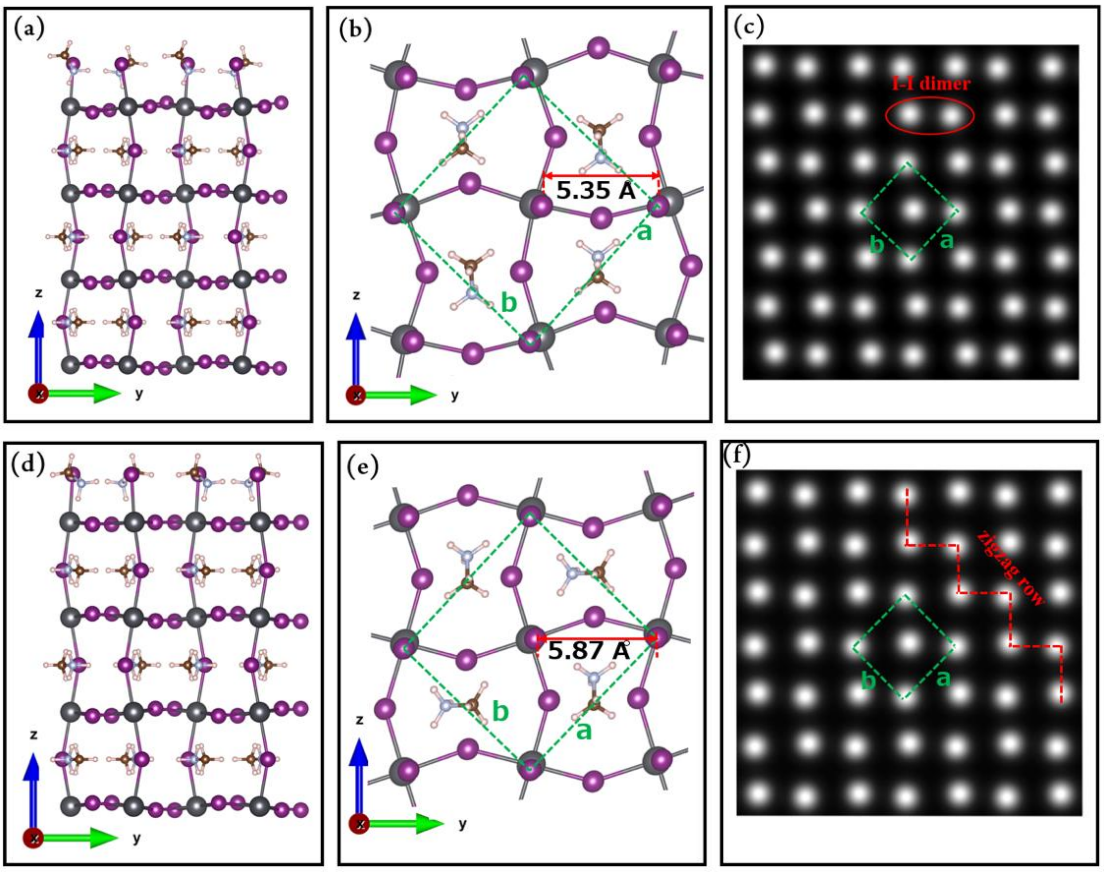

Figure 3.14: DFT calculation for $MAPbI_3$ (001) surface for dimer phase with (a) side, (b) top view, and (c) simulated STM image and zigzag phase with (d) side, (e) top view, and (f) simulated STM image. Color code in (a)-(e): Pb (dark gray), I (purple), Cl (green), N (brown), C (ice blue), H (light pink).

In addition, the lattice constant measured by STM is in good agreement with DFT calculations (a=9.0 Å, b=8.4 Å) of $MAPbI_3$ [13]. On the basis of our DFT calculation, it is shown that the orthorhombic $MAPbI_3$ films are terminated by an MA-I layer for both dimer and zigzag structures (Figure 3.15a-b). Furthermore, the calculated $MAPbI_3$ slab model consists of four MA-I and Pb-I layer units on the c-axis. By DFT calculation, it is proved that MA plays a crucial role in phase transition and surface reconstruction [13] and has minimum contribution to the electronic properties of $MAPbI_3$ perovskite.

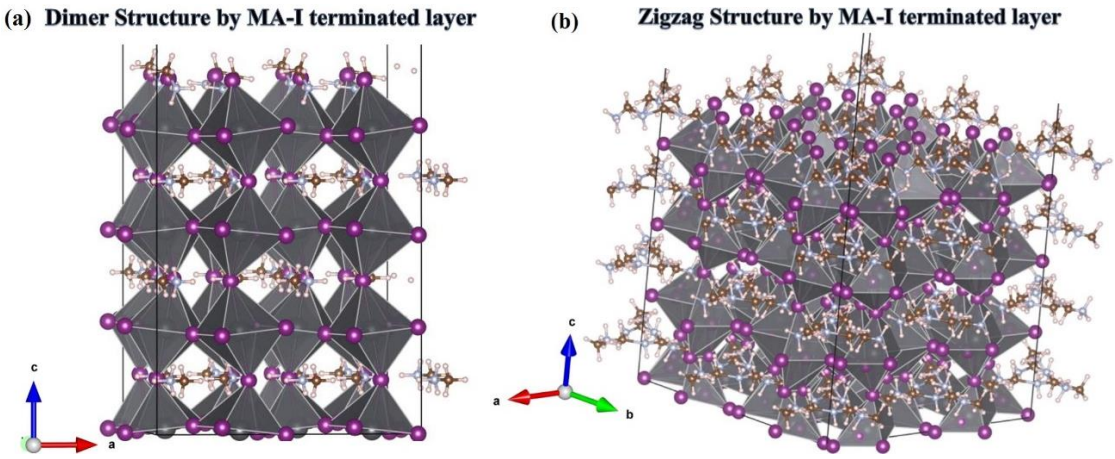

Figure 3.15: DFT calculated model for $MAPbI_3$ MA-I layer terminated surface for (a) Dimer phase (b) Zigzag phase.

In addition, the MA^+ cations were visualized as shown in Figure 3.16(a-b) in pristine $MAPbI_3$ thin films by STM. The same MA molecules were visualized in ref. [12] for $MAPbBr_3$ solution-processed single crystal. By comparing images in Figures 3.16(a-b), it is obvious that the visualization of MA molecules has changed the contrast of dimer visualization even having similar tunneling conditions. Although the dimers have the same apparent height (Figure 3.16a-b) but with different contrast. It shows that the MA orientation influences the I anions. Usually, MA molecules are not visible with dimers in $MAPbI_3$ surface, but rarely some certain tunneling condition favors scanning of the MA molecules.

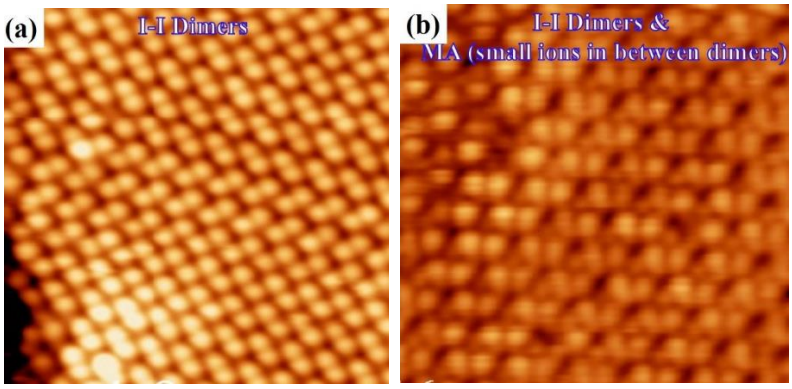

Figure 3.16: (a-b) LT-STM image of MA molecules visualization in dimer structure (Scan area = 8.2 × 8.2 nm^2; Sample bias voltage = –2.5 V; Tunneling current = 100 pA).

To confirm the $MAPbI_3$ precursors in the ultra-thin film on Au (111), X-ray photoelectron spectroscopy (XPS) was used for measurements. By XPS characterization, the presence of I-3d, Pb 3f, C-1s, and N-1s (Figure 3.17) has confirmed with the ratio of [Pb]: [I] = [1] : [3], which forms the $MAPbI_3$ structure. Furthermore, Au-4f peaks have also been observed in the measured spectra, which is because of the ultra-thin film ~4nm of $MAPbI_3$ and the 10 nm depth profiling measurements limits of XPS. Therefore, the Au-4f peaks might influence the bandgap of $MAPbI_3$.

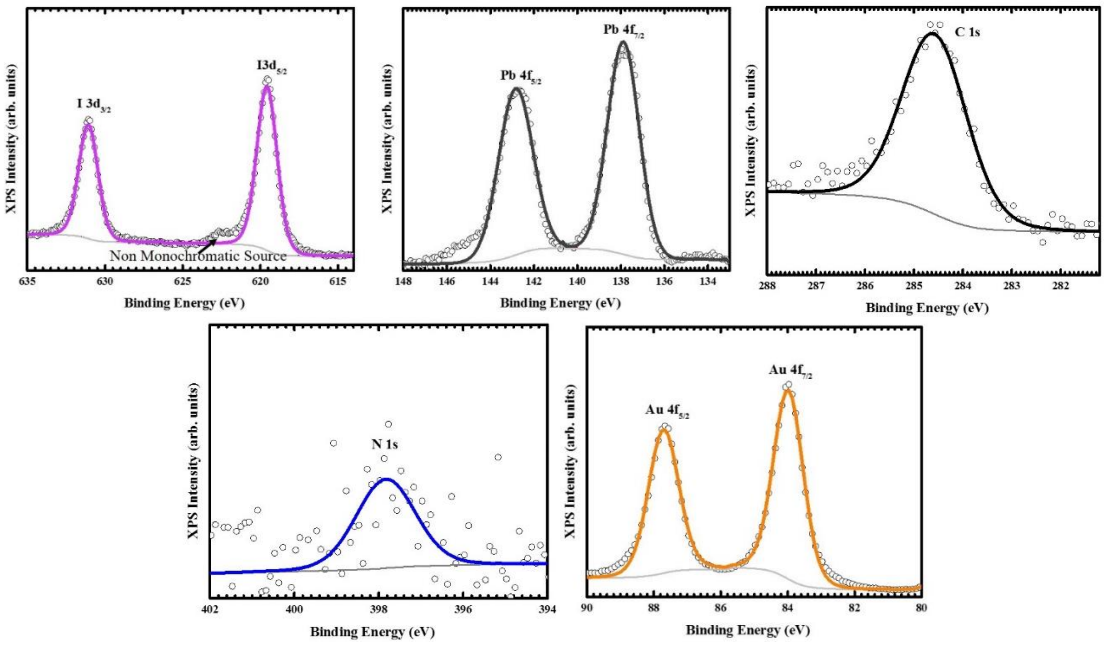

$MAPbI_3$ Deposition Time	Pb-4f & I-3d Ratios	$MAPbI_3$
3 minutes	Pb=1, I = 3	$MAPbI_3$

Figure 3.17: XPS spectra for illustrating the chemical composition of pristine $MAPbI_3$ thin film. The non-monochromatic peaks are observed in the spectra because our XPS system doesn't have a monochromator. Therefore, the Kβ energy appears in the spectra.

Furthermore, evaporation of I molecules for a long/short time in the UHV chamber can contaminate the chamber because of the volatile nature of I. For example, clean Au (111) was transferred into the STM chamber through the contaminated chamber and by STM scanning we observed the I network on the clean Au (111) surface as shown in Figure 3.18(a-c). Therefore, after the first thermal evaporation of MAI and PbI_2 in the UHV chamber for fabricating the $MAPbI_3$ thin films, we employed the titanium sublimation pump (TSP) for cleaning the chamber. After this experience, in every subsequent thermal evaporation of MAI and PbI_2 in the UHV chamber, the TSP was turned on at least for 24 hours by running it after every 1hour to clean the contaminated chamber before opening the gate valve for transferring the sample into STM chamber. Therefore, it is recommended to always clean the chamber by using TSP overnight before transferring any sample because I will certainly contaminate the samples and the adjacent chambers.

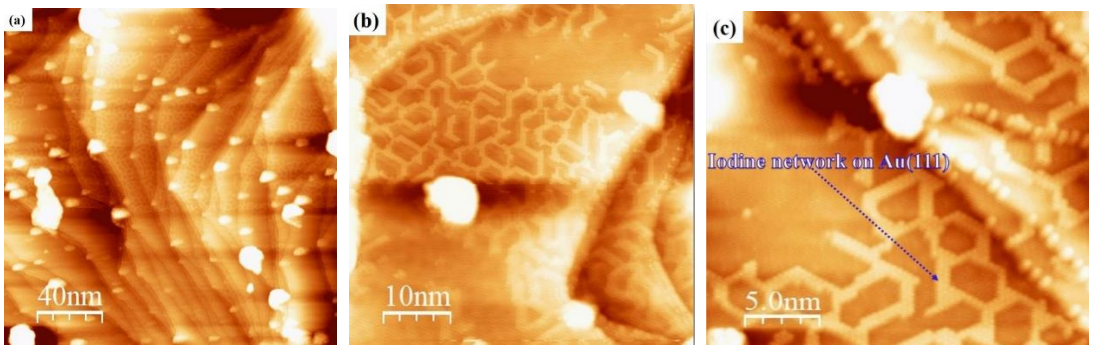

Figure 3.18: Iodine networks on clean Au (111) after transferring through the UHV deposition chamber. (a) LT-STM image of large area of I networks on Au (111) terraces (Scan area = 200 × 200 nm^2; Sample bias voltage = –3.0 V, Tunneling current = 700 pA). (b) LT-STM topographies of I networks on one of Au (111) terrace (Scan area = 50 × 50 nm^2; Sample bias voltage = –3 V, Tunneling current = 700 pA). (c) LT-STM image of I networks and step edges of Au (111) terraces (Scan area = 25 × 25 nm^2; Sample bias voltage = –3 V, Tunneling current = 700 pA).

3.4.3 Bandgap measurement by UPS & IPES

Figure 3.19 shows the bandgap of pristine $MAPbI_3$ measured by UPS and IPES. The valance band (VB) was measured by UPS (blue line spectra) and the acquired work function (ϕ) was 5.8 ± 0.2 eV while the literature reported ϕ is 3.90 eV [163]. IPES was used to measure the conduction band (CB) as shown by red line spectra in Figure 3.18. Our acquired bandgap of pristine $MAPbI_3$ ultra-thin film deposited on Au (111) is 1.45 eV, while the reported bandgap is between 1.5 to 1.6 eV [164]. The minor difference in the bandgap of our ultra-thin film bandgap and the literature reported bandgap of bulk $MAPbI_3$ is likely due to the substrate effect of Au (111) influencing the bandgap of this ultra-thin film. Additionally, that the conduction band edge is below the Fermi level is likely due to the heavy n-type doping characteristic of the perovskite film or the electron gun 300meV error shift.

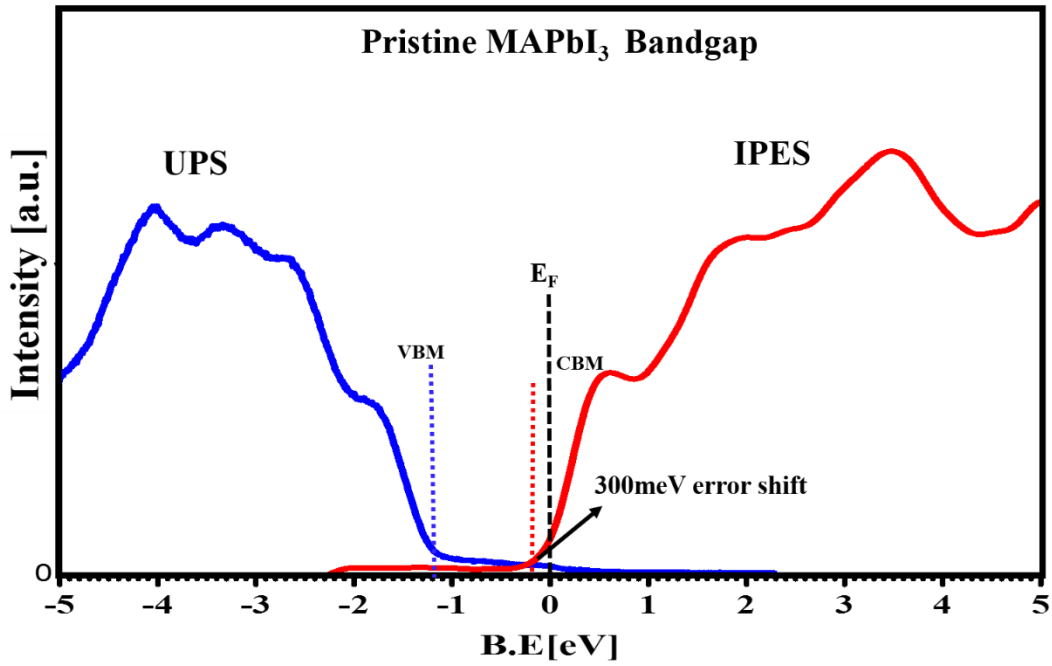

Figure 3.19: The experimental bandgap of pristine $MAPbI_3$.

3.5 Summary

In this chapter, we first discuss the protocol optimization of MAI and found that the short deposition time did not add any MAI layer on Au (111) substrate, which was confirmed by XPS. Although, the I-3d and Pb-4f peaks were observed, C-1s and N-1s were not found, which evidence that this sample does not have MA molecules. By increasing the deposition time to more than 1 min of MAI, the C-1s and N-1s peaks have been observed in the XPS spectra and confirmed the MA presence with I and Pb. The optimized protocol fabricated MAI ultra-thin film was scanned by LT-STM and achieved four different molecular layers (ML) of MAI on Au (111) with four different atomic structures namely I hexagonal, snaky chain of dimers, non-strip and stripe structures formed by dimers. Then, MAI was co-evaporated with PbI_2 to fabricate the $MAPbI_3$ ultra-thin under UHV conditions. We found only PbI_2 with two different hexagonal strip and random structures by LT-STM scanning and Pb-4f and I-3d peaks by XPS after the first $MAPbI_3$ sample fabrication, which was annealed overnight at RT in UHV and the MAI was completely desorbed in UHV. For this sample, we did not observe any C-1s and N-1s peaks by XPS and no MAI atomic structures by LT-STM. Another $MAPbI_3$ sample was fabricated by following the similar fabrication protocol, but only annealed for 3 h at RT under UHV and we achieved the $MAPbI_3$ high-resolution STM images and by XPS each of precursors concentration ratio. Two structures of dimer and zigzag have been found for the $MAPbI_3$. MA two-fold and four-fold movement is the cause of dimerization of the I-I pair and the zigzag structure. On the basis of DFT calculation, it is found that MA plays a crucial role in forming the geometry and does not contribute to the electronic properties of $MAPbI_3$. In our STM movie, an interesting scenario of switching of the dimer to zigzag and zigzag to dimer was also observed by the I ions migration during the STM scanning during the initial short time. Furthermore, the unexpected effects of I thermal evaporation in UHV that leads to chamber contamination has been experienced during the ultra-thin film fabrication process and found that running the TSP overnight

after each fabrication of sample is crucial for minimizing the chamber contamination. Finally, the bandgap of 1.45 eV in ultra-thin $MAPbI_3$ film has been measured by UPS /IPES, which is almost consistent with the literature reported bandgap.

Chapter 4: Atomic-Scale Evidence of Chlorine Incorporation in Perovskite Methylammonium Lead Iodide and its Effects on Stability

4.1 Introduction

Pioneering works have demonstrated that hybrid organic-inorganic perovskites (ABX_3, A is MA^+; B is Pb^{2+}; X is I^-, Br^-, Cl^-.) as a light harvest layer show a great potential in solar cell applications [1-3]. In the past decade, the perovskite solar cells (PSCs) have garnered an intensive research interest in academia, due to the rapid increase in efficiencies from 3.8% [3] to 25.5% [4]. The advantages of perovskites in solar cell applications include facile fabrication, high absorption coefficient, bandgap tunability, charge carrier mobility, low non-radiative recombination rates, and long charge carrier diffusion lengths. However, perovskite solar cells undergo relatively fast degradation due to extrinsic (such as oxygen, moisture, UV-light, temperature) and intrinsic factors (such as material stability of various layers in PSCs, built-in electric field, interfacial chemical reactions) [165].

To solve the extrinsic and intrinsic instability problems, mixing of halide anions (I, Br, Cl) at the X site of the perovskite ABX_3 structure has been proposed [166 167 168]. As an example, it has been suggested that mixing $MAPbI_3$ with Cl could greatly improve the stability of perovskite material against moisture, thermal heat, and light [7]. Furthermore, Cl addition to the perovskite film has shown to be a good candidate for enhancing power conversion efficiencies of the device [8]. Snaith and coworkers showed that the $MAPbI_3$ perovskite films incorporated with Cl exhibited good light-harvesting capabilities, and the absorption spectra were stable to prolonged light exposure, as demonstrated by 1000 hours of constant illumination under simulated full sunlight [7]. Cl addition in the perovskite precursors solution was reported to improve $MAPbI_3$ optoelectronic properties (e.g., diffusion lengths for electrons and holes of ~130 nm and ~90-105 nm in $MAPbI_3$ increase by approximately 10 times in $MAPb(I_{1-x}Cl_x)_3$ to ~1069 nm and ~1213 nm, respectively) [169 170 171]. Despite the tremendous advantages provided by Cl for enhancing perovskite optoelectronic properties and stability, the question that Cl is incorporated in the crystal lattice of $MAPbI_3$ is still a topic under debate [172].

Several reports proposed that Cl is absent in the final $MAPbI_3$ film or it is below the detection limits of the analytical instruments [173]. Therefore, chloride-containing compounds (e.g., MACl, $PbCl_2$) were considered as additives that mainly improve $MAPbI_3$ film morphology [174 175 176 172 177]. However, some preliminary reports based on X-ray diffraction (XRD), and absorption spectroscopy[178 179], indicate that although

most of Cl leaves the final perovskite film during the post-annealing process, a small amount of Cl is incorporated in the $MAPbI_3$ crystal lattice. Based on density functional theory (DFT) calculations, Mosca and coworkers reported that the maximum amount of Cl in the bulk of $MAPbI_3$ is 3-4% [180]. Early theoretical calculations suggested a small amount of Cl may exist in grain boundaries and plays a role in defect passivation [181]. Although it is generally accepted that a small amount of Cl can be incorporated in $MAPbI_3$, a consensus has not been reached regarding the location of these Cl species in the perovskite lattice [169 182].

In the past few years, scanning tunneling microscopy (STM) has been demonstrated to be a suitable technique to study the surface structure and electronic properties of perovskite materials down to the atomic level [15 14 16 12 156 13 183]. The real space lateral atomic resolution of STM made it a technique of choice for unrevealing the location of Cl ions in the perovskite film. In this work, for the first time we determine the configuration of Cl incorporation in the surface lattice of $MAPbI_3$ ultra-thin film (~5 nm). By using STM with the assistance of DFT calculations, we show with atomic-scale precision the exact location of the Cl ions at the surface of the perovskite film. X-ray photoelectron spectroscopy (XPS) was used to measure the concentration of each precursor. While ultraviolet photoemission spectroscopy (UPS) and inverse photoemission spectroscopy (IPES) were used to show the impact of the Cl incorporation on $MAPbI_3$ band structure. We found that the incorporation of Cl ions on the $MAPbI_3$ surface significantly alters its electronic properties, by widening the bandgap of $MAPbI_3$ from 1.45 eV to 1.65 eV. At last, we determined the optimal Cl concentration that leads to the enhanced stability of $MAPbI_3$ surfaces. Similar to our previous STM works, [14 15] it is important to point out that STM can be used to characterize mainly the surface (and possibly the subsurface) atomic structures of perovskite materials. Therefore, STM cannot provide a complete picture of the bulk structures of perovskites, but our study does offer valuable insights into the surface/interface properties which are important to understand the underlying mechanisms behind: (i) Cl diffusion into the perovskite film [184 185 186], (ii) passivation of surface defects by Cl [129 187].

4.2 Deposition of $PbCl_2$ on clean Au (111)

$PbCl_2$ is an inorganic compound that consists of two covalently bonded chlorine atoms to a central lead atom (Figure 4.1). It has a boiling point of 950 ^{0}C while the melting point is 501 ^{0}C. In water, it is poorly soluble. The bandgap of $PbCl_2$ is 3.794 eV and has an orthorhombic crystal structure with lattice parameters a= 7.620 Å, b= 4.534 Å, and c= 9.045 Å as shown in Figure 4.1.

Before depositing $PbCl_2$ on $MAPbI_3$ ultra-thin films, a protocol for the $PbCl_2$ deposition conditions need be established. The protocol consists of an initial thermalization of the K-cell with $PbCl_2$ for three hours in the ultra-high vacuum chamber under the pressure of 1.9 x 10^{-8} Torr. After thermalization, $PbCl_2$ was deposited on clean Au (111) for different times (e.g., 1, 2, 3, 4 min) keeping the K-cell temperature at 584 K.

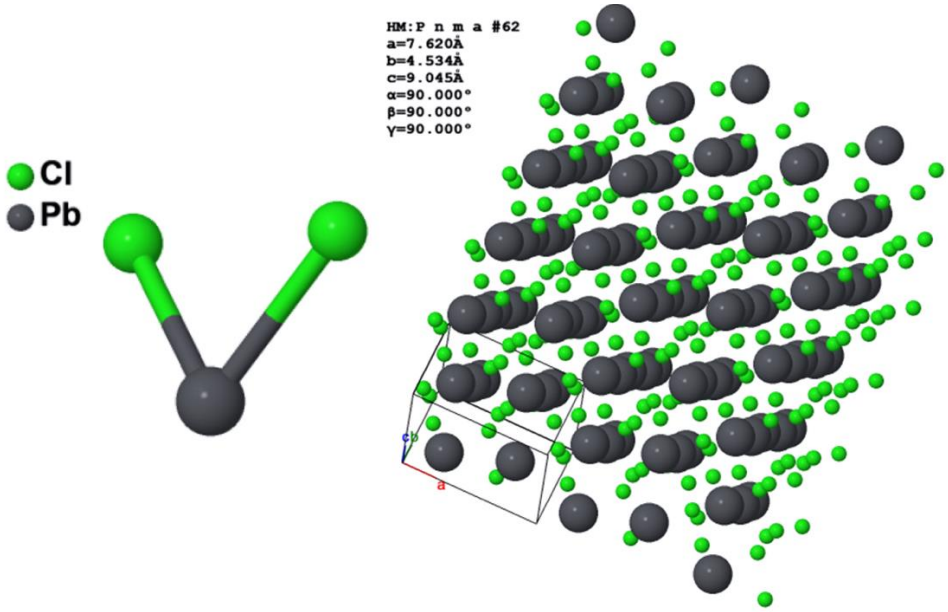

Figure 4.1: $PbCl_2$ crystal structure [188].

4.2.1 XPS characterization for the $PbCl_2$ concentration

$PbCl_2$ was deposited incrementally for 1 and 2 min on Au (111) but Cl and Pb were not detected by XPS characterization. Subsequently, $PbCl_2$ was deposited for an additional 2 min on the same sample, corresponding to a total time of 4 min deposition. This time the XPS peaks corresponding to Cl 2p and Pb 4f have been observed with the chemical composition of [Pb]: [Cl] =1: 2.8 as depicted in Figure 4.2.

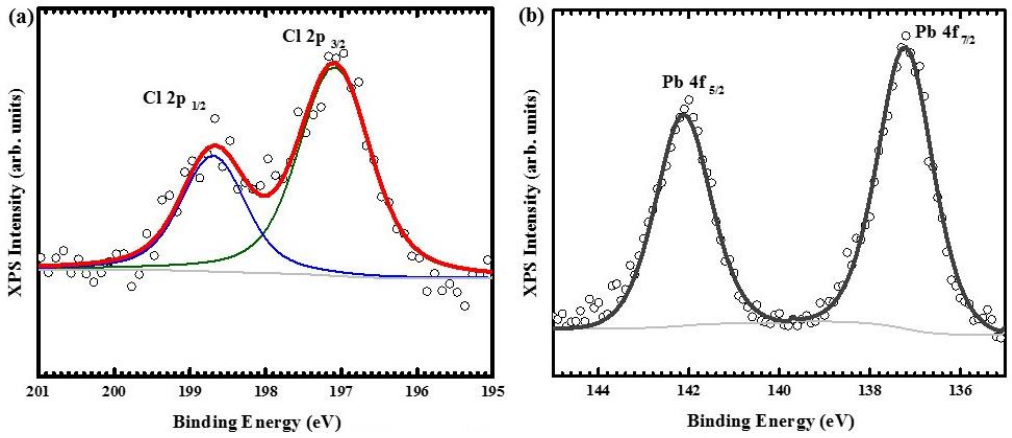

Figure 4.2: XPS spectra show the chemical information of 4 min deposition of $PbCl_2$.

4.2.2 Atomic resolution imaging by LT-STM

After confirmation by XPS, the $PbCl_2$ deposited Au (111) sample was transferred into the STM chamber for STM experiments. Figure 4.3 shows the high-resolution images of the $PbCl_2$ decorated step edges of Au (111). We achieved a partially covered 0.5 ML of $PbCl_2$ on Au (111) surface by observing the grain boundaries formation. These STM

images provided the confirmation of $PbCl_2$ deposition on Au (111), after which we proceeded to deposit $PbCl_2$ on $MAPbI_3$ ultra-thin film.

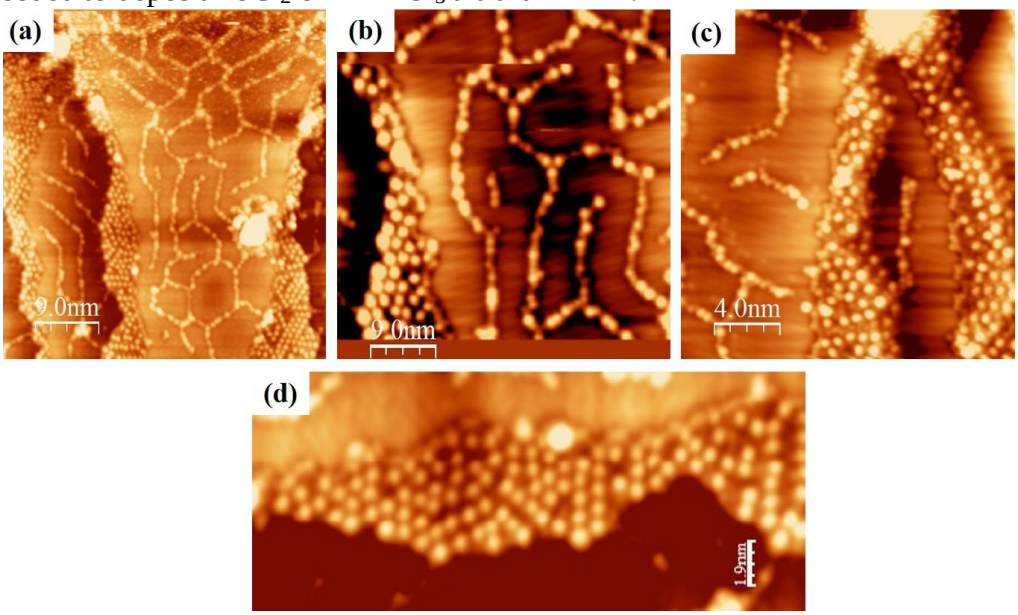

Figure 4.3: High-resolution LT-STM images of $PbCl_2$ on clean Au (111).

4.3 Depositing $PbCl_2$ on top of pristine $MAPbI_3$ ultra-thin film

Presently, no atomic-scale research has been done to understand the influence of Cl incorporation on the structural and electronic properties of halide perovskite materials (e.g., $MAPbI_3$=$CH_3NH_3PbI_3$). Halide additives have been suggested to solve the thermal instability and ambient air induced degradation problems of perovskites. Among studied additives, Cl was found to be an eligible candidate for improving the power conversion efficiencies (PCEs) and degradation issues in perovskite solar cells. Instabilities and degradation occur in perovskite materials due to the interaction of water, oxygen, light, and temperature stimuli during solar cell operation. To solve the instabilities and degradation problems in perovskite materials for stable solar cells, we underline the fundamental processes of the instabilities and degradation of perovskite at the atomic scale. In this study, scanning tunneling microscopy (STM) and density functional theory (DFT) calculations provide a fundamental understanding of the origin of the Cl interactions with $MAPbI_3$ and provide useful hints for the design of stable and high-performance perovskite solar cells. Our atomic-scale results provide information about different Cl concentrations that plays an important role in $MAPbI_3$. (1) We found that at low coverage, Cl does not incorporate in $MAPbI_3$ surface lattice (corroborated by X-ray photoelectron spectroscopy measurements). (2) However, with increasing Cl concentration, it is possible to visualize Cl ions on $MAPbI_3$ surfaces. With a concentration of [Cl]:[I] ~ 18% ($MAPbI_{2.54}Cl_{0.46}$), we observed that Cl ions are mostly incorporated close to the grain boundaries, (3) Additionally, Cl incorporation was also observed in the center regions of grains that have different structures (namely, the dimer and zigzag structures). (4) Our study evidence that Cl can substitute I ions

of surface lattice structure and/or fill the surface I-vacancies in $MAPbI_3$. (5) Furthermore, the Cl additive alters the bandgap of $MAPbI_3$ from 1.45 eV to 1.65 eV.

4.4 Surface characterization and methods

Cl incorporated $MAPbI_3$ ultra-thin films on clean Au (111) was studied in an ultrahigh vacuum (UHV) system by STM (base pressure $< 2 \times 10^{-10}$ Torr). Au (111) was used as the substrate following our previous studies [12] First, the Au (111) substrate was cleaned in UHV conditions by three cycles of Ne^+ sputtering (7.5×10^{-5} Torr; 60 min) followed by annealing at 773 K for 20min. $MAPbI_3$ perovskite films were prepared by co-evaporating PbI_2 and MAI precursors at the temperatures of 516 K and 395 K, respectively, for 3min. During the co-deposition of PbI_2 and MAI, the Au (111) substrate was kept at a temperature of 132 K to ensure a high sticking coefficient of MAI. After evaporation, the sample was annealed at room temperature for 3 h. This protocol leads to $MAPbI_3$ films with a thickness of 4~5 nm and with typical grain sizes ranging from 8 nm to 15 nm (Figure 4.4a). Cl incorporated $MAPbI_3$ samples were obtained by sublimating $PbCl_2$ for different times (namely, 1 min, 2 min, 4 min, 6 min, 8 min, and 12 min) on top of the pristine $MAPbI_3$ films using a thermal evaporator heated at 593 K. The samples were in situ transferred to a low-temperature scanning tunneling microscope (LT-STM, Scienta Omicron GmbH) for characterization. The STM measurements were performed at 77 K using Pt/Ir tips and with the bias voltage applied to the sample. After the STM characterization, the samples were in situ transferred to the analysis chamber (base pressure of $\sim 2 \times 10^{-10}$ Torr) equipped with a hemispherical electron energy analyzer (EA 125, Scienta Omicron GmbH), unfiltered He discharge lamp (HIS 13, Scienta Omicron GmbH; He-Iα = 21.22 eV for UPS with an energy resolution of ~0.15 eV, and a dual-anode (Al-Kα = 1486.6 eV and Mg-Kα = 1253.6 eV) non-monochromatic X-ray source (DAR 400, Scienta Omicron GmbH) for XPS with an energy resolution of ~0.8 eV. IPES (LE-1, ALS Technology Co., Ltd.) [189] was performed in a separate vacuum system, and the sample transfer was conducted with the aid of a custom-designed vacuum suitcase (Ferrovac GmbH), which ensures no air exposure during sample transfer. For the quantitative analyses of peak positions, line widths, and relative areas of the Pb-4f, I-3d, C-1s, N-1s, and Cl-2p components, the raw XPS spectra were fitted with Gaussian-Lorentzian functions in the CASA XPS software.

The DFT results in this chapter were obtained by our theory collaborators Prof. Wanjian Yin and Dr. Zhendong Guo from Soochow University China. Density functional theory (DFT) calculations were performed by using the VASP code[158] with the standard frozen-core projector augmented-wave (PAW) method [160] and the Perdew−Burke−Ernzerhof (PBE) exchange-correlation functional [159]. For the plane-waves, a cutoff of 450 eV was employed. The nonlocal van der Waals interactions were considered by using the Becke−Jonson damping DFT-D3 method. [190] No spin-orbital coupling (SOC) was considered in this work. The lattice parameters (a = 8.84 Å, b = 8.47 Å, and c = 12.65 Å) of the $MAPbI_3$ unit cell in the orthorhombic phase were achieved through structural relaxation with adopting a $4 \times 4 \times 4$ Monkhorst−Pack grid. The MAPbI3 (010) surfaces were modeled by using the 2×2 slabs with a vacuum thickness of 20 Å. Each surface model contained eight atomic layers, among which the bottom four layers were always kept fixed at their bulk positions and the other layers were fully relaxed until the atomic forces converged within 0.01 eV/Å (Figure 4.7). For all

calculations involving the surfaces, the Brillouin zone was sampled at the sole Γ-point. From the electronic ground state structure, STM images were obtained by using the p4vasp code. All MD simulations were carried out by using the canonical (NVT) ensemble with the temperature being controlled at 300K through the Nosé-Hoover thermostat. The surface energies (E_s) reported in Table 1 are calculated by using the following equation:

$$E_s = E_{slab} - E_{bulk}, \quad (1)$$

Where E_{slab} is the total energy of the relaxed surface model and E_{bulk} is the total energy of the relaxed bulk model, which also contains eight atomic layers, like the surface one. To evaluate the stability of Cl incorporated $MAPbI_3$ surface, we consider the following reaction [14] :

$$MAPb(I_{1-x}Cl_x)_3 + \frac{3x}{2} \cdot PbI_2 \rightarrow MAPbI_3 + \frac{3x}{2} \cdot PbCl_2. \quad (2)$$

Hence, the decomposition energy of $MAPb(I_{1-x}Cl_x)_3$ is given by:

$$E_{dec} = E(MAPbI_3) - E(MAPb(I_{1-x}Cl_x)_3) + \frac{3x}{2}[E(PbCl_2) - E(PbI_2)], \quad (3)$$

Where $E(MAPbI_3)$ and $E(MAPb(I_{1-x}Cl_x)_3)$ are the total energies of pristine and Cl-incorporated $MAPbI_3$ surfaces, respectively. For perovskites, the decomposition energy is widely used to characterize their stability. The larger decomposition energy implies a more stable structure.

4.5 Atomic resolution imaging of $PbCl_2$ deposition for different times

Initially, the $MAPbI_3$ films (~4-5 nm) were grown on Au (111) by in situ thermal evaporation following the previously reported recipe (see Experimental Section) [13]. The UHV grown $MAPbI_3$ films show a polycrystalline nature composed of multiple grains with typical grain sizes varying from 8 nm to 15 nm (Figure 4.4 a). Within a grain, the surface of $MAPbI_3$ shows the dimmer and zig-zag structures (Figures 4.4 b-d and 4.5 a), as previously observed for $MAPbI_3$ films [156]. In the dimer phase, the formation of I-I pairs was found, which results from the reorientation of MA cations [13]. Such configurations were also observed in both thin films and single crystals of $MAPbBr_3$ [12, 14, 16]. To achieve the incorporation of Cl ion in perovskite films, 4 different evaporation times (see section 4.4. surface characterization and methods section) of $PbCl_2$ were explored. First, we deposited $PbCl_2$ for 1 min onto the pristine $MAPbI_3$ thin film but Cl incorporation was not observed by XPS measurements. After increasing the evaporation time of $PbCl_2$ to 4 min (Figure 4.5b-c) and 6 min, darker protrusions with a lower apparent height and smaller diameter started to appear in the STM images (dashed circles in Figures 4.4c-f). The deposition thickness was estimated by depositing $PbCl_2$ for 4 min directly on a clean Au (111) surface, which determines the 0.5 ML sample coverage by STM (Figure 4.3). On basis of 0.5 ML coverage, we have estimated 0.75 ML coverage for 6 min and 1.5 ML coverage for 12 min deposition time.

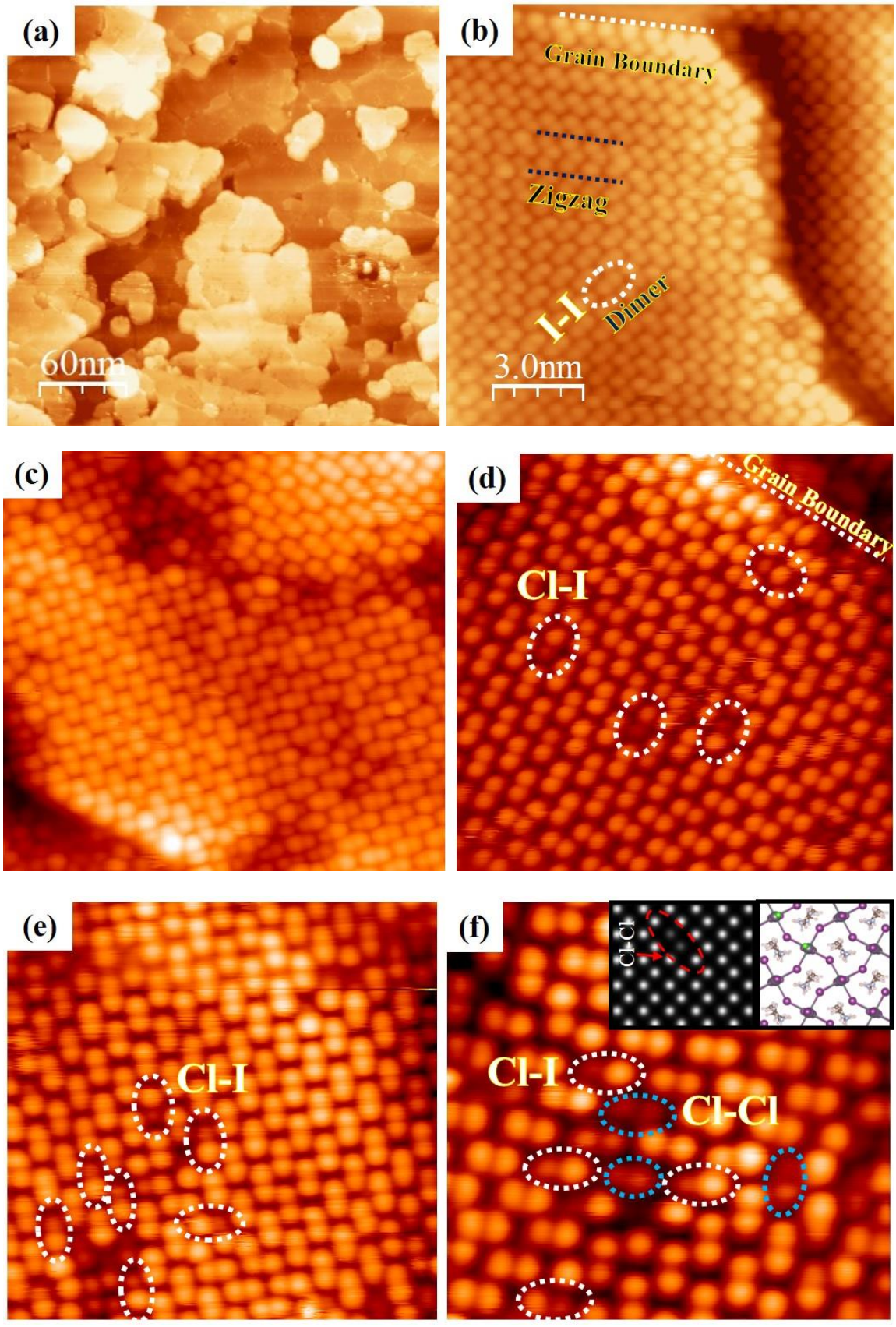
(a)
60nm
(b)
Grain Boundary
Zigzag
I-I Dimer
3.0nm
(c)
(d)
Grain Boundary
Cl-I
(e)
Cl-I
(f)
Cl-Cl
Cl-I
Cl-Cl

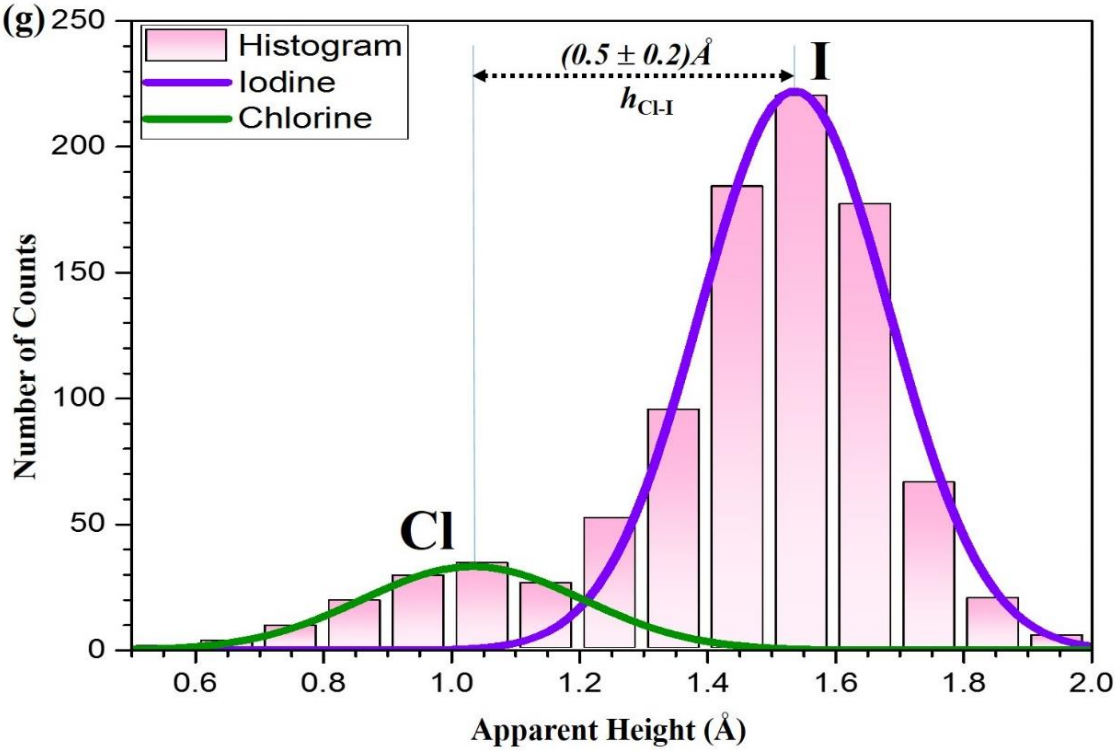

Figure 4.4: LT-STM images of the surface of the pristine $MAPbI_3$ perovskite thin film and the 0.75 ML of $PbCl_2$ incorporated $MAPbI_3$ perovskite thin film deposited on Au (111). (a) Large area of pristine $MAPbI_3$ showing the typical grains (scan area = 300 × 300 nm^2; Sample bias voltage= –2.5 V; Tunneling current = 50 pA). (b) I-I dimer structures on the pristine $MAPbI_3$ thin film surface (scan area = 14 × 14 nm^2; Sample bias voltage= –2.5 V; Tunneling current = 50 pA). (c) 0.75 ML of $PbCl_2$ incorporated $MAPbI_3$ grains (scan area = 14.5 × 14.5 nm^2; Sample bias voltage= –2.5 V; Tunneling current = 50 pA). (d) I-I dimers and Cl incorporated pair structures (white dashed circles) in the center, close to the grain boundary (white dashed line) and inside a grain (Scan area = 10 × 10 nm^2, Sample bias voltage = –2.70 V, Tunneling current = 51 pA). (e) Different Cl-I pairs orientation in the grain (scan area =10× 10 nm^2, Sample bias voltage = –2.50 V, Tunneling current = 100 pA). (f) Cl-Cl and Cl-I pairs in the grain(scan area = 7 × 7 nm^2; Sample bias voltage = –2.50 V, Tunneling current = 60 pA). The insets in (f) show the simulated STM image and structural configuration of the Cl-Cl pair (Blue dashed circle) in the dimer structure. (g) Histogram of the apparent height distribution of I and Cl anions. The surface concentration in $MAPbI_3$ is 14.8 ± 0.6%, which was obtained from 900 statistical points.

We have prepared 7 samples and found this observation was reproducible for the 0.75 ML of PbCl2 on MAPbI3. Figure 4.4g presents the histogram of the apparent height distribution observed at the surface of MAPbI3 perovskite after Cl ions incorporation (0.75 ML of PbCl2). The protrusion statistics were obtained from 12 STM images acquired on different macroscopic areas of the same sample and are reproducible from sample to sample. The distribution of the apparent height values for protrusions observed in these STM images (~900 protrusions) is illustrated by the histogram shown in Figures 4.4g, which reveals that the dark protrusions observed in the STM images have an average height of about 0.5±0.2 Å lower than the neighboring iodine ions (Figures 4.6a-b and 4.6d-e).

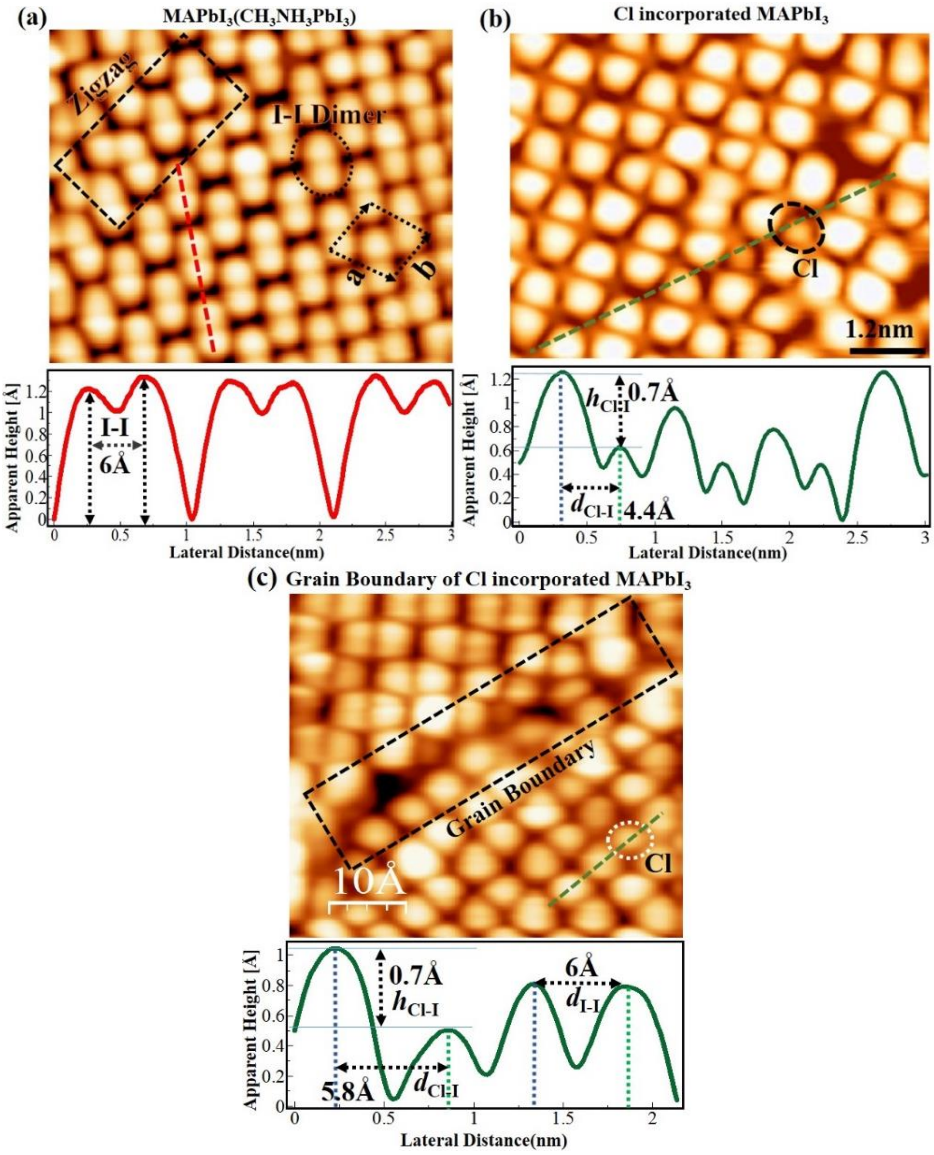

Figure 4.5. LT-STM images of pristine and Cl incorporated $MAPbI_3$ perovskite thin films deposited on Au (111). (a) High resolution image of iodine dimer (labeled by black dashed ellipse) and iodine zigzag (labeled by black dashed rectangle) structure (Scan area = 4 × 4.5 nm^2, Sample bias voltage = –2.70 V; Tunneling current = 10 pA). Height profiles of observed domain labeled by red broken lines. (b) LT-STM image of $PbCl_2$ (4 min-deposition) incorporation in the center of a grain of $CH_3NH_3PbI_3$ perovskite. Height profiles of observed Cl incorporation in dimers labeled by a black dashed circle (Scan area = 3.7 × 4.8 nm^2, Sample bias voltage = –2.50V; Tunneling current = 100 pA). (c) Incorporated Cl close to the grain boundary labeled by the black dashed rectangle. Height profile of observed Cl depression close to the grain boundary labeled by a white dashed circle (Scan area = 4.6 × 5.3 nm^2, Sample bias voltage = –2.50V; Tunneling current = 100 pA).

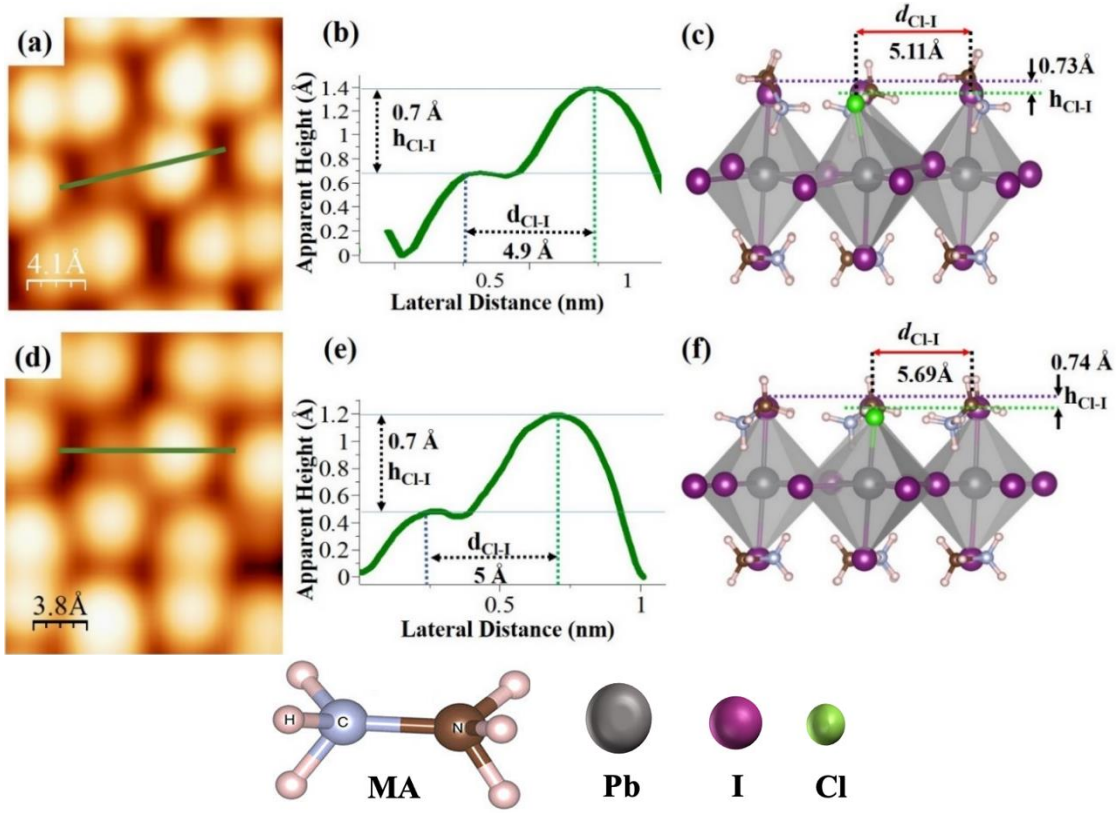

Figure 4.6. STM images of Cl incorporation in a dimer and zigzag structure of $MAPbI_3$(a) High-resolution STM image showing one Cl ion that forms a pair with one I ion in a dimer structure (Scan area = 2 × 2 nm^2; Sample bias voltage = –2.50 V, Tunneling current = 20 pA). (b) Height profile and bond length of the observed I-Cl dimer in (a). (c) DFT simulated height profile and bond length for the I-Cl dimer in (a). (d) High-resolution STM image showing one Cl ion that forms a pair with one I ion in a zigzag structure (Scan area = 2.2 × 1.9 nm^2; Sample bias voltage = –2.50 V, Tunneling current = 20 pA). (e) Height profile and bond length of observed I-Cl zigzag structure in (d). (f) DFT simulated height profile and bond length of observed I-Cl zigzag structure in (d). Color code in **(c)** and **(f)**: Pb (dark gray), I (purple), Cl (green), N(brown), C (ice blue), H (light Pink).

To unravel the origin of the dark protrusions observed in the STM images of $MAPbI_3$ after $PbCl_2$ deposition, we performed DFT calculations by using the Vienna ab initio simulation package (VASP) (see the Methods Section). By tentatively assigning the dark protrusions to Cl ions, we obtained simulated STM images of the Cl-incorporated $MAPbI_3$ surfaces. The simulated images reproduce accurately the dimer and zigzag phases observed experimentally for the $MAPbI_3$ surface (Figure 4.7). Our calculations also reproduce the lowering of the apparent height due to Cl incorporation matching well the experimental STM images (Figures 4.6a and 4.6d). The incorporated Cl ions in the simulated models were found to be 0.73-0.74 Å (Figures 4.6c and 4.6f) lower than their neighboring I ions, which agrees well with the experimental value of ~0.7 Å (Figures 4.6b and 4.6e). Also, we found that the experimental bond length (d_{Cl-I}) of Cl-I pairs (~4.9 and ~5.0 Å) in the dimer and zigzag phases (Figures 4.6b and 4.6e) was also in line with the simulated results, which were 5.11 and 5.69 Å, respectively (Figures 4.6c and 4.6f and Figures 4.7b and 4.7e).

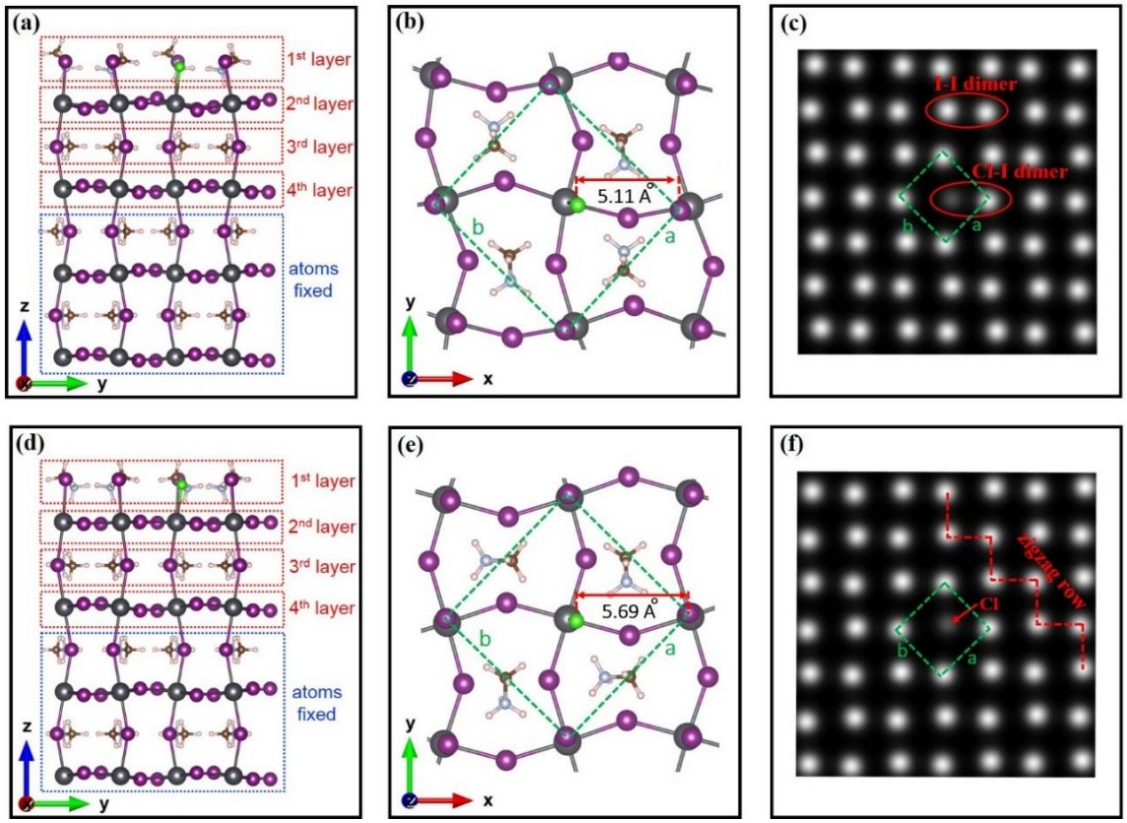

Figure 4.7: Geometrical dimer and zigzag structures of Cl incorporated $MAPbI_3$ (001) surfaces obtained by DFT calculations. (a) The side view, (b) Top view of Cl incorporated dimer structure and Cl-I bond length. (c) Simulated STM image. (d) The side view, (e) Top view of Cl incorporated zigzag structure and Cl-I bond length. (f) Simulated STM image.

Based on the experimental STM data in combination with these DFT calculations and XPS measurement results (Figures 4.8, 4.9 and 4.16), we can safely conclude the dark protrusions in our STM images of the $MAPbI_3$ surface after 0.5 ML and 0.75 ML of $PbCl_2$ deposition are Cl ions that substitute iodine in the perovskite lattice. For simplicity, in the following discussions, we denote Cl-incorporated $MAPbI_3$ as MAPb $(I_{1-x}Cl_x)_3$ with x representing the amount of Cl ions at the surface.

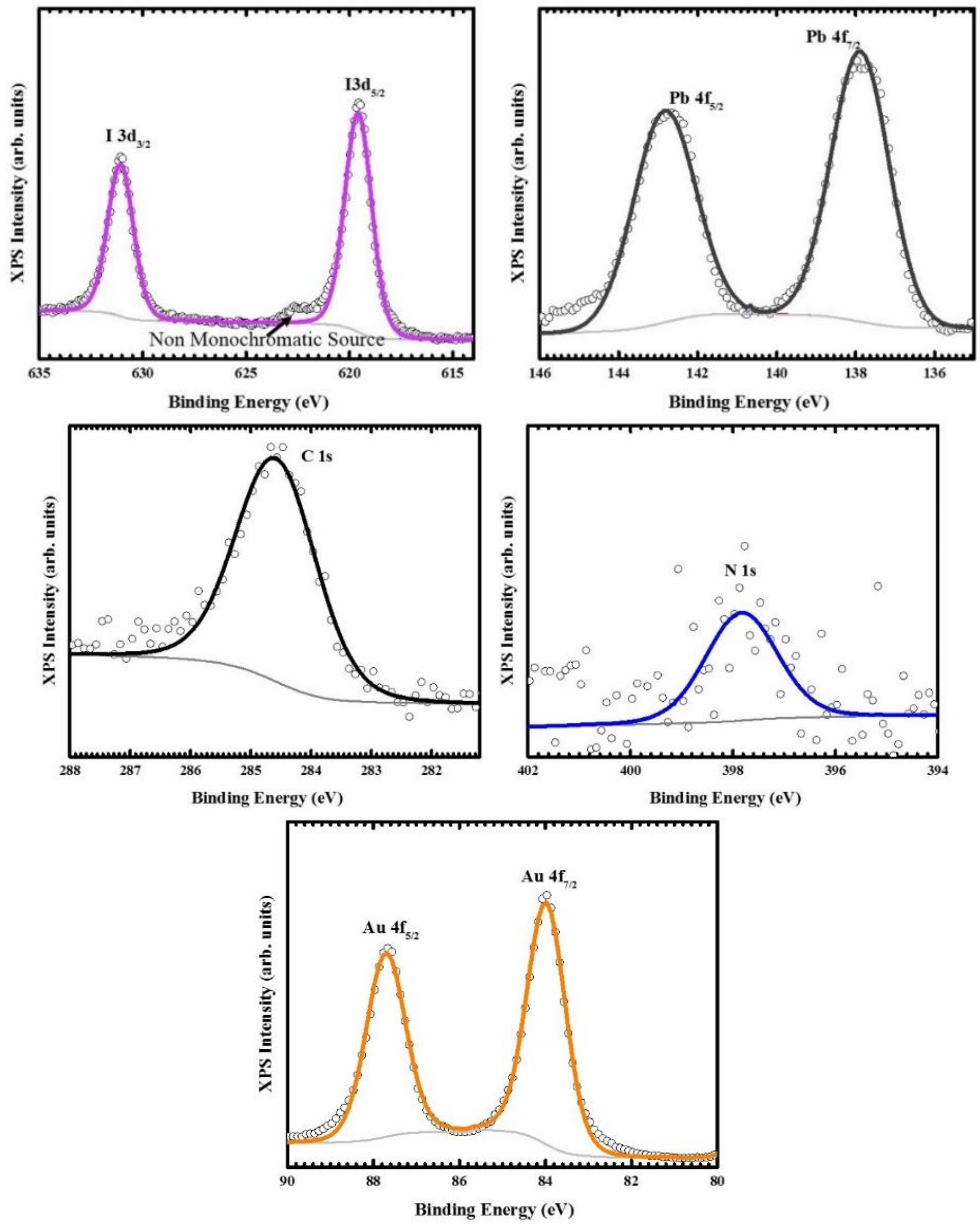

$MAPbI_3$ Deposition Time	Pb 4f & I 3d Ratios	$MAPbI_3$
3 minutes	Pb=1, I=3	$MAPbI_3$

Figure 4.8. XPS spectra for illustrating the chemical composition of pristine $MAPbI_3$ thin film. The non-monochromatic peaks are observed in the spectra because our XPS system doesn't have a monochromator. Therefore, the Kβ energy appears in the spectrums.

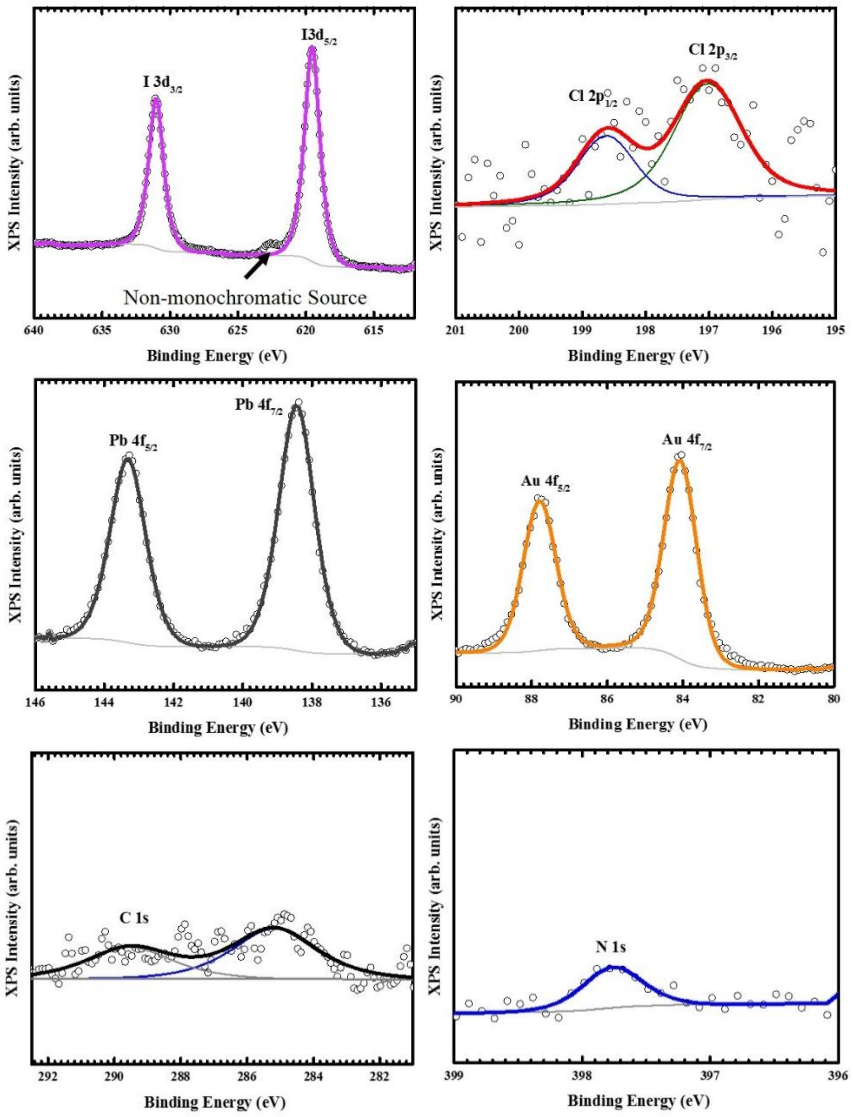

$MAPbI_3$ Deposition Time	Pb 4f, I 3d & Cl 2p Ratios	$MAPb(I_{1-x}Cl_x)_3$
6 minutes	Pb=1, I=2.8, Cl=0.21	$MAPbI_{2.59}Cl_{0.21}$

Figure 4.9. XPS spectra illustrating the chemical composition of $MAPbI_3$ thin film after 0.75 ML deposition of $PbCl_2$ molecules.

Based on all the STM images that we acquired, the general trend is that on the surface of $MAPb(I_{1-x}Cl_x)_3$, most Cl ions were observed in the regions close to the grain boundaries and only a few in the center of the grains (Figures 4.4c-f and Figures 4.5b-c). The substitution of I ions by Cl ions was observed for both the dimer and zigzag structures (Figures 4.6a and 4.6d). The majority of incorporated Cl ions were found to form Cl-I pairs with neighboring I ions (see the dashed circles in Figure 4.4d-f). Note that DFT calculations suggest that the dimer structures associated with both the pristine and Cl-incorporated surfaces are more stable than the zigzag ones by about 0.030 eV, in good agreement with the energy difference of 0.034 eV reported in a previous study [13]. In addition, the experimental STM images (Figure 4.4f) also show a few incorporated Cl

ions bonding together to form the Cl-Cl pairs. The possibility for the appearance of these Cl-Cl pair was also confirmed by DFT calculations, with the simulated STM image (see the inset in Figure 4.4f) reproducing well the Cl-Cl configurations observed in the STM experiments.

4.6 Several configurations of adjacent and non-adjacent Cl-I pairs in the $PbCl_2$ deposited $MAPbI_3$

Figure 4.10 shows several configurations for adjacent (Figures 4.10a and 4.10d) and non-adjacent Cl-I pairs (Figure 4.10g) in the dimer structure observed in STM experiments. DFT calculations verified the possibilities of these configurations (Figures 4.10b-c, 4.10e-f, and 4.10h-i) as well as predicted several other possible configurations for the adjacent and non-adjacent Cl-I pairs in the dimer and zigzag structures, as shown in (Figures 4.11 and 4.12). Note that these configurations in the dimer (Figures 4.10 and Figure 4.11) or zigzag (Figure 4.12) structures have rather close total energies, which rationalizes the variety of configurations for two Cl-I pairs observed in Figure 4.10.

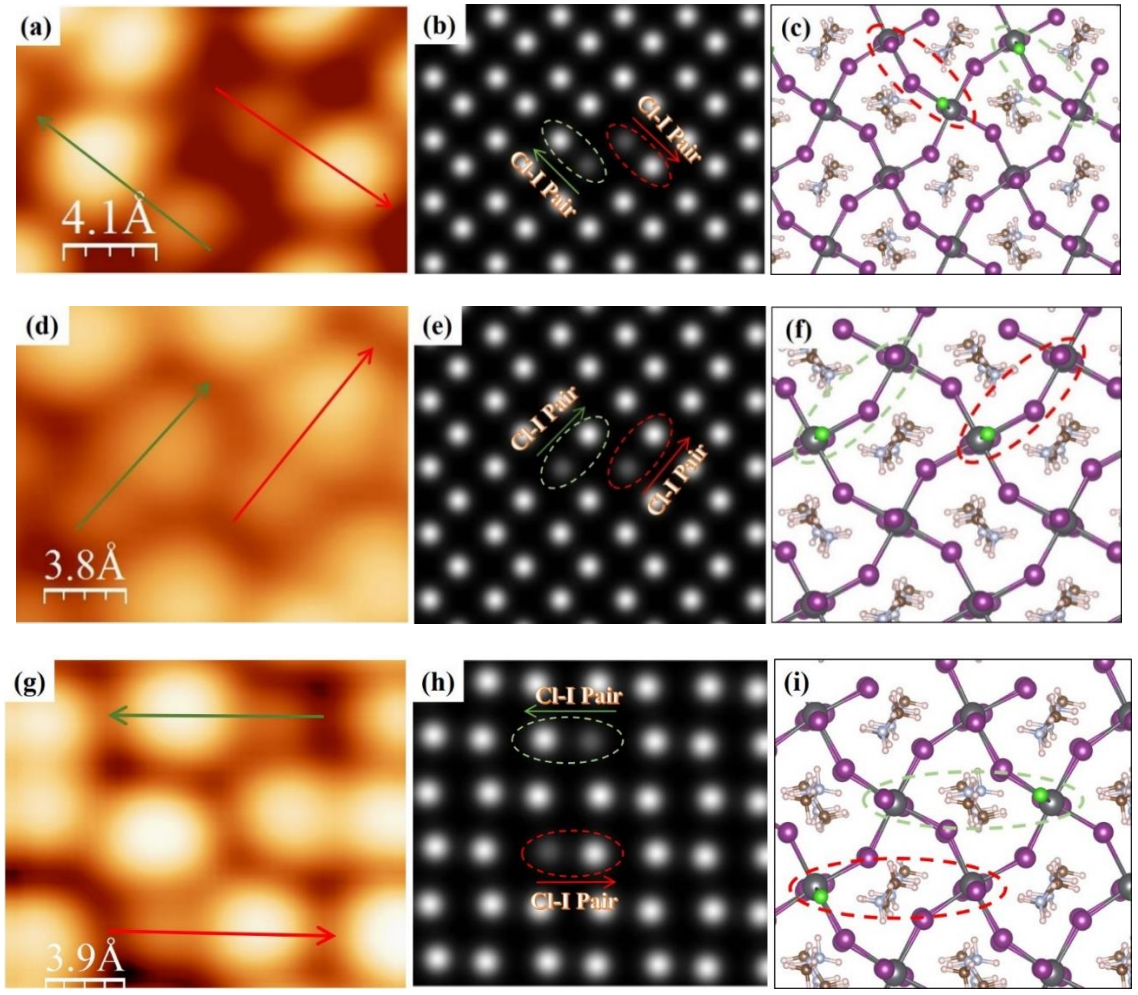

Figure 4.10. STM images of different configurations of Cl-I pairs in the dimer structure. (a) High-resolution STM image of two adjacent Cl-I pairs with opposite directions; arrows indicate the direction from Cl to I ion in the dimer (Scan area = 1 × 1.6 nm^2; Sample bias voltage = –2.50 V, Tunneling current = 30 pA). (b-c) Simulated STM image and atomic model for the two Cl-I pairs observed in (a). (d) High-resolution STM image of two adjacent Cl-I pairs showing the same parallel orientation; arrows indicate the direction from Cl to I ion in the dimer (Scan area = 1.4 × 1.8 nm^2; Sample bias voltage = –2.50 V, Tunneling current =30 pA) in two parallel dimers in the small grain in Figure 1 (d-f). (e-f) Simulated STM image and atomic model for the two Cl-I pairs observed in (d). (g) High-resolution STM image of two non-adjacent Cl-I pairs with opposite directions (Scan area =1.7 × 2 nm^2; Sample bias voltage = –2.50 V, Tunneling current = 30 pA) (h-i) Simulated STM image and atomic model for the two Cl-I pairs observed in (g). Color code in (c), (f), and (i): Pb (dark gray), I(purple), Cl (green), N (brown), C (ice blue), H (light Pink).

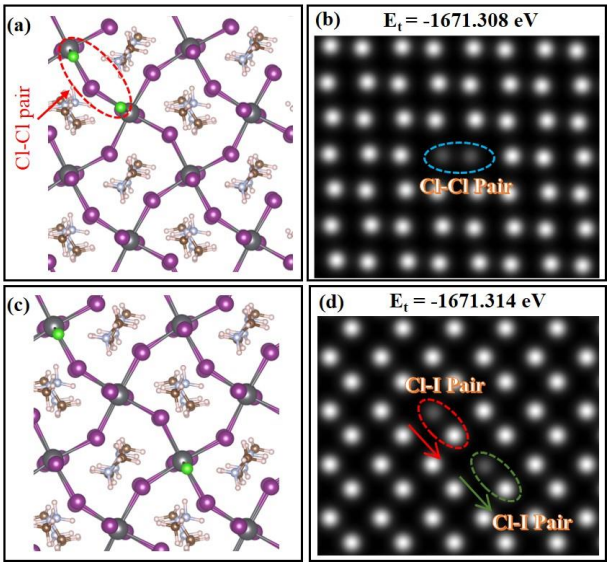

Figure 4.11: Possible configurations of one Cl-Cl pair and two Cl-I pairs appearing in the dimer phase predicted by DFT calculation. E_t=Total energy.

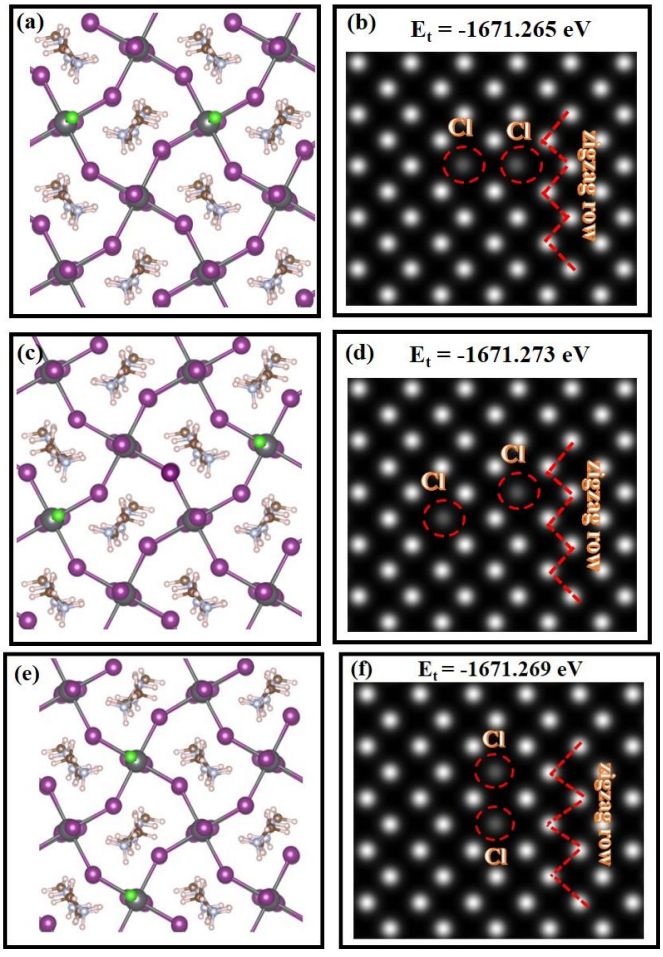

Figure 4.12: Possible configurations of two Cl-I pairs appearing in the zigzag phase predicted by DFT calculation. E_t=Total energy.

4.7 High concentration of $PbCl_2$ leads to degradation of $MAPbI_3$ and fully covered the surface of $MAPbI_3$

We attempted to increase the deposition time of $PbCl_2$ to 8 min to achieve more Cl ion incorporation in the dimer and zigzag structures but observed the significant degradation of the $MAPbI_3$ film (Figure 4.13, Figure 4.14). We further increased the deposition time of $PbCl_2$ to 12 min to achieve more Cl ions incorporation in the dimer and zigzag structures but we observed that the $MAPbI_3$ film was completely covered by the 1.5 ML of $PbCl_2$ (Figure 4.15). Additionally, the XPS (Figure 4.16) confirmed the Cl ratio increased in 12 min deposition to 0.8 which is 0.6 higher than the 6 min Cl deposition concentration in $MAPbI_3$ thin films. Note that through XPS measurements (Figure 4.16) for the fully covered $MAPbI_3$ surface by $PbCl_2$, we observed higher Cl concentration in comparison with samples after shorter $PbCl_2$ deposition.

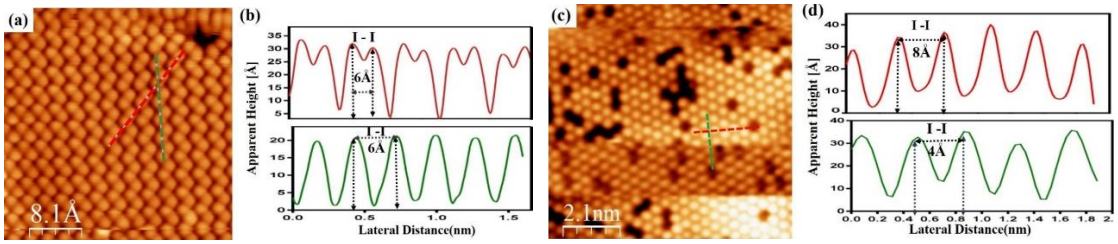

Figure 4.13. Comparison of LT-STM topography for pristine $MAPbI_3$ thin film with degraded sample after 1 ML of $PbCl_2$ deposition (a) pristine $MAPbI_3$ thin film (Scan area=4.3 × 4.3nm^2, Sample bias voltage = -2.50 V, Tunneling current = 30 pA).(b) Height profiles along the dashed lines (red and green) in (a). (c) Degraded $MAPbI_3$ thin film after 8-min deposition of $PbCl_2$ (Scan area= 20 × 20nm^2, Sample bias voltage = -2.50 V, Tunneling current = 20 pA). (d) Height profiles along the dashed lines (red and green) in (b)

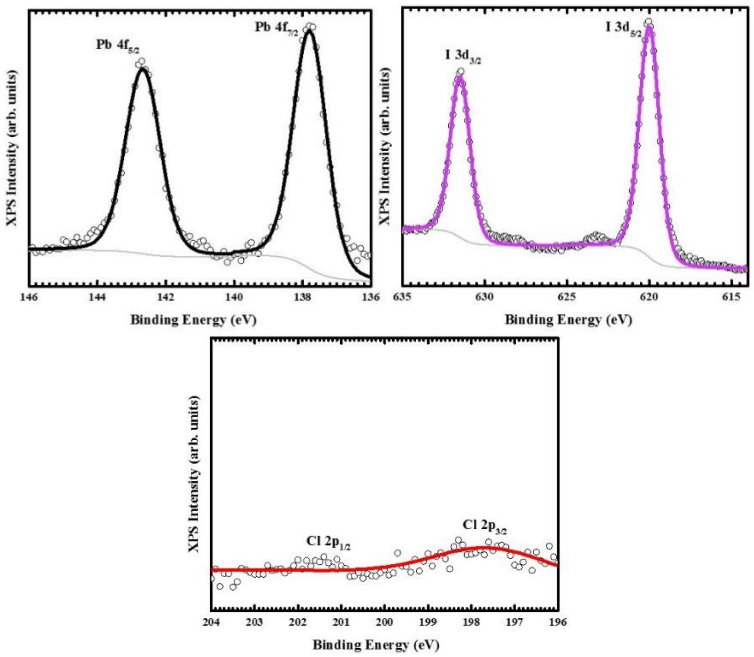

Figure 4.14. XPS spectra illustrating the chemical composition of degraded $MAPbI_3$ thin film

after 1 ML deposition of $PbCl_2$ molecules.

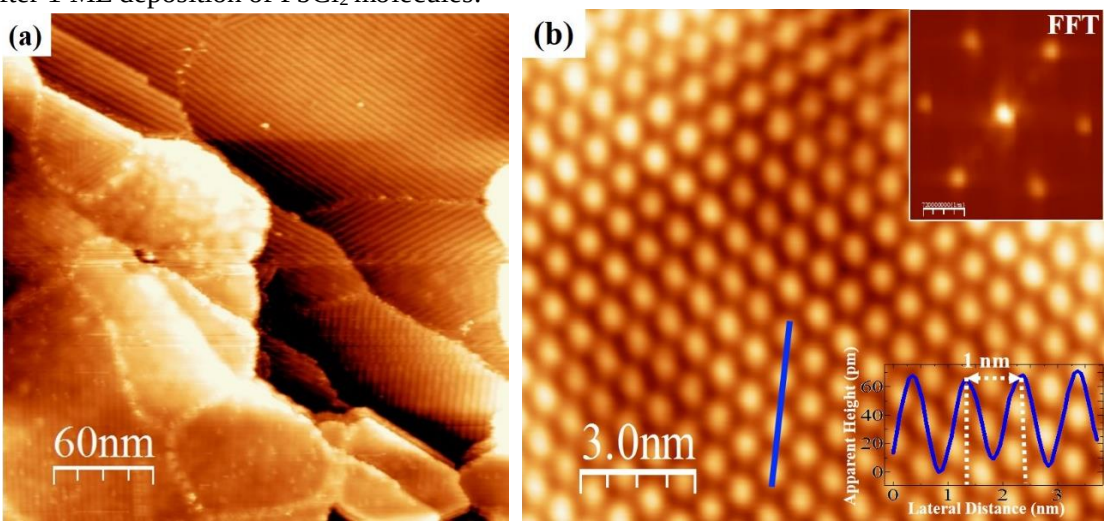

Figure 4.15: STM images of the $MAPbI_3$ thin film after1.5ML of $PbCl_2$ deposition. (a) Large area STM topography image of $PbCl_2$ fully covering $MAPbI_3$ thin film (Scan area= 300 × 300 nm^2, Sample bias voltage = –2.50 V, Tunneling current =400 pA). (b) High-resolution STM image of the $PbCl_2$ surface structure located in the center of a grain. (Scan area=13 × 15nm^2 (Sample bias voltage = –2.50 V, Tunneling current = 400 pA). Inset: the height profiles along the solid blue line and Fast Fourier Transform (FFT) images showing the hexagonal structure of $PbCl_2$.

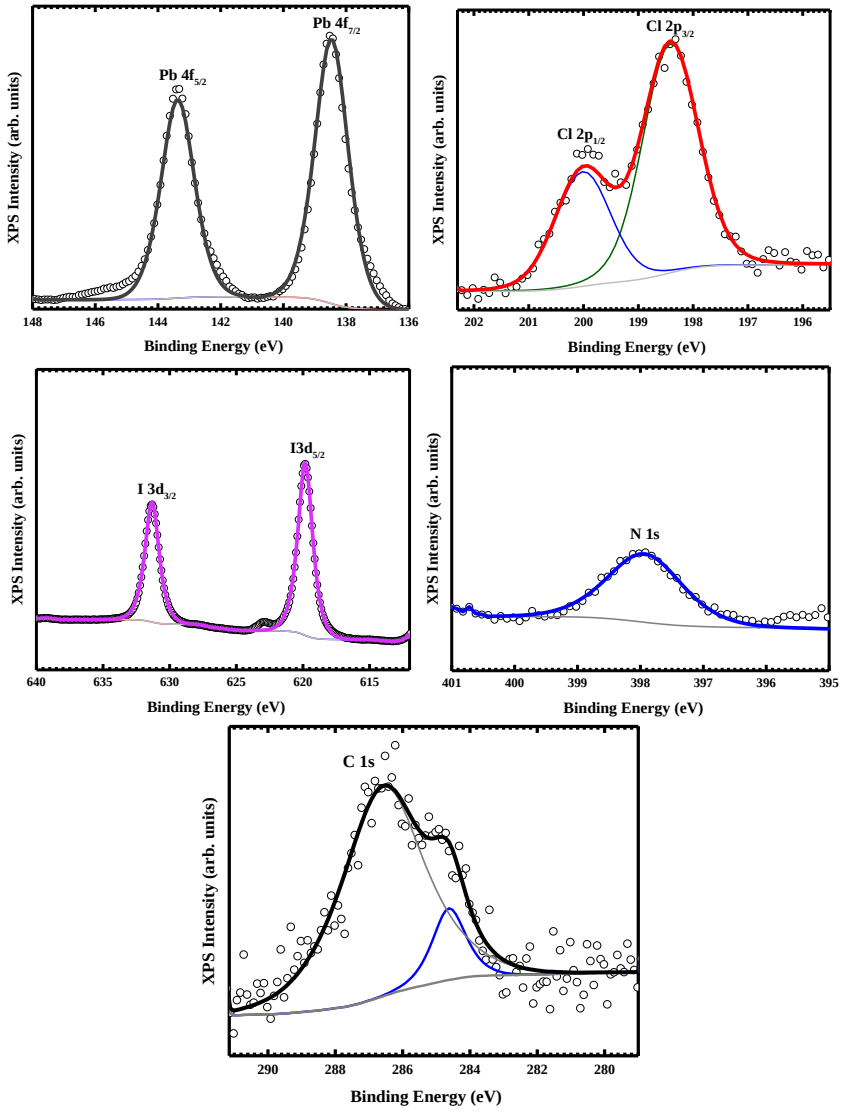

$MAPbI_3$ Deposition Time	Pb 4f, I 3d & Cl 2p Ratios	$MAPb(I_{1-x}Cl_x)_3$
12 minutes	Pb=1, I=3.5, Cl=0.8	$MAPbI_{2.7}Cl_{0.8}$

Figure 4.16.: XPS spectra illustrating the chemical composition of $MAPbI_3$ thin film after 1.5 ML deposition of $PbCl_2$ molecules.

Considering the fact that the 1 min deposition of $PbCl_2$ did not lead to the surface incorporation of Cl ions in the $MAPbI_3$ film, we deduced that the stable Cl surface incorporation should correspond to those samples after 0.5 ML and 0.75 ML deposition of $PbCl_2$. According to the histogram shown in Figure 4.4g, the [Cl] : ([Cl] + [I]) concentration of 14.8 ± 0.6% was extracted for the Cl incorporated $MAPbI_3$ (i.e., $MAPb(I_{0.85}Cl_{0.15})_3$). However, according to the XPS results (Figure 4.9), incorporated Cl concentration of 40% was determined, which significantly differs from the concentration extracted from the STM histogram analysis (Figure 4.4g). This is because XPS measurements not only probe Cl ions mixed in the top surface layer but also those in sub-surface layers.

4.8 Influence of Cl incorporation on the electronic properties of $MAPbI_3$ by UPS & IPES characterization with DFT calculated bandgap

We further investigated the influences of the incorporated Cl ions on the electronic properties of $MAPbI_3$ films by UPS/IPES (Figure 4.17a). Based on the UPS and IPES measurement results, the bandgap of the pristine $MAPbI_3$ film was determined to be 1.45 eV. After Cl incorporation with 0.75 ML deposition of $PbCl_2$, the bandgap increases to 1.65 eV (0.20 eV larger than that of the pristine $MAPbI_3$ film), suggesting that the incorporation of Cl ions can effectively tune the electronic properties of $MAPbI_3$ [178 191].

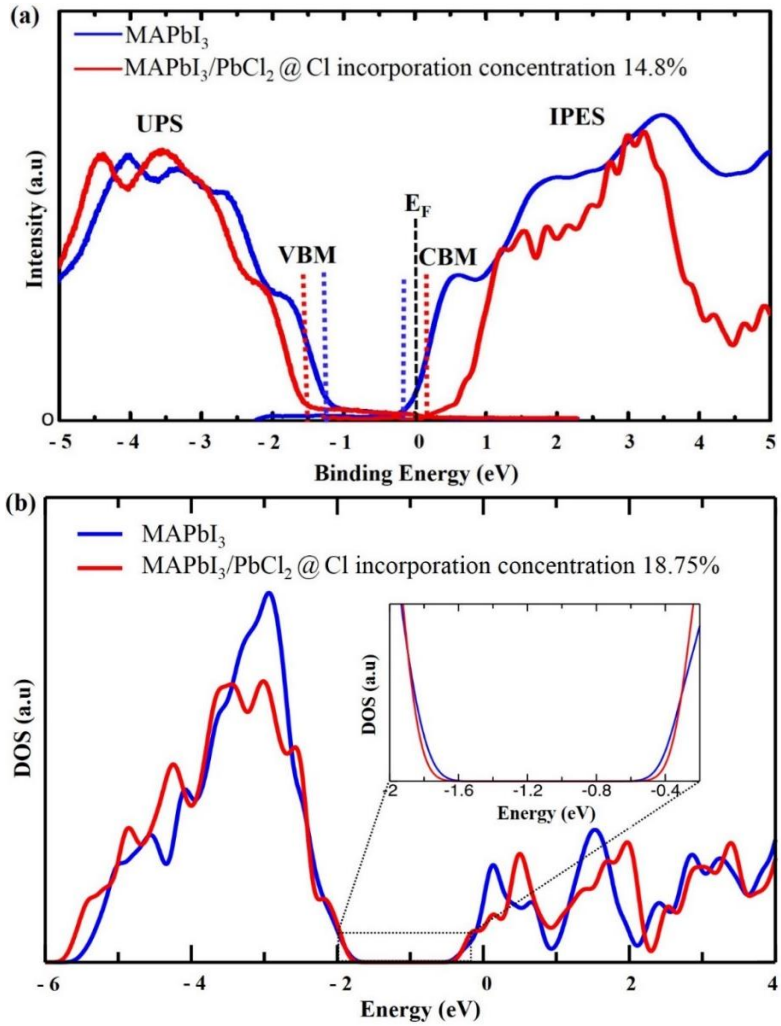

Figure 4.17. Experimental and DFT calculated bandgap of pristine and Cl incorporated $MAPbI_3$ (a) Experimental ultraviolet and inverse photoemission spectroscopy (UPS-IPES) spectra of the pristine (blue) and Cl-incorporated (red) $MAPbI_3$ surfaces. (b) Calculated DOS of the pristine and Cl-incorporated $MAPbI_3$ surfaces. For the latter, Cl ions are incorporated into the top four layers of the model at the [Cl] : ([Cl] + [I]) concentration of 18.75%. VBM=Valance band maximum, CBM= Conduction band minimum. A wider bandgap is observed after Cl incorporation.

Our STM and XPS results suggest that Cl ions are not only incorporated in the top layer but also the sub-surface layers. To determine the main factor that causes the surface bandgap change, we calculated the bandgaps (Figure 4.18) of the $MAPbI_3$ surface models with Cl ions being only incorporated in the top one, top two, and top four layers as a function of the incorporation ratio (assuming the same Cl concentration for all the relevant layers when Cl ions are incorporated into multiple layers), as shown in Figure 4.18. It is seen that there are no substantial bandgap changes when Cl ions are only mixed into the top layer, being the same as that for Cl-incorporated $MAPbBr_3$ [14]. But when Cl ions are contained in the sub-surface layers, the bandgap increases fast with the increasing chlorine incorporation concentration. This trend is even clearer in the case of Cl ions being incorporated in the top four layers. This indicates that the bandgap enlargement observed in the experiment is mainly a synergic effect of the Cl incorporation in the multiple surface layers (or in other words, more a bulk film effect rather than a surface effect). From Figure 4.19, we can realize that Cl ions are at least incorporated in the top four layers of the surface model consisting of a total of 8 ML (monolayer) of the perovskite lattice structure (here we consider the MAI layer as a layer and the PbI_2 layer as another layer), as only under this situation the increase of the bandgap (~0.204 eV) determined by UPS/IPES measurements can be well reproduced by our DFT calculations. In this context, we further calculated the density of states (DOS) for the pristine $MAPbI_3$ surface and that with Cl ions incorporated in the top four layers at the concentration of 18.75%, being quite close to the surface Cl ratio of (14.8% ± 0.6%) determined by STM. The comparison of DOS in Figure 4.17b also confirmed that incorporated Cl ions would enlarge the bandgap of $MAPbI_3$ by 0.2eV as a result of the upward and downward shift of the valance and conduction band edges, respectively (Figure 4.17b), which is consistent with the experimental observation (Figure 4.17a).

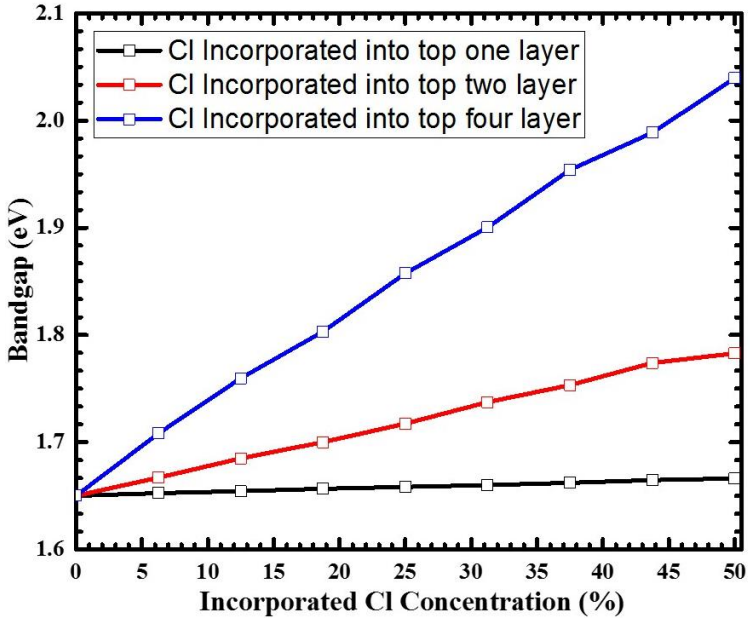

Figure 4.18. Calculated bandgaps of the $MAPbI_3$ surface model with Cl atoms only being incorporated in the dimer into the top one (black), top two (red), and top four layers (Blue) as a function of the incorporation ratio.

4.9 More stable surface by incorporation of Cl atoms

Another interesting aspect of Cl incorporation in $MAPbI_3$ perovskite comes from a previous report suggesting that Cl could potentially increase the stability of perovskite solar cell devices [192]. To unravel the origin of the enhanced stability of the Cl-incorporated $MAPbI_3$ surface, we evaluated the changes in the decomposition energy of the MAPb $(I_{1-x}Cl_x)_3$ film for different Cl incorporation concentrations through DFT calculations. Here, we consider two different incorporation modes: (1) Cl ions only being incorporated in the top layer of the surface, corresponding to Figure 4.19a; (2) Cl ions only being incorporated in the second layer, corresponding to Figure 4.19b. It is noticed that upon increasing the incorporated Cl amount, the decomposition energies profiles for both incorporation modes show firstly an increase, and then a decrease. The increase of the decomposition energy is related to the stronger bond strength of Cl-Pb compared to that of I-Pb [193-194]. This bond strength originates from the radius of Cl^- being smaller than that of I^-, causing a shorter bond length and in turn a stronger electrostatic interaction between bonded Cl^- and Pb^{2+} than that between bonded I^- and Pb^{2+}. However, the incorporation of the smaller Cl^- ion in the inorganic lattice of $MAPbI_3$ also induces the strain, which in turn pushes up the total energy of the system. At low Cl concentrations (i.e. below 18.75%), the influence of the strain on the total energy of the system is not predominant. But when the Cl concentration exceeds a threshold, the strain overrides the benefit of the stronger Cl–Pb bond, leading to the reduction in the decomposition energy. An increase of the decomposition energy after low concentrations of Cl incorporation suggests higher stability of the $MAPbI_3$ film concerning external stimuli such as temperature and, X-ray beams [195]. Also, it is found that the maximum increase of the decomposition energy for the incorporation in the second layer (Figure 4.19b) is 0.08 eV larger than that for the incorporation in the top layer (Figure 4.19a), which indicates that Cl ions mixed into the sub-surface layers play a more significant role in stabilizing the $MAPbI_3$ surface than those in the top layer.

In Figure 4.19b, the predicted optimal incorporation concentration of Cl into the second layer is 25%, being noticeably higher than that of the top layer (18.75%), which is consistent with our XPS measurements showing that the concentration in the sub-surface layers is higher than that in the top layer. We can also understand this experimental finding from the viewpoint of energy, according to Figure 4.19. At a fixed incorporated chlorine concentration, the higher decomposition energy corresponds to the lower total energy of MAPb $(I_{1-x}Cl_x)_3$. It can be seen from Figure 4.19 that when the incorporated concentration is less than ~40%, the total energy of MAPb $(I_{1-x}Cl_x)_3$ with the incorporation in the second layer is lower than that with the incorporation in the top layer, indicating that Cl ions prefer to stay in the sub-surface layers.

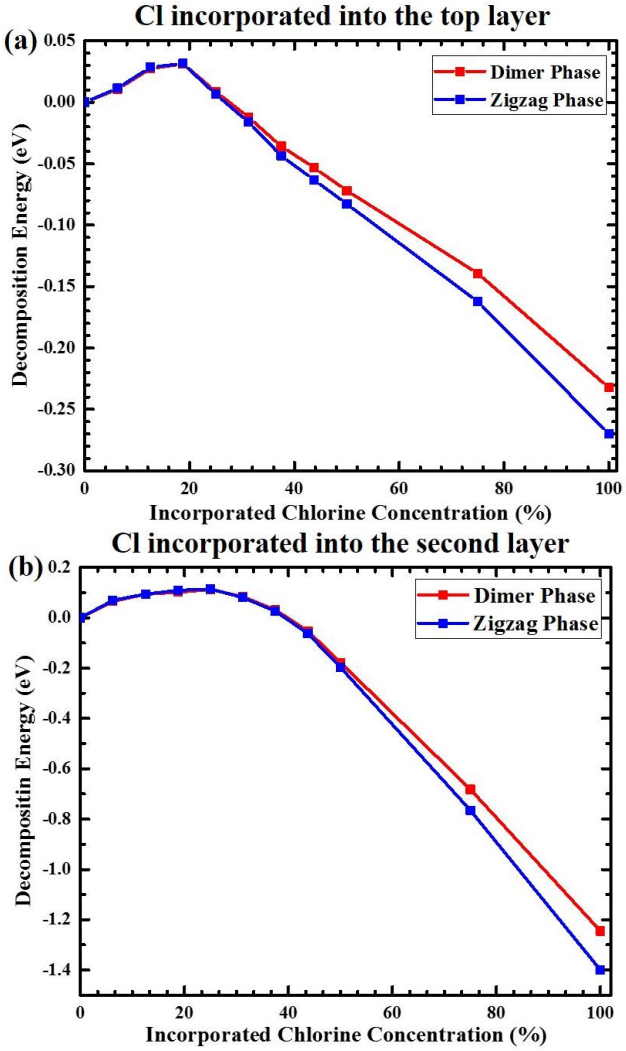

Figure 4.19. The decomposition energy difference between the top and second layer of Cl-incorporation in $MAPbI_3$ surface is determined by DFT calculations. (a) Cl ions are only incorporated in the top layer, and (b) Cl ions are only incorporated in the second layer.

This finding is consistent with the experimental observation that the incorporated Cl concentration in the sub-surface layers is higher than that in the top layer. Moreover, it is found that the decomposition energies within the positive range of both the dimer and zigzag phases differ negligibly, which corroborates the experimental observation of Cl ions incorporated in the surface structure with the dimer and zigzag phases simultaneously. Last but not least, when the incorporated [Cl] : ([Cl] + [I]) concentration is higher than ~25% for incorporation in the top layer and higher than ~40% for incorporation in the second layer, the decomposition energy of $MAPbI_{3-x}Cl_x$ becomes negative, meaning that $MAPb(I_{1-x}Cl_x)_3$ cannot exist stably, which determines in principle that the incorporated concentration for stable $MAPb(I_{1-x}Cl_x)_3$ samples will not exceed 25% in the top layer and 40% in the second layer. These predicted upper limits are consistent with our experimental results showing the incorporated chlorine concentration of 14.8±0.6% in the top layer and 40% on average in several other sub-surface layers. To further understand the influence of Cl ions on the stability of Cl-incorporated $MAPbI_3$ surfaces, we also

calculated the surface energies of the pristine $MAPbI_3$ surface and that with one I^- being substituted by Cl^- in the top layer, which is summarized in Table 1.

Perovskite	Dimer	Zigzag
$MAPbI_3$	6.354	6.385
$MAPb(I_{1-x}Cl_x)_3$	6.278	6.314

Table 1: Calculated surface energy (in eV) of the pristine and Cl-incorporated $MAPbI_3$ surfaces in the dimer and zigzag structures.

Note that the incorporation of one Cl atom in the $MAPbI_3$ surface leads to a surface energy decrease of 76 meV and 71 meV for the dimer and zigzag structures, respectively (Table 1), which can also explain the stabilization effect of Cl ions on the $MAPbI_3$ surfaces. Also, we performed molecular dynamics (MD) simulations of pristine and Cl-incorporated $MAPbI_3$ surfaces with the dimer structure to examine the impact of Cl ions on the vibration of I and Pb atoms in the top and second layer, by calculating the average moving distances for Pb and I atoms during the 1 ps MD simulation, which are shown in Table 2.

	$MAPbI_3$	$MAPb(I_{1-x}Cl_x)_3$ (One Cl atom in the 1st Layer)	$MAPb(I_{1-x}Cl_x)_3$ (One Cl atom in the 2nd Layer)
d_{I1} (Å)	2.477	2.475	2.428
d_{I2} (Å)	2.605	2.481	2.336
d_{Pb} (Å)	2.009	2.008	1.934

Table 2: The average moving distances for the I ion in the 1st layer (d_{I1}) and that in the 2nd layer (d_{I2}) and the Pb ion in the 2nd layer (d_{Pb}) during 1 ps MD simulation.

These results allow us to analyze the stabilization effect of incorporated Cl ions on the $MAPbI_3$ surface from the viewpoint of kinetics. It is noticed that the incorporation of one Cl ion in the top or second layer suppresses the vibration of Pb and I ions in the 1st and 2nd layer of the surface (Figure 4.7). The weaker vibration of the inorganic lattice will to some extent suppress the diffusion of some intrinsic defects, such as iodine vacancy and interstitial defects, which contributes to the improved stability of $MAPb(I_{1-x}Cl_x)_3$ surfaces. It is interesting to point out that the Cl ion incorporated in the second layer generates a more obvious impact on lowering the vibration strength of Pb and I atoms than the Cl atom in the top layer, being consistent with the analysis for the decomposition energy in Figure 4.19. In conclusion, our DFT calculations verify that the incorporation of Cl ions indeed stabilizes the $MAPbI_3$ surface from the viewpoints of both thermodynamics and kinetics.

4.10 FTIR and XRD characterization for stability test of $PbCl_2$ deposited $MAPbI_3$

To investigate the impact of 17-20% Cl ions incorporation on the stability of $MAPbI_3$ on basis of our STM experimental and DFT calculated data, we have fabricated the solution-processed pristine $MAPbI_3$ film as thick as ~ 400 nm thickness and another

$MAPbI_3$ film (~400 nm) with subsequent thermal deposition of $PbCl_2$ (~70 nm) and the degradation was measured by FTIR and XRD. The Cl incorporated sample was kept in the N_2 glove box and characterized for one year for stability test (Figure 4.20a) and found that this sample was remarkably stable for the whole year as shown from the FTIR (Figure 4.20a) and XRD spectrum (Figure 4.21). In the XRD spectrum, the characteristic peak at 14.13^0 indicates the $MAPbI_3$ which corresponds to the lattice plane (110).
By comparison of obtained FTIR spectra confirmed that around 14-18% of Cl incorporation enhances the stability of $MAPbI_3$ thick films, where the pristine $MAPbI_3$ sample has degraded at the 57^{th} day (Figure 4.20b). Also, we confirmed the similar results for another batch of sample and obtained similar stability for the Cl incorporated $MAPbI_3$ sample. As it is observed from the Cl incorporated $MAPbI_3$ spectrum that the stretching mode of NH_3^+ at $3133cm^{-1}$ prevails from the 1^{st} day to one year to confirm the presence of $MAPbI_3$ (Figure 4.20a). While in the pristine $MAPbI_3$ FTIR spectrum (Figure 4.20b), it is obvious that the NH_3^+ stretching mode has disappeared and confirmed the degradation of this sample on the 57^{th} day.

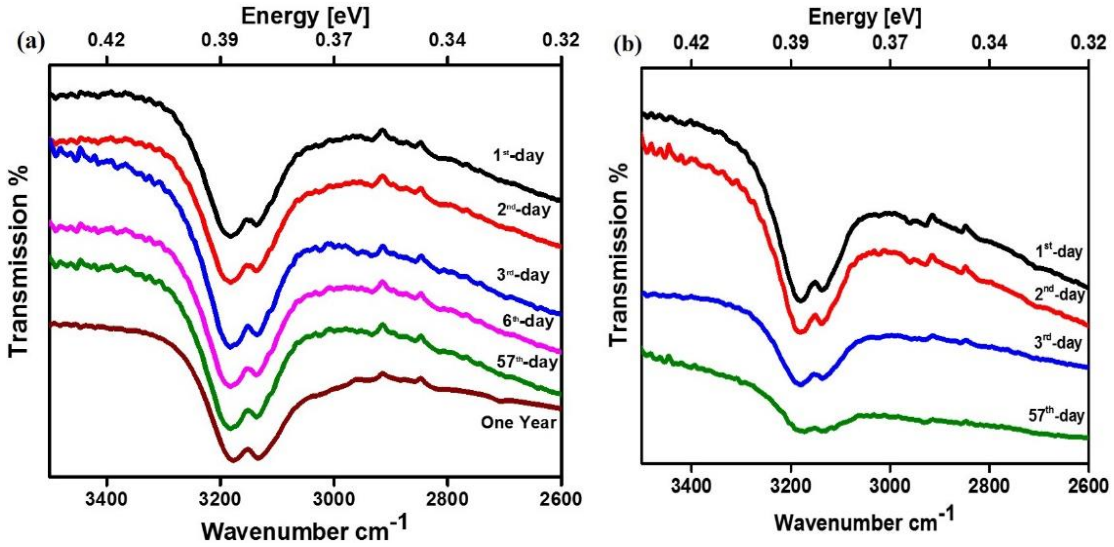

Figure 4.20. Time evolution of FTIR spectrum corresponding to solution-processed (a) ~70 nm $PbCl_2$ deposited $MAPbI_3$ film and (b) Pristine $MAPbI_3$ (~400 nm) thick film.

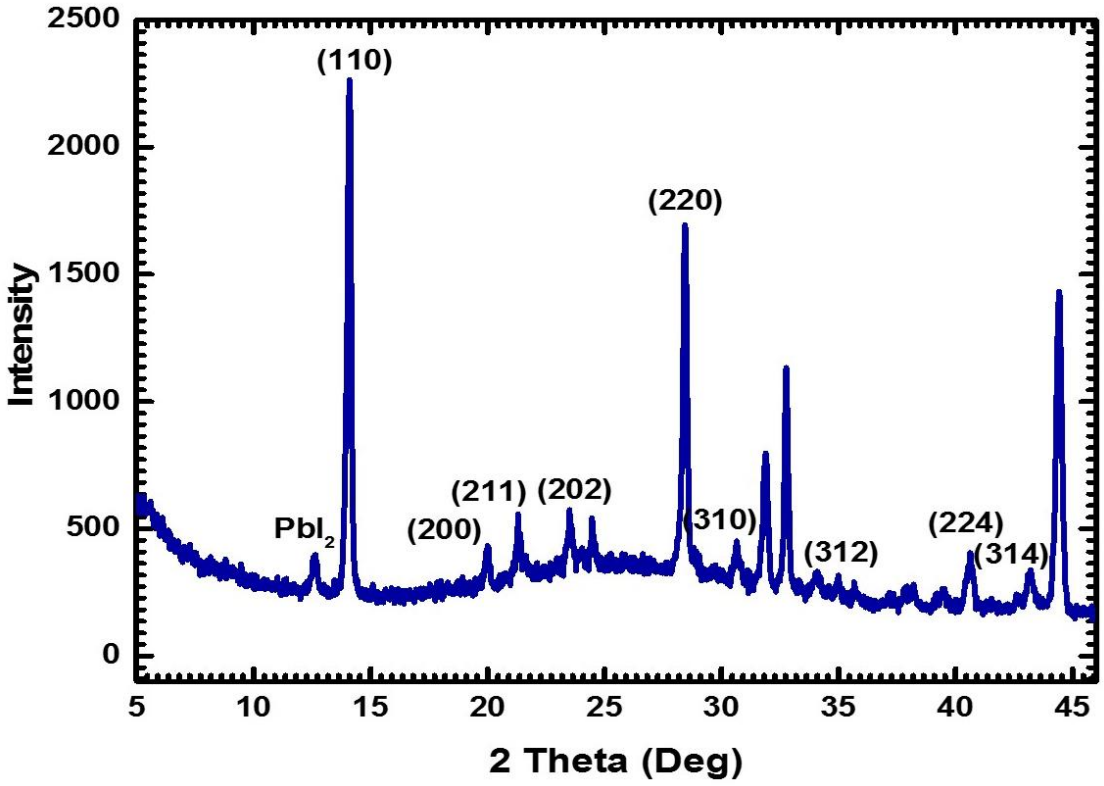

Figure 4.21. One-year stability test measurements by XRD spectroscopy corresponding to solution-processed $MAPbI_3$ film with ~70 nm $PbCl_2$ incorporation.

Additionally, to test the stability of Cl-incorporated $MAPbI_3$ thick films in the air. We exposed the one year aged Cl incorporated $MAPbI_3$ sample in the N_2 glove box to the air for the stability test. We have achieved the 18 days stable $MAPbI_3$. In Figure 4.22a, we showed the FTIR spectrum comparison of the first day, stable until the 18th day and the degraded 19th-day pattern. Furthermore, the sample characterized by XRD (Figure 4.22b), which shows the comparison of the 1st-day air-exposed spectrum to the 19th-day degraded pattern, contains that the characteristic peak at 14.13^0 corresponding to $MAPbI_3$ (110) has flattened indicating the degradation of the $MAPbI_3$ sample. Therefore, the FTIR/XRD stability measurements have shown the influence of 14-18% Cl incorporation on the enhanced stability of $MAPbI_3$ samples.

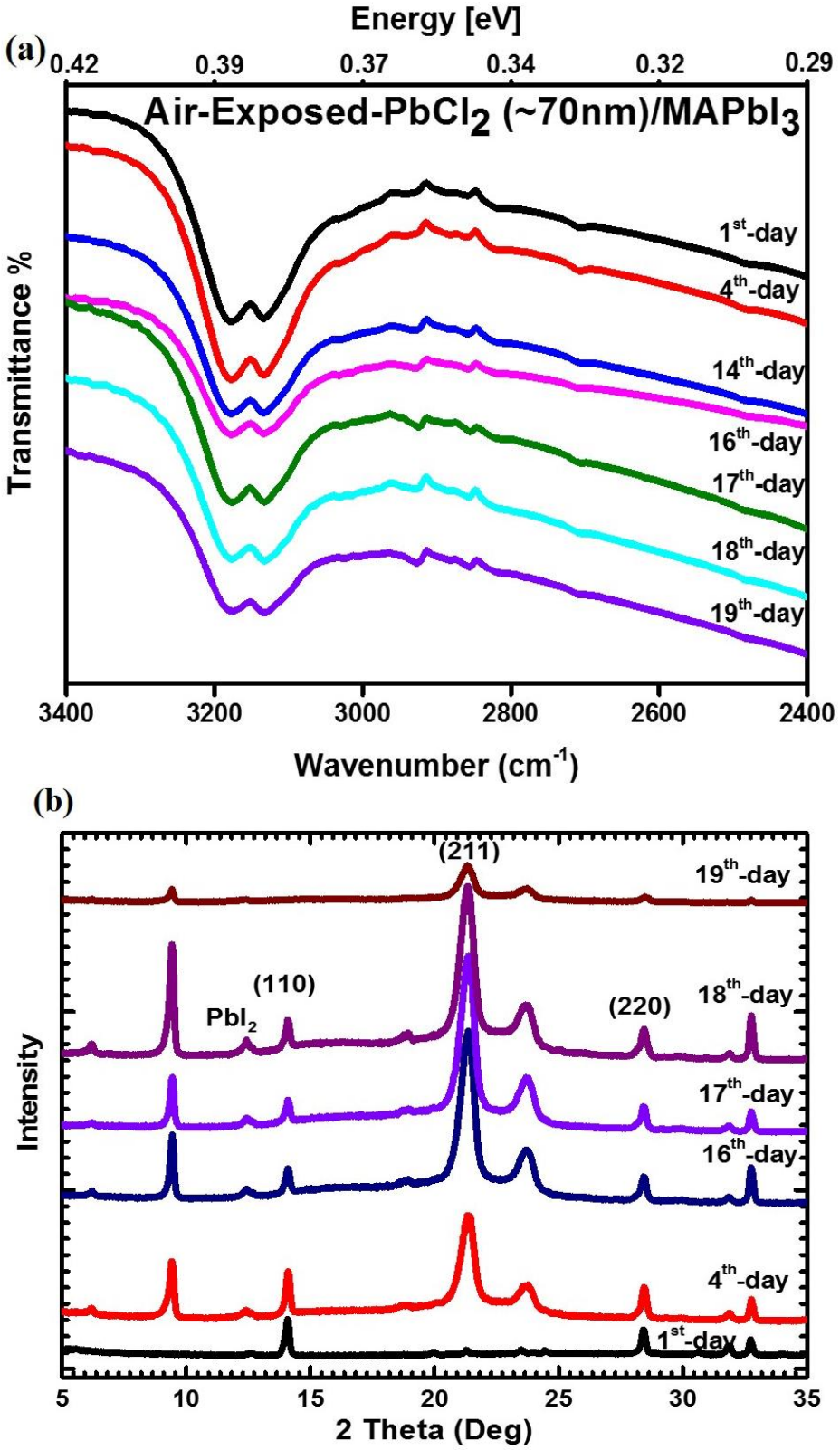

Figure 4.22. Sample exposed in air for 19 days stability test measurements by (a) FTIR and (b) XRD spectrum corresponding to solution-processed $MAPbI_3$ incorporated by ~70 nm $PbCl_2$.

After the stability evidence of $MAPbI_3$ with the ~70nm $PbCl_2$ by FTIR and XRD, we have fabricated the solution-processed ~400nm thick film of $MAPbI_3$ on FTO coated glass substrate and by thermal deposition, ~70 nm $PbCl_2$ deposited on top of $MAPbI_3$, which is the 14-18% of ~400 nm. By SEM, the cross-section of the prepared sample has been scanned and found that the ~70 nm thick $PbCl_2$ layer, added an extra layer on the $MAPbI_3$ thick film (Figure 4.23), which was protecting the $MAPbI_3$ from degradation but doesn't incorporate in the $MAPbI_3$ lattice. This extra added $PbCl_2$ layer would shift the energy level in the actual solar cell device and might change the PCE and FF.

Therefore, for making more stable and high-efficiency perovskite solar cells we suggest to deposit 2.8 nm thin layer of $PbCl_2$ on the $MAPbI_3$ surface because according to atomically proved in surface 14-18% of Cl concentration makes $MAPbI_3$ more stable, so for this purpose 2.8 nm is 14% of 20 nm surface layer of ~400 nm thick film. In this way, the extra layer of $PbCl_2$ would not be added to the $MAPbI_3$ surface in the solar cell configuration and would not affect the PCE and stability of solar cells.

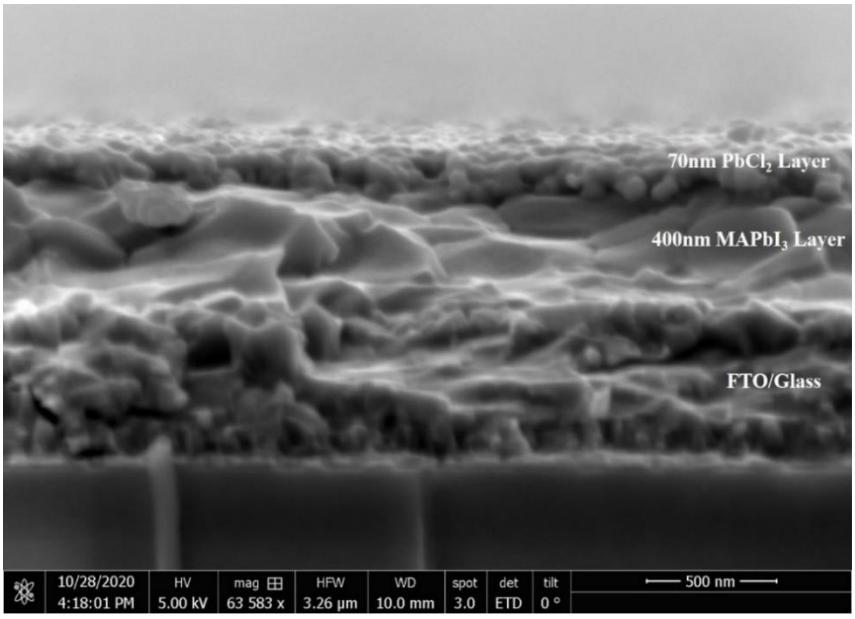

Figure 4.23. SEM image of solution-processed $MAPbI_3$ incorporated by ~70 nm $PbCl_2$ on FTO/glass substrate.

4.11 Summary

In this chapter, we studied the atomic-scale structure of Cl incorporated $MAPbI_3$ surfaces by STM. It is found that Cl ions are incorporated in both the $MAPbI_3$ surface and sub-surface layers. Most of the Cl ions incorporated on the surface were found to be close to the grain boundaries, but some are also found at the center of the grains for both the dimer and zigzag structures of $MAPbI_3$. Additionally, our results confirm that Cl ions are not present at the surface of $MAPbI_3$ at short deposition times by XPS measurements, and with a sufficiently long time of $PbCl_2$ deposition (e.g., 12 min), the $MAPbI_3$ surface is fully covered by 1.5 ML of $PbCl_2$. Moreover, the surface bandgap of $MAPbI_3$ is found to be increased by approximately 0.2 eV from 1.45 eV to 1.65 eV when 0.75 ML of $PbCl_2$ is deposited onto the $MAPbI_3$ surface. DFT calculations reproduce the bandgap increase

observed in the experiment for similar incorporated Cl concentration. The incorporation of Cl in the subsurface layers was found to have a stronger impact on the bandgap with respect to Cl ions substitution at only the topmost surface layer. DFT calculation and MD simulation, reveal a strong increase of the perovskite stability for low Cl concentration (below 18.75%). The increase of stability is even more pronounced when substituting the Cl ions in the subsurface layer with respect to the top surface layer. The perovskite material was found to be stabilized both thermodynamically and kinetically. Therefore, we suggest, if we keep the Cl concentration around 14-18% in $MAPbI_3$ thick films, we will be able to increase the stability of $MAPbI_3$ perovskite solar cells which was verified through our FTIR and XRD measurements for the Cl incorporated $MAPbI_3$ thick films. Therefore, this study has proven from the atomic scale study to the bulk film stability process. Our findings provide insights for further understanding of the perovskite material and a more rational design of the future high stability perovskite solar cells.

Chapter 5: Distinct Atomic Structure Investigation of Thermally Evaporated Pb and $PbCl_2$ on Au (111)

5.1 Introduction

We used $PbCl_2$ as an additive to improve the stability of $MAPbI_3$ as mentioned in previous chapter 4 providing insights on Cl incorporation on $MAPbI_3$ surface. Our proposed $PbCl_2$ deposition procedure on $MAPbI_3$ generated a new question why Pb ions are not observed in STM topographies and why only Cl ions incorporate in $MAPbI_3$. These questions turned our research direction towards the finding of Pb in PVSK. Therefore, a set of control experiments were conducted to understand whether Pb is present in $MAPbI_3$ PVSK. First, metallic Pb deposition experiments were conducted on Au (111) to optimize the protocol before depositing it on $MAPbI_3$. Based on the $PbCl_2$ STM topographies (chapter 4 section 4.2.2), it was not clear whether the observed ions were Pb or Cl. Therefore, LT-STM high-resolution images were aimed on Pb deposited Au (111) to provide morphological differences between Pb and Cl ions on Au (111) surface, which will be discussed in detail in Section 5.4.

Currently, why Pb cannot be observed by STM on $MAPbI_3$ surface remains elusive. On the basis of DFT calculated models (see section 3.4.2 in chapter 3), it is shown that $MAPbI_3$ has the MAI terminated surface, corroborating the observation of I-I dimers reconstructed surfaces by STM. DFT calculations propose also the formation of Pb–I terminated surface for $MAPbI_3$[196 197], but up to date, no experimental evidence has been provided. Furthermore, after $PbCl_2$ deposition in $MAPbI_3$ ultra-thin films, why only Cl (and not Pb) incorporation is observed in the $MAPbI_3$ surface structure? Tentatively, we proposed four hypotheses for the Pb presence in $MAPbI_3$ films (Figures 5.1 - 5.4) as described below.

(i) Upon $PbCl_2$ impingement on $MAPbI_3$ surface, Pb and Cl are adsorbed on the surface of $MAPbI_3$ (Figure 5.1)

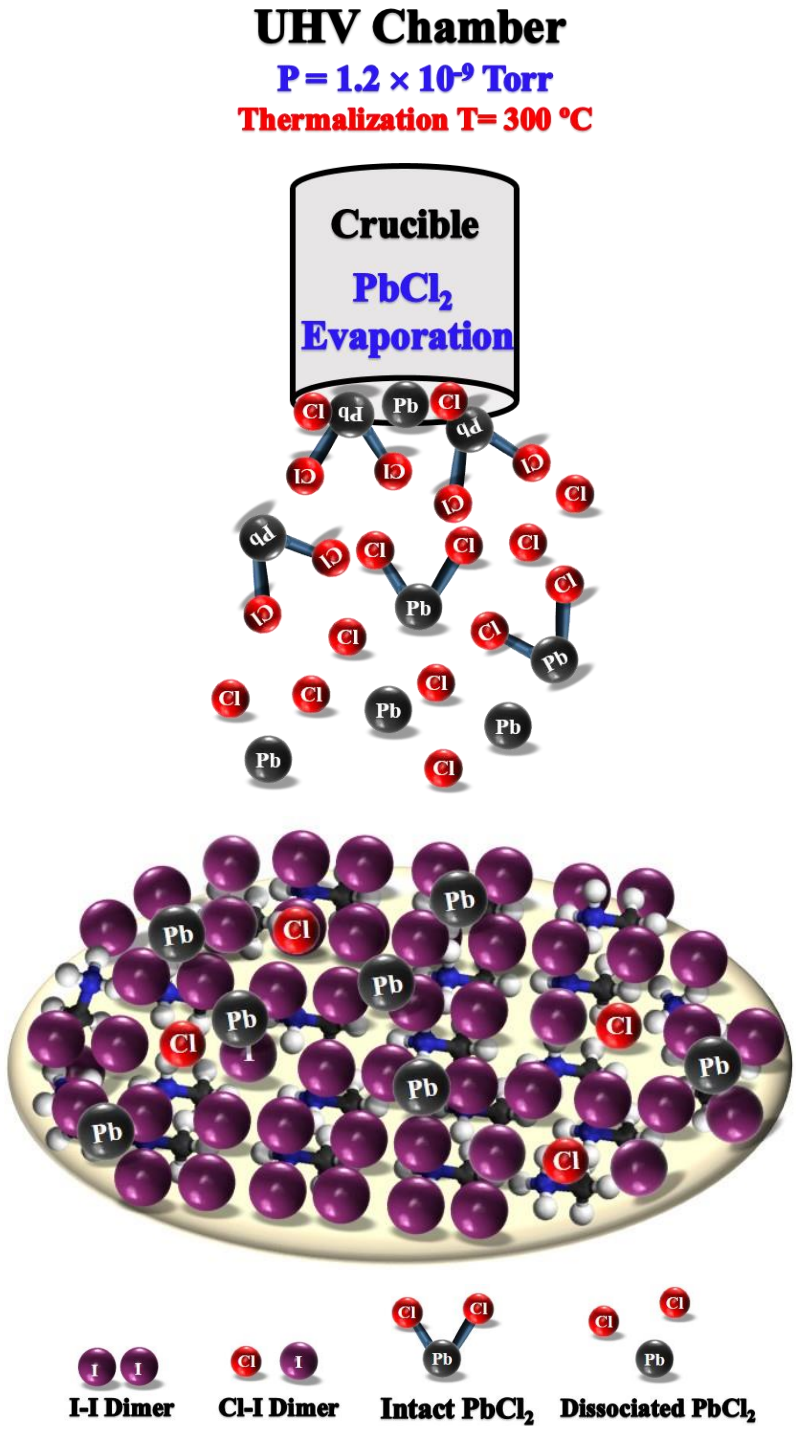

Figure 5.1: Pb adsorbed on the $MAPbI_3$ surface.

(ii) Upon $PbCl_2$ impingement on $MAPbI_3$, Pb dissociates from Cl and desorbed in vacuum (Figure 5.2).

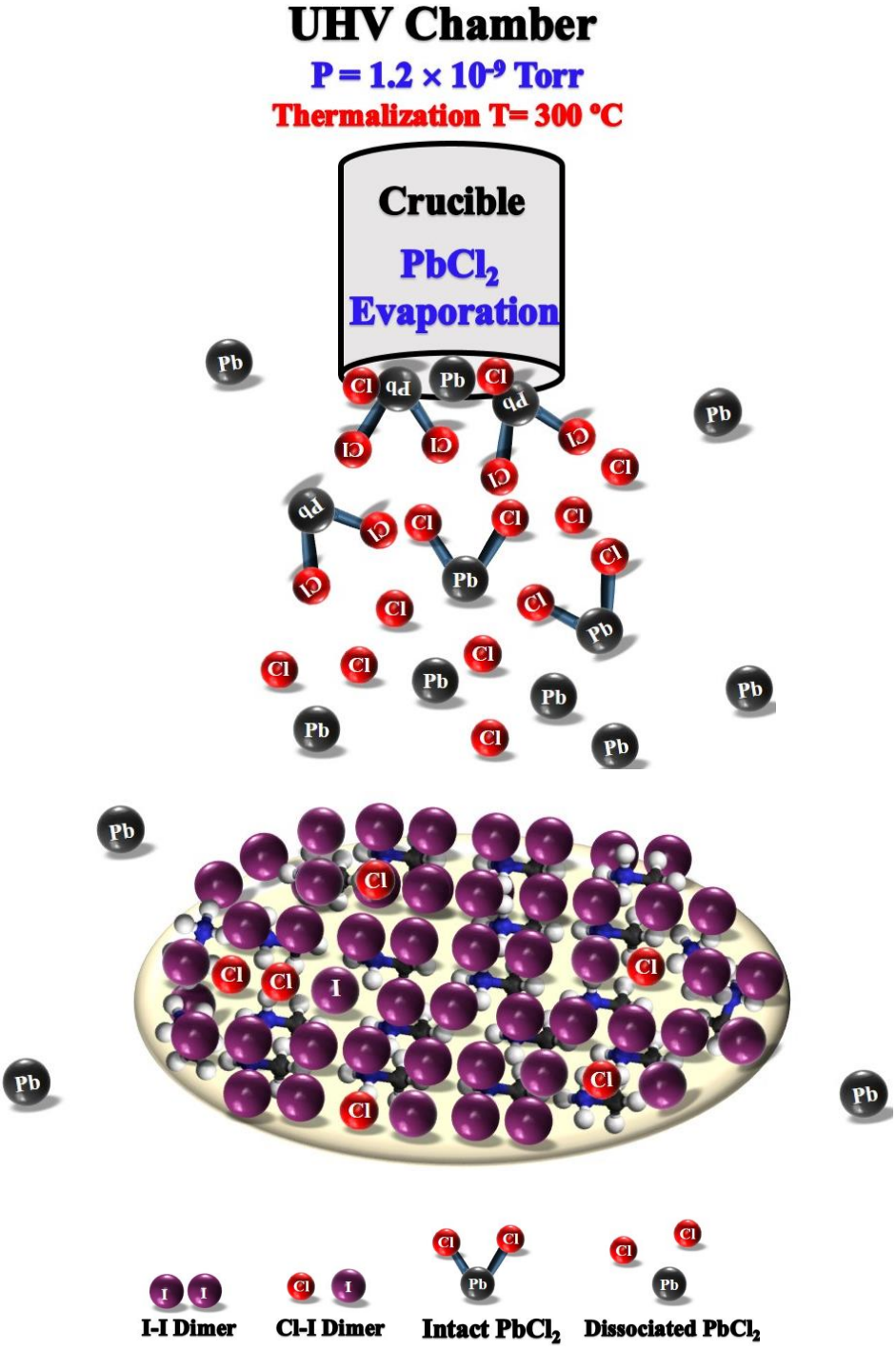

Figure 5.2: Pb desorbed in vacuum and only Cl incorporate in $MAPbI_3$

(iii) During the thermalization of the crucible at 300 ºC, some $PbCl_2$ molecules dissociate to Pb and Cl (Figure 5.3). The disassociated Cl and intact $PbCl_2$ molecules evaporate to the substrate. The dissociated Pb accumulates in the crucible of the evaporator.

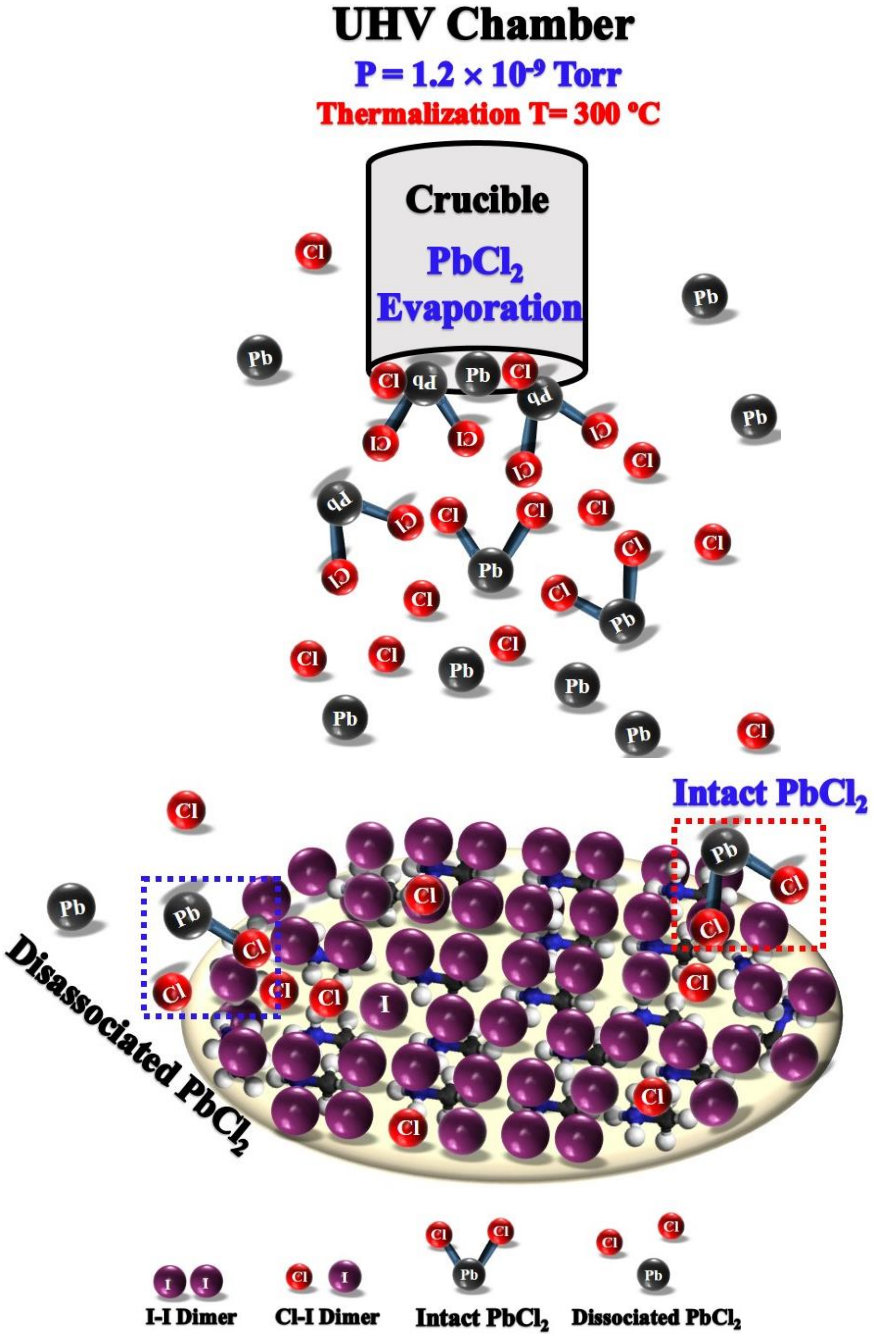

Figure 5.3: Pb and Cl dissociated on a surface and only Cl incorporate in $MAPbI_3$.

From Figure 5.3, it is proposed that only Cl incorporates in the $MAPbI_3$ lattice from the sublimated elements and the surface does not provide an energetically favorable

energy for $PbCl_2$ molecules to adhere. In addition, the surface also does not provide the favorable energy to Pb to passivate on the $MAPbI_3$ surface.

(iv) Pb diffused in the $MAPbI_3$ subsurface or diffused into the interface between $MAPbI_3$ and Au (111)

If Pb diffuses to the interface or into the $MAPbI_3$ subsurface (Figure 5.4), an increase in Pb concentration in the $MAPbI_3$ film is expected. Thus, XPS measurements (Figure 5.5) were performed, comparing Pb concentration in pristine and 6 min $PbCl_2$ deposited $MAPbI_3$ samples. The intensity increase of Pb 4*f* signals in XPS spectra provides the evidence that the Pb concentration increased by depositing the $PbCl_2$ in ~4 nm ultra-thin film of $MAPbI_3$ as well as the positive shift in binding energy (B.E.) has occurred in the Pb 4f peaks, which can be a cause of the diffusion process of Pb into the subsurface. The second reason that can also be assumed about the shift in the B.E. of Pb is that it can be occurring because of accidental differential charging as our current XPS system does not have a monochromator

On basis of XPS measurements, the hypothesis of Pb diffusion to the $MAPbI_3$ subsurface is corroborated. The XPS spectra are the raw data plot without any normalization to only show the difference in the increased concentration and the shift in the Pb 4*f* B.E.

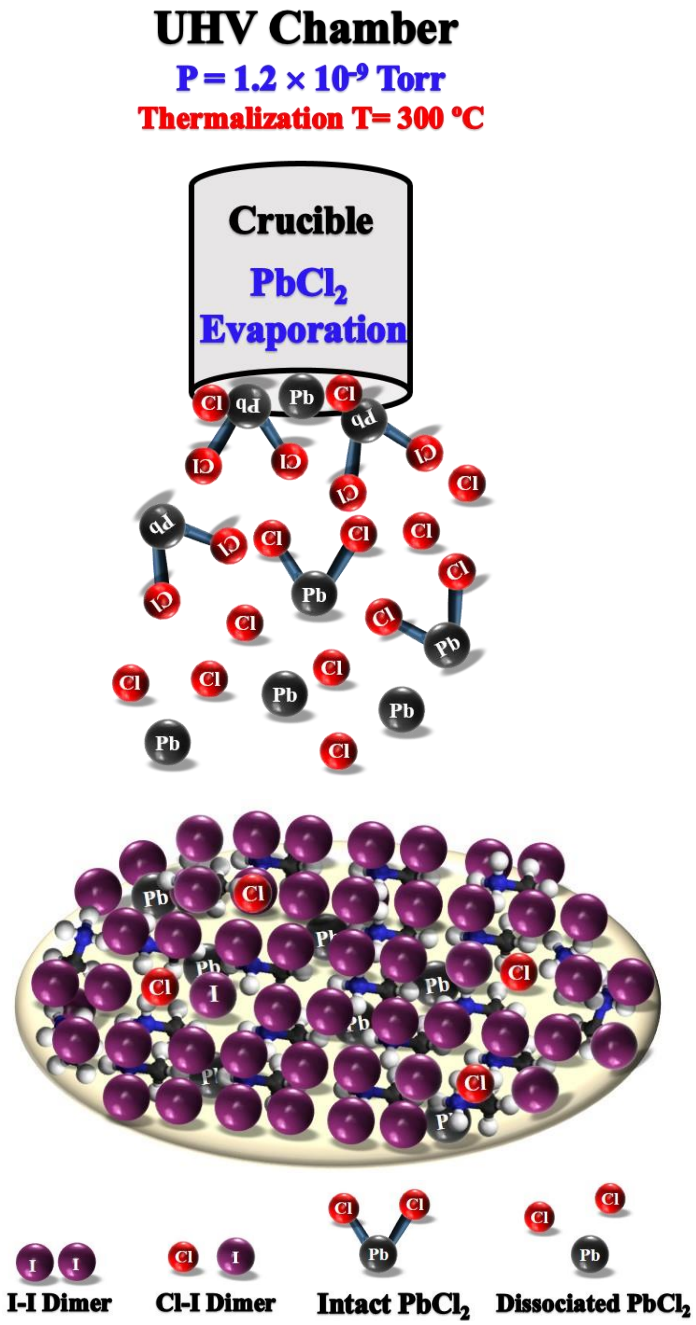

Figure 5.4: Pb diffused to the interface of Au (111) and $MAPbI_3$.

As future plan, the atomic scale topography evidence could be provided by LT-STM after the stepwise etching of each ML of $PbCl_2$ deposited on $MAPbI_3$. For this purpose, gas cluster ion beam sputtering (GCIB) will be used to controllably etch smoothly ML by ML. LT-STM scanning will be used for the atomic resolution imaging to understand the presence of Pb in the $MAPbI_3$ crystal structure after each ML etching.

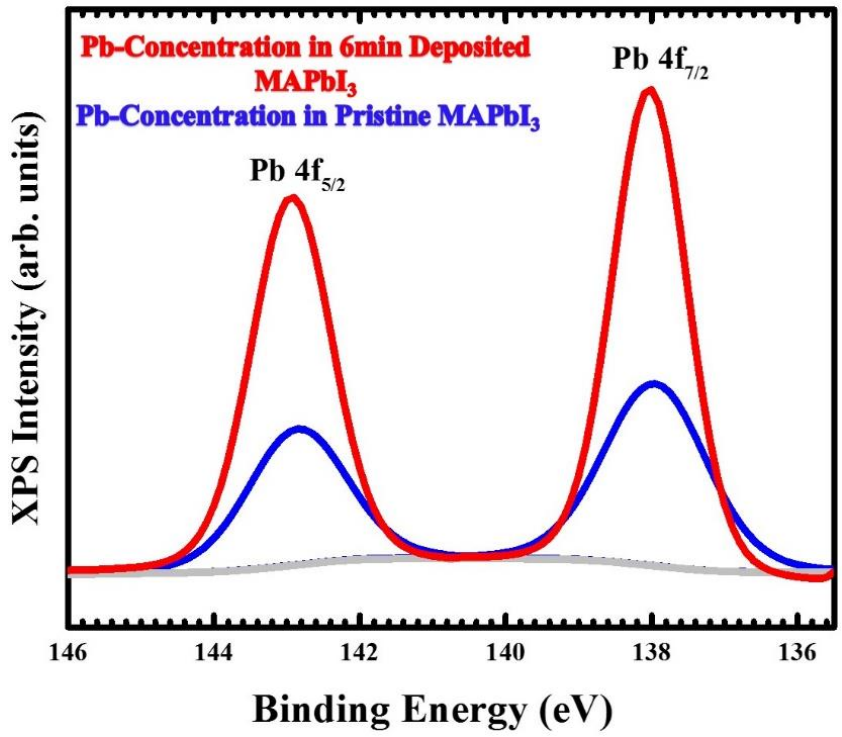

Figure 5.5: XPS spectra of Pb concentrations comparison in pristine and 6 min $PbCl_2$ deposited $MAPbI_3$ samples.

The other three hypotheses made in Section 5.1 about Pb presence in $MAPbI_3$ will be discussed in Section 5.4 based on the atomic resolution STM images of $PbCl_2$ deposited MLs on Au (111) to understand the surface structure. However, considering the complexity of STM images, the atomic structure of only Pb on Au (111) is required to be analyzed and understood before providing the interpretation of $PbCl_2$ on Au (111) STM images.

In the future, by depositing only Pb on $MAPbI_3$ surface and conducting LT-STM images, we could explore the diffusion, substitution, or adsorption mechanism and also can try to find the origin of degradation of PVSK by Pb migration. It will be a novel idea if we could provide evidence of the origin of the degradation by Pb migration or disassociation from the octrahedra in PVSK crystal structure.

There are three main factors, which trigger the degradation of PVSK: (i) temperature, (ii) humidity, and (iii) UV-light illumination. We could also be able to answer how Pb is affected by these three parameters because it might be a reason that Pb disturbs the halide position and/or act as driving force for Pb to migrate. If we could answer this question, it could help the device community to improve the PSC stability by not only focusing on halide migration but also taking into account the Pb disturbance on the PVSK.

5.2 Methods

For the controlled Pb deposition on $MAPbI_3$, the Pb deposition protocol was optimized on Au (111) by thermal evaporation. The Pb protocol was optimized by trying different deposition times and temperatures. Metallic-Pb was filled in a crucible in Knudsen cell (K-cell) and thermalized at a chamber pressure of $5.6x10^{-9}$ Torr. The boiling point of Pb is 327 ^{0}C [198]. In these experiments, the K-Cell temperature was limited to 600 ^{0}C (Figure 5.6a). Au (111) was cleaned by sputtering and annealing (Chapter 4, Section 4.4) before Pb deposition. Pb was deposited on clean Au (111) at a chamber pressure of $1.2x10^{-9}$ Torr. The sample has been transferred to STM chamber right after the Pb deposition and the high-resolution images were achieved. Theoretically calculated phase of Pb is cubic (Figure 5.6b). In the constant current STM images acquired at 77 K, the Pb structure with cubic phase is expected on Au (111). Pb crystallizes in the cubic space group Fm-3m. Twelve equivalent bonded Pb atoms form an edge, cuboctahedra of face sharing $PbPb1_2$, and a mixture of the corner. All lengths of the Pb–Pb bonds are 5.05 Å [198].

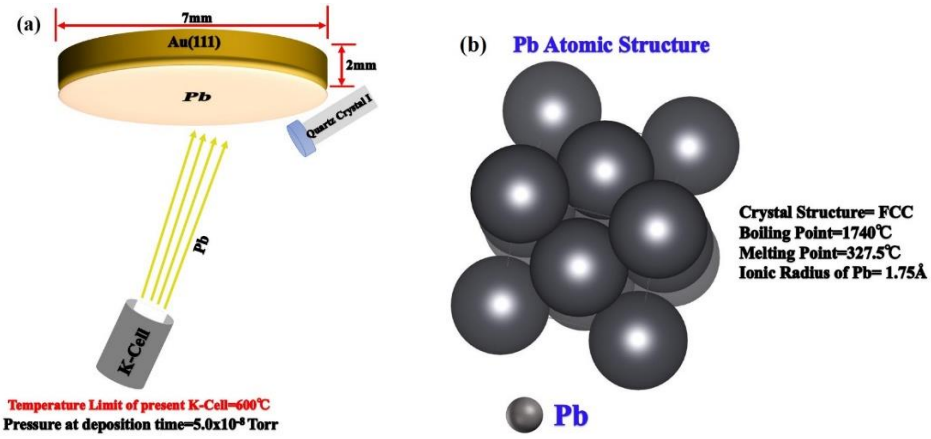

Figure 5.6: Illustration of Pb deposition and calculated atomic model. (a) Illustration of Pb deposition in UHV chamber. (b) Calculated atomic model of Pb[198]. Pb Crystal Structure=FCC, Ionic Radius of Pb = 1.75 Å.

5.3 LT-STM topographies of Pb deposition on Au (111) for different times to optimize the deposition protocol

Figure 5.7 (a-b) shows the LT-STM investigated structures of large terraces of Pb MLs grown on Au (111) by using the fabrication protocol (Section 5.2) for 4 min deposition. The high-resolution images of fully covered Au (111) by the Pb MLs were

observed (Figure 5.7 a,c). The resulting height profile of a topmost ML of Pb is 2.0 Å (Figure 5.6b). The STM image reveals the topmost and the second ML. It is anticipated that the Au (111) surface is fully covered, by many monolayers (MLs) of Pb. With this temperature and time of Pb deposition, it is expected that it will cover the $MAPbI_3$ surface completely in future experiments and the Pb interaction with $MAPbI_3$ will not be observed. From STM images (Figure 5.7a,c), it is observed that the Pb ML consists of the Pb-Pb dimer structure in parallel rows formed in different angles and also single and double pairs of Pb-Pb dimers (Figure 5.7c-d, f-g). The experimental line profile with 5.2 Å gap corresponding to each Pb-Pb dimer (Figure 5.6 e, h) is consistent with the calculated Pb-Pb bond length of 5.02 Å [198]. More, the FFT map (inset in Figure 5.7a) shows the cubic phase of the Pb structure.

Our obtained STM images of Pb-Pb dimer structure on Au (111) is completely different than the previously reported moiré pattern structure of Pb on Au (111) [199]. Two reasons can be anticipated for the different structure of Pb: the deposition temperature in our experiments was 600 K by using vacuum thermal evaporation while the reported group has used only 300 K thermalization temperature by using electron beam evaporation and the post-annealing of the sample at 400 K [199]. In our experiments, no post-annealing of sample was performed, because we were interested in the adlayer of Pb on Au (111) for only the protocol optimization for the future experiments of the interaction of Pb on the surface of $MAPbI_3$. Therefore, to not form an alloy PbAu (111), the Pb deposited Au (111) was not post annealed and was directly transferred at 77 K.

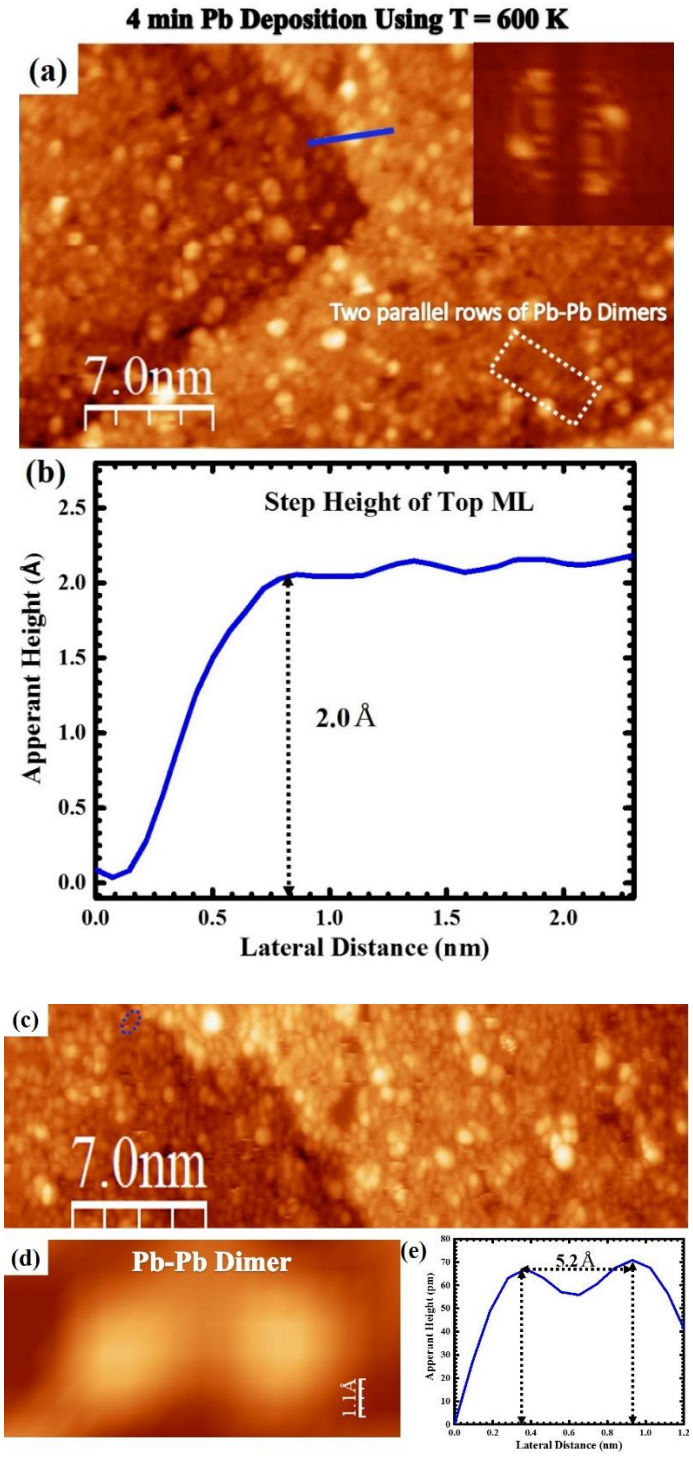
4 min Pb Deposition Using T = 600 K
(a)
Two parallel rows of Pb-Pb Dimers
7.0nm
(b)
Step Height of Top ML
Apperant Height (Å)
2.0 Å
Lateral Distance (nm)
(c)
7.0nm
(d)
Pb-Pb Dimer
1.1Å
(e)
5.2 Å
Apperant Height (pm)
Lateral Distance (nm)

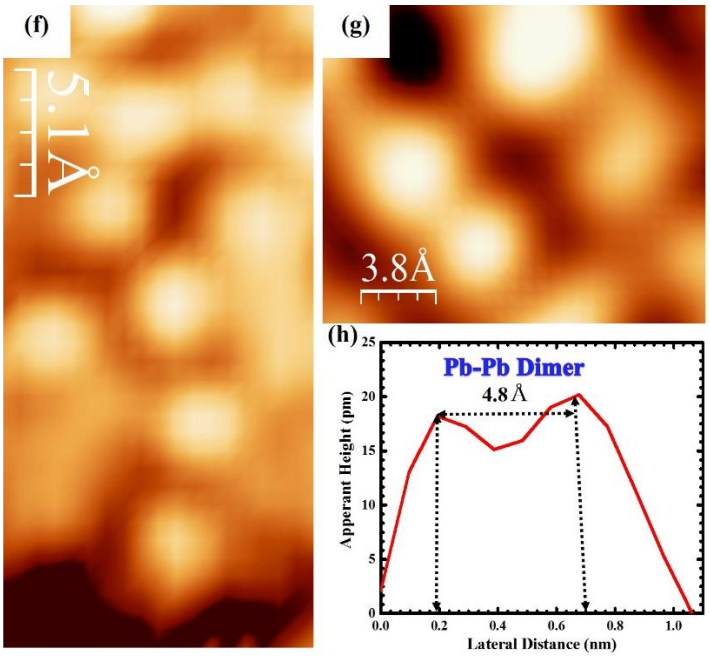

Figure 5.7: LT-STM images of 4 min deposited Pb thin films on Au (111). (a) LT-STM image of a fully covered Pb MLs on Au (111) (Scan area = 21 × 35 nm^2; Sample bias voltage = 4 V, Tunneling current = 300 pA). The inset in (a) show the FFT image of the cubic Pb structure. (b) Height profile = 2.0 Å of a topmost ML. (c) A close up image of (a) to show the Pb-Pb dimers orientation (Scan area = 12 × 35 nm^2; Sample bias voltage = 4 V, Tunneling current = 300 pA). (d) Zoom in image of the Pb-Pb dimer marked by blue ellipse in (c) (Scan area =11 × 5.5 $Å^2$; Sample bias voltage = 4 V, Tunneling current = 300 pA). (f-g) Formation of different Pb-Pb dimer structures (Sample bias voltage = 4 V, Tunneling current = 300 pA). (h) Line profile of Pb-Pb bond gap = 4.8 Å.

For theoretical support and interpretation of our obtained STM topographies of Pb on Au (111) (Figure 5.8 a, c), we simulated the CIF files of the atomic model of Au (111) and Pb (111) in VESTA [198]. With this simulated model, we can observe the Au (111) interface with Pb (111) and the unit cell parameters. The Pb-Pb bond length on Au (111) surface is 5.05 Å which is matching well with obtained LT-STM topographies of Pb unit cell in Figure 5.8b.

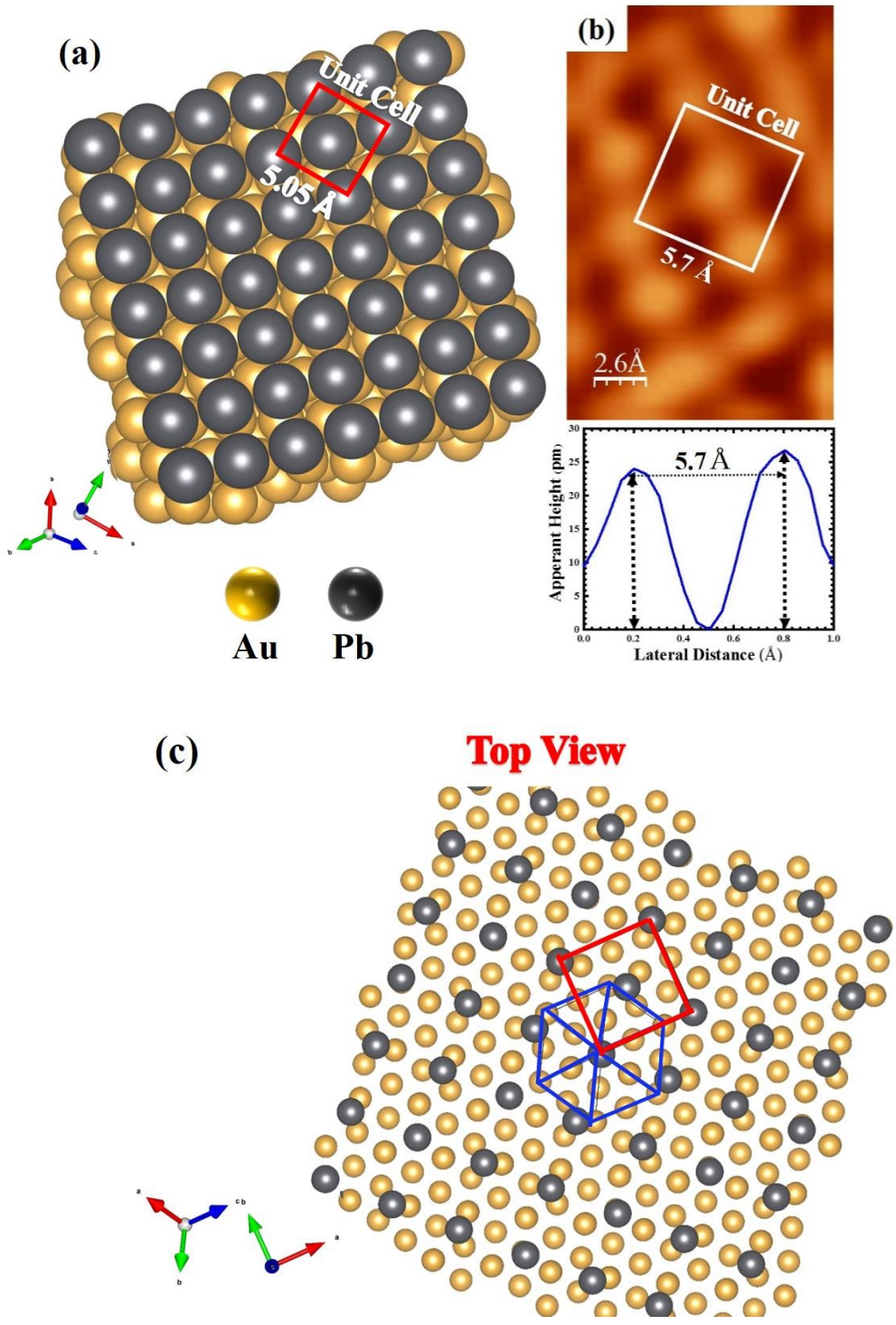

Figure 5.8. Comparison of LT-STM and VESTA Pb model. (a) VESTA visualized Pb (111) on Au (111) surface and bond length for the Pb-Pb dimer. (b) High-resolution STM image showing a Pb-Pb dimer unit cell with the line profile of 5 Å (Scan area = 20 × 13 $Å^2$; Sample bias voltage = 3.90 V, Tunneling current = 500 pA). (c) VESTA simulated top view with a unit cell of Pb (Marked as a red square) and Au unit cell (Marked as blue hexagonal).

5.3.1 Protocol optimization by reducing deposition time and temperature for achieving sub-ML or 1 ML of Pb on Au (111)

In Section 5.3, the atomic structure of Pb in multilayer coverage deposited on Au (111) was characterized by STM. Sub-ML coverage of Pb on Au (111) is also important to be characterized by STM to understand the interface properties between Pb and Au (111). Furthermore, Pb deposition protocol aiming sub-ML coverage on $MAPbI_3$ needs to be developed to be able to probe the interaction of Pb with $MAPbI_3$ by STM. Pb deposited Au (111) from prior sample preparation trials were cleaned by the cycles of sputtering and annealing protocol (Chapter 3 section 3.2) until the Pb 4*f* signals monitored by XPS were below the detection limit of the instrument. For achieving sub-ML or a maximum of 1 ML of Pb deposition, only one parameter of the deposition time in the protocol was varied while the thermalization temperature of 327 ºC was kept constant (i.e., same temperature used in the 4 min deposition). The Pb deposition time was sequentially reduced from 4 min to 2 min, 30 s, 15 s, and 5 s at 327 ºC (Figure 5.9). For each of Pb deposition times, the sample was transferred to the STM at 77 K for scanning at constant current mode. All the deposition times above resulted in fully covered Pb surface on Au (111) with the same height profile of ~1.8 Å corresponding to the ML of Pb as shown in Figure 5.9 (b,d,f,h) and with the similar Pb-Pb dimer structures.

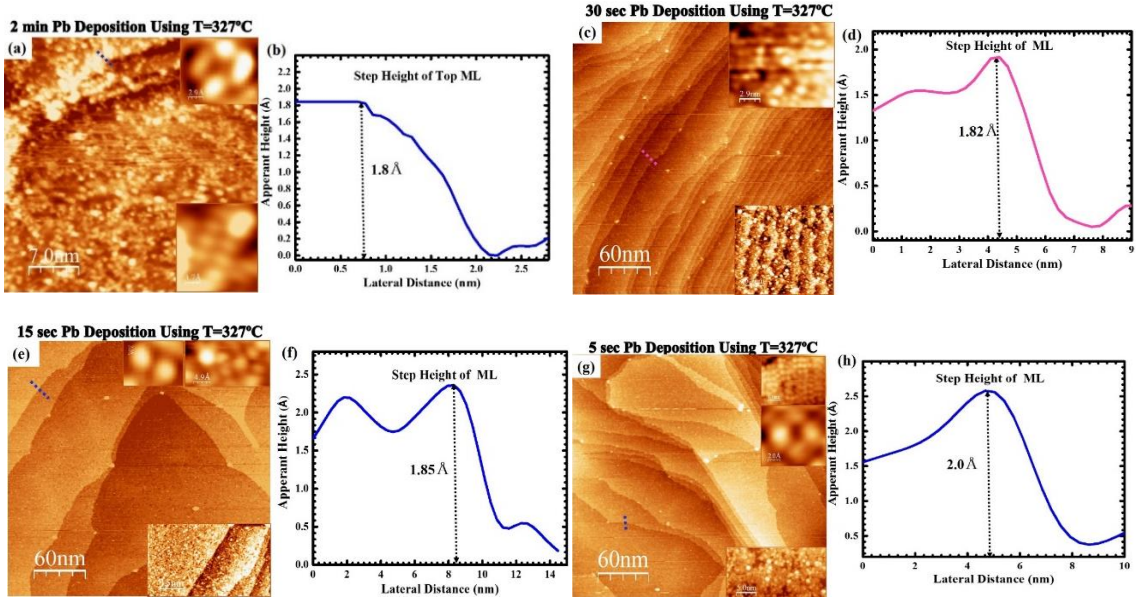

Figure 5.9: LT-STM images of Pb depositions for different times. (a) LT-STM images of fully covered 2 min deposited Pb ML on Au (111) (Scan area = 35 × 35 nm^2; Sample bias voltage = 3.30 V, Tunneling current = 500 pA). (b) Step height profile of Pb ML = 1.8 Å. (c) LT-STM images of fully covered 30 sec deposited Pb MLs on Au (111) (Scan area = 300 × 300 nm^2; Sample bias voltage = 3.50 V, Tunneling current = 500 pA). (d) Step height profile of Pb ML = 1.82 Å. (e) LT-STM images of fully covered 15 s deposited Pb MLs on Au (111) (Scan area = 300 × 300 nm^2; Sample bias voltage = 4 V, Tunneling current = 500 pA). (f) Step height profile of Pb ML = 1.85 Å. (g) LT-STM images of fully covered 5 s deposited Pb MLs on Au (111) (Scan area = 300 × 300 nm^2; Sample bias voltage = 4 V, Tunneling current = 500 pA). (h) Step height profile of Pb ML = 2.0 Å. Insets in (a,c,e,g): zoom in of the crystal structure of Pb-Pb dimers.

The four different deposition times above were not able to generate the aimed sub-ML or 1 ML deposited Pb layer on Au(111). Therefore, the temperature was decreased from 327 °C to 219 °C to decrease the flux rate of Pb. Pb deposition for 10 s did not fully cover the Au (111), i.e., with the optimized parameters of lower temperature and shorter time, a partially covered Au (111) surface by Pb was achieved (Figure 5.10a-d). With this low deposition temperature, the Au terraces with less concentration of Pb and with a similar height profile of ~2.0 Å corresponding to 1 ML height of Pb was obtained. Our obtained images (Figure 5.10a-d) show three different domains on a 7 mm diameter Au (111) substrate. In one domain, the Au (111) step edges are covered with the series of Pb-Pb dimers (Figure 5.10b) and few dimers have adhered on the Au terraces. In another domain (Figure 5.10c), the terrace was covered by an ordered ML of Pb-Pb dimers, which showed the atomic structure of Pb on Au (111) and it was in good

agreement with the visualized atomic models CIF files in VESTA (Figure 5.8a). Furthermore, the ML height profile of ~1.8 – 2.0 Å is similar to the previously prepared Pb deposited MLs. Figure 5.10 (d) shows the partially covered Au terraces with the Pb-Pb dimers in a single row and also the Pb-Pb dimers form (Figure 5.10e-g). One structure of Pb has been observed from the obtained results in all experiments that the Pb also dimerized on Au (111) surface.

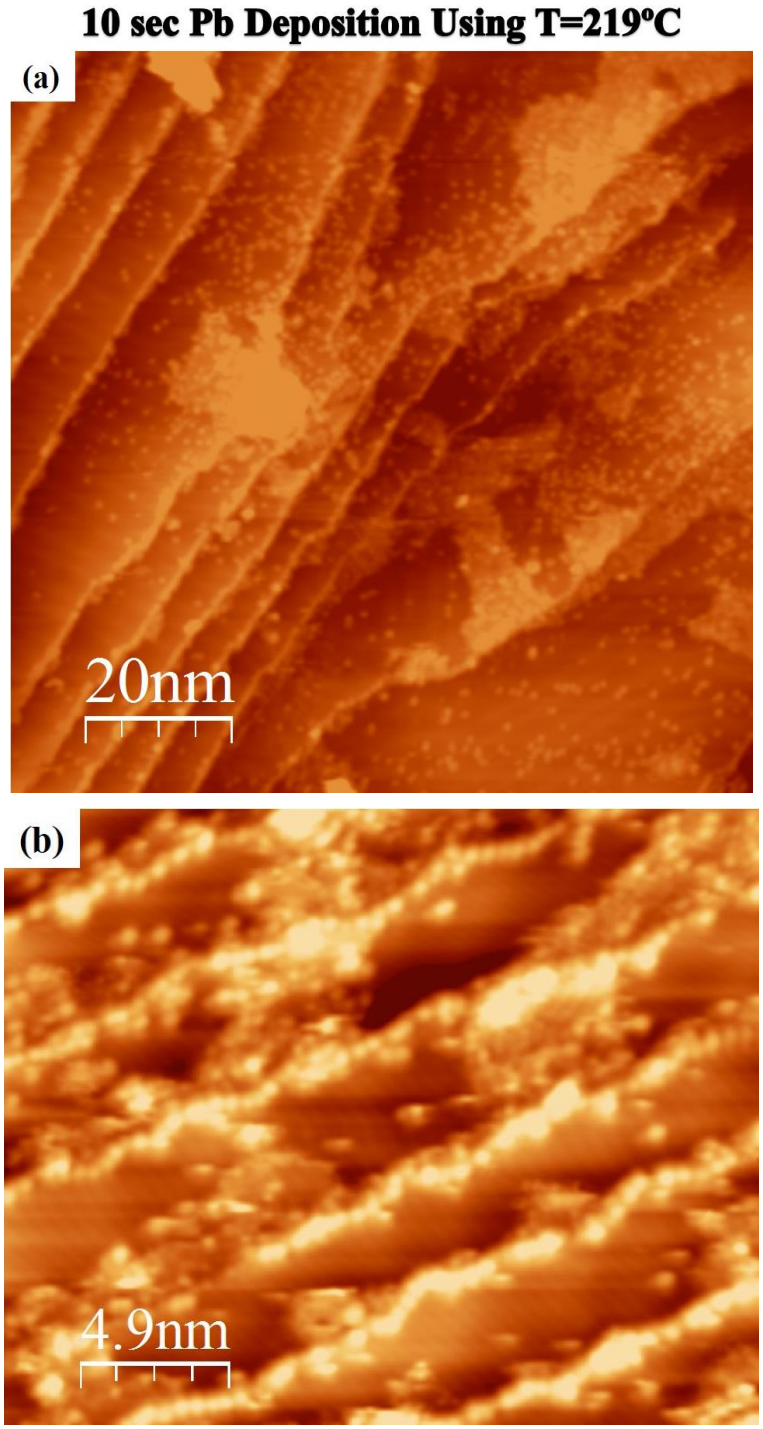

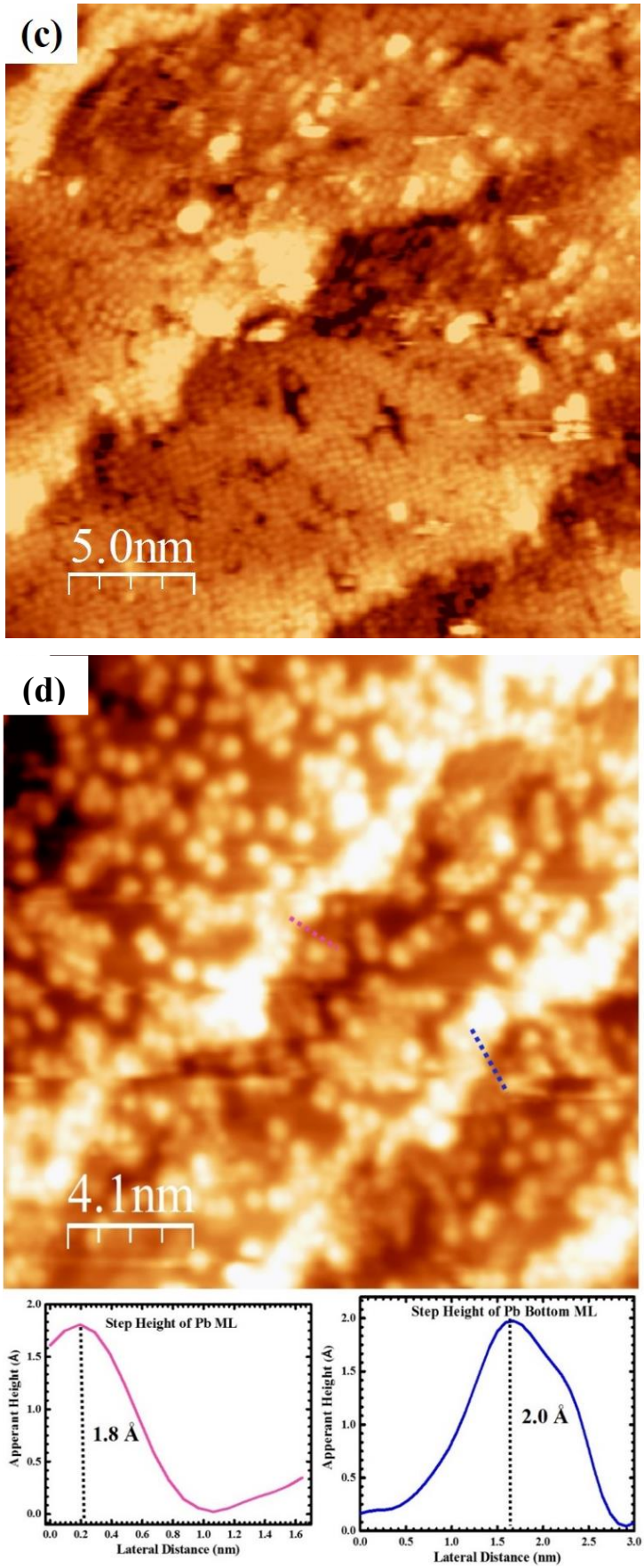
(c)
5.0nm
(d)
4.1nm
Step Height of Pb ML
1.8 Å
Apperant Height (Å)
Lateral Distance (nm)
Step Height of Pb Bottom ML
2.0 Å
Apperant Height (Å)
Lateral Distance (nm)

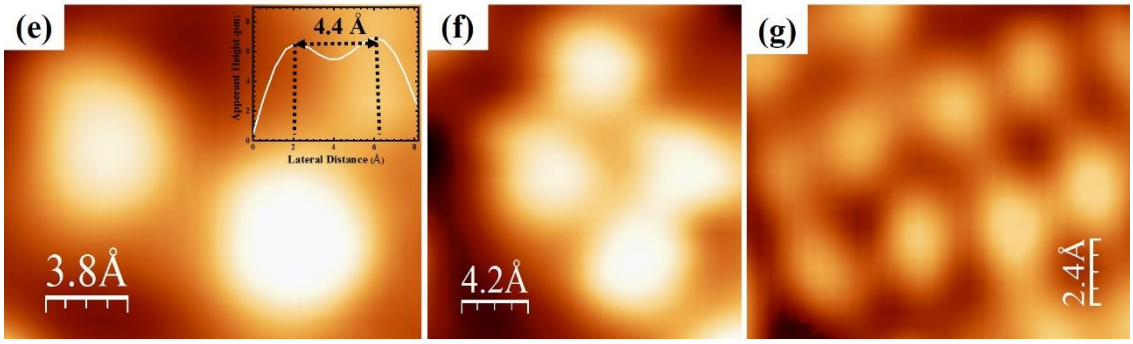

Figure 5.10: LT-STM images of 10 s deposited Pb MLs on Au (111) using 219 ^{0}C temperature. (a) High resolution image of partially covered Pb ML on Au (111) (Scan area = 100 × 100 nm^2; Sample bias voltage = 3.70 V, Tunneling current = 500 pA). (b) High resolution image of partially covered Pb sub-ML on Au (111) (Scan area = 18 × 18 nm^2; Sample bias voltage = 3.80 V, Tunneling current = 500 pA). (c) LT-STM image of 1 ML of Pb on Au (111) (Scan area = 25 × 25 nm^2; Sample bias voltage = 3.90 V, Tunneling current = 500 pA). (d) LT-STM image of partially covered Pb ML on Au (111) (Scan area = 36 × 36 nm^2; Sample bias voltage = 3.70 V, Tunneling current = 500 pA). Step height profiles of Pb MLs are shown in pink and blue dashed curves in (d). (e-f) Zoom in of the crystal structure of Pb-Pb dimers in different orientation.

Pb Deposition	Deposition Time	Deposition Temperature	Comments
1st Trial	4 min	327 °C	We observed Pb-Pb dimers structure and all Au (111) terraces were completely covered with Pb MLs.
2nd Trail	2 min	327 °C	We observed Pb-Pb dimers convoluted structure even after reducing the time of deposition from 4 min to 2 min.
3rd Trail	30 sec	327 °C	We observed Pb-Pb dimers convoluted structures even after reducing the time of deposition from 2 min to 30 sec.
4th Trail	15 sec	327 °C	We observed a similar structure for 15 sec as was observed for previous long depositions duration.
5th Trail	5 sec	327 °C	We observed a similar structure even for 5 sec as was observed for previous depositions times.
6th Trail	10 sec	219 °C	By reducing the evaporation temperature from 327 °C to 219 °C to decrease the flux of lead, we observed partially covered Au (111) terraces and ordered structure of Pb-Pb dimers.

Table 1: Describes the six trials of Pb deposition by varying the deposition duration and temperature.

In conclusion, Table 1 shows the summary of all deposition conditions and their effect on the concentration of Pb deposition. By using this optimized protocol, the Pb will be deposited on $MAPbI_3$ surface in future experiments and will attempt to ratify the hypothesis (Section 5.1) about Pb presence in PVSK at the atomic scale by using LT-STM and also the $PbCl_2$ atomic structure on Au (111) substrate in the next section.

5.4 $PbCl_2$ deposited Au (111)

As described by LT-STM images of $PbCl_2$ in Chapter 4, Section 4.2, no discussion or evidence has been provided about what ions were observed by STM, i.e., Pb^{2+} or Cl^-? It was crucial to first elucidate the adsorption of $PbCl_2$ on Au (111) at the atomic scale. Although from XPS spectra it was confirmed that both Cl^- and Pb^{2+} ions are deposited on Au (111) (See Figure 4.2, Chapter 4). But on the basis of obtained LT-STM high-resolution images of metallic-Pb deposition on Au (111) in Section 5.3, now it can be deduced experimentally what ions were observed for $PbCl_2$ on Au (111).

Figure 5.11a shows the large area of $PbCl_2$ deposited MLs on Au (111) with two different structures, covered step edges, and the formed layout of grains in the center of covered edges. Also, it was found that the ~ 1.7 – 2.0 Å (Figure 5.11b-c) step height corresponds to 2 MLs of $PbCl_2$, which was estimated based on the step heights ~ 0.85 Å of individual ML in Figure 5.12(a-c). LT-STM image (Figure 5.12a, d-e) shows the two distinct dimers arrangements as attributed to Pb-Pb (blue dashed ellipse) dimers and Cl-Cl dimers (red dashed ellipse). For attributing the dimers to Pb-Pb and Cl-Cl dimers, the atomic model of orthorhombic $PbCl_2$ on Au (111) was simulated by using CIF files in VESTA software (Figure 5.12f-g).

Figure 5.12g illustrates the atomic structure of the simulated supercell of $PbCl_2$ and Au (111) interface. According to the atomic model, the distance between $PbCl_2$ layers with respect to Au (111) surface is 5.8 Å. During the atomistic simulation, it was observed that if the distance between the $PbCl_2$ layers decreased less than 5.8 Å, then the $PbCl_2$ will incorporate in Au (111) lattice, which does not comply with our assumption of the surface interaction of $PbCl_2$ with Au (111) because, in the fabrication process, no post-annealing was employed after deposition. With high-temperature post-annealing, PbAu alloying can be formed because at high-temperature $PbCl_2$ decomposes to Pb and Cl. It is observed from the atomic model that Cl ions bind on Au (111) surface while Pb adsorbed on the Cl ions formed layers as shown in the simulated Figure 5.12f-g. On the basis of the line profiles, the LT-STM image also reveals that the bottom ML is formed of Cl-Cl dimers (small dark protrusions) with a bond length of ~ 4.2 Å and on top of the Cl^- dimers (Figure 5.11a, 5.12a) the Pb^{2+} ions passivated in the form of Pb-Pb dimers (bright protrusion) with a bond length of ~ 8.2 Å (Figure 5.12e).

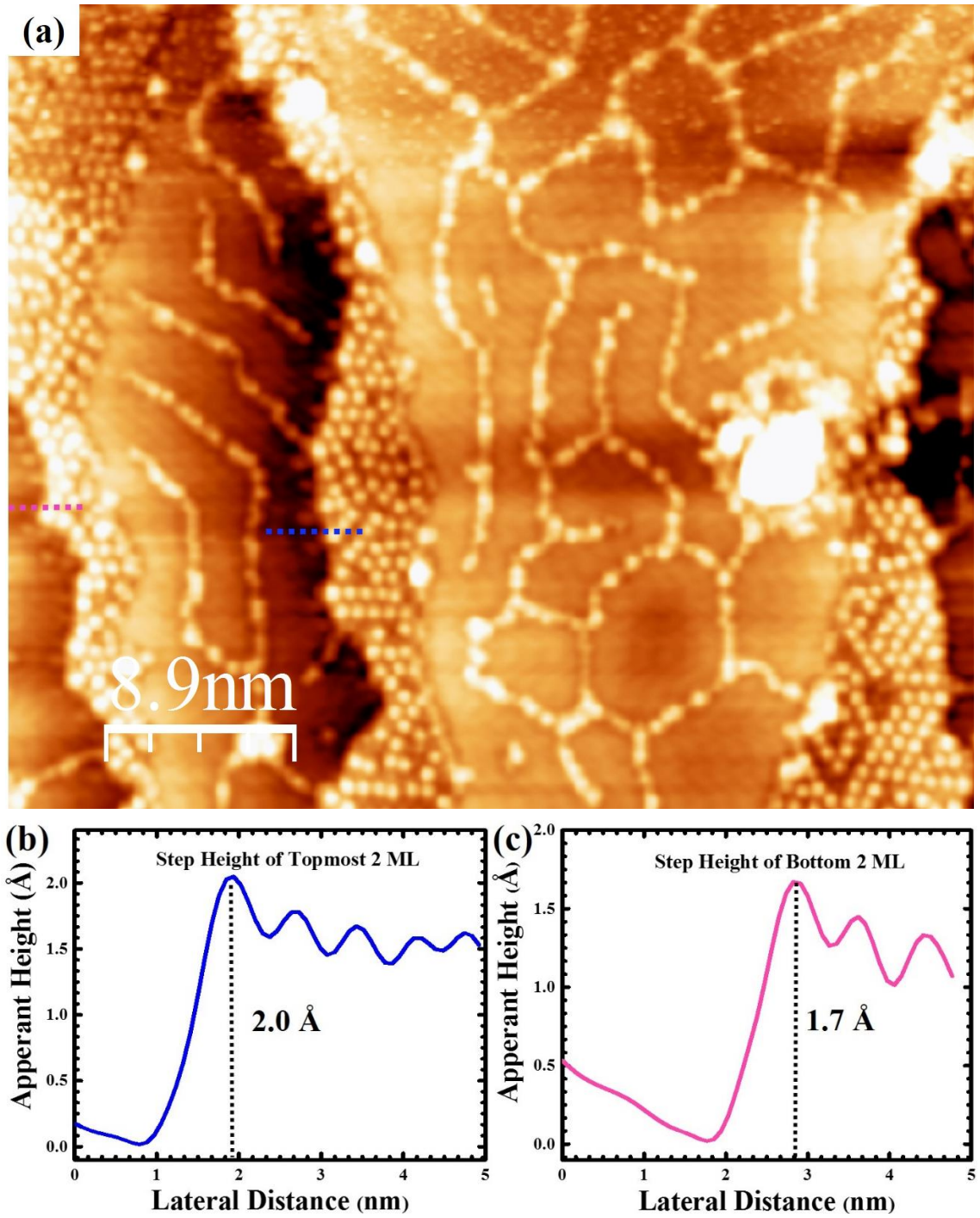

Figure 5.11: (a) LT-STM images of $PbCl_2$ deposited Au (111) (Scan area = 30× 30 nm^2; Sample bias voltage = -2.50 V, Tunneling current = 100 pA) (b-c) Height profiles of two MLs of $PbCl_2$.

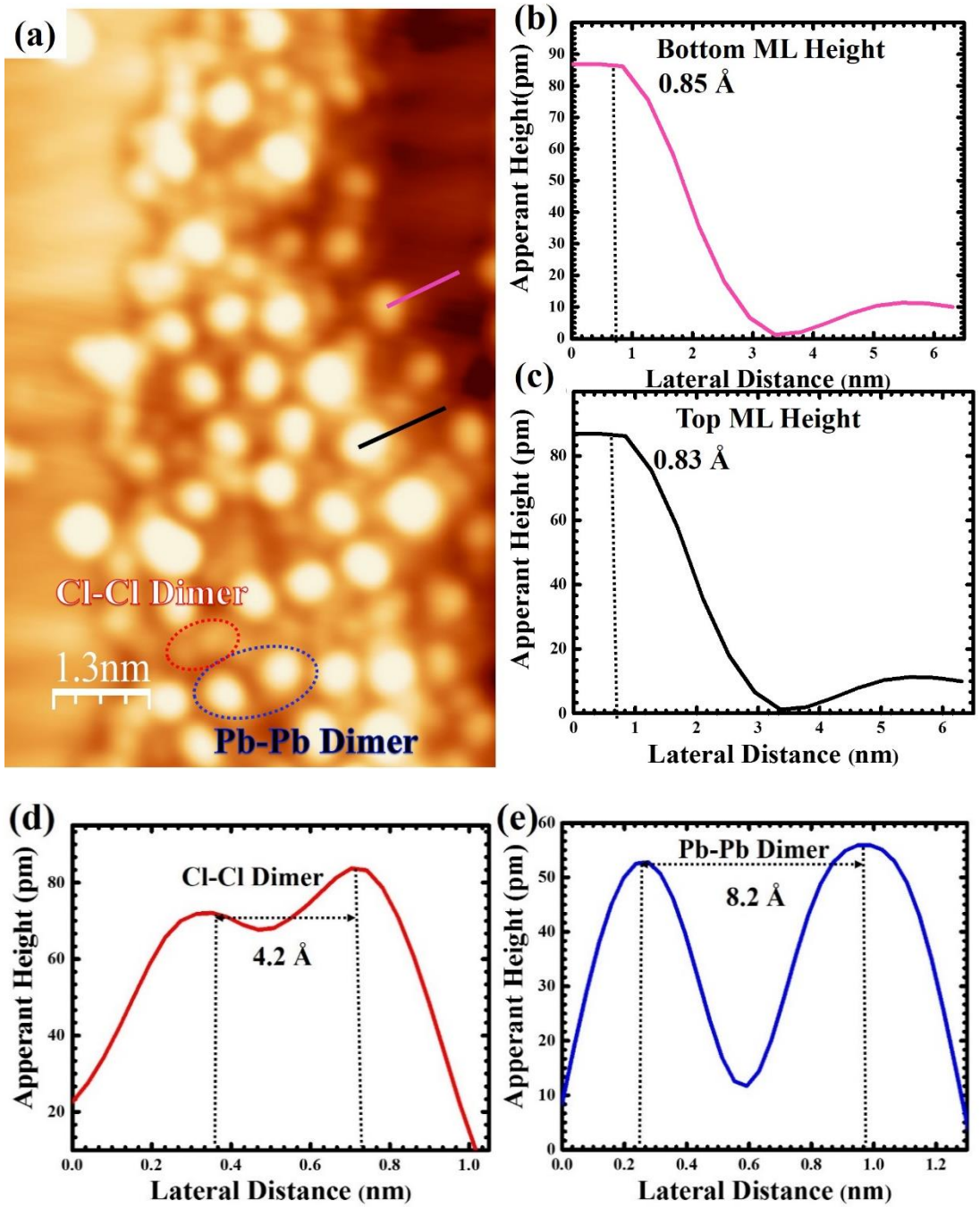
(a)
Cl-Cl Dimer
1.3nm
Pb-Pb Dimer
(b)
Bottom ML Height
0.85 Å
Apperant Height(pm)
Lateral Distance (nm)
(c)
Top ML Height
0.83 Å
Apperant Height (pm)
Lateral Distance (nm)
(d)
Cl-Cl Dimer
4.2 Å
Apperant Height (pm)
Lateral Distance (nm)
(e)
Pb-Pb Dimer
8.2 Å
Apperant Height (pm)
Lateral Distance (nm)

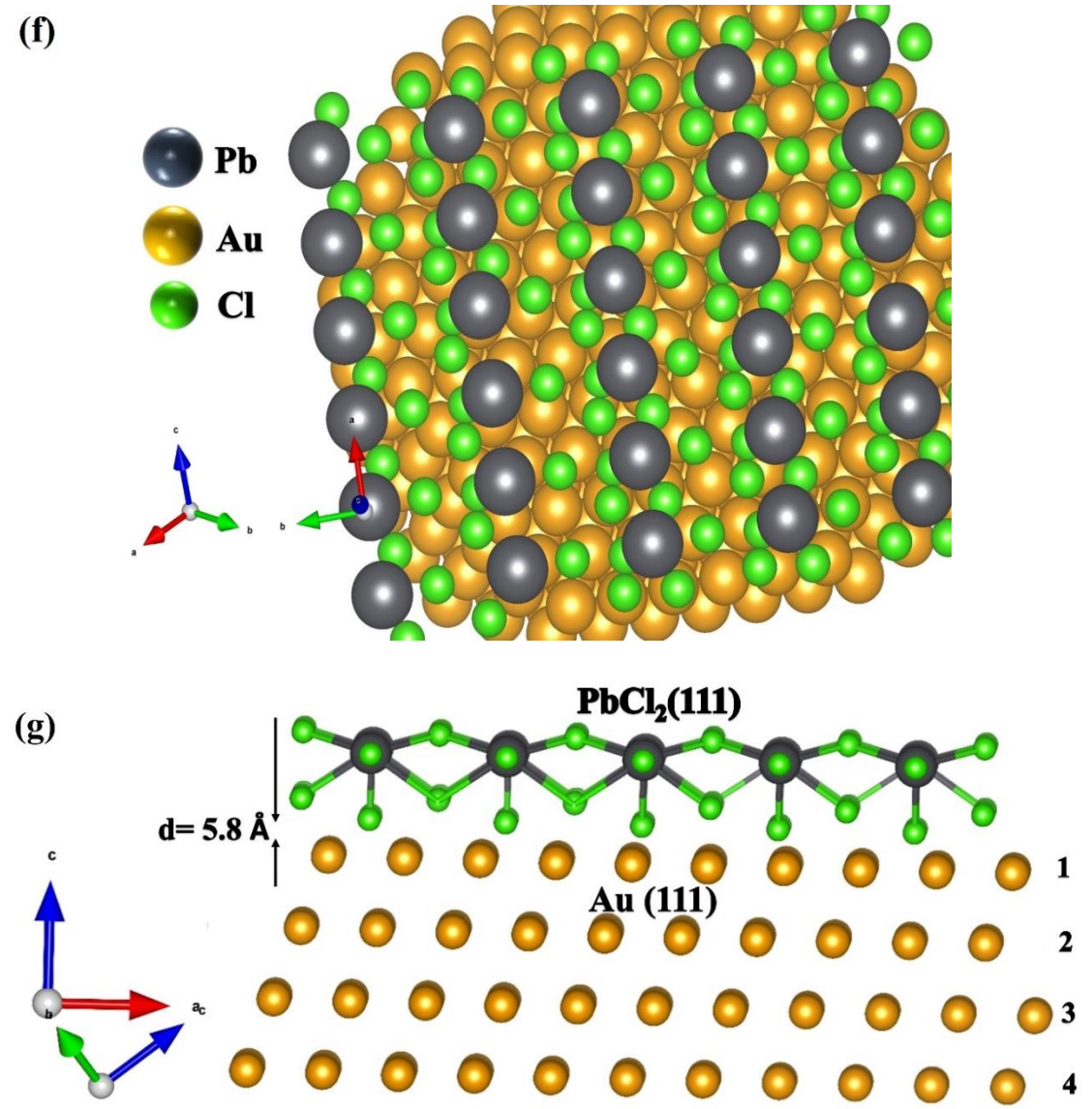

Figure 5.12: Comparison of $PbCl_2$ atomic structure of LT-STM images and VESTA model (a) LT-STM images of 3 min $PbCl_2$ deposited MLs on Au (111) (Scan area = 10.5 × 7 nm^2; Sample bias voltage = -2.50 V, Tunneling current = 100 pA). (b-c) Height profiles of two MLs of $PbCl_2$ (d) Line profile of Cl-Cl dimer= 4.2 Å. (d-e) Line profile of Cl-Cl dimer = 4.2 Å and Pb-Pb dimer = 8.2 Å. (f) Top view of the atomic structure of $PbCl_2$ one ML stacking on Au (111). (g) Side view of the atomic structure of the interface of $PbCl_2$ and Au (111) substrate represented by four atomic layers, where the one Cl^- in the $PbCl_2$ unit cell covers Au (111) atoms in the top layer (fcc) by 5.8 Å gap distance.

Furthermore, two different structures were observed at step edges of Au (111). One was the two parallel rows configurations of bright protrusions in different angles of Pb-Pb dimers (Figure 5.13a-b), which is attributed on basis of only Pb adsorbed ML configuration on Au (111) in Figure 5.10c. And the other was formed of the unit cell of

$PbCl_2$ (Figure 5.13c-f) attributed on the basis of Visualilized atomic models CIF files in VESTA (Figure 5.12f). Both observed configurations provide evidence of intact and the disassociated $PbCl_2$ molecules adsorption on Au (111) surface. These findings confirm our two proposed hypotheses in Section 5.1 that when $PbCl_2$ is thermalized both the intact and the disassociated $PbCl_2$ molecules are sublimated. More statistics would be required for claiming the percentage of intact and dissociated $PbCl_2$ molecules in the thermalized evaporated flux of $PbCl_2$. It should be noted that the hypotheses made in Section 5.1 were studied based on the $PbCl_2$ deposition on Au (111) surface. Nevertheless, we can deduce that both the intact and the dissociated $PbCl_2$ molecules are also deposited on the $MAPbI_3$ surface after the crucible thermalization at 300 °C. These hypotheses could be further confirmed if DFT calculation would be performed for investigating the structure and mechanical interactions of intact and disassociated molecules on Au (111) and $MAPbI_3$ surfaces.

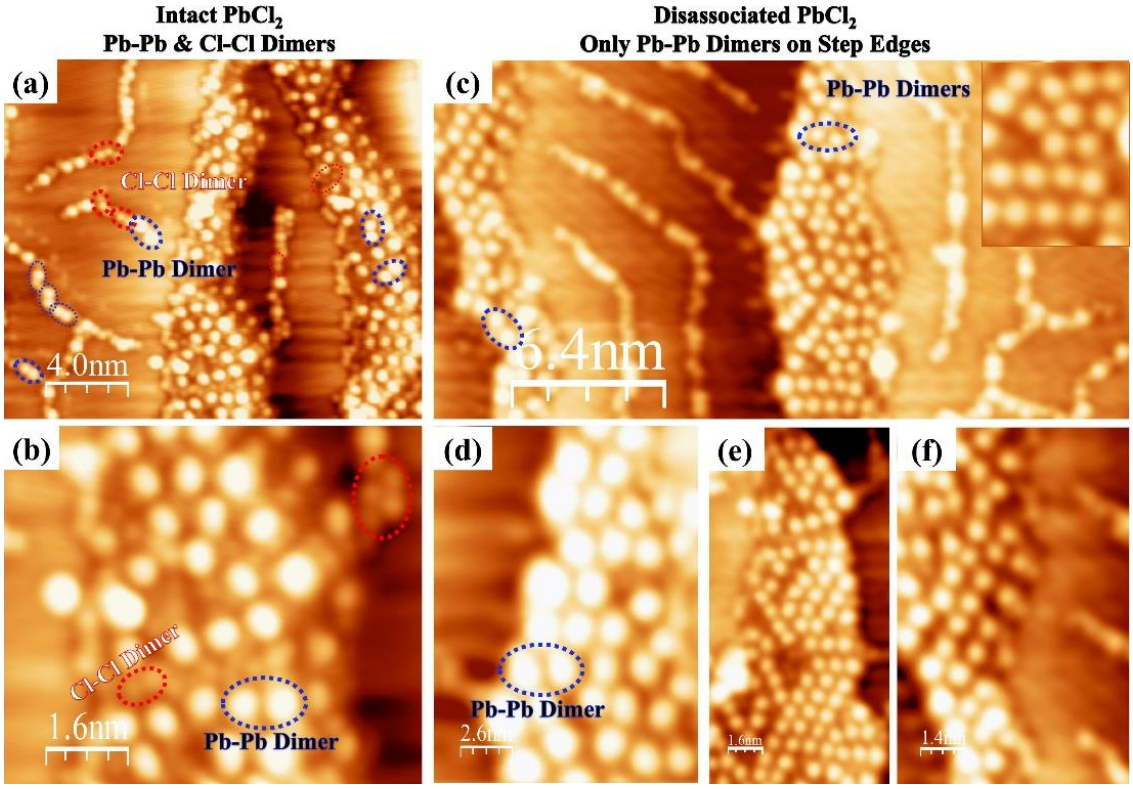

Figure 5.13: Comparison of LT-STM images of $PbCl_2$ and Pb deposited structure on Au (111). (a-b) LT-STM images of intact $PbCl_2$ structure on Au (111). (c-f) LT-STM images of disassociated $PbCl_2$ structure on Au (111).

Figure 5.14a shows the further obtained structural information of a unit cell of $PbCl_2$ covered Au (111), which contains Cl-Cl dimer 1 at around ~ 85° angle from Cl-Cl

dimer 2 and one Cl^- ion shared with another unit cell Cl^- to form a Cl-Cl dimer 1. The Pb-Pb dimer is shared by two unit cells and form a series of Pb-Pb dimers with bright protrusions on the surface of Cl-Cl dimers. The observed STM unit cell of $PbCl_2$ is in good agreement with the VESTA simulated unit cell by comparing the Cl-Cl dimer bond length 3.6 Å and 7.3 Å bond length of Pb-Pb dimer (Figure 5.14b-c,d-f). It is also observed (Figure 5.14d) from the line profile of Cl-Cl dimers that the height of one Cl is lower than that of the other Cl in a dimer 1, which is also similar to the simulated dimer height.

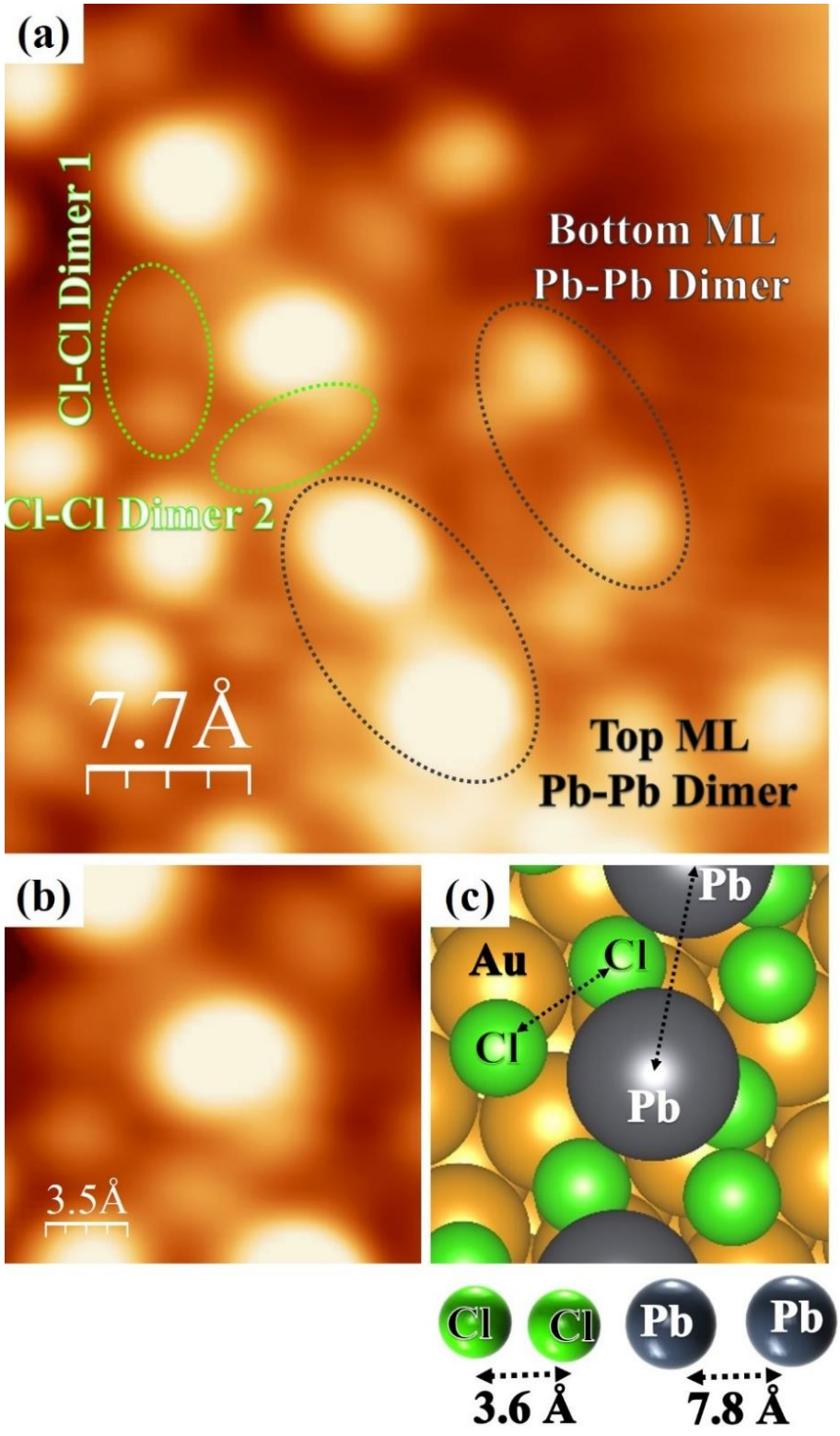
(a)
Cl-Cl Dimer 1
Cl-Cl Dimer 2
Bottom ML
Pb-Pb Dimer
7.7Å
Top ML
Pb-Pb Dimer
(b)
3.5Å
(c)
Pb
Au
Cl
Cl
Pb
Cl
Cl
Pb
Pb
3.6 Å
7.8 Å

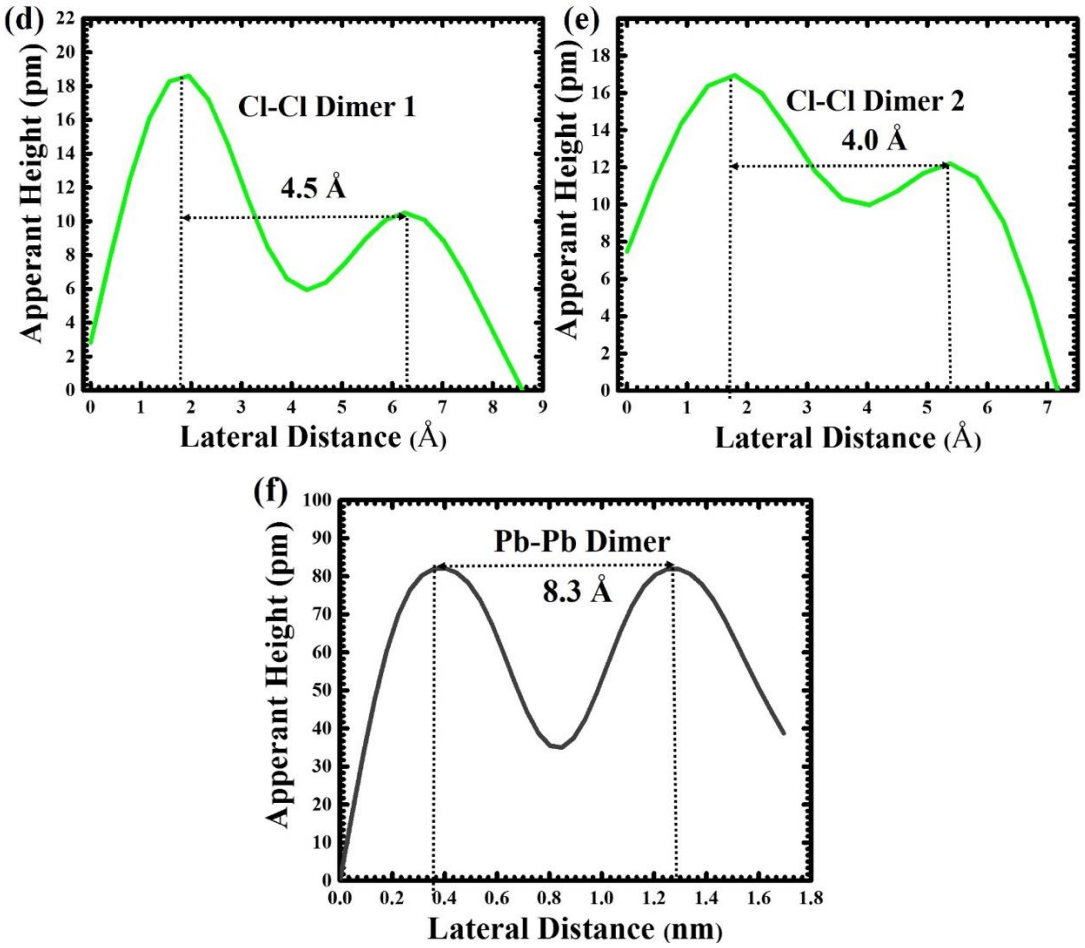

Figure 5.14: Line profiles of Pb-Pb and Cl-Cl dimers. (a) LT-STM images comparison of $PbCl_2$ deposited on Au (111), Pb-Pb dimer (black dashed ellipse) and Cl-Cl dimers (green dashed ellipse)(Scan area = 10× 10 $Å^2$; Sample bias voltage = -2.50 V, Tunneling current = 100 pA). (b) High resolution STM image of a unit cell of $PbCl_2$ (Scan area = 17 × 17 $Å^2$; Sample bias voltage = -2.50 V, Tunneling current = 100 pA). (c) VESTA simulated unit cell of $PbCl_2$ on Au (111). (d-e) Line profile of Cl-Cl dimer = 4.5 Å. (f) Line profile of Pb-Pb dimer = 8.3 Å.

5.4.1 Filled, unfilled grains and grain boundaries

Another interesting structure has been observed (Figure 5.15a-e) in the formed grains. Some grains are filled with pairs of ions (black dashed rectangle) and some grains are empty (blue dashed rectangle). The first assumption about the filled grains was attributed to C 1s contamination. However, the XPS survey (Figure 5.15) showed no C 1s peak and only Pb and Cl peaks were observed (Table 2. Pb: Cl =1: 2.8). The pairs of ions observed in the filled grains (Figure 5.15b-c) are attributed to Cl-Cl dimers because the line profile of 4 Å matches well to the line profiles of Cl-Cl dimers in Figure 5.14(b-d). Thus, it can be assumed that the disassociated Cl from the $PbCl_2$ molecules filled the

grains because no Pb-Pb dimers are observed inside the grains. This interesting observation of Cl disassociation verifies another hypothesis proposed in Section 5.1 about the disassociation of molecules. Furthermore, it is observed from Figure 5.15(d-e) that disassociated Cl does not adhere to the surface of every grain-network space because, in the empty grain-networks, herringbone reconstruction of Au (111) is observed.

In addition, Figure 5.17(a-b) illustrates the zoom in structures of grain boundaries with an interesting fact that the grain boundaries are formed by the Cl-Cl dimers (red dashed ellipse) and followed up by Pb-Pb dimer (blue dashed ellipse) on top. In addition, only Pb ions were also observed on the grain boundaries (white dashed circle). This assumption has been provided by the matching well line profiles of observed dimers Cl-Cl and Pb-Pb in Figure 5.17(c-d). It can also be proposed that the grain boundaries may be formed by the disassociated or intact molecules of $PbCl_2$ deposited on the substrate.

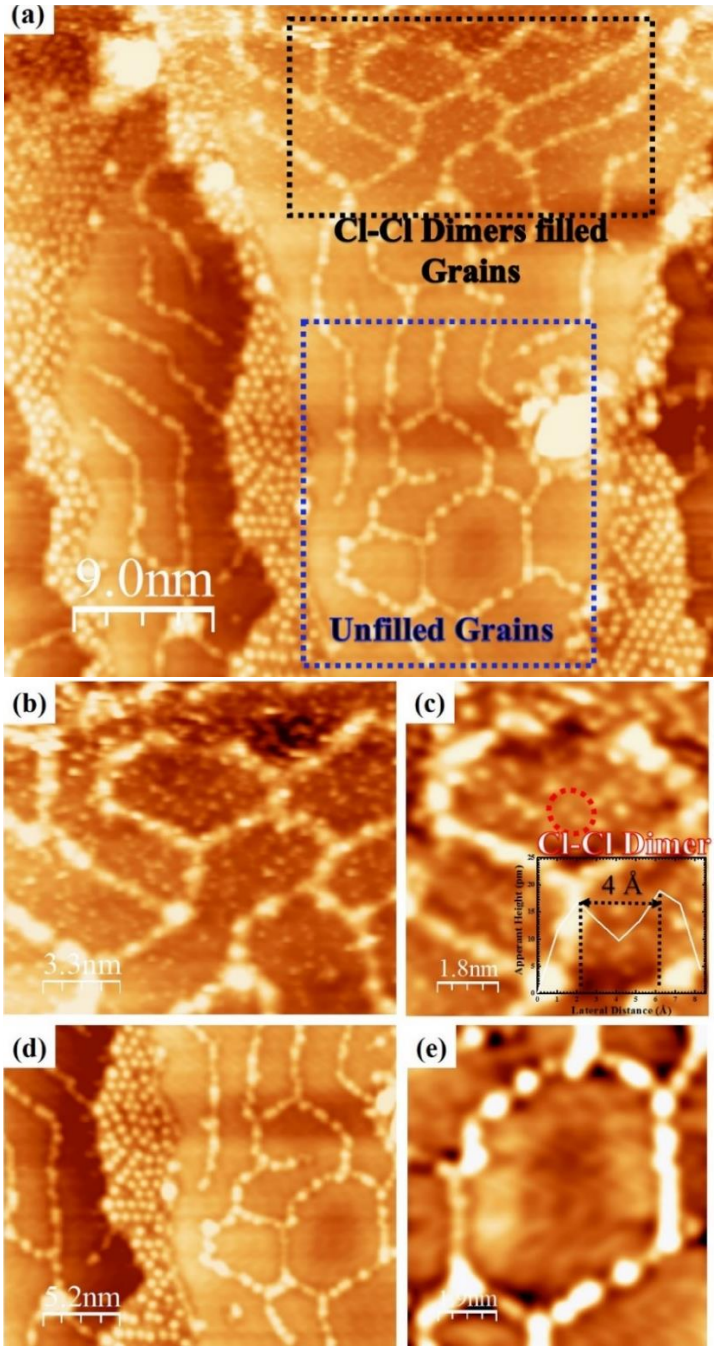

Figure 5.15: Cl-Cl dimers filled and unfilled grains. (a) LT-STM images of $PbCl_2$ deposited Au (111) (Scan area = 30× 30 nm^2; Sample bias voltage = -2.50 V, Tunneling current = 100 pA). (b-c) High resolution STM images of Cl-Cl dimers filled grains (Scan area = 15 × 15 nm^2; Sample bias voltage = -2.50 V, Tunneling current = 100 pA). (d-e) High resolution STM images of unfilled grains (Scan area = 15 × 15 nm^2; Sample bias voltage = -2.50 V, Tunneling current = 100 pA).

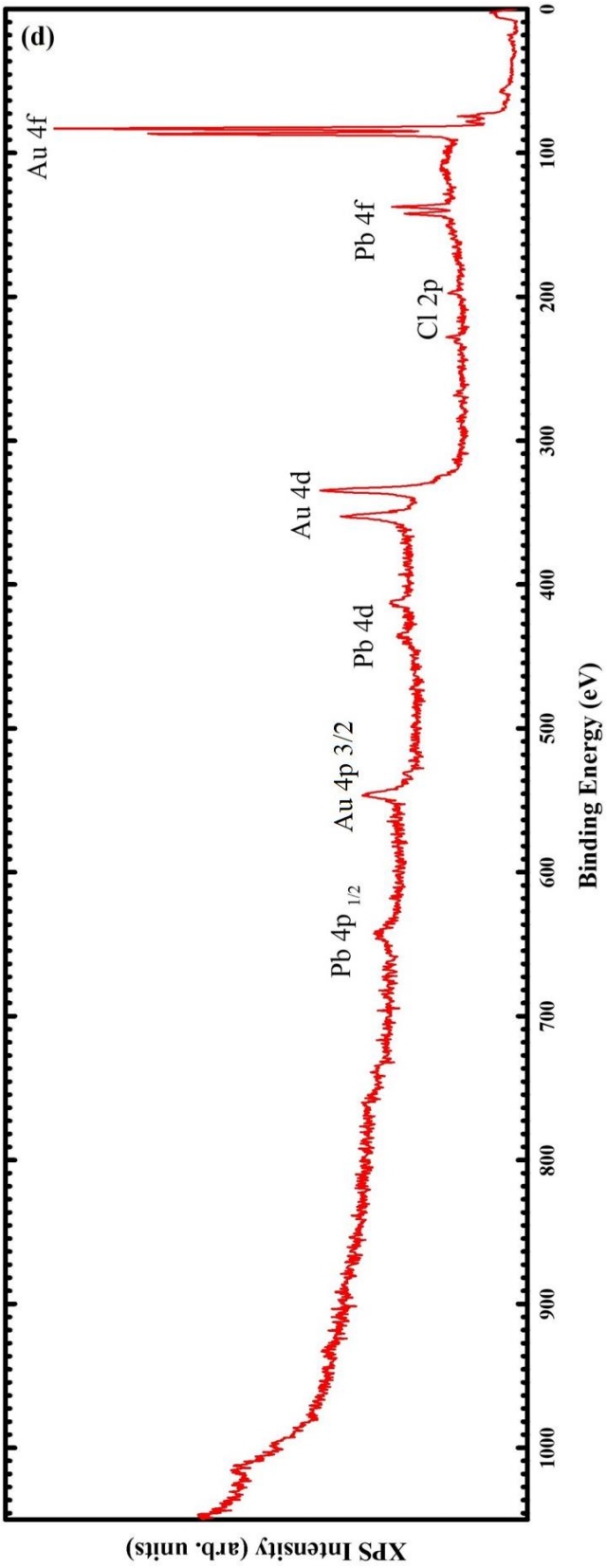

Figure 5.16: XPS measured survey of $PbCl_2$ on Au (111).

$PbCl_2$ Deposition Time	Pb 4f & Cl 2p Ratios
3 minutes	Pb=1, Cl=2.8

Table 2. XPS measured precursor's ratios of $PbCl_2$ on Au (111).

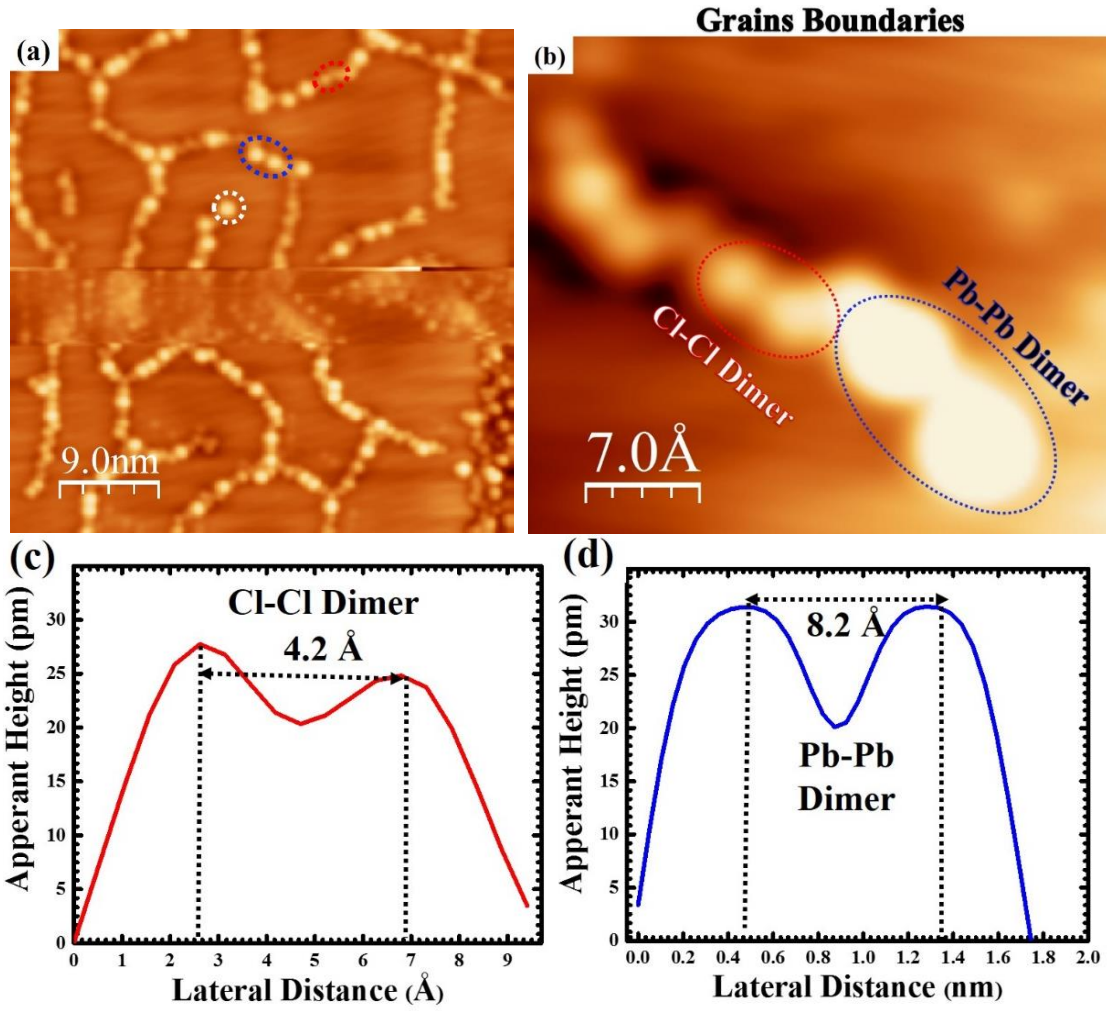

Figure 5.17: $PbCl_2$ grains formation. (a) LT-STM images of grain boundaries formed by Cl-Cl dimers and Pb-Pb dimers on top of Cl-Cl-dimers (Scan area = 20 × 20 nm^2; Sample bias voltage = -2.50 V, Tunneling current = 100 pA). (b) High resolution STM images of a grain boundary, Cl-Cl dimer (red dashed ellipse) and Pb-Pb dimer (blue dashed ellipse) (Scan area = 5 × 5 $Å^2$; Sample bias voltage = -2.50 V, Tunneling current = 100 pA). (c-d) Line profile of Pb-Pb and Cl-Cl dimers.

5.5 Summary

To summarize the whole discussion of the new findings in this chapter, we comprehensively discussed the atomic structures of Pb and $PbCl_2$ deposition on Au (111) for providing the evidence to our proposed four hypotheses (adsorption, disassociation,

diffusion, and intact molecule adsorption) about the presence of Pb in $MAPbI_3$ surface. From the Pb concentration comparison by XPS, the measured ratios of pristine and 6 min $PbCl_2$ deposited $MAPbI_3$, it is observed that Pb concentration (i.e., Pb 4f signal) has been increased after $PbCl_2$ deposition. In addition, the B.E. shift in Pb 4f also provided some insight on the diffusion of Pb into the surface of $MAPbI_3$. To understand the other proposed hypotheses, Pb is required to be deposited on $MAPbI_3$ surface in future experiments. For this purpose, the Pb protocol was optimized first on the Au (111) by thermalizing at 327 ºC and depositing for different times namely 4 min, 2 min, 30 sec, 15 sec and 5 sec. Despite the different deposition times, only fully covered Au (111) terraces were obtained by LT-STM, which was not sufficient for the Pb deposition on $MAPbI_3$ in future experiments. Therefore, to obtain the one ML of Pb, the thermalization temperature was decreased to 219 ºC and the time of deposition was shorten to only 10 s. With this protocol, the partially covered Au (111) surface by Pb ML was obtained and the Pb atomic structure with single Pb-Pb dimer, in two pairs of dimers and the parallel rows of dimers has been obtained by LT-STM images.

More, the $PbCl_2$ deposited on Au (111) atomic structures has been comprehensively discussed by LT-STM topographies. According to the obtained results, Cl-Cl and Pb-Pb dimers were observed on the Au (111) surface and was matching well with the Visualilized atomic models CIF files in VESTA structures. The two types of structures, intact $PbCl_2$ unit cells and only Pb-Pb dimers bright protrusions covered step edges of Au (111) were found. Based only on Pb deposited atomic structures observed on Au (111), it was deduced that the bright protrusion rows of Pb-Pb dimers are the cause of the disassociated $PbCl_2$ molecules.

Furthermore, the disassociated and intact $PbCl_2$ were observed and provided the experimental evidence to our proposed hypotheses that during thermalization or adhesion on the surface of $MAPbI_3$, some $PbCl_2$ disassociate and some adhere in the intact molecule on Au (111) surface. By Cl-Cl dimers filled grains, it was observed that not only disassociated Pb adhere on the surface but also the disassociated Cl forms the Cl-Cl dimer in the filled grains. In addition, it was found that not all grains were filled by disassociated Cl-Cl dimers because the herringbone structure of Au (111) was observed in the other unfilled grains.

Another interesting finding was observed that the Cl-Cl dimers formed the grain boundaries and the Pb-Pb dimers were passivated on the top of Cl-Cl dimers. More, some single Pb ions were observed too on the grain boundaries. But by comparison to the only Pb ML on Au (111) that no grain boundaries were observed. Therefore, it can be comprehended that the grain boundaries are formed because of halides as shown also for

only iodine networks on Au (111) in Chapter 3. Based of all these interesting findings, Pb will be deposited in the future on $MAPbI_3$ surface to investigate the interaction of Pb in PVSK and to understand Pb's role in the $MAPbI_3$ after depositing the additives.

Chapter 6: Investigation of Potassium Iodide Atomic Structures on Au (111) and Deposition on $MAPbI_3$

6.1 Introduction

Alkali metal halides were proposed as additives to improve the performance of PSCs. Potassium iodide (KI) was the first choice in our studies because among various alkali metal cations, K [81,133] has been demonstrated to effectively improve the perovskite solar cell performance. These improvements in PCEs are associated with grain boundaries (GBs) in PVSK films, i.e., increased grain sizes (from 140 nm to 220 nm) lead to a lower density of electronic trap states [81]. Accumulation of K^+ was observed in the grain boundaries and a long carrier lifetime was also confirmed for the K deposited PSCs resulting in increased performance from 15.56% to 18.16% after the monovalent alkali cation mixing. Moreover, it was confirmed that the positive effect on $MAPbI_3$ is due to the K additive. Due to the small ionic radius, K^+ can be incorporated into the crystal structure. Therefore, K^+ cations help increase the stability by preventing the undesirable phase transition of PVSK [81]. Stranks and co-workers have also confirmed the positive effect of K additive in mixed cations (Cs, FA, MA) PSCs [124]. The K additive increased the PCE to 17.9% due to the bandgap tuning to 1.78 eV and also led to the long-term stability over one-month [124]. In addition, K mixed PVSK can lead to larger bandgap values, which can be useful for tandem solar cells. It appears that additives can maximize the charge transport and passivate surface traps in devices, but the fundamental origin at the atomic scale of these effects has not been studied yet. The better understanding of the effects of the K additives on PVSK can aid the precise control of the film property for the next generation of highly stable solar cells. To understand the KI doping in PSCs, the atomic structure of KI needs to be understood first, which has not been investigated yet.

In this chapter, we demonstrate the atomic structure of the cubic KI structure (space group Fm-3m) on Au (111). The KI ultra-thin film deposited on Au (111) was studied in the UHV system by LT-STM. Furthermore, the KI protocol optimization was demonstrated and then deposited on $MAPbI_3$. Only XPS measurements are performed for

the KI deposition on $MAPbI_3$ because the LT-STM scanning will be performed in future experiments.

6.2 KI Protocol Optimization

The protocol of KI sublimation in UHV was required to be optimized because currently no vacuum evaporation fabrication protocol is available in the literature. The boiling point of KI is 1330 ^{0}C [200] and based on this temperature, the KI filled crucible was heated up in Knudsen cell (K-cell) at a chamber pressure of $3.4x10^{-10}$ Torr. The maximum operating temperature with the available K-cell is 600 ^{o}C in our UHV system. In these experiments, the K-cell temperature was limited to 400 ^{o}C. KI was deposited on clean Au (111) for 3 min at a chamber pressure of $1.5x10^{-9}$ Torr (Figure 6.1). Au (111) was cleaned by sputtering and annealing cycles by using the cleaning protocol described in Chapter 3, Section 3.2.2. In addition, the calculated atomic model of a cubic KI unit cell value of 5.05 Å is illustrated in Figure 6.2(a-b). Figure 6.2c shows that the K^+ is ionically bonded in the cage of I^- ions. Furthermore, one K^+ bonds to six I^- atoms to form a corner-sharing KI octahedra as shown in Figure 6.2(c). The tilt angles for corner-sharing octahedral is 0° [200].

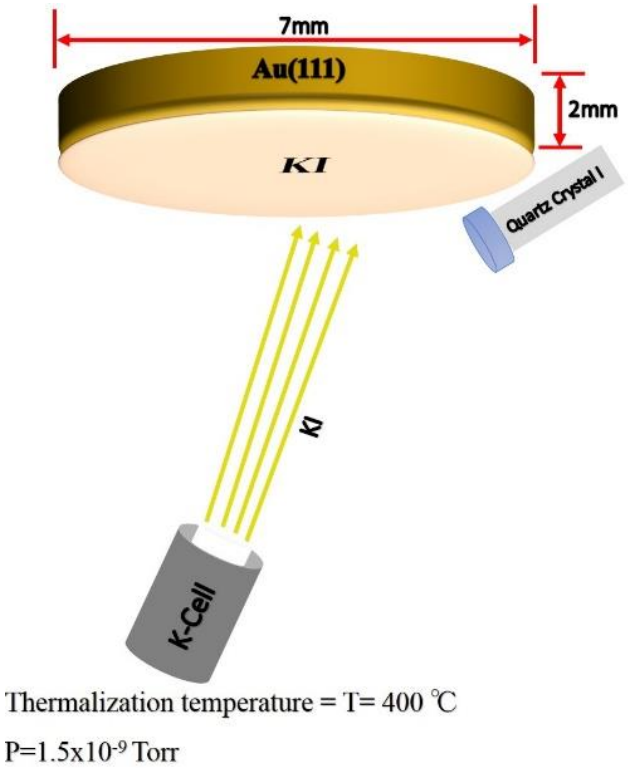

Figure 6.1: KI deposition demonstration of on a clean Au (111) substrate in a UHV chamber.

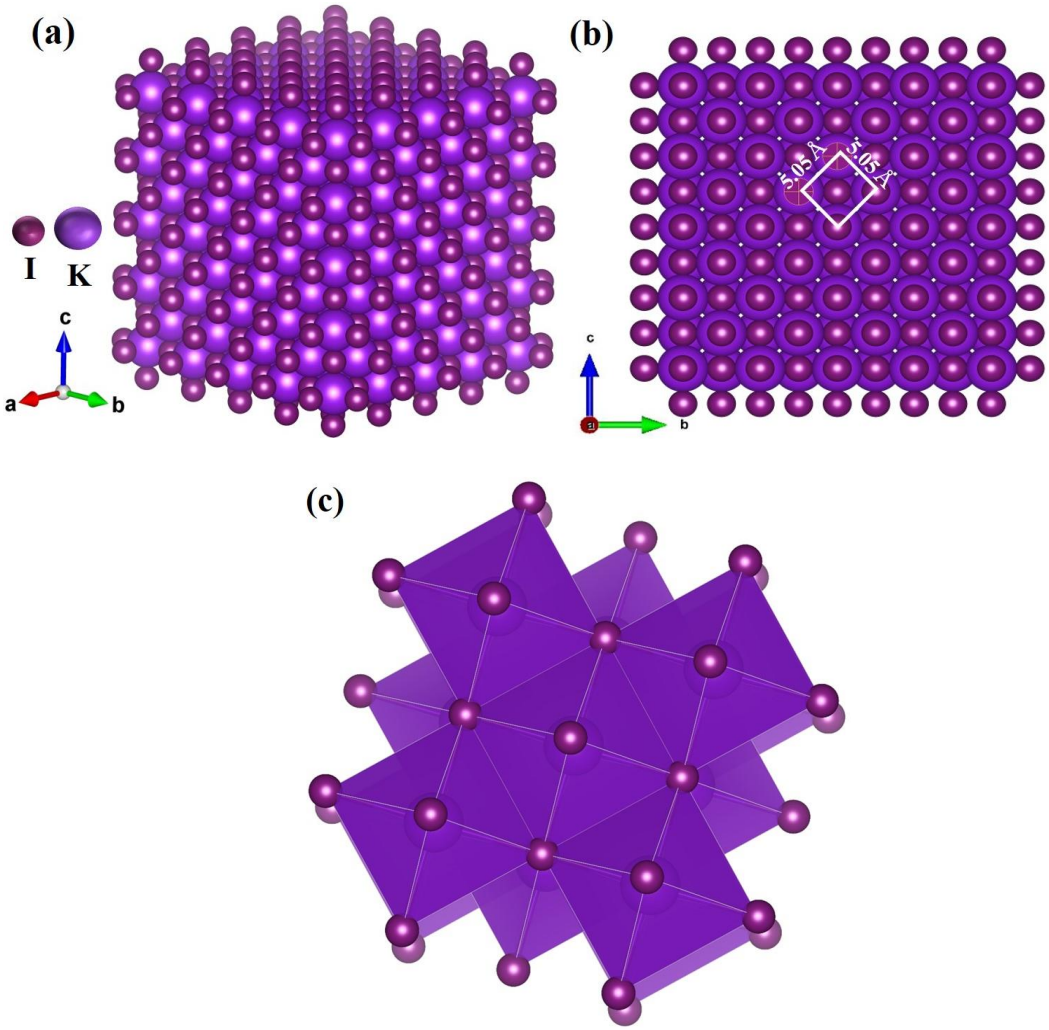

Figure 6.2: Visualized atomic models CIF files in VESTA. (a) Side view of atomic model of KI. (b) Top view of the atomic model of KI with unit cell [200]. (c) Polyhedral atomic model of KI.

XPS measurements were performed on KI films deposited on Au (111) as shown in Figure 6.3. The K to I ratio is 2.6, which shows that the amount of potassium is larger than iodine. Further experiments and DFT calculations are required to understand the deviation from [K] : [I] = 1. One possibility is that the interface layer with Au (111) and the top surface is constituted by K^+ as depicted in Figure 6.2.

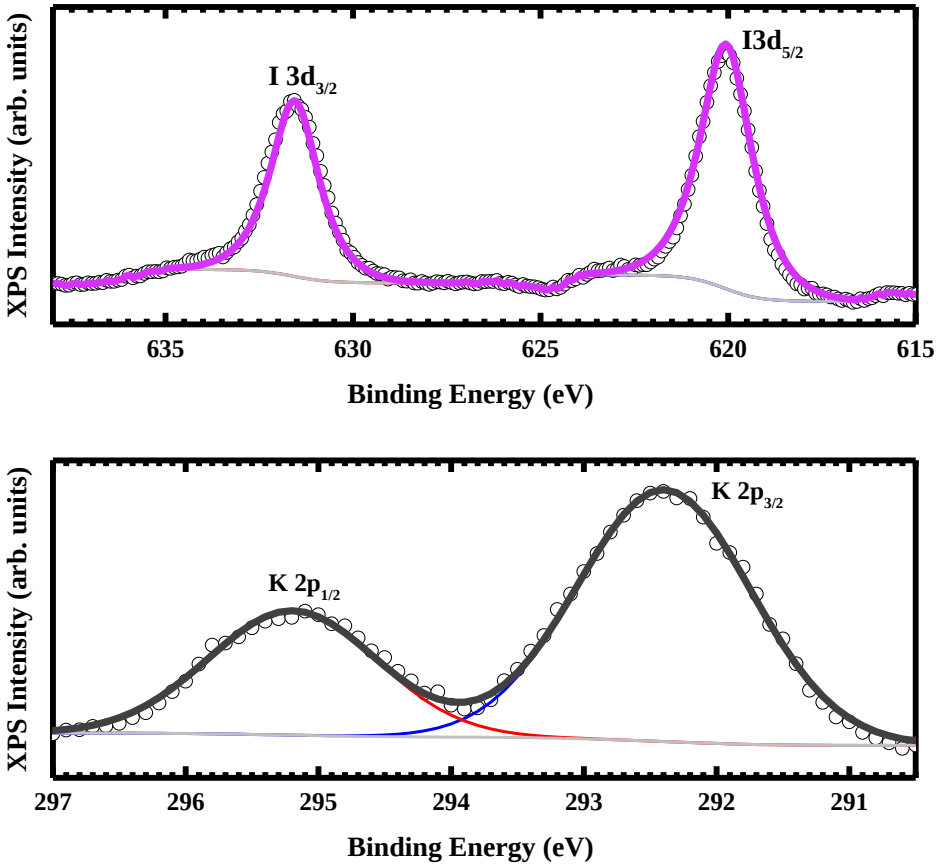

Figure 6.3: XPS spectra of I 3d and K 2p core-level regions showing the chemical information of the KI ultra-thin film on Au (111).

6.3 STM Topographies of the KI Atomic Structure on Au (111)

To obtain the atomic-resolution topographies of KI, the sample was transferred to STM after XPS measurements. The atomic-scale images by STM were acquired at 4.5 K. Solid KI has a cubic structure (Figure 6.2). Based on the STM images (Figure 6.4), ultra-thin films of KI follow a similar trend of the cubic structure on Au (111). However, DFT calculations will be required for a complete structural determination of KI on Au (111). In Figure 6.4(a-b), the step edge is observed indicating an area of the KI film with two distinct MLs. The bottom layer was formed by squared structure (Figure 6.4c) and with many I vacancies (V_I) (inset in Figure 6.4c). While the topmost layer with a step height of 0.5 Å (Figure 6.4b) also shows the square structure but with predominant parallel rows of bright protrusions as adatoms. Furthermore, the topmost layer has a well-defined grain boundary composed of I^- ions as demonstrated in the inset in Figure 6.4a. The line profile of the I-adatoms with bright protrusion in the parallel row (marked by a green solid line) is shown in Figure 6.4d with a 9 Å gap between two I-adatoms, which is much larger than the measured I-I gap (5.9 Å) in the unit cell of KI on Au (111) in Figure

6.4e.

It is challenging to provide the STM interpretation without DFT calculations regarding which ion (K^+ or I^-) corresponds to the observed bright protrusions in the ordered square pattern. However, based on the Visualilized atomic models CIF files in VESTA s (Figure 6.2a-c, inset in Figure 6.4e), the bright protrusions were deduced to correspond to I^- ions instead of K^+ ions. As it can be seen from the polyhedral model of KI (Figure 6.2c), the K^+ ions are covered in a cage of I^- ions. Based on the simulated model, we can deduce that the observed surface by LT-STM is the I^- ions terminated surface of KI on Au (111) substrate.

From the step edge height profile (0.5 Å) in Figure 6.4a, it is confirmed that the observed height corresponds to the KI ML instead of Au (111) step edge height (2.5 Å). Additionally, some bright ion pairs (Figure 6.4f-g) were observed on the square structure surface by excluding the bright protrusions I^- ions rows. By measuring the line profile of the bright pair structure, it was found that they are the adatoms I-I dimer structures, which were compared with the observed I-I dimers in previous LT-STM images (Chapter 4). Furthermore, many I vacancies (marked by a blue dashed ellipse) have been observed in the bottom layer (inset in Figure 6.4c). It can be observed that only one I^- ion is missing from the unit cell of five I^- ions and this one I^- ion vacancy behavior is repeatedly similar in every I^- ion vacant unit cells in the ML of KI. The I^- ion vacancy might be caused by the weak bonding of I^- with K^+ in octrahedra or not the fully grown ML of KI.

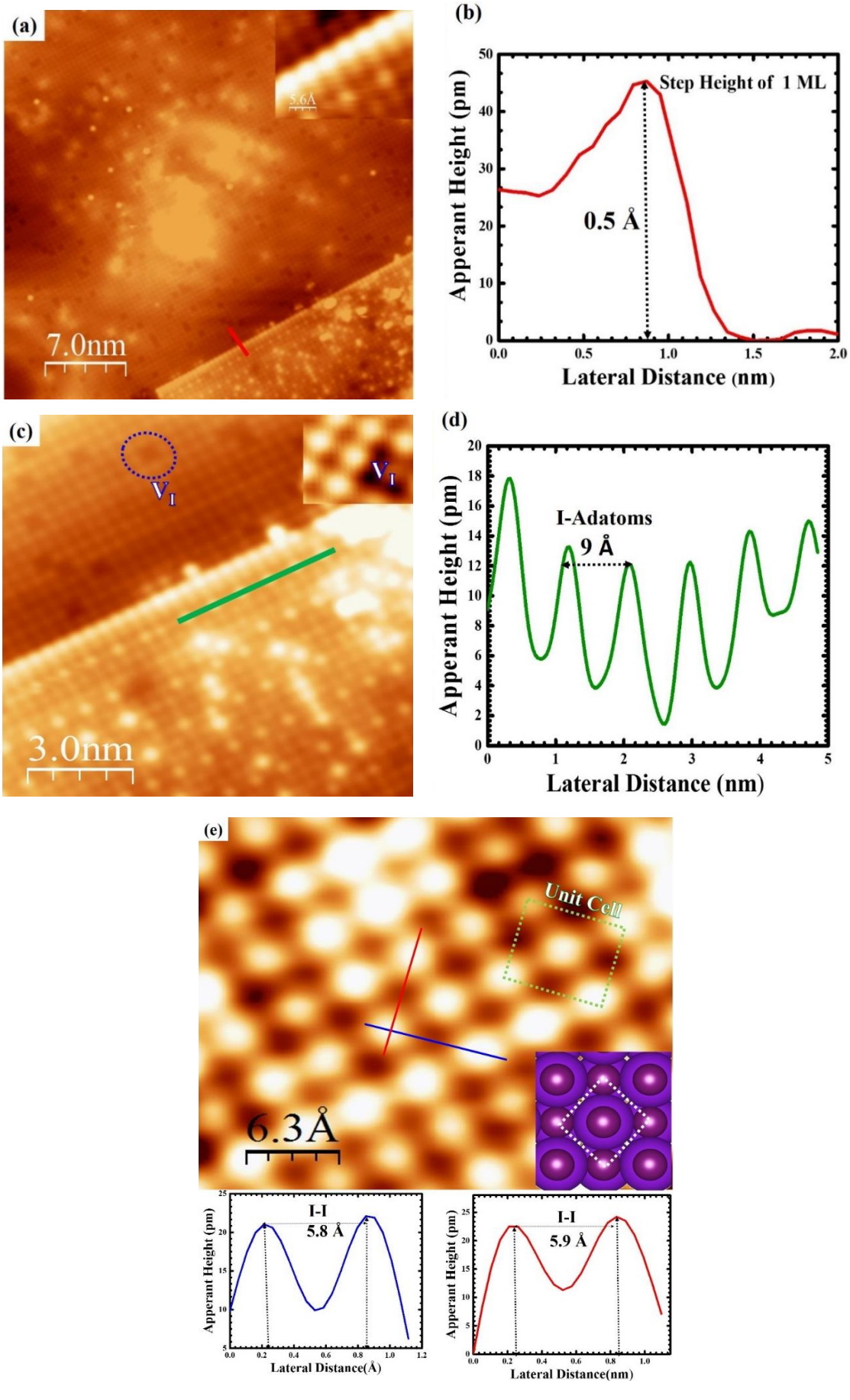
(a)
5.6Å
7.0nm
(b)
Step Height of 1 ML
0.5 Å
Apperant Height (pm)
Lateral Distance (nm)
(c)
V_I
V_I
3.0nm
(d)
I-Adatoms
9 Å
Apperant Height (pm)
Lateral Distance (nm)
(e)
Unit Cell
6.3Å
I-I
5.8 Å
Apperant Height (pm)
Lateral Distance(Å)
I-I
5.9 Å
Apperant Height (pm)
Lateral Distance(nm)

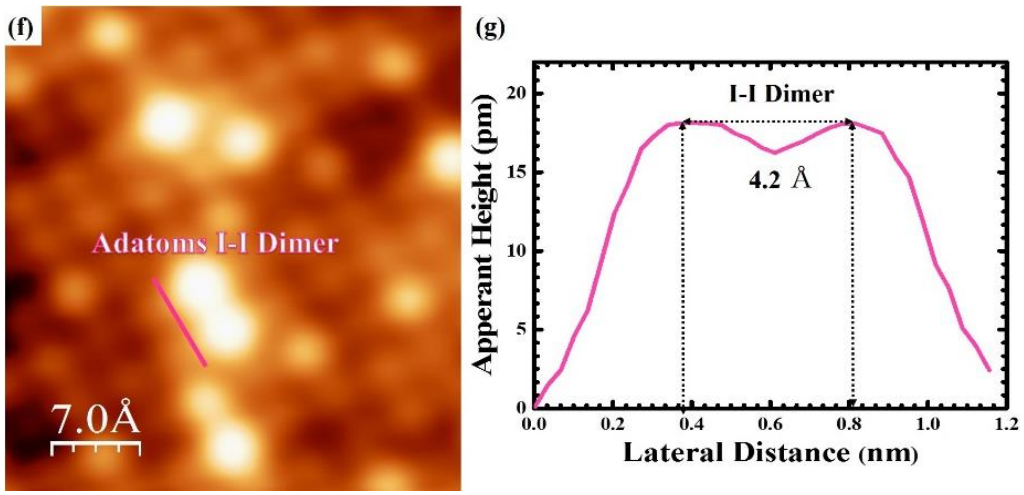

Figure 6.4: LT-STM images of the 3 min deposited cubic KI thin films on Au (111). (a) High-resolution image of the bottom completed KI layer and the topmost uncompleted layer on Au (111). Inset shows the I ions forming a step edge (Scanning area=34.5 × 36 nm^2, Bias voltage = + 4.50 V, Tunneling current = 900 pA). (b) Height profile of the measured uncompleted topmost layer in (a). (c) High-resolution image of the KI film with two layers. Periodically spaced bright protrusion of adatoms I ions parallel to the step edge is marked with green line. Inset shows the KI unit cell with I vacancy (Scanning area=11 × 12 nm^2, Bias voltage = + 4.50 V, Tunneling current = 900 pA). (d) Line profile measured on the bright protrusions marked with a green line in (c). (e) Zoom-in of the crystal structure of KI with line profiles of the unit cell. Inset shows the calculated unit cell of KI. (f) Adatoms I-I dimers on the squared structure surface (Scanning area= 35 × 33 $Å^2$, Bias voltage = + 4.50 V, Tunneling current = 900 pA). (g) Line profile of the measured I-I dimers in (f).

To confirm the reproducibility of the KI optimized protocol, we conducted another KI 3 min deposition on Au (111). This time, it was observed that two different structures were found on the surface with squared structure and some amorphous structures too as depicted in Figure 6.5(a-c). Moreover, it was noticed from the step height profile of each MLs on the large area (Figure 6.5a) LT-STM image that the height of each ML was ~ 1.2 -1.5 Å which is double in thickness than the previously observed step height in Figure 6.4(a). Moreover, the lattice parameters as depicted in Figure 6.5(d-e) were well matched with the previously observed lattice parameters form I-I squared structure in Figure 6.4(e). To investigate the reason for the amorphous structure observed on this sample, later it was found that the UHV chamber was contaminated by CuPc, therefore we observed this amorphous structure on the KI surface. To overcome this issue, the chamber was thoroughly cleaned and the KI precursor was refreshed in the K-Cell. The

degassing of KI was performed for around 5 hours after the chamber closing to make sure that all contaminants have been removed from the KI crucible after refreshing.

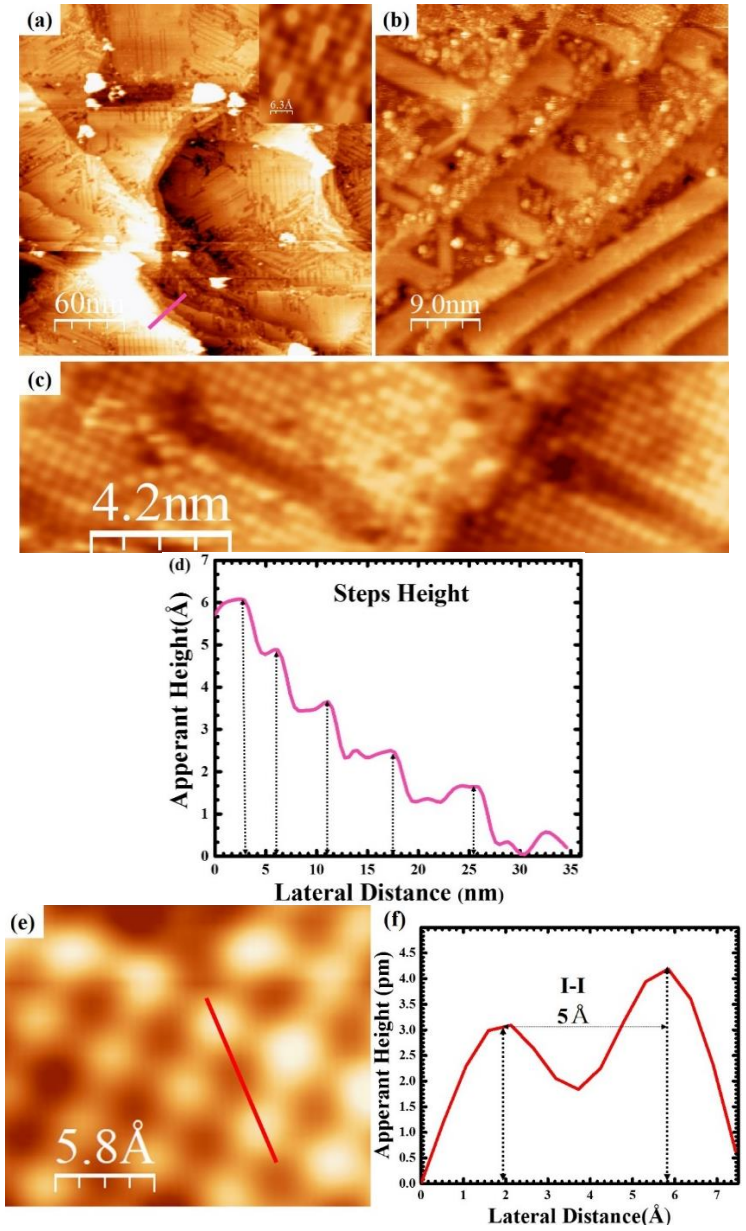

Figure 6.5: LT-STM images of 3 min deposited cubic KI thin films on Au (111). (a) LT-STM image of a large area showing squared structure and amorphous structure (Scanning area= 300 × 300 nm^2, Bias voltage = + 4.50 V, Tunneling current = 900 pA). (b) High-resolution image of fully covered amorphous structure on Au (111) (Scanning area= 47 × 47 nm^2, Bias voltage = + 4.50 V, Tunneling current = 900 pA). (c) High-resolution LT-STM image of only squared structure domain (Scanning area= 6 × 21 nm^2, Bias voltage = + 4.50 V, Tunneling current = 900 pA). (d) Height profile of the measured MLs in (a). (e) Zoom-in of the crystal structure of KI unit cell. (f) Line profile of the measured I-I squared structure in (e).

After refreshing KI and a long time of degassing (5 hours), another KI sample was prepared by following the similar fabrication protocol as previously used. It was found that the Au (111) terraces are uniformly covered with the KI ultra-thin films (Figure 6.6a). A less defective KI MLs were observed (Figure 6.6b) with I-I squared structure and exhibited an ML height of ~1.45 Å (inset in Figure 6.6b). Furthermore, the experimental lattice parameter (Figure 6.6c, inset) of the KI square structure observed on this sample was consistent with the calculated lattice parameters (Figure 6.6d). Here, no parallel rows of I adatoms were observed on uniformly smooth MLs of KI, which shows that in Figure 6.4(c) was the uncompleted topmost layer of KI with the missing K^+ ions. Also, the fully formed ML exhibits the nominal height of 1.45 Å, which is three times greater than 0.5 Å of the height profile of the uncompleted topmost layer in Figure 6.4c. In addition, the uniformly covered one ML height is identical to the one ML height in Figure 6.5(d) for two structures (squared and amorphous) MLs of KI on Au (111). Additionally, it can also be seen that the fully covered ML with uniform square structure have fewer I vacancies in comparison with the uncompleted layers in the previous sample. It is observed that the unit cell of KI from the high-resolution STM images consists of four bright protrusions of I^- anions as described in Figure 6.6(c-d) and also consistent with the lattice parameters with the other samples observed structures formed by four bright protrusions I^- ions. Table 1 describes the three depositions on three different samples with the summary of outcomes of LT-STM images.

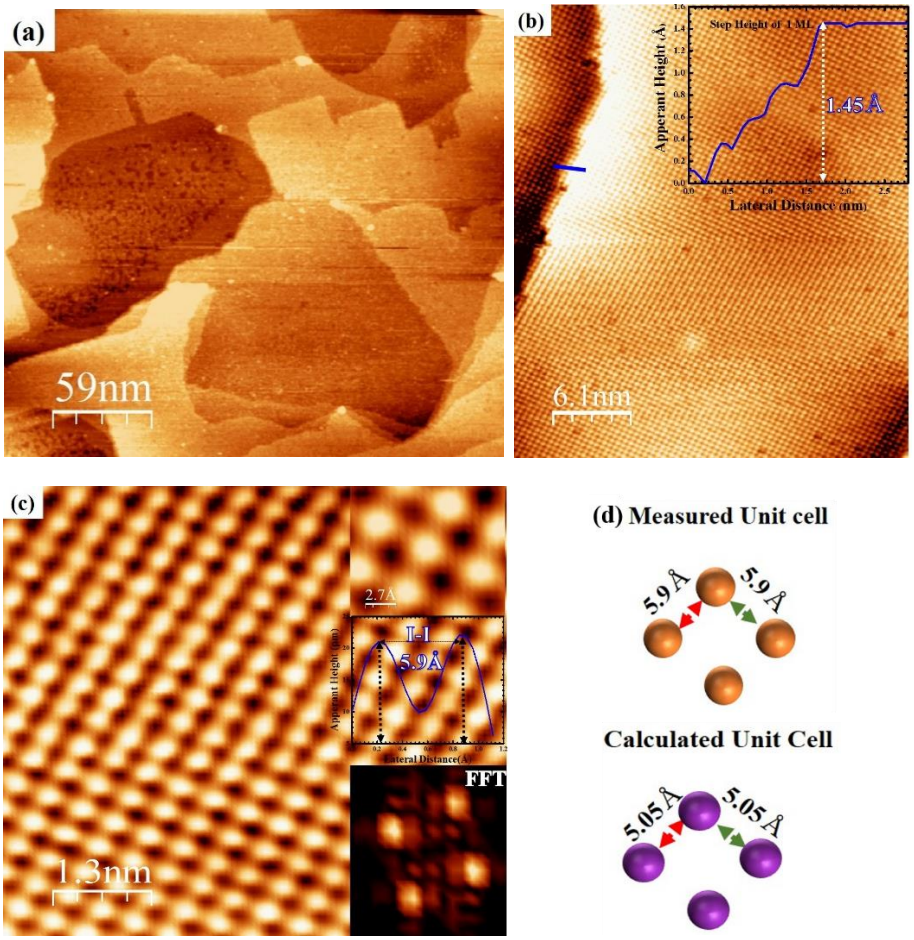

Figure 6.6: Third trial of LT-STM images of 3 min deposited cubic KI thin films on Au (111). (a) High-resolution image of a large area of fully covered KIMLs on Au (111) (Scan area = 300 × 300 nm^2; Sample bias voltage = + 4.5 V, Tunneling current = 900 pA). (b) High-resolution image of two completed MLs with squared structure (Scan area = 36.5 × 31 nm^2; Sample bias voltage = + 4.5 V, Tunneling current = 900 pA). (c) Zoom-in of the crystal structure of KI with inset of unit cell, line profile and FFT of unit cell (Scan area = 6 × 6.5 nm^2; Sample bias voltage = + 4.5 V, Tunneling current = 900 pA). (d) Comparison of measured and calculated lattice parameter of KI. [200].

KI Deposition	Deposition Time	STM Analysis	Comments
1st Trial	3 min	KI with iodine protrusion	We observed bright protrusion on the KI surface, which might be Iodine adatoms because chamber I, was in full time used for $MAPbI_3$ deposition
2nd Trial	3 min	KI & Amorphous	We observed KI but with amorphous domains because the KI crucible was contaminated by CuPc which was used by another STM group member. More, as KI was not in use for a year and the preparation chamber might have opened three times but after that KI was not degassed. Therefore, it might be a reason for amorphous domains.
3rd Trail	3 min	Only KI	We achieved KI thin film covering uniformly the Au (111) step edges!

Table 6.1: The summary of three trials of KI deposition on Au (111).

Furthermore, it can also be stated that Au (111) has a relatively strong interaction with I^- ions than K^+. Therefore, it can be deduced that the first the I^- ML formed and provided the passivation surface to the growth of KI films on Au (111) surface as depicted in VESTA simulated KI structure on Au (111) (Figure 6.7).

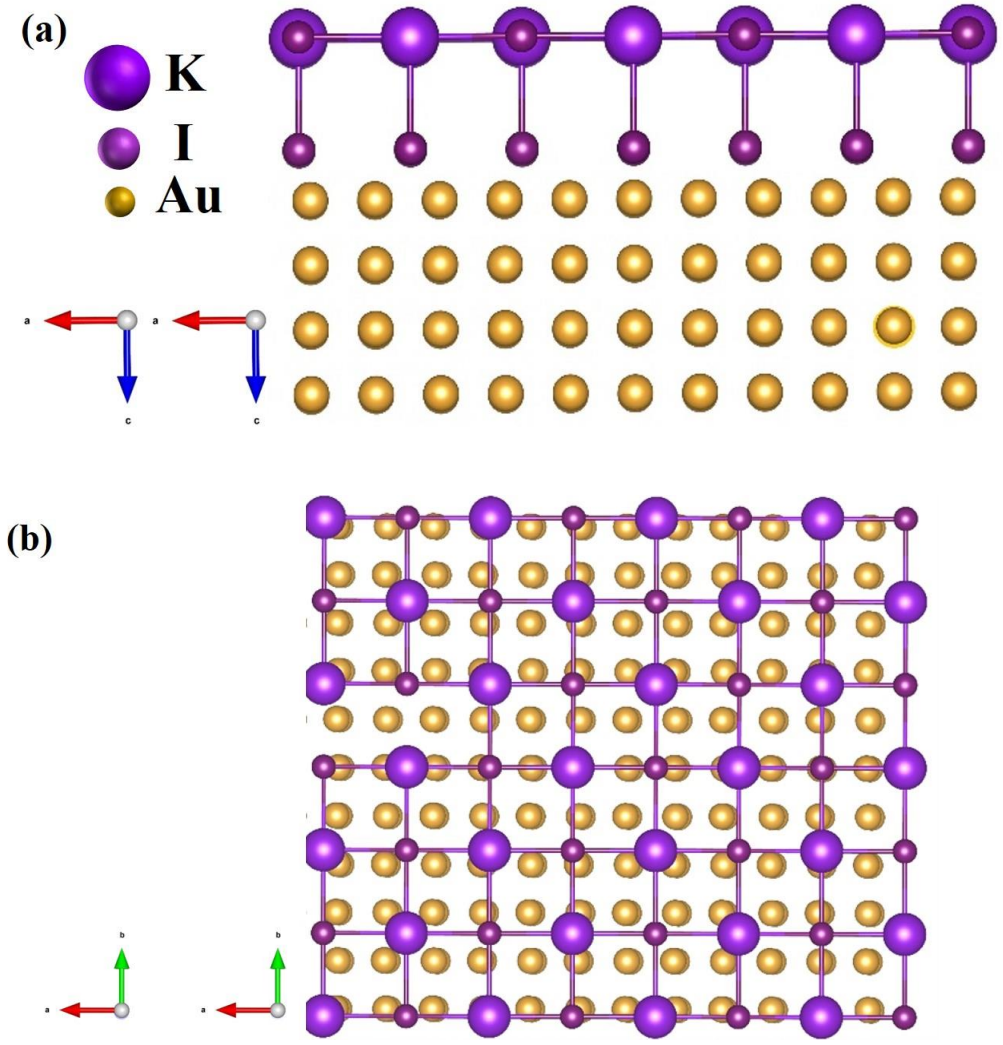

Figure 6.7: VESTA simulated Fcc KI on Fcc Au (111). (a) Side view. (b) Top view.

We also observed a small grain of KI (Figure 6.8). It should be noted that only one grain has been observed during all STM imaging on all domains. Therefore, we can assume that as the coverage of MLs increases by increasing the KI deposition time, it might start forming the proper grains as we have observed in this thesis for other halides in Chapters 4 and 5. Furthermore, the small grain also shows I vacancies in unit cells and no large deviations regarding unit cell lattice parameters are observed when compared to the unit cells of large area uniformly covered MLs.

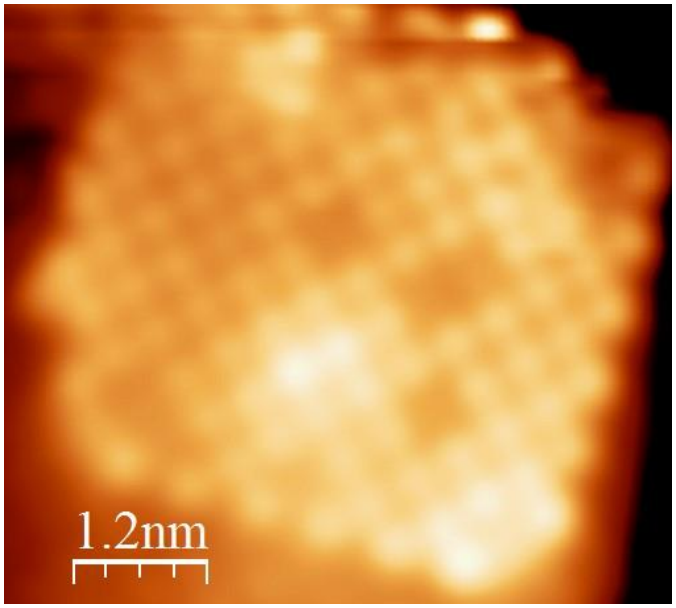

Figure 6.8: LT-STM image of a small grain of KI on the topmost ML (Scan area = 5 × 6 nm^2; Sample bias voltage = + 4.5 V, Tunneling current = 900 pA).

6.4 XPS Characterization of KI on $MAPbI_3$ Ultra-Thin-Film

After optimizing the KI protocol, 90 s KI was deposited on pristine $MAPbI_3$. Immediately after deposition, the sample was transferred into an XPS chamber for chemical composition analysis. As shown in Figure 6.9, K 2p peaks were below the detection limits of XPS instrument. The Pb 4f, I 3d, and N 1s core-level regions confirmed the pristine $MAPbI_3$ concentration. In the subsequent step, KI was deposited for an additional 3 min on the same sample followed by XPS characterization. The total deposition time of 4.5 min of KI on $MAPbI_3$ resulted in observable K peaks in XPS spectra (Figure 6.10).

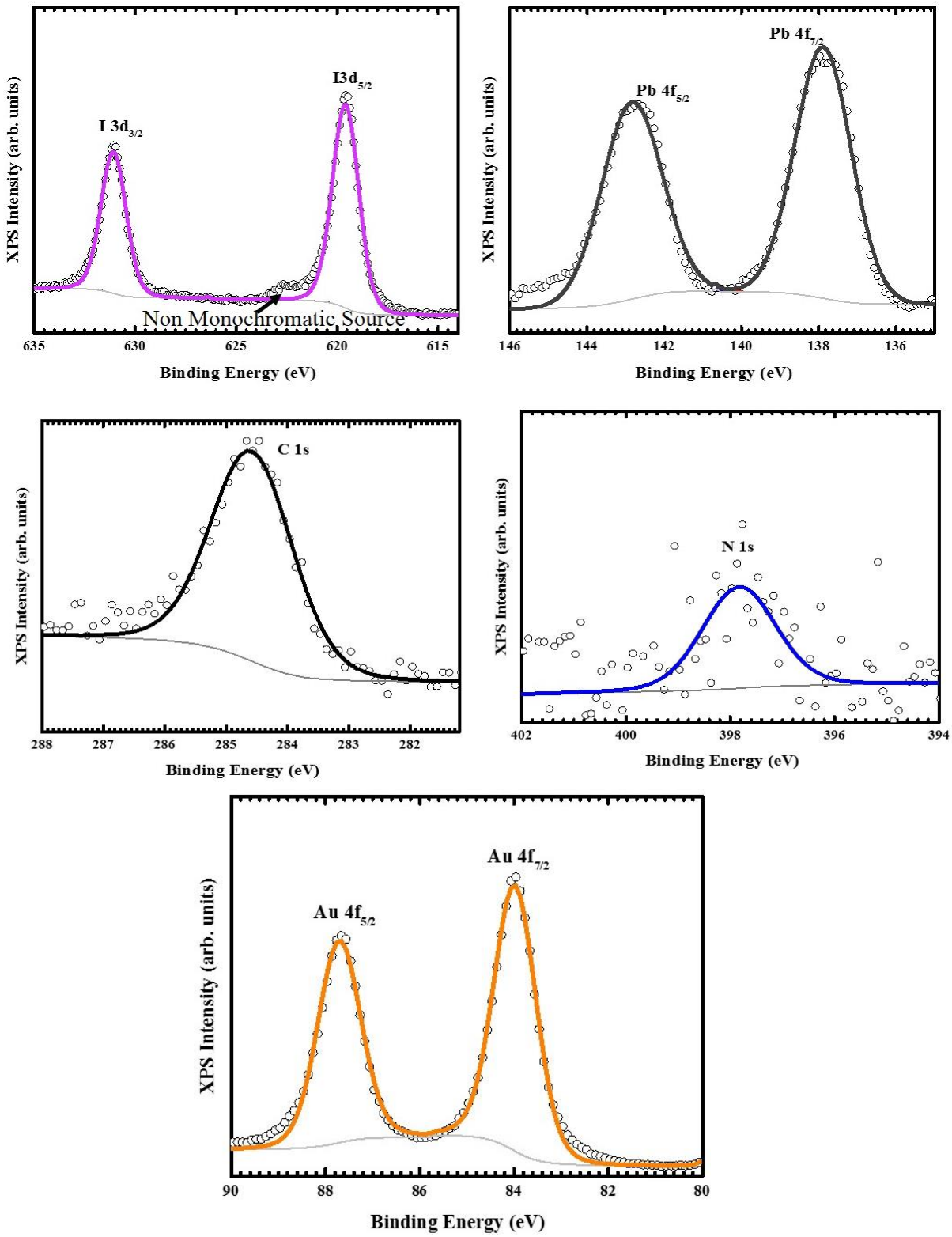

Figure 6.9: XPS spectra showing the chemical information of 90 s deposited KI on $MAPbI_3$ with no observed K 2p peaks.

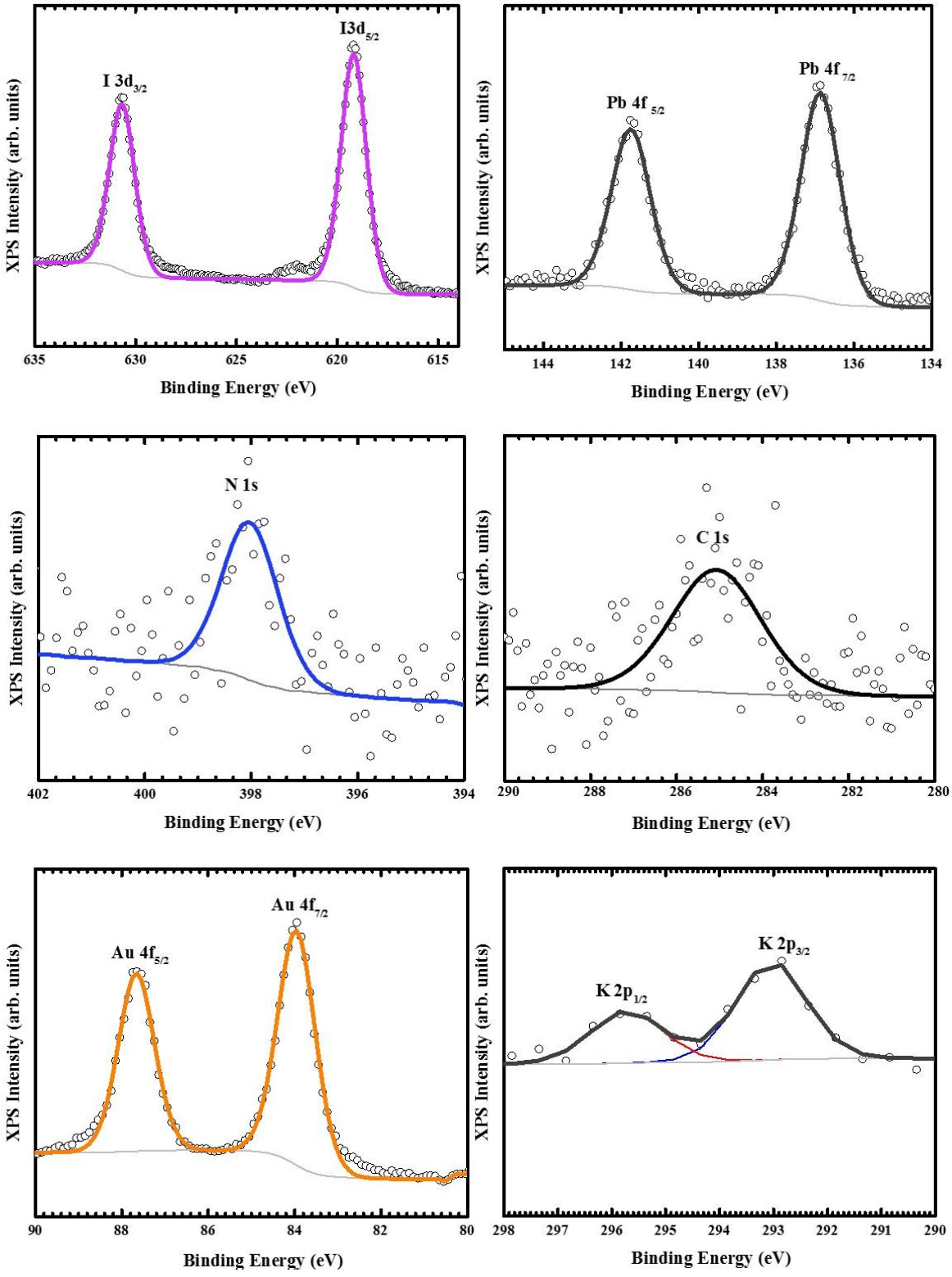

Figure 6.10: XPS spectra showing the chemical information of 4.5 min KI deposition on $MAPbI_3$, with observed K peak.

6.5 Summary

In summary, we investigated and optimized the KI protocol first by thermalizing KI at 400 ºC in the K-Cell by using a UHV chamber at a pressure of $3.4x10^{-10}$ Torr. Before the KI deposition on $MAPbI_3$, three different KI on Au (111) samples were fabricated to examine the KI structure according to the deposition conditions. In the first KI deposited sample, it was observed that two layers were formed on Au (111) surface where the bottom ML was a completely formed ML showing the square structure of four I ions while the topmost was an uncompleted KI ML. The topmost ML had a height of 0.5 Å and also the bright protrusion of I adatoms in parallel rows with the line gap of 9 Å were observed on the square structure of four I ions formed unit cell. The bond length of I-I ions in square structure was attributed based on VESTA simulated unit cell parameters. More, a few adatoms of I-I dimers were also observed on the topmost uncompleted ML, though on the bottom completed ML, no adatoms I-I dimers and the bright protrusion parallel rows of I ions were found.

By the second deposition of KI, the square and the amorphous structure were observed on Au (111) surface. The square structure consisted with the measured and calculated lattice parameter of KI with the first KI deposited sample. The cause of amorphous structure was found later that the chamber was contaminated by CuPc which was overcome by cleaning and refreshing the KI in the K-cell and degassing for at least 5 hours after closing the UHV chamber to remove all the contamination.

The third sample was fabricated by using the similar protocol of KI deposition on Au (111). We observed fully and uniformly covered Au (111) terraces by KI MLs on this sample. The uniform completed MLs did not have any bright protrusion I adatoms parallel rows and no adatoms I-I dimers were found. Additionally, the height profile of one ML of uniform KI ML was obtained as ~1.45 Å, which also confirmed the assumption of the uncompleted topmost ML on the first fabricated sample were the height of the topmost ML was only 0.5 Å. It was also observed that the full ML coverage had a lower density of I vacancies in comparison with the I vacancies in the first sample uncompleted MLs. It was deduced that in the LT-STM images we observed the I terminated surface by only observing the I ion's bright protrusions which formed from the four I ions unit cell in the KI square structure. Moreover, it was stated that the first I ions ad layer formed on an inert Au (111) hexagonal packed surface and served as a passivation layer for the growth of the cubic KI structure.

After obtaining the high-resolution LT-STM images of KI on Au (111), we deposited KI on pristine $MAPbI_3$ for 90 s and performed the XPS characterization but no K 2p peaks were acquired, therefore KI was deposited for an additional 3 min on the same

sample and by XPS characterization the K 2p peaks were observed, which confirmed the deposition of KI on $MAPbI_3$. After the successful deposition of KI on $MAPbI_3$, the next step will be to obtain the high-resolution LT-STM images in the future to investigate the K in the lattice structure of $MAPbI_3$ to understand and optimize the efficient concentration of K additive in the $MAPbI_3$ for high performance stable solar cells.

Chapter 7: Conclusion and outlook

7.1 Conclusion

This thesis focuses on the fundamental understanding of pristine $MAPbI_3$ and additives effects on $MAPbI_3$ at the atomic scale for improving the stability and performance of future PSCs by using the obtained optimal concentration ratios. To understand the pristine and additives deposited $MAPbI_3$ at the atomic scale, the first step is optimization of the fabrication protocols in the UHV by using thermal evaporation, and characterization by XPS, UPS, and IPES. Initially, the protocol growth of controlled monolayers (MLs) of MAI for the fabrication of $MAPbI_3$ ultra-thin films on Au (111) was optimized and the atomic-scale imaging was carried out by LT-STM at 77 K to reduce the thermal drift during scanning. Four different atomic structures were observed for MAI, namely stripe, non-stripe, iodine (I) hexagonal, and snaky chain of I-I dimers. Additionally, high-resolution atomic images of the PbI_2 showed the characteristic hexagonal stripe structure, where the lattice parameters were consistent with the literature reported lattice parameters.[154] For $MAPbI_3$, the I-I dimer and zigzag phases were observed by LT-STM and supported by DFT calculation. UPS and IPES were used to extract the bandgap of 1.45 eV in pristine $MAPbI_3$. To improve the stability of pristine $MAPbI_3$, the atomic-scale study was carried out by the halide Cl deposition as additives on $MAPbI_3$ surface. It is found that the Cl concentration plays a crucial role in the $MAPbI_3$ stability at the atomic scale by LT-STM and DFT calculations and in the thick films, which were characterized by FTIR and XRD for the stability tests. The optimized 14.8 ± 0.6 % Cl concentration improved the surface stability of $MAPbI_3$, which was found from the viewpoint of kinetics and thermodynamics by DFT and MD calculations. The optimal optimized concentration also tuned the bandgap from 1.45 eV to 1.65 eV, which was verified by DFT calculation. Interestingly, it was found that the Cl incorporated dimer structure is more stable than the zigzag phase in $MAPbI_3$. All theoretical calculations in this thesis were performed by Prof. Wanjian Yin and Dr. Zhendong Guo from Soochow University, China.

Based on the fact that only Cl ions were observed in $MAPbI_3$ surface crystal structure by LT-STM while Pb ions were not observed upon $PbCl_2$ deposition, we conducted additional controlled experiments: atomic structure investigation of Pb and $PbCl_2$ on the Au (111) substrate. First, the Pb protocol was optimized by trying two different temperatures of 327 ºC and 219 ºC and various deposition times to obtain controlled growth of Pb MLs on the Au (111) substrate. The optimized Pb protocol and the acquired atomic structure of Pb, forms the basis for the future studies of Pb deposition

on $MAPbI_3$ to understand the atomic structure of Pb and its interaction with $MAPbI_3$ crystal and to understand whether Pb is incorporated only on the surface or has the affinity to be incorporated in the subsurface layers of $MAPbI_3$ structure.

To understand the $PbCl_2$ interaction on the $MAPbI_3$ surface and subsurface layer four hypotheses were proposed that were supported by the investigation of $PbCl_2$ atomic structures on Au (111). Based on the high-resolution atomic-scale images of the $PbCl_2$ MLs on Au (111), $PbCl_2$ molecules sublimate both in their intact molecular form and the disassociated form from the crucible at a temperature of 310 ºC. The disassociated Pb and Cl ions form the Cl-Cl and Pb-Pb dimer structures on Au (111). It was also observed that the Au (111) surface offers a relatively strong interaction with Cl ions leading to the formation of a Cl layer on Au (111). On top of the Cl layer, the Pb-Pb dimers were identified, which is supported by the visualized atomic models cif files in VESTA. An interesting fact was found that if only the metallic-Pb was deposited on Au (111), no grain formation was observed. However, in the $PbCl_2$ deposited MLs on Au (111), the structure of grain boundaries were observed, which can be proposed that Cl ions are the origin for the formation of grain boundary structure.

To find the optimal concentration of alkali metals for the stability of future PSCs, we first chose K, which is standing out among other tested alkali metals regarding the high performance and long-term operational stability of PVSK solar cells. For the alkali metals deposition on $MAPbI_3$, the protocol of KI was required to be optimized first on the Au (111) substrate to understand the atomic structure because no literature is available on the atomic scale study of KI. Three different samples of KI were fabricated to confirm reproducibility. Based on the visualized atomic models CIF files in VESTA the square structure observed by LT-STM was attributed to I-I ions because the K^+ ions are covered with the I octrahedra. Moreover, it can be deduced that the observed structure by LT-STM is the I terminated surface of KI. The completed MLs have a square I-I structure with a lattice parameter of 5.9 Å, which is consistent with the visualized atomic models CIF files in VESTA lattice parameters. The height of 1.45 Å of one ML was acquired from the large area LT-STM obtained images. Also, the uncompleted KI MLs were observed in the form of bright protrusions I adatoms parallel rows on the surface of I-I squared structures with a step height of ~ 0.5 Å. In addition, a higher density of I vacancies was observed in the uncompleted MLs in comparison with the completed MLs. Thus, the optimized protocol was used to deposit the KI on the $MAPbI_3$ surface but with 90 s, no KI was found in the $MAPbI_3$ surface by XPS characterization, which could be associated with the detection limits of the XPS system. Therefore, KI was deposited for an additional 3 min (i.e, total deposition of 4.5 min), and the K 2p peaks were confirmed by XPS on the $MAPbI_3$ surface.

7.2 Topics for further investigation in the future

The atomic-scale investigation of the optimum concentration of Cl deposited $MAPbI_3$ for the surface stability and the Pb observation by LT-STM has been completed in this thesis. It will be interesting to continue this research by conducting the LT-STM experiments on a Cl incorporated sample after post-anneal treatment at 100^{o}C to confirm where Cl diffuses or leaves the surface of $MAPbI_3$.This will answer the mystery of Cl presence in PVSK. Moreover, the moisture, and UV illumination effects on the Cl incorporated $MAPbI_3$ samples will be also interesting to investigate at atomic scale. It is known that UV illumination, moisture, and high temperatures degrade the pristine $MAPbI_3$. In addition, the complete solar cell can be fabricated by using the optimal Cl concentration of 14.8 ± 0.6 % for only the surface layers of the thick films. In addition, FTIR and XRD techniques can provide further insights into the degradation dynamics of Cl incorporated $MAPbI_3$.

Another interesting atomic-scale study is to use TiO_2 substrates instead of Au (111), which will provide the atomic-scale interaction of Cl deposited $MAPbI_3$ and give the directions towards the more stable PSCs. TiO_2 is one of the most popular inorganic n-type semiconductors employed as ETL in PVSK solar cells. The KI fabrication protocol has been optimized in this thesis successfully, so it will be interesting to continue this research by depositing it on $MAPbI_3$ to find the optimal concentration for the future stable and high performance PVSK solar cells with the continuity of finding the UV illumination, temperature and moisture effects at atomic scale by using LT-STM.

These future experiments are challenging but can make a strong connection between surface science and solar cell devices.

References:

1. Ramanujam, J.; Singh, U. P., Copper indium gallium selenide based solar cells - a review. *Energy & Environmental Science* **2017,** *10* (6), 1306-1319.

2. Li, J.; Wang, H.; Chin, X. Y.; Dewi, H. A.; Vergeer, K.; Goh, T. W.; Lim, J. W. M.; Lew, J. H.; Loh, K. P.; Soci, C.; Sum, T. C.; Bolink, H. J.; Mathews, N.; Mhaisalkar, S.; Bruno, A., Highly Efficient Thermally Co-evaporated Perovskite Solar Cells and Mini-modules. *Joule* **2020,** *4* (5), 1035-1053.

3. Kojima, A.; Teshima, K.; Shirai, Y.; Miyasaka, T., Organometal Halide Perovskites as Visible-Light Sensitizers for Photovoltaic Cells. *Journal of the American Chemical Society* **2009,** *131* (17), 6050-6051.

4. laboratory, N. R. E. Best research-Cell Efficiencies. https://www.nrel.gov/pv/assets/images/efficiency-chart-20180716.jpg.

5. Yin, W. J.; Shi, T.; Yan, Y., Unique Properties of Halide Perovskites as Possible Origins of the Superior Solar Cell Performance. *Advanced Materials* **2014,** *26* (27), 4653-4658.

6. Razza, S.; Castro-Hermosa, S.; Carlo, A. D.; Brown, T. M., Research Update: Large-area deposition, coating, printing, and processing techniques for the upscaling of perovskite solar cell technology. *APL Materials* **2016,** *4* (9), 091508.

7. Baikie, T.; Fang, Y.; Kadro, J. M.; Schreyer, M.; Wei, F.; Mhaisalkar, S. G.; Graetzel, M.; White, T. J., Synthesis and crystal chemistry of the hybrid perovskite (CH3NH3)PbI3 for solid-state sensitised solar cell applications. *Journal of Materials Chemistry A* **2013,** *1* (18), 5628-5641.

8. Umari, P.; Mosconi, E.; De Angelis, F., Relativistic GW calculations on CH3NH3PbI3 and CH3NH3SnI3 Perovskites for Solar Cell Applications. *Scientific Reports* **2014,** *4*, 4467.

9. Lee, B.; Lee, S.; Cho, D.; Kim, J.; Hwang, T.; Kim, K. H.; Hong, S.; Moon, T.; Park, B., Evaluating the Optoelectronic Quality of Hybrid Perovskites by Conductive Atomic Force Microscopy with Noise Spectroscopy. *ACS Applied Materials & Interfaces* **2016,** *8* (45), 30985-30991.

10. Zhang, D.; Zhu, Y.; Liu, L.; Ying, X.; Hsiung, C.-E.; Sougrat, R.; Li, K.; Han, Y., Atomic-resolution transmission electron microscopy of electron beam-sensitive crystalline materials. *Science* **2018,** *359* (6376), 675-679.

11. Zhang, L.; Ju, M.-G.; Liang, W., The effect of moisture on the structures and properties of lead halide perovskites: a first-principles theoretical investigation. *Physical Chemistry Chemical Physics* **2016,** *18* (33), 23174-23183.

12. Ohmann, R.; Ono, L. K.; Kim, H.-S.; Lin, H.; Lee, M. V.; Li, Y.; Park, N.-G.; Qi, Y. B., Real-Space Imaging of the Atomic Structure of Organic-Inorganic Perovskite.

J. Am. Chem. Soc. **2015,** *137* (51), 16049-16054.

13. She, L.; Liu, M.; Zhong, D., Atomic Structures of CH3NH3PbI3 (001) Surfaces. *ACS Nano* **2016,** *10* (1), 1126-1131.

14. Hieulle, J.; Wang, X.; Stecker, C.; Son, D.-Y.; Qiu, L.; Ohmann, R.; Ono, L. K.; Mugarza, A.; Yan, Y.; Qi, Y. B., Unraveling the Impact of Halide Mixing on Perovskite Stability. *J. Am. Chem. Soc.* **2019,** *141* (8), 3515-3523.

15. Hieulle, J.; Luo, S.; Son, D.-Y.; Jamshaid, A.; Stecker, C.; Liu, Z.; Na, G.; Yang, D.; Ohmann, R.; Ono, L. K.; Zhang, L.; Qi, Y. B., Imaging of the Atomic Structure of All-Inorganic Halide Perovskites. *J. Phys. Chem. Lett.* **2020,** *11, 3*, 818-823.

16. Stecker, C.; Liu, K.; Hieulle, J.; Ohmann, R.; Liu, Z.; Ono, L. K.; Wang, G.; Qi, Y. B., Surface Defect Dynamics in Organic-Inorganic Hybrid Perovskites: From Mechanism to Interfacial Properties. *ACS Nano* **2019,** *13* (10), 12127-12136.

17. Gao, P.; Grätzel, M.; Nazeeruddin, M. K., Organohalide lead perovskites for photovoltaic applications. *Energy & Environmental Science* **2014,** *7* (8), 2448-2463.

18. Walsh, A., Principles of Chemical Bonding and Band Gap Engineering in Hybrid Organic-Inorganic Halide Perovskites. *The Journal of Physical Chemistry C* **2015,** *119* (11), 5755-5760.

19. Walsh, A.; Watson, G. W., The origin of the stereochemically active Pb(II) lone pair: DFT calculations on PbO and PbS. *Journal of Solid State Chemistry* **2005,** *178* (5), 1422-1428.

20. Goldschmidt, V. M., Krystallbau und chemische Zusammensetzung. *Berichte der deutschen chemischen Gesellschaft (A and B Series)* **1927,** *60* (5), 1263-1296.

21. Amat, A.; Mosconi, E.; Ronca, E.; Quarti, C.; Umari, P.; Nazeeruddin, M. K.; Grätzel, M.; De Angelis, F., Cation-Induced Band-Gap Tuning in Organohalide Perovskites: Interplay of Spin-Orbit Coupling and Octahedra Tilting. *Nano Letters* **2014,** *14* (6), 3608-3616.

22. https://www.webelements.com/iodine/atom_sizes.html, I. i. r.

23. Travis, W.; Glover, E. N. K.; Bronstein, H.; Scanlon, D. O.; Palgrave, R. G., On the application of the tolerance factor to inorganic and hybrid halide perovskites: a revised system. *Chemical Science* **2016,** *7* (7), 4548-4556.

24. Wan - Jian, Y.; Tingting, S.; Yanfa, Y., Unique Properties of Halide Perovskites as Possible Origins of the Superior Solar Cell Performance. *Advanced Materials* **2014,** *26* (27), 4653-4658.

25. Milot, R. L.; Eperon, G. E.; Snaith, H. J.; Johnston, M. B.; Herz, L. M., Temperature-Dependent Charge-Carrier Dynamics in CH3NH3PbI3 Perovskite Thin Films. *Advanced Functional Materials* **2015,** *25* (39), 6218-6227.

26. Li, C.; Lu, X.; Ding, W.; Feng, L.; Gao, Y.; Guo, Z., Formability of ABX3 (X = F, Cl, Br, I) halide perovskites. *Acta Crystallographica Section B* **2008,** *64* (6),

702-707.

27. Kieslich, G.; Sun, S.; Cheetham, A. K., An extended Tolerance Factor approach for organic-inorganic perovskites. *Chemical Science* **2015,** *6* (6), 3430-3433.

28. Stoumpos, C. C.; Kanatzidis, M. G., The Renaissance of Halide Perovskites and Their Evolution as Emerging Semiconductors. *Accounts of Chemical Research* **2015,** *48* (10), 2791-2802.

29. Geng, W.; Zhang, L.; Zhang, Y.-N.; Lau, W.-M.; Liu, L.-M., First-Principles Study of Lead Iodide Perovskite Tetragonal and Orthorhombic Phases for Photovoltaics. *The Journal of Physical Chemistry C* **2014,** *118* (34), 19565-19571.

30. Yin, W.-J.; Yang, J.-H.; Kang, J.; Yan, Y.; Wei, S.-H., Halide perovskite materials for solar cells: a theoretical review. *Journal of Materials Chemistry A* **2015,** *3* (17), 8926-8942.

31. Tailor, N. K.; Abdi-Jalebi, M.; Gupta, V.; Hu, H.; Dar, M. I.; Li, G.; Satapathi, S., Recent progress in morphology optimization in perovskite solar cell. *Journal of Materials Chemistry A* **2020,** *8* (41), 21356-21386.

32. Chen, Q.; De Marco, N.; Yang, Y.; Song, T.-B.; Chen, C.-C.; Zhao, H.; Hong, Z.; Zhou, H.; Yang, Y., Under the spotlight: The organic-inorganic hybrid halide perovskite for optoelectronic applications. *Nano Today* **2015,** *10* (3), 355-396.

33. Habisreutinger, S. N.; Leijtens, T.; Eperon, G. E.; Stranks, S. D.; Nicholas, R. J.; Snaith, H. J., Carbon Nanotube/Polymer Composites as a Highly Stable Hole Collection Layer in Perovskite Solar Cells. *Nano Letters* **2014,** *14* (10), 5561-5568.

34. Li, Y.; Cooper, J. K.; Buonsanti, R.; Giannini, C.; Liu, Y.; Toma, F. M.; Sharp, I. D., Fabrication of Planar Heterojunction Perovskite Solar Cells by Controlled Low-Pressure Vapor Annealing. *The Journal of Physical Chemistry Letters* **2015,** *6* (3), 493-499.

35. Kim, H.-S.; Lee, C.-R.; Im, J.-H.; Lee, K.-B.; Moehl, T.; Marchioro, A.; Moon, S.-J.; Humphry-Baker, R.; Yum, J.-H.; Moser, J. E.; Grätzel, M.; Park, N.-G., Lead Iodide Perovskite Sensitized All-Solid-State Submicron Thin Film Mesoscopic Solar Cell with Efficiency Exceeding 9%. *Scientific Reports* **2012,** *2*, 591.

36. Burschka, J.; Pellet, N.; Moon, S.-J.; Humphry-Baker, R.; Gao, P.; Nazeeruddin, M. K.; Grätzel, M., Sequential deposition as a route to high-performance perovskite-sensitized solar cells. *Nature* **2013,** *499*, 316.

37. Chen, Q.; Zhou, H.; Hong, Z.; Luo, S.; Duan, H.-S.; Wang, H.-H.; Liu, Y.; Li, G.; Yang, Y., Planar Heterojunction Perovskite Solar Cells via Vapor-Assisted Solution Process. *Journal of the American Chemical Society* **2014,** *136* (2), 622-625.

38. Ono, L. K.; Wang, S.; Kato, Y.; Raga, S. R.; Qi, Y., Fabrication of semi-transparent perovskite films with centimeter-scale superior uniformity by the hybrid deposition method. *Energy & Environmental Science* **2014,** *7* (12), 3989-3993.

39. Wang, S.; Ono, L. K.; Leyden, M. R.; Kato, Y.; Raga, S. R.; Lee, M. V.; Qi, Y., Smooth perovskite thin films and efficient perovskite solar cells prepared by the hybrid deposition method. *Journal of Materials Chemistry A* **2015,** *3* (28), 14631-14641.

40. Chandrasekhar, P. S.; Kumar, N.; Swami, S. K.; Dutta, V.; Komarala, V. K., Fabrication of perovskite films using an electrostatic assisted spray technique: the effect of the electric field on morphology, crystallinity and solar cell performance. *Nanoscale* **2016,** *8* (12), 6792-6800.

41. Zhou, Y.; Yang, M.; Wu, W.; Vasiliev, A. L.; Zhu, K.; Padture, N. P., Room-temperature crystallization of hybrid-perovskite thin films via solvent-solvent extraction for high-performance solar cells. *Journal of Materials Chemistry A* **2015,** *3* (15), 8178-8184.

42. Deng, Y.; Wang, Q.; Yuan, Y.; Huang, J., Vividly colorful hybrid perovskite solar cells by doctor-blade coating with perovskite photonic nanostructures. *Materials Horizons* **2015,** *2* (6), 578-583.

43. Monteiro Lunardi, M.; Wing Yi Ho-Baillie, A.; Alvarez-Gaitan, J. P.; Moore, S.; Corkish, R., A life cycle assessment of perovskite/silicon tandem solar cells. *Progress in Photovoltaics: Research and Applications* **2017,** *25* (8), 679-695.

44. Li, N.; Niu, X.; Chen, Q.; Zhou, H., Towards commercialization: the operational stability of perovskite solar cells. *Chemical Society Reviews* **2020,** *49* (22), 8235-8286.

45. Qiu, L.; He, S.; Ono, L. K.; Liu, S.; Qi, Y., Scalable Fabrication of Metal Halide Perovskite Solar Cells and Modules. *ACS Energy Letters* **2019,** *4* (9), 2147-2167.

46. Corporation, N. E. a. I. T. D. O. N. a. T., NEDO and Toshiba Develops World's Largest Film-based Perovskite Photovoltaic Module
—703 cm2 module achieves 11.7% power conversion efficiency—. **2018,18 June**.

47. Chen, Y.; Zhang, L.; Zhang, Y.; Gao, H.; Yan, H., Large-area perovskite solar cells - a review of recent progress and issues. *RSC Advances* **2018,** *8* (19), 10489-10508.

48. Zhai, P.; Su, T.-S.; Hsieh, T.-Y.; Wang, W.-Y.; Ren, L.; Guo, J.; Wei, T.-C., Toward clean production of plastic perovskite solar cell: Composition-tailored perovskite absorber made from aqueous lead nitrate precursor. *Nano Energy* **2019,** *65*, 104036.

49. Jung, H. S.; Han, G. S.; Park, N.-G.; Ko, M. J., Flexible Perovskite Solar Cells. *Joule* **2019,** *3* (8), 1850-1880.

50. Lu, S.; Sun, Y.; Ren, K.; Liu, K.; Wang, Z.; Qu, S. Recent Development in ITO-free Flexible Polymer Solar Cells *Polymers (Basel)* [Online], 2017. PubMed.

.

51. Li, Y.; Meng, L.; Yang, Y.; Xu, G.; Hong, Z.; Chen, Q.; You, J.; Li, G.; Yang, Y.; Li, Y., High-efficiency robust perovskite solar cells on ultrathin flexible substrates. *Nature Communications* **2016,** *7*, 10214.

52. Yu, Z.; Perera, I. R.; Daeneke, T.; Makuta, S.; Tachibana, Y.; Jasieniak, J. J.; Mishra, A.; Bäuerle, P.; Spiccia, L.; Bach, U., Indium tin oxide as a semiconductor material in efficient p-type dye-sensitized solar cells. *NPG Asia Materials* **2016,** *8* (9), e305-e305.

53. Etgar, L.; Gao, P.; Xue, Z.; Peng, Q.; Chandiran, A. K.; Liu, B.; Nazeeruddin, M. K.; Grätzel, M., Mesoscopic CH3NH3PbI3/TiO2 Heterojunction Solar Cells. *Journal of the American Chemical Society* **2012,** *134* (42), 17396-17399.

54. Salado, M.; Fernández, M. A.; Holgado, J. P.; Kazim, S.; Nazeeruddin, M. K.; Dyson, P. J.; Ahmad, S., Towards Extending Solar Cell Lifetimes: Addition of a Fluorous Cation to Triple Cation-Based Perovskite Films. *ChemSusChem* **2017,** *10* (19), 3846-3853.

55. Hu, Y.; Diao, X.; Wang, C.; Hao, W.; Wang, T., Effects of heat treatment on properties of ITO films prepared by rf magnetron sputtering. *Vacuum* **2004,** *75* (2), 183-188.

56. Way, A.; Luke, J.; Evans, A. D.; Li, Z.; Kim, J.-S.; Durrant, J. R.; Lee, H. K. H.; Tsoi, W. C., Fluorine doped tin oxide as an alternative of indium tin oxide for bottom electrode of semi-transparent organic photovoltaic devices. *AIP Advances* **2019,** *9* (8), 085220.

57. Sung, H.; Ahn, N.; Jang, M. S.; Lee, J.-K.; Yoon, H.; Park, N.-G.; Choi, M., Transparent Conductive Oxide-Free Graphene-Based Perovskite Solar Cells with over 17% Efficiency. *Advanced Energy Materials* **2015,** *6*, 1501873.

58. Lu, H.; Ma, Y.; Gu, B.; Tian, W.; Li, L., Identifying the optimum thickness of electron transport layers for highly efficient perovskite planar solar cells. *Journal of Materials Chemistry A* **2015,** *3* (32), 16445-16452.

59. Ke, W.; Fang, G.; Liu, Q.; Xiong, L.; Qin, P.; Tao, H.; Wang, J.; Lei, H.; Li, B.; Wan, J.; Yang, G.; Yan, Y., Low-Temperature Solution-Processed Tin Oxide as an Alternative Electron Transporting Layer for Efficient Perovskite Solar Cells. *Journal of the American Chemical Society* **2015,** *137* (21), 6730-6733.

60. Gouda, L.; Gottesman, R.; Ginsburg, A.; Keller, D. A.; Haltzi, E.; Hu, J.; Tirosh, S.; Anderson, A. Y.; Zaban, A.; Boix, P. P., Open Circuit Potential Build-Up in Perovskite Solar Cells from Dark Conditions to 1 Sun. *The Journal of Physical Chemistry Letters* **2015,** *6* (22), 4640-4645.

61. Tseng, Z.-L.; Chiang, C.-H.; Wu, C.-G., Surface Engineering of ZnO Thin Film for High Efficiency Planar Perovskite Solar Cells. *Scientific Reports* **2015,** *5*, 13211.

62. Zhu, L.; Shao, Z.; Ye, J.; Zhang, X.; Pan, X.; Dai, S., Mesoporous BaSnO3 layer based perovskite solar cells. *Chemical Communications* **2016,** *52* (5), 970-973.

63. Roose, B.; Baena, J.-P. C.; Gödel, K. C.; Graetzel, M.; Hagfeldt, A.; Steiner, U.; Abate, A., Mesoporous SnO2 electron selective contact enables UV-stable perovskite solar cells. *Nano Energy* **2016,** *30*, 517-522.

64. Mahmood, K.; Swain, B. S.; Kirmani, A. R.; Amassian, A., Highly efficient perovskite solar cells based on a nanostructured WO3-TiO2 core-shell electron transporting material. *Journal of Materials Chemistry A* **2015,** *3* (17), 9051-9057.

65. Dong, Q.; Liu, F.; Wong, M. K.; Djurišić, A. B.; Ren, Z.; Shen, Q.; Ng, A.; Surya, C.; Chan, W. K. In *Indium oxide-based perovskite solar cells*, SPIE OPTO, SPIE: 2016; p 8.

66. Tao, C.; Neutzner, S.; Colella, L.; Marras, S.; Srimath Kandada, A. R.; Gandini, M.; Bastiani, M. D.; Pace, G.; Manna, L.; Caironi, M.; Bertarelli, C.; Petrozza, A., 17.6% stabilized efficiency in low-temperature processed planar perovskite solar cells. *Energy & Environmental Science* **2015,** *8* (8), 2365-2370.

67. Ahn, N.; Kwak, K.; Jang, M. S.; Yoon, H.; Lee, B. Y.; Lee, J.-K.; Pikhitsa, P. V.; Byun, J.; Choi, M., Trapped charge-driven degradation of perovskite solar cells. *Nature Communications* **2016,** *7*, 13422.

68. Heo, J. H.; Han, H. J.; Kim, D.; Ahn, T. K.; Im, S. H., Hysteresis-less inverted CH3NH3PbI3 planar perovskite hybrid solar cells with 18.1% power conversion efficiency. *Energy & Environmental Science* **2015,** *8* (5), 1602-1608.

69. Enhanced stability of perovskite solar cells using hydrophobic organic fluoropolymer. *Applied Physics Letters* **2018,** *113* (2), 023902.

70. Hu, Y.; Bai, F.; Liu, X.; Ji, Q.; Miao, X.; Qiu, T.; Zhang, S., Bismuth Incorporation Stabilized α-CsPbI3 for Fully Inorganic Perovskite Solar Cells. *ACS Energy Letters* **2017,** *2* (10), 2219-2227.

71. Jeon, N. J.; Noh, J. H.; Yang, W. S.; Kim, Y. C.; Ryu, S.; Seo, J.; Seok, S. I., Compositional engineering of perovskite materials for high-performance solar cells. *Nature* **2015,** *517*, 476.

72. Wu, Q.; Xue, C.; Li, Y.; Zhou, P.; Liu, W.; Zhu, J.; Dai, S.; Zhu, C.; Yang, S., Kesterite Cu2ZnSnS4 as a Low-Cost Inorganic Hole-Transporting Material for High-Efficiency Perovskite Solar Cells. *ACS Applied Materials & Interfaces* **2015,** *7* (51), 28466-28473.

73. Pool, V. L.; Dou, B.; Van Campen, D. G.; Klein-Stockert, T. R.; Barnes, F. S.; Shaheen, S. E.; Ahmad, M. I.; van Hest, M. F. A. M.; Toney, M. F., Thermal engineering of FAPbI3 perovskite material via radiative thermal annealing and in situ XRD. *Nature Communications* **2017,** *8*, 14075.

74. Son, D.-Y.; Lee, J.-W.; Choi, Y. J.; Jang, I.-H.; Lee, S.; Yoo, P. J.; Shin, H.; Ahn, N.; Choi, M.; Kim, D.; Park, N.-G., Self-formed grain boundary healing layer for highly efficient CH3 NH3 PbI3 perovskite solar cells. *Nat Energy* **2016,** *1*, 16081.

75. Momblona, C.; Gil-Escrig, L.; Bandiello, E.; Hutter, E. M.; Sessolo, M.; Lederer, K.; Blochwitz-Nimoth, J.; Bolink, H. J., Efficient vacuum deposited p-i-n and n-i-p perovskite solar cells employing doped charge transport layers. *Energy &*

Environmental Science **2016,** *9* (11), 3456-3463.

76. Ono, L. K.; Juarez-Perez, E. J.; Qi, Y., Progress on Perovskite Materials and Solar Cells with Mixed Cations and Halide Anions. *ACS Applied Materials & Interfaces* **2017,** *9* (36), 30197-30246.

77. Kim, J.; Kim, H. P.; Teridi, M. A. M.; Yusoff, A. R. b. M.; Jang, J., Bandgap tuning of mixed organic cation utilizing chemical vapor deposition process. *Scientific Reports* **2016,** *6*, 37378.

78. Park, Y. H.; Jeong, I.; Bae, S.; Son, H. J.; Lee, P.; Lee, J.; Lee, C.-H.; Ko, M. J., Inorganic Rubidium Cation as an Enhancer for Photovoltaic Performance and Moisture Stability of HC(NH2)2PbI3 Perovskite Solar Cells. *Advanced Functional Materials* **2017,** *27* (16), 1605988.

79. Zhang, M.; Yun, J. S.; Ma, Q.; Zheng, J.; Lau, C. F. J.; Deng, X.; Kim, J.; Kim, D.; Seidel, J.; Green, M. A.; Huang, S.; Ho-Baillie, A. W. Y., High-Efficiency Rubidium-Incorporated Perovskite Solar Cells by Gas Quenching. *ACS Energy Letters* **2017,** *2* (2), 438-444.

80. Stranks, S. D.; Eperon, G. E.; Grancini, G.; Menelaou, C.; Alcocer, M. J. P.; Leijtens, T.; Herz, L. M.; Petrozza, A.; Snaith, H. J., Electron-Hole Diffusion Lengths Exceeding 1 Micrometer in an Organometal Trihalide Perovskite Absorber. *Science* **2013,** *342* (6156), 341-344.

81. Son, D.-Y.; Kim, S.-G.; Seo, J.-Y.; Lee, S.-H.; Shin, H.; Lee, D.; Park, N.-G., Universal Approach toward Hysteresis-Free Perovskite Solar Cell via Defect Engineering. *Journal of the American Chemical Society* **2018,** *140* (4), 1358-1364.

82. Bi, D.; Yi, C.; Luo, J.; Décoppet, J.-D.; Zhang, F.; Zakeeruddin, Shaik M.; Li, X.; Hagfeldt, A.; Grätzel, M., Polymer-templated nucleation and crystal growth of perovskite films for solar cells with efficiency greater than 21%. *Nat Energy* **2016,** *1*, 16142.

83. Shin, S. S.; Yeom, E. J.; Yang, W. S.; Hur, S.; Kim, M. G.; Im, J.; Seo, J.; Noh, J. H.; Seok, S. I., Colloidally prepared La-doped BaSnO₃ electrodes for efficient, photostable perovskite solar cells. *Science* **2017,** *356* (6334), 167-171.

84. Zhao, X.; Kim, H.-S.; Seo, J.-Y.; Park, N.-G., Effect of Selective Contacts on the Thermal Stability of Perovskite Solar Cells. *ACS Applied Materials & Interfaces* **2017,** *9* (8), 7148-7153.

85. Kim, G.-W.; Kang, G.; Kim, J.; Lee, G.-Y.; Kim, H. I.; Pyeon, L.; Lee, J.; Park, T., Dopant-free polymeric hole transport materials for highly efficient and stable perovskite solar cells. *Energy & Environmental Science* **2016,** *9* (7), 2326-2333.

86. Liu, J.; Wu, Y.; Qin, C.; Yang, X.; Yasuda, T.; Islam, A.; Zhang, K.; Peng, W.; Chen, W.; Han, L., A dopant-free hole-transporting material for efficient and stable perovskite solar cells. *Energy & Environmental Science* **2014,** *7* (9), 2963-2967.

87. Cheng, M.; Li, Y.; Safdari, M.; Chen, C.; Liu, P.; Kloo, L.; Sun, L., Efficient Perovskite Solar Cells Based on a Solution Processable Nickel(II) Phthalocyanine and Vanadium Oxide Integrated Hole Transport Layer. *Advanced Energy Materials* **2017,** *7* (14), 1602556.

88. Wang, F.; Endo, M.; Mouri, S.; Miyauchi, Y.; Ohno, Y.; Wakamiya, A.; Murata, Y.; Matsuda, K., Highly stable perovskite solar cells with an all-carbon hole transport layer. *Nanoscale* **2016,** *8* (23), 11882-11888.

89. Liu, Z.; Zhu, A.; Cai, F.; Tao, L.; Zhou, Y.; Zhao, Z.; Chen, Q.; Cheng, Y.-B.; Zhou, H., Nickel oxide nanoparticles for efficient hole transport in p-i-n and n-i-p perovskite solar cells. *Journal of Materials Chemistry A* **2017,** *5* (14), 6597-6605.

90. Tseng, Z.-L.; Chen, L.-C.; Chiang, C.-H.; Chang, S.-H.; Chen, C.-C.; Wu, C.-G., Efficient inverted-type perovskite solar cells using UV-ozone treated MoOx and WOx as hole transporting layers. *Solar Energy* **2016,** *139*, 484-488.

91. Bashir, A.; Shukla, S.; Lew, J. H.; Shukla, S.; Bruno, A.; Gupta, D.; Baikie, T.; Patidar, R.; Akhter, Z.; Priyadarshi, A.; Mathews, N.; Mhaisalkar, S. G., Spinel Co3O4 nanomaterials for efficient and stable large area carbon-based printed perovskite solar cells. *Nanoscale* **2018,** *10* (5), 2341-2350.

92. Dunlap-Shohl, W. A.; Daunis, T. B.; Wang, X.; Wang, J.; Zhang, B.; Barrera, D.; Yan, Y.; Hsu, Julia W. P.; Mitzi, D. B., Room-temperature fabrication of a delafossite CuCrO2 hole transport layer for perovskite solar cells. *Journal of Materials Chemistry A* **2018,** *6* (2), 469-477.

93. Igbari, F.; Li, M.; Hu, Y.; Wang, Z.-K.; Liao, L.-S., A room-temperature CuAlO2 hole interfacial layer for efficient and stable planar perovskite solar cells. *Journal of Materials Chemistry A* **2016,** *4* (4), 1326-1335.

94. Zhang, H.; Wang, H.; Chen, W.; Jen, A. K.-Y., CuGaO2: A Promising Inorganic Hole-Transporting Material for Highly Efficient and Stable Perovskite Solar Cells. *Advanced Materials* **2017,** *29* (8), 1604984.

95. Rao, H.; Sun, W.; Ye, S.; Yan, W.; Li, Y.; Peng, H.; Liu, Z.; Bian, Z.; Huang, C., Solution-Processed CuS NPs as an Inorganic Hole-Selective Contact Material for Inverted Planar Perovskite Solar Cells. *ACS Applied Materials & Interfaces* **2016,** *8* (12), 7800-7805.

96. Christians, J. A.; Fung, R. C. M.; Kamat, P. V., An Inorganic Hole Conductor for Organo-Lead Halide Perovskite Solar Cells. Improved Hole Conductivity with Copper Iodide. *Journal of the American Chemical Society* **2014,** *136* (2), 758-764.

97. Qin, P.; Tanaka, S.; Ito, S.; Tetreault, N.; Manabe, K.; Nishino, H.; Nazeeruddin, M. K.; Grätzel, M., Inorganic hole conductor-based lead halide perovskite solar cells with 12.4% conversion efficiency. *Nature Communications* **2014,** *5*, 3834.

98. Madhavan, V. E.; Zimmermann, I.; Baloch, A. A. B.; Manekkathodi, A.; Belaidi,

A.; Tabet, N.; Nazeeruddin, M. K., CuSCN as Hole Transport Material with 3D/2D Perovskite Solar Cells. *ACS Applied Energy Materials* **2020,** *3* (1), 114-121.

99. Jin, I. S.; Lee, J. H.; Noh, Y. W.; Park, S. H.; Jung, J. W., Molecular doping of CuSCN for hole transporting layers in inverted-type planar perovskite solar cells. *Inorganic Chemistry Frontiers* **2019,** *6* (8), 2158-2166.

100. Zhao, K.; Munir, R.; Yan, B.; Yang, Y.; Kim, T.; Amassian, A., Solution-processed inorganic copper(i) thiocyanate (CuSCN) hole transporting layers for efficient p-i-n perovskite solar cells. *Journal of Materials Chemistry A* **2015,** *3* (41), 20554-20559.

101. Han, G. S.; Yoo, J. S.; Yu, F.; Duff, M. L.; Kang, B. K.; Lee, J.-K., Highly stable perovskite solar cells in humid and hot environment. *Journal of Materials Chemistry A* **2017,** *5* (28), 14733-14740.

102. Arora, N.; Dar, M. I.; Hinderhofer, A.; Pellet, N.; Schreiber, F.; Zakeeruddin, S. M.; Grätzel, M., Perovskite solar cells with CuSCN hole extraction layers yield stabilized efficiencies greater than 20%. *Science* **2017**.

103. Jeon, N. J.; Lee, J.; Noh, J. H.; Nazeeruddin, M. K.; Grätzel, M.; Seok, S. I., Efficient Inorganic-Organic Hybrid Perovskite Solar Cells Based on Pyrene Arylamine Derivatives as Hole-Transporting Materials. *Journal of the American Chemical Society* **2013,** *135* (51), 19087-19090.

104. Niu, G.; Li, W.; Meng, F.; Wang, L.; Dong, H.; Qiu, Y., Study on the stability of CH3NH3PbI3 films and the effect of post-modification by aluminum oxide in all-solid-state hybrid solar cells. *Journal of Materials Chemistry A* **2014,** *2* (3), 705-710.

105. Abate, A.; Correa-Baena, J.-P.; Saliba, M.; Su'ait, M.; Bella, F., *Perovskite solar cells from the lab to the assembly line*. 2017; Vol. 24.

106. Kato, Y.; Ono, L. K.; Lee, M. V.; Wang, S.; Raga, S. R.; Qi, Y., Silver Iodide Formation in Methyl Ammonium Lead Iodide Perovskite Solar Cells with Silver Top Electrodes. *Advanced Materials Interfaces* **2015,** *2* (13), 1500195.

107. Abate, A.; Correa-Baena, J.-P.; Saliba, M.; Su'ait, M. S.; Bella, F., Perovskite Solar Cells: From the Laboratory to the Assembly Line. *Chemistry – A European Journal* **2018,** *24* (13), 3083-3100.

108. Xiao, Y.; Han, G.; Zhou, H.; Wu, J., An efficient titanium foil based perovskite solar cell: using a titanium dioxide nanowire array anode and transparent poly(3,4-ethylenedioxythiophene) electrode. *RSC Advances* **2016,** *6* (4), 2778-2784.

109. Hagfeldt, A.; Boschloo, G.; Sun, L.; Kloo, L.; Pettersson, H., Dye-Sensitized Solar Cells. *Chemical Reviews* **2010,** *110* (11), 6595-6663.

110. Wu, Z.; Song, T.; Sun, B., Carbon-Based Materials Used for Perovskite Solar Cells. *ChemNanoMat* **2017,** *3* (2), 75-88.

111. Bi, C.; Shao, Y.; Yuan, Y.; Xiao, Z.; Wang, C.; Gao, Y.; Huang, J.,

Understanding the formation and evolution of interdiffusion grown organolead halide perovskite thin films by thermal annealing. *Journal of Materials Chemistry A* **2014,** *2* (43), 18508-18514.

112. Rajput, P.; Tiwari, G. N.; Sastry, O. S.; Bora, B.; Sharma, V., Degradation of mono-crystalline photovoltaic modules after 22years of outdoor exposure in the composite climate of India. *Solar Energy* **2016,** *135*, 786-795.

113. Kim, N.-K.; Min, Y. H.; Noh, S.; Cho, E.; Jeong, G.; Joo, M.; Ahn, S.-W.; Lee, J. S.; Kim, S.; Ihm, K.; Ahn, H.; Kang, Y.; Lee, H.-S.; Kim, D., Investigation of Thermally Induced Degradation in CH3NH3PbI3 Perovskite Solar Cells using In-situ Synchrotron Radiation Analysis. *Scientific Reports* **2017,** *7* (1), 4645.

114. Zhou, H.; Chen, Q.; Li, G.; Luo, S.; Song, T.-b.; Duan, H.-S.; Hong, Z.; You, J.; Liu, Y.; Yang, Y., Interface engineering of highly efficient perovskite solar cells. *Science* **2014,** *345* (6196), 542-546.

115. Moisture assisted perovskite film growth for high performance solar cells. *Applied Physics Letters* **2014,** *105* (18), 183902.

116. Heo, J. H.; Im, S. H.; Noh, J. H.; Mandal, T. N.; Lim, C.-S.; Chang, J. A.; Lee, Y. H.; Kim, H.-j.; Sarkar, A.; Nazeeruddin, M. K.; Grätzel, M.; Seok, S. I., Efficient inorganic-organic hybrid heterojunction solar cells containing perovskite compound and polymeric hole conductors. *Nature Photonics* **2013,** *7*, 486.

117. Philippe, B.; Park, B.-W.; Lindblad, R.; Oscarsson, J.; Ahmadi, S.; Johansson, E. M. J.; Rensmo, H., Chemical and Electronic Structure Characterization of Lead Halide Perovskites and Stability Behavior under Different Exposures-A Photoelectron Spectroscopy Investigation. *Chemistry of Materials* **2015,** *27* (5), 1720-1731.

118. Whitfield, P. S.; Herron, N.; Guise, W. E.; Page, K.; Cheng, Y. Q.; Milas, I.; Crawford, M. K., Structures, Phase Transitions and Tricritical Behavior of the Hybrid Perovskite Methyl Ammonium Lead Iodide. *Scientific Reports* **2016,** *6*, 35685.

119. Saliba, M.; Matsui, T.; Seo, J.-Y.; Domanski, K.; Correa-Baena, J.-P.; Nazeeruddin, M. K.; Zakeeruddin, S. M.; Tress, W.; Abate, A.; Hagfeldt, A.; Grätzel, M., Cesium-containing triple cation perovskite solar cells: improved stability, reproducibility and high efficiency. *Energy & Environmental Science* **2016,** *9* (6), 1989-1997.

120. Chu, Z.; Yang, M.; Schulz, P.; Wu, D.; Ma, X.; Seifert, E.; Sun, L.; Li, X.; Zhu, K.; Lai, K., Impact of grain boundaries on efficiency and stability of organic-inorganic trihalide perovskites. *Nature Communications* **2017,** *8* (1), 2230.

121. Ito, S.; Tanaka, S.; Manabe, K.; Nishino, H., Effects of Surface Blocking Layer of Sb2S3 on Nanocrystalline TiO2 for CH3NH3PbI3 Perovskite Solar Cells. *The Journal of Physical Chemistry C* **2014,** *118* (30), 16995-17000.

122. Li, Y.; Cooper, J. K.; Liu, W.; Sutter-Fella, C. M.; Amani, M.; Beeman, J. W.;

Javey, A.; Ager, J. W.; Liu, Y.; Toma, F. M.; Sharp, I. D., Defective TiO2 with high photoconductive gain for efficient and stable planar heterojunction perovskite solar cells. *Nature Communications* **2016,** *7*, 12446.

123. Sherkar, T. S.; Momblona, C.; Gil-Escrig, L.; Ávila, J.; Sessolo, M.; Bolink, H. J.; Koster, L. J. A., Recombination in Perovskite Solar Cells: Significance of Grain Boundaries, Interface Traps, and Defect Ions. *ACS Energy Letters* **2017,** *2* (5), 1214-1222.

124. Abdi-Jalebi, M.; Andaji-Garmaroudi, Z.; Cacovich, S.; Stavrakas, C.; Philippe, B.; Richter, J. M.; Alsari, M.; Booker, E. P.; Hutter, E. M.; Pearson, A. J.; Lilliu, S.; Savenije, T. J.; Rensmo, H.; Divitini, G.; Ducati, C.; Friend, R. H.; Stranks, S. D., Maximizing and stabilizing luminescence from halide perovskites with potassium passivation. *Nature* **2018,** *555*, 497.

125. Noh, J. H.; Im, S. H.; Heo, J. H.; Mandal, T. N.; Seok, S. I., Chemical Management for Colorful, Efficient, and Stable Inorganic-Organic Hybrid Nanostructured Solar Cells. *Nano Letters* **2013,** *13* (4), 1764-1769.

126. Lee, M. M.; Teuscher, J.; Miyasaka, T.; Murakami, T. N.; Snaith, H. J., Efficient Hybrid Solar Cells Based on Meso-Superstructured Organometal Halide Perovskites. *Science* **2012,** *338* (6107), 643-647.

127. Edri, E.; Kirmayer, S.; Kulbak, M.; Hodes, G.; Cahen, D., Chloride Inclusion and Hole Transport Material Doping to Improve Methyl Ammonium Lead Bromide Perovskite-Based High Open-Circuit Voltage Solar Cells. *The Journal of Physical Chemistry Letters* **2014,** *5* (3), 429-433.

128. Yu, H.; Wang, F.; Xie, F.; Li, W.; Chen, J.; Zhao, N., The Role of Chlorine in the Formation Process of "CH3NH3PbI3-xClx" Perovskite. *Advanced Functional Materials* **2014,** *24* (45), 7102-7108.

129. de Quilettes, D. W.; Vorpahl, S. M.; Stranks, S. D.; Nagaoka, H.; Eperon, G. E.; Ziffer, M. E.; Snaith, H. J.; Ginger, D. S., Impact of microstructure on local carrier lifetime in perovskite solar cells. *Science* **2015,** *348* (6235), 683-686.

130. Misra, R. K.; Aharon, S.; Li, B.; Mogilyansky, D.; Visoly-Fisher, I.; Etgar, L.; Katz, E. A., Temperature- and Component-Dependent Degradation of Perovskite Photovoltaic Materials under Concentrated Sunlight. *The Journal of Physical Chemistry Letters* **2015,** *6* (3), 326-330.

131. Tunable bandgap in hybrid perovskite CH3NH3Pb(Br3-yXy) single crystals and photodetector applications. *AIP Advances* **2016,** *6* (4), 045115.

132. Saliba, M.; Matsui, T.; Domanski, K.; Seo, J.-Y.; Ummadisingu, A.; Zakeeruddin, S. M.; Correa-Baena, J.-P.; Tress, W. R.; Abate, A.; Hagfeldt, A.; Grätzel, M., Incorporation of rubidium cations into perovskite solar cells improves photovoltaic performance. *Science* **2016,** *354* (6309), 206-209.

133. Zhao, W.; Yao, Z.; Yu, F.; Yang, D.; Liu, S., Alkali Metal Doping for Improved CH3NH3PbI3 Perovskite Solar Cells. *Advanced Science* **2018,** *5* (2), 1700131.

134. Bag, S.; Durstock, M. F., Large Perovskite Grain Growth in Low-Temperature Solution-Processed Planar p-i-n Solar Cells by Sodium Addition. *ACS Applied Materials & Interfaces* **2016,** *8* (8), 5053-5057.

135. Bai, X.; Zou, X.; Zhu, J.; Pei, Y.; Yang, Y.; Jin, W.; Chen, D., Effect of Rb doping on modulating grain shape and semiconductor properties of MAPbI3 perovskite layer. *Materials Letters* **2018,** *211*, 328-330.

136. Au - Abdi-Jalebi, M.; Au - Dar, M. I.; Au - Sadhanala, A.; Au - Senanayak, S. P.; Au - Grätzel, M.; Au - Friend, R. H., Monovalent Cation Doping of CH3NH3PbI3 for Efficient Perovskite Solar Cells. *JoVE* **2017,** (121), e55307.

137. Sears, F. W. S., G.L., Thermodynamics, Kinetic Theory, and Statistical Thermodynamics. **1975**, pp. 286-291.

138. http://tools.thermofisher.com/content/sfs/brochures/D16099~.pdf.

139. Bisquert, J.; Qi, Y.; Ma, T.; Yan, Y., Advances and Obstacles on Perovskite Solar Cell Research from Material Properties to Photovoltaic Function. *ACS Energy Letters* **2017,** *2* (2), 520-523.

140. Marco, F.; Roberto, M., Basics of Thin Film Solar Cells. **2013**.

141. Bonnell, D. A.; Kalinin, S. V., Scanning probe microscopy for energy research. **2013**.

142. STM, http://www.hk-phy.org/atomic_world/stm/stm03_e.html.

143. Jin, H.; Debroye, E.; Keshavarz, M.; Scheblykin, I. G.; Roeffaers, M. B. J.; Hofkens, J.; Steele, J. A., It's a trap! On the nature of localised states and charge trapping in lead halide perovskites. *Materials Horizons* **2020,** *7* (2), 397-410.

144. K. Siegbahn, E. A., Nova Acta Regiae Soc.Sci., Ser. IV, ; Physics., N. P. i., **(1967),** *Vol. 20*.

145. Scientific, T. XPS/UPS/IPES. https://xpssimplified.com/UPS.php.

146. https://www.ulvac-phi.com/en/products/xps/versaprobe-iii/leips/.

147. https://www.jst.go.jp/chizai/en/cips_details/pdf_2/5-20.pdf, H. Y., Low Energy Inverse Photoemission Spectroscopy (LEIPS).

148. Pavia, D. L.; Lampman, G. M.; Kriz, G. S.; Vyvyan, J. R., INTRODUCTION TO SPECTROSCOPY. *Fourth Edition* (Fourth Edition).

149. Ramaiah, G.; Ramesh.K.P; Bhatia, D., Structural Analysis Of Merino Wool, Pashmina And Angora Fibers Using Analytical Instruments Like Scanning Electron Microscope And Infra-Red Spectroscopy. *International Journal of Engineering Technology Science and Research 2394-3386* **2017,** *4*, 112-125.

150. https://jascoinc.com/learning-center/theory/fundamentals-ftir-spectroscopy/.

151. https://serc.carleton.edu/research_education/geochemsheets/techniques/SXD.html.

152. https://www.specs-group.com/fileadmin/user_upload/products/application-notes/ANote_EnviroESCA__401_Gas_Cluster_Ion_Beam__GCIB__sputtering_with_EnviroESCA.pdf.

153. Kojima, A.; Teshima, K.; Shirai, Y.; Miyasaka, T., Organometal Halide Perovskites as Visible-Light Sensitizers for Photovoltaic Cells. *J. Am. Chem. Soc.* **2009,** *131*, 6050.

154. PbI2, ID:mp-22893, https://materialsproject.org/materials/mp-22893/#.

155. Haiss, W.; Sass, J. K.; Gao, X.; Weaver, M. J., Iodine adlayer structures on Au(111) as discerned by atomic-resolution scanning tunnelling microscopy: relation to iodide electrochemical adsorption. *Surface Science* **1992,** *274* (3), L593-L598.

156. She, L.; Liu, M.; Li, X.; Cai, Z.; Zhong, D., Growth and interfacial structure of methylammonium lead iodide thin films on Au(111). *Surf.Sci* **2017,** *656*, 17-23.

157. Li, J.; Li, R.-F.; Wang, G.-C., A Systematic Density Functional Theory Study of the C-N Bond Cleavage of Methylamine on Metals. *The Journal of Physical Chemistry B* **2006,** *110* (29), 14300-14303.

158. Kresse, G.; Furthmüller, J., Efficient iterative schemes for ab initio total-energy calculations using a plane-wave basis set. *Phys. Rev. B* **1996,** *54* (16), 11169-11186.

159. Perdew, J. P.; Burke, K.; Ernzerhof, M., Generalized Gradient Approximation Made Simple. *PRL* **1996,** *77* (18), 3865-3868.

160. Kresse, G.; Joubert, D., From ultrasoft pseudopotentials to the projector augmented-wave method. *Phys. Rev. B* **1999,** *59* (3), 1758-1775.

161. Weaver, C.; Brown, L. C., Diffusion in evaporated films of gold-lead. *The Philosophical Magazine: A Journal of Theoretical Experimental and Applied Physics* **1963,** *8* (92), 1379-1393.

162. Yang, C.-H.; Yau, S.-L.; Fan, L.-J.; Yang, Y.-W., Deposition of lead iodide films on Rh(100) electrodes from colloidal solutions--the effect of an iodine adlayer. *Surface Science* **2003,** *540* (2), 274-284.

163. Caputo, M.; Cefarin, N.; Radivo, A.; Demitri, N.; Gigli, L.; Plaisier, J. R.; Panighel, M.; Di Santo, G.; Moretti, S.; Giglia, A.; Polentarutti, M.; De Angelis, F.; Mosconi, E.; Umari, P.; Tormen, M.; Goldoni, A., Electronic structure of MAPbI3 and MAPbCl3: importance of band alignment. *Scientific Reports* **2019,** *9* (1), 15159.

164. Leguy, A. M. A.; Azarhoosh, P.; Alonso, M. I.; Campoy-Quiles, M.; Weber, O. J.; Yao, J.; Bryant, D.; Weller, M. T.; Nelson, J.; Walsh, A.; van Schilfgaarde, M.; Barnes, P. R. F., Experimental and theoretical optical properties of methylammonium lead halide perovskites. *Nanoscale* **2016,** *8* (12), 6317-6327.

165. Li, N.; Niu, X.; Chen, Q.; Zhou, H., Towards commercialization: the operational stability of perovskite solar cells. *Chem. Soc. Rev* **2020**.

166. Qiu, L.; He, S.; Ono, L. K.; Qi, Y., Progress of Surface Science Studies on ABX3-Based Metal Halide Perovskite Solar Cells. *Advanced Energy Materials n/a* (n/a), 1902726.

167. Saliba, M., Polyelemental, Multicomponent Perovskite Semiconductor Libraries through Combinatorial Screening. *Adv. Energy Mater.* **2019,** *9* (25), 1803754.

168. Jeon, N. J.; Noh, J. H.; Yang, W. S.; Kim, Y. C.; Ryu, S.; Seo, J.; Seok, S. I., Compositional engineering of perovskite materials for high-performance solar cells. *Nature* **2015,** *517* (7535), 476-480.

169. Dunlap-Shohl, W. A.; Zhou, Y.; Padture, N. P.; Mitzi, D. B., Synthetic Approaches for Halide Perovskite Thin Films. *Chemical Reviews* **2019,** *119* (5), 3193-3295.

170. Ono, L. K.; Juarez-Perez, E. J.; Qi, Y. B., Progress on Perovskite Materials and Solar Cells with Mixed Cations and Halide Anions. *ACS Applied Materials & Interfaces* **2017,** *9* (36), 30197-30246.

171. Pool, V. L.; Gold-Parker, A.; McGehee, M. D.; Toney, M. F., Chlorine in PbCl2-Derived Hybrid-Perovskite Solar Absorbers. *Chemistry of Materials* **2015,** *27* (21), 7240-7243.

172. Liu, Z.; Ono, L. K.; Qi, Y. B., Additives in metal halide perovskite films and their applications in solar cells. *J. Energy Chem* **2020,** *46*, 215-228.

173. Ng, T.-W.; Chan, C.-Y.; Lo, M.-F.; Guan, Z. Q.; Lee, C.-S., Formation chemistry of perovskites with mixed iodide/chloride content and the implications on charge transport properties. *J. Mater. Chem. A* **2015,** *3* (17), 9081-9085.

174. Wang, M.; Li, B.; Siffalovic, P.; Chen, L.-C.; Cao, G.; Tian, J., Monolayer-like hybrid halide perovskite films prepared by additive engineering without antisolvents for solar cells. *J. Mater. Chem. A* **2018,** *6* (31), 15386-15394.

175. Bouchard, M.; Hilhorst, J.; Pouget, S.; Alam, F.; Mendez, M.; Djurado, D.; Aldakov, D.; Schülli, T.; Reiss, P., Direct Evidence of Chlorine-Induced Preferential Crystalline Orientation in Methylammonium Lead Iodide Perovskites Grown on TiO2. *J. Am. Chem. Soc.* **2017,** *121* (14), 7596-7602.

176. Muscarella, L. A.; Hutter, E. M.; Sanchez, S.; Dieleman, C. D.; Savenije, T. J.; Hagfeldt, A.; Saliba, M.; Ehrler, B., Crystal Orientation and Grain Size: Do They Determine Optoelectronic Properties of MAPbI3 Perovskite? *J. Phys. Chem. Lett.* **2019,** *10* (20), 6010-6018.

177. Odysseas Kosmatos, K.; Theofylaktos, L.; Giannakaki, E.; Deligiannis, D.; Konstantakou, M.; Stergiopoulos, T., Methylammonium Chloride: A Key Additive for Highly Efficient, Stable, and Up-Scalable Perovskite Solar Cells. *Energy Environ. Sci.* **2019,** *2* (2), 79-92.

178. Li, Y.; Sun, W.; Yan, W.; Ye, S.; Peng, H.; Liu, Z.; Bian, Z.; Huang, C., High-Performance Planar Solar Cells Based On CH3NH3PbI3-xClx Perovskites with

Determined Chlorine Mole Fraction. *Adv. Funct. Mater* **2015,** *25* (30), 4867-4873.

179. Zhang, H.; Liao, Q.; Wang, X.; Hu, K.; Yao, J.; Fu, H., Controlled Substitution of Chlorine for Iodine in Single-Crystal Nanofibers of Mixed Perovskite MAPbI3-xClx. *Small* **2016,** *12* (28), 3780-3787.

180. Colella, S.; Mosconi, E.; Fedeli, P.; Listorti, A.; Gazza, F.; Orlandi, F.; Ferro, P.; Besagni, T.; Rizzo, A.; Calestani, G.; Gigli, G.; De Angelis, F.; Mosca, R., MAPbI3-xClx Mixed Halide Perovskite for Hybrid Solar Cells: The Role of Chloride as Dopant on the Transport and Structural Properties. *Chem. Mater.* **2013,** *25* (22), 4613-4618.

181. Yin, W.-J.; Chen, H.; Shi, T.; Wei, S.-H.; Yan, Y., Origin of High Electronic Quality in Structurally Disordered CH3NH3PbI3 and the Passivation Effect of Cl and O at Grain Boundaries. *Adv. Electron. Mater* **2015,** *1* (6), 1500044.

182. Mosconi, E.; Amat, A.; Nazeeruddin, M. K.; Grätzel, M.; De Angelis, F., First-Principles Modeling of Mixed Halide Organometal Perovskites for Photovoltaic Applications. *J. Phys. Chem. C* **2013,** *117* (27), 13902-13913.

183. Cai, L.; She, L. M.; Qin, H. L.; Xu, L.; Zhong, D. Y., Monolayer methylammonium lead iodide films deposited on Au(111). *Surf. Sci.* **2018,** *675*, 78-82.

184. Ralaiarisoa, M.; Busby, Y.; Frisch, J.; Salzmann, I.; Pireaux, J.-J.; Koch, N., Correlation of annealing time with crystal structure, composition, and electronic properties of CH3NH3PbI3-xClx mixed-halide perovskite films. *Phys. Chem. Chem. Phys.* **2017,** *19* (1), 828-836.

185. Starr, D. E.; Sadoughi, G.; Handick, E.; Wilks, R. G.; Alsmeier, J. H.; Köhler, L.; Gorgoi, M.; Snaith, H. J.; Bär, M., Direct observation of an inhomogeneous chlorine distribution in CH3NH3PbI3-xClx layers: surface depletion and interface enrichment. *Energy Environ. Sci.* **2015,** *8* (5), 1609-1615.

186. Colella, S.; Mosconi, E.; Pellegrino, G.; Alberti, A.; Guerra, V. L. P.; Masi, S.; Listorti, A.; Rizzo, A.; Condorelli, G. G.; De Angelis, F.; Gigli, G., Elusive Presence of Chloride in Mixed Halide Perovskite Solar Cells. *J. Phys. Chem. Lett.* **2014,** *5* (20), 3532-3538.

187. Nan, G.; Zhang, X.; Abdi Jalebi, M.; Andaji-Garmaroudi, Z.; Stranks, S.; Lu, G.; Beljonne, D., How Methylammonium Cations and Chlorine Dopants Heal Defects in Lead Iodide Perovskites. *Adv. Energy Mater.* **2018,** *8*, 1702754.

188. AFLOW, ENCYCLOPEDIA OF CRYSTALLOGRAPHIC PROTOTYPES.

189. A Yoshida, H., Principle and application of low energy inverse photoemission spectroscopy: A new method for measuring unoccupied states of organic semiconductors. 2015.

190. Grimme, S.; Antony, J.; Ehrlich, S.; Krieg, H., A consistent and accurate ab initio parametrization of density functional dispersion correction (DFT-D) for the 94

elements H-Pu. *J. Chem. Phys.* **2010,** *132* (15), 154104.

191. Fang, Y.; Dong, Q.; Shao, Y.; Yuan, Y.; Huang, J., Highly narrowband perovskite single-crystal photodetectors enabled by surface-charge recombination. *Nat. Photonics* **2015,** *9* (10), 679-686.

192. Cao, X.; Zhi, L.; Jia, Y.; Li, Y.; Zhao, K.; Cui, X.; Ci, L.; Ding, K.; Wei, J., Enhanced efficiency of perovskite solar cells by introducing controlled chloride incorporation into MAPbI3 perovskite films. *Electrochim. Acta* **2018,** *275*, 1-7.

193. Darwent, B. d.; National Standard Reference Data, S., Bond dissociation energies in simple molecules. **1970.**

194. Cottrell, T. L., The strengths of chemical bonds. **1958.**

195. Lu, C.; Choi, I. T.; Woo, M. Y.; Kim, C. K.; Kim, C. H.; Kim, H. K., Well-grown low-defect MAPbI3-xClx films for perovskite solar cells with over 20% efficiency fabricated under controlled ambient humidity conditions. *Electrochim. Acta* **2019,** *326*, 134950.

196. Geng, W.; Tong, C.-J.; Tang, Z.-K.; Yam, C.; Zhang, Y.-N.; Lau, W.-M.; Liu, L.-M., Effect of surface composition on electronic properties of methylammonium lead iodide perovskite. *Journal of Materiomics* **2015,** *1* (3), 213-220.

197. Li, Q.; Chen, Z.; Tranca, I.; Gaastra-Nedea, S.; Smeulders, D.; Tao, S., Compositional effect on water adsorption on metal halide perovskites. *Applied Surface Science* **2021,** *538*, 148058.

198. Simulation, P. a. m. V., Pb atomic model by VESTA Simulation. *https://materialsproject.org/materials/mp-20483/*.

199. Crepaldi, A.; Pons, S.; Frantzeskakis, E.; Calleja, F.; Etzkorn, M.; Seitsonen, A. P.; Kern, K.; Brune, H.; Grioni, M., Combined ARPES and STM study of Pb/Au(111) Moir¥'e structure: One overlayer, two symmetries. *Physical Review B* **2013,** *87* (11), 115138.

200. https://zola.lbl.gov/materials/mp-22898/#, KI Calculated Atomic Model.